Rudolf Neu

Tungsten as a Plasma Facing Material in Fusion Devices

IPP 10/25
December 2003

Tungsten as a plasma facing material in fusion devices

Habilitationsschrift

Der Fakultät für Mathematik und Physik

der Eberhard-Karls-Universität zu Tübingen

vorgelegt

von

Rudolf Neu

Max-Planck-Institut für Plasmaphysik

D-85748 Garching

2003

Contents

1. Introduction

Energy has turned out to be one of the most important resources of modern times. The strongly growing population and the progressive development of the evolving countries causes a rapid growth in energy consumption. A large part of this energy is made available by burning fossil fuels. Not only are these resources limited, but there is also now world wide recognition that the production of CO_2 provokes the 'so-called green house effect', which leads to global warming with strong impacts on the human society.
In the long term, there may be only three alternative ways to supply the energy: fission, renewables and fusion. It is unlikely that one of them will be sufficient on its own.
Fission, in its usual form as boiling water or high pressure reactors, can only supply energy for a medium period of time due to limited ressources, but the fast breeding reactor which is technically fastidious could solve this problem. However, at the moment, there is little consensus on the use of fission power.
The renewable energies (solar, wind, tides, plants, ...) already deliver some energy and a great potential is foreseen by its proponents, but their large-scale technical application is not yet proven [1].
Fusion is the least developed of the three alternatives, but it has, nevertheless a high potential for future energy supply since its raw materials are deuterium and lithium, which are largely available. There are two major principles in fusion: inertial confinement fusion (ICF) and magnetically confinement fusion (MCF). In the concept of inertial fusion a deuterium/tritium pellet is rapidly compressed (ns-range) to densities of about 10^{31} particles/m^3 and the fusion reaction takes place before the expansion sets in. The compression is currently driven by a strong laser pulse ($E \approx 100$ kJ (NOVA, 1985) from 2008 onwards $E \approx 1$ MJ (NIF), but a future reactor may use a heavy ion beam as a driver (see [2–6] and references therein). A major problem with ICF is how to overcome dynamical Rayleigh Taylor instabilities during the compression phase and to supply drivers with efficiencies high enough for economic energy production.
MCF uses toroidal magnetic field configurations to confine a hot ($kT \approx 10$ keV) and rather thin plasma ($n \approx 10^{20}$ particles/m^3). The heating is provided externally by neutral beam injection (NBI) or radio-frequency (RF) heating. The concept is explained in more detail in the appendix (A.2). Although no power plant could be built up to now, two tokamak experiments (see A.2), namely the American experiment TFTR (Tokamak

Fusion Test Reactor) and the European JET (Joint European Torus) in particular have demonstrated successfully the production of substantial fusion power (over 10 MW, [7] and references therein).

The next step in MCF research will be the construction of a device, which produces much more fusion power than that which is externally provided for heating (power amplification $Q > 10$), named ITER(-FEAT) [8,9]. The physics basis for ITER is assembled in [10]. The ITER design meets all the objectives of demonstrating the scientific and technological feasibility of controlled fusion, allowing some margins in physics and technology. Nevertheless, a very important question, which has to be addressed in the context of this future research reactor, is the choice of the armour materials for the first wall.

During the last two decades of fusion research almost all fusion devices have implemented low-Z carbon based materials as plasma facing materials (PFM). This has improved the performance of these devices significantly and was important for the steady increase of the fusion product of pressure and energy confinement. Optimisation of the core plasma performance was the main driver for graphite, and a large operational experience and database exists with these materials as plasma facing components, which allow a reliable prediction of the core plasma performance for future devices. Graphite materials are used in general with the help of special wall conditioning procedures like boronisation or siliconisation [11, 12] which reduce the oxygen impurities and improve the density control. However, the development of ITER needs an integrated approach where several requirements have to be fulfilled simultaneously. While the contamination of the core plasma by impurities released from the walls must be kept below a critical level [10], the plasma facing components (PFCs) have to exhaust the α-particle fusion and external heating power together with the helium ash and to withstand off normal high heat loads from disruptions, vertical displacement events (VDEs), edge localised modes (ELMs) or runaway generation. For economic reasons a sufficient lifetime of the first wall components is essential. One of the most critical issues from the present view is the long term retention of the radioactive tritium fuel in the wall components which has to be limited and controlled for reasons of fuel supply, safety and also public acceptance of fusion energy [10]. The concerns and disadvantages of graphite materials are related to the latter points and, generally speaking, coupled with its chemical interaction with hydrogen and oxygen. Chemical erosion [13] leads to significant erosion yields even under low temperature, cold plasma conditions and can seriously limit the lifetime under special conditions. A review on the current status of the use of carbon based PFC is found in [14]. Since the plasma is to a large extent a closed system, the released carbon impurities migrate long distances and can finally form thick deposits on special locations. These deposits are hydrogen rich and, as the tritium experiments in JET and TFTR have demonstrated, contain a major fraction of the total tritium fuel supplied to the machines [15, 16]. Extrapolation of the fuel retention to a steady state burning fusion

plasma is difficult but we have to be prepared that retention might be unacceptable and will not allow the operation of the device with tritium on a longer time scale [17–19]. This is a very serious concern and calls urgently for reconsidering the choice of plasma facing components in general. The most promising alternative category of plasma facing materials are high-Z materials. These materials have acceptable thermo-mechanical properties, the possible advantage of very low or negligible erosion at low plasma temperatures and a moderate uptake of tritium [20]. These advantages compete with their strong poisoning effect of the plasma due to cooling by radiation losses, if the impurity source is too high and/or impurity transport leads to accumulation in the central plasma. After the first negative experiences due to strong central cooling through tungsten at the Princeton Large Torus (PLT) [21] and through Mo at JT-60 [22] high-Z material was no longer used (except for high field/high density devices). Only recently, driven by the needs of a reactor, experiments using Mo and W as PFC were resumed (see [23] for further reference).

A strong effort has been put into tungsten investigations at the Garching tokamak ASDEX Upgrade (see B.1). Although much smaller than a future reactor, there are a lot of properties which are relevant to reactor studies. Namely, the closely scaled geometry of the device, especially of the divertor, and plasma edge parameters very close to that envisaged in a reactor. After preparatory experiments concerning the performance of coatings, detection of tungsten in the plasma and probe erosion, a fully coated tungsten divertor was installed in ASDEX Upgrade during 1996. As a further step in the tungsten programme, W was used as a PFC in the main chamber in order to pursue the aim of the total elimination of carbon. During the experimental campaign in 2000 an area of 1.2 m^2 of the central column was coated with W and actually, since 2002 ASDEX Upgrade has been operated with an almost completely W covered central column. During the experiments performed at ASDEX Upgrade, the tungsten influx was very low and normally the radiation from W comprised only a minor fraction of the total radiation. For the first time, the influx as well as the W concentration could be quantified by the sensitive spectroscopic tools which were developed. Spectral lines from a broad range of ionisation states were recorded in the VUV and the soft X-ray spectral region and the spectra could be simulated by *ab initio* atomic physics calculations to a very satisfactory level. The experiments proved that the use of W as a PFM is feasable in a divertor tokamak and it could be shown that central heating, which will prevail in a fusion reactor, allows the central W concentration to be reduced very efficiently.

Although quite a few questions are addressed in ASDEX Upgrade and other fusion devices, there are some relevant areas which have to be encountered in other dedicated experiments. These will be described shortly in Sec. 2. The experimental tools, which were developed particularly for these investigations are described in Chap. 3. In Chap. 4 the results of the spectroscopic investigations and their comparison to *ab initio* atomic

physics calculations are discussed. In Chap. 5 a theoretical description of the transport processes relevant to the tungsten investigations is given. The W experiments stated above and their results are described in Chap. 6 and the comparison with experiments at other devices as well as the resulting perspectives for a reactor are given in Chap. 7. The last chapter (Chap. 8) summarises the results and gives some concluding remarks. The basic concepts of magnetically confined nuclear fusion, the tokamak device ASDEX Upgrade, as well as the main plasma diagnostics are given in the Appendix.

2. Background

The use of tungsten as a plasma facing material in a fusion device is primarily motivated by its superior thermo-mechanical properties and its very low erosion under steady state operation conditions. However, besides these very specific advantages there are a lot of properties which are relevant in the fusion reactor environment. Each of them has to be addressed in specific experimental and theoretical approaches to specify the behaviour of tungsten in an integrated approach. Only a few of these properties can be covered here, as a complete assessment would go beyond the scope of this work. In this chapter, detailed reasons for the investigation of tungsten will be given and the current research on subjects, which cannot be treated further, will be presented.

2.1 Role of Impurities in an Ignited Plasma

In a zero dimensional model the condition for ignition is given as the power balance of the energy producing fusion reaction (see A.1.1) and the energy losses which can be approximated by the empirical energy confinement time (see A.1.2). However, equation A.9 can only be used to get a rough estimate for ignition, since there the energy confinement time τ_E only represents the transport losses. The effect of impurities can be treated in more detail, by taking into account losses by radiation (the plasma is optically thin for most of the frequencies) and dilution of the fuel. All light impurities are fully ionised in fusion relevant plasmas. Therefore the loss originating from impurity radiation is purely due to Bremsstrahlung (see high temperature part of radiation loss parameters in Fig. 2.1) and can be given as

$$P_{brems} = c_1 \cdot n^2 \cdot Z_{eff} \cdot (kT)^{1/2} \ . \tag{2.1}$$

c_1 is a constant ($c_1 = 5.4 \cdot 10^{-37}$ $\mathrm{Wm^3keV^{-1/2}}$) and Z_{eff} gives the factor of the enhancement of the Bremsstrahlung over the one from a pure hydrogen plasma. It is defined as

$$Z_{eff} = \frac{\Sigma_j n_j Z_j^2}{\Sigma_j n_j Z_j} = \frac{\Sigma_j n_j Z_j^2}{n}, \tag{2.2}$$

where in the last part the quasi-neutrality $n = \Sigma_j n_j Z_j$ of the plasma is used. However, in the case of the involvement of high-Z impurities, Z_{eff} can no longer be used to

characterise the radiation losses, since high-Z elements will not be fully ionised and they can radiate substantial power by line radiation. Therefore, the impurities will be treated explicitely in the power balance investigations presented below.

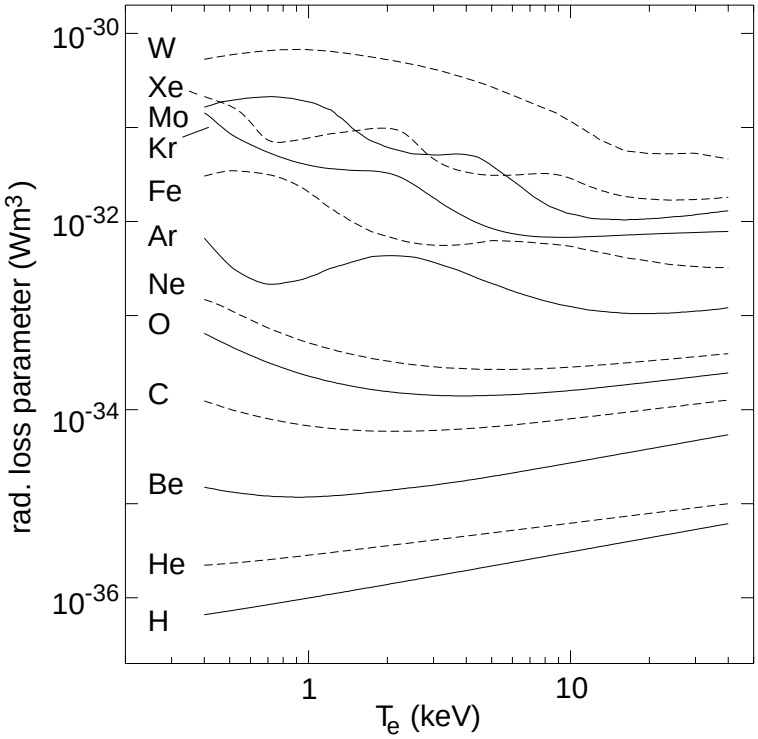

Figure 2.1: Radiation loss parameter calculated within the average ion model in coronal equilibrium [24, 25].

In this context He plays a distinct role because power production and dilution are closely coupled via the residence time of the He ions in the plasma. This residence time is given by the transport of the He ash inside the plasma as well as by the probability by which the He is pumped once it reached the plasma edge. Both processes are subsumed under an effective He confinement time τ^*_{He}, which can be formally expressed by the He content over the fusion rate, which in steady state must equal the exhaust rate:

$$\frac{n_i^2}{4} < \sigma v >= \frac{n_{He}}{\tau^*_{He}} = \frac{f_{He} n}{\varrho \tau_E} \tag{2.3}$$

with

$$\varrho = \frac{\tau^*_{He}}{\tau_E}. \tag{2.4}$$

and f_{He} being the fraction of He. In the presence of He ash and of an additional impurity with charge number Z and fraction f_z the fraction of fuel ions (or dilution parameter) f_i can be written as:

$$f_i = \frac{n_i}{n} = 1 - 2f_{He} - Zf_z \tag{2.5}$$

The fusion power density is then given by

$$P_\alpha = \frac{n^2}{4} f_i^2 < \sigma v > E_\alpha, \tag{2.6}$$

where E_{fusion} has already been replaced by E_α.
The radiation losses can now be treated explicitly by taking the temperature dependent radiation loss parameters L (see Fig. 2.1) from the atomic physics calculations available from the literature [24, 25]

$$P_{rad} = n^2(f_i L_H + f_{He} L_{He} + f_z L_z). \tag{2.7}$$

Finally, the equation for the transport losses P_{transp} has to be rewritten, taking all particle densities explicitly into account:

$$P_{transp} = \frac{3}{2}\frac{kT}{\tau_E} n(2 - f_{He} - (Z-1)f_z) \tag{2.8}$$

Putting together eqs. 2.6 to eq. 2.8 one gets the following

$$(n\tau_E)_{ignit} = \frac{6kT(2 - f_{He} - (Z-1)f_z)}{< \sigma v > E_\alpha f_i^2 - 4(f_i L_H + f_{He} L_{He} + f_z L_z)} \tag{2.9}$$

as condition for ignition. Together with eqs. 2.3 and 2.5 equation 2.9 leads to a cubic equation for f_{He} which is discussed to some extent in [26]. In general, two physically meaningful solutions exist for f_{He} at a given ϱ. The lower value, also lying at lower $n\tau_E$, is the so-called confinement limited 'low He concentration mode' typically at $f_{He} \approx 5-15\%$. The other solution lies at $f_{He} \approx 15-30\%$ and is called dilution limited 'high He concentration mode'. The area of the operational space critically depends on the ϱ parameter. For the unrealistic value of $\varrho = 0$ only eq. 2.9 (with $f_{He} = 0$) holds and there is no upper limit for $n\tau_E$. For $\varrho \geq 15$ there is no stationary solution any more. The problems of He exhaust are dealt with in great detail in [27, 28]. Present day devices yield values $\varrho \leq 5$, and the He exhaust capability of ITER FEAT is designed to reach $\varrho \approx 5$ [29]. Therefore $\varrho = 5$ is adopted in the following calculations.

The operational space is additionally limited by impurities, which cause additional losses by radiation and dilution. Figure 2.2 demonstrates this for the impurities carbon and tungsten. Increasing their fraction, the operational window narrows quickly until there is finally no steady state solution at all. The maximum tolerable values are 3.0×10^{-2} in the case of C and 1.2×10^{-4} for W. As can be judged from Fig. 2.2, there is already a considerable reduction of the operational space for smaller concentrations. For tungsten the minimum in $n\tau_E$ is also shifted to higher T due to the decreasing radiation loss parameter L_W (see Fig. 2.1). The right part of the figure gives the fraction of the losses $P_{dilute}^{loss}/P_{rad}^{loss}$, where the denominator accounts for the loss of fusion power by dilution through He and the impurities, and P_{rad}^{loss} is given by eq. 2.7. For

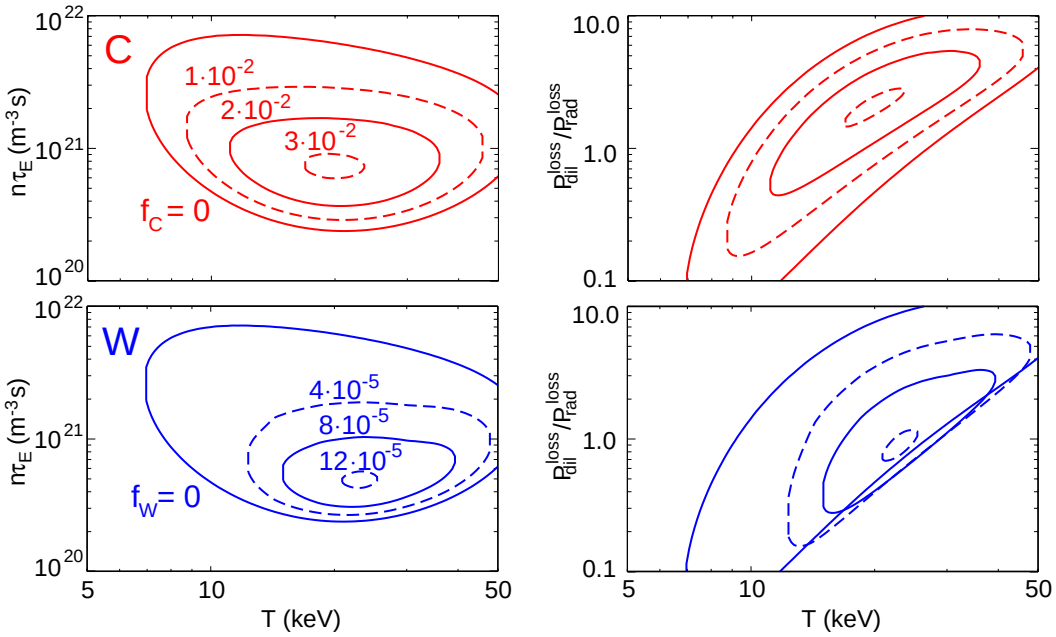

Figure 2.2: Left part: Condition for ignition $n\tau_E$ as a function of the ion temperature for different fractions of carbon (top) and tungsten (bottom). Note the different fractions for C and W. Right part: Ratio of the power loss by dilution to the power loss by radiation for C (top) and W (bottom) for the cases shown in the left part. All calculations are performed for $\varrho = \tau^*_{He}/\tau_E = 5$.

the 'high He concentration mode', the losses by dilution are higher as already stated at the beginning of the section. This is also true for the lower root in the case of higher carbon fractions. However, in case of tungsten as impurity, the loss through radiation is much more pronounced reflecting the much larger radiation loss parameter L_W.

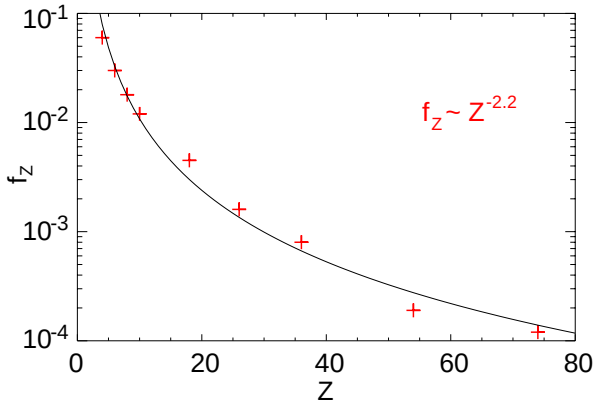

Figure 2.3: Z-dependence of the limit for the specific impurity concentration which will prevent ignition (calculation see text).

Fig. 2.3 shows the Z-dependence of the limit for the concentration which will prevent ignition, calculated under the same assumptions as given above and using the radiation loss parameters of [24, 25]. The fitted exponent should only serve as a guideline for the overall trend of the limit, since for high-Z elements, which are not fully ionised around the working point of the fusion reactor, the ionisation equilibria and the radiation will depend on the detailed structure of the ion. The value of the exponent $x = 2.2$ reflects the fact that the Bremsstrahlung, the recombina-

tion radiation and the losses by dilution are proportional to Z^2. This result is very similar to the early work of [30], but the absolute values of the concentration limits are lower since the effect of He is treated explicitly in this work. It has to be pointed out that an ignited plasma has to be operated much below these limits in order to maintain a sufficiently large operational space (see Fig. 2.2). Most of the future devices (see Sec. 7.2) foresee a material mix for the first wall components and the injection of low-Z or medium-Z elements to cool the plasma edge by radiation. This in turn will lead to even lower concentrations allowed for the individual impurities.

2.2 Erosion Processes by Particle Loads

During steady state operation, erosion by particle fluxes is identified to be the main external impurity source. These eroding particles can be plasma and impurity ions from the edge plasma, as well as high energy particles from the core mainly as neutrals from charge exchange processes. For a given background plasma and location, the central impurity contamination depends linearly on the source. Therefore, low erosion rates not only lead to longer lifetimes of the PFCs, but also to a lower impurity content. Erosion due to particle bombardment depends on the mass ratio of incident particles to surface atoms, the particle energy and flux density, the surface temperature, and other factors, as for example the chemistry between the reaction partners. The following subsections present a short overview of the physical understanding of erosion mechanisms in fusion devices.

Physical Sputtering

Physical sputtering results from elastic energy transfer from incident particles to target atoms. Surface atoms can be ejected if enough energy is transferred to overcome the surface binding energy E_s. This energy originates directly from bombarding ions or through a collision cascade involving other target atoms. At low ion energies, where the transferred energy to surface atoms is comparable with the surface binding energy, the sputtering yield decreases strongly and becomes zero below a threshold energy. The theory of physical sputtering is well-understood [31] and the threshold energy, E_{th}, for the onset of sputtering from light projectiles on a substrate consisting of heavier species can be determined from momentum and energy conservation in an elastic collision:

$$E_{th} = \frac{(m_p + m_t)^4}{4 m_p m_t (m_p - m_t)^2} E_s \tag{2.10}$$

where m_p and m_t are the projectile mass and target mass respectively. For elements considered as plasma-facing materials the surface binding energy varies only by a factor of 2.5, while the atomic mass ranges from 9 AU (Be) to 184 AU (W). This makes the threshold energy for light ions strongly dependent on the target mass. For plasma-facing materials, such as C and W, experimental sputtering data exist for H, D and He in the energy range from 10 eV up to 10 keV and they are extended to higher energies and to tritium by computer simulations [32]. The energy dependence of the yield, Y, at normal incidence can be described by the following expression:

$$Y = Q S_n(E) (1 - \frac{E_{th}}{E})^2 (1 - (\frac{E_{th}}{E})^{\frac{2}{3}}) \tag{2.11}$$

where $S_n(E)$ gives the energy dependence of the energy deposited in elastic collisions [33]. The parameters Q and E_{th} are tabulated for many ion-target combinations [32]. The

strong dependence of the sputtering yield on E_{th} leads to a pronounced dependence on atomic target mass for light ions and energies below 1 keV [31]. At grazing incidence the erosion yield is enhanced relative to the yield at normal incidence, as more energy is deposited within the near-surface layer. However, surface roughness tends to reduce the pronounced dependence of the sputtering yield on the angle of incidence. Until recently there was consensus that physical sputtering does not depend on surface temperature, but new experiments with sputtering on liquid metals seem to show an increase of Y far below the evaporation threshold [34, 35]. The energy distribution of sputtered atoms shows a mean value equivalent to $E_s/2$ [36] and therefore the energy of the sputtered atoms does not depend strongly on the material.

Chemical Erosion

For carbon, chemical reactions with incident hydrogen and oxygen ions lead to the formation of volatile molecules (hydrocarbon and CO). In principle, a chemically increased erosion yield could also be expected for tungsten by the formation of oxides with low surface binding energy. However, the amount of oxygen is greatly reduced in present day devices ($c_O \leq 1\%$) and the situation will improve even more in a fusion device with a higher duty cycle. Therefore, chemical erosion induced by O will not be treated further within this work, especially since the influence on the W erosion was found to be negligible [37].
Chemical erosion of carbon with hydrogen isotopes is a complicated multi-step process that depends on particle energy and flux, surface temperature and material properties. It dominates the carbon erosion at low ion energies, i.e. below 100 eV and at elevated temperatures. It is also found during simultaneous bombardment with inert gas or self-ions and thermal atomic hydrogen atoms. Three processes determine the chemical erosion of carbon under low energy bombardment [13]:

- Y_{therm}: The reaction of thermalised ions via hydrogenation of carbon atoms to CH_3-C complexes. At temperatures above 400 K CH_3 radicals can be released, while at temperatures above 600 K recombinative H_2 release again reduces the yield of this process.

- Y_{dam}: The thermal reaction is enhanced by radiation damage, which is characterised by a threshold energy for damage production and provides open bonds for hydrogen attachment. This process depends strongly on the crystalline perfection of the carbon material and consequently maximum yields between 10^{-3} for pyrolytic graphite and 10^{-1} for amorphous a-C:H layers are observed.

- Y_{surf}: At low surface temperature the hydrocarbons cannot be released thermally, but due to their low surface binding energy ($\approx$ 1 eV) impinging ions can sput-

ter them more easily than the carbon atoms at the surface ($E_s \approx 7.4$ eV). This process is called ion induced desorption of hydrocarbons and it is similar to the physical sputtering described above. The later two processes depend on the hydrogen isotope and Y_{therm} also depends on the impinging hydrogen flux. The processes have been reviewed recently [13], however, there is still no final answer to the flux dependence of chemical erosion.

Whereas for high-Z metals the sputtering yield is simply given by the physical sputtering, the sum

$$Y_{tot} = Y_{phys} + Y_{therm}(1 + DY_{dam}) + Y_{surf} \tag{2.12}$$

has to be taken into account in the case of carbon (D is a parameter depending on the hydrogen isotope [13]). As a consequence, there is virtually no lower threshold in the energy for carbon erosion leading to the drawbacks described in Sec. 2.3.2.

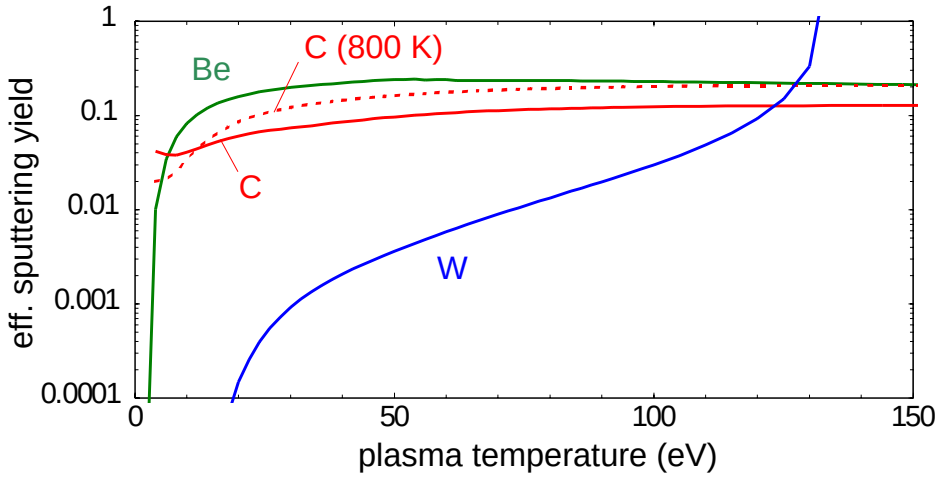

Figure 2.4: Erosion yield for Be, C, and W as a function of plasma temperature. Self-sputtering has been taken into account.

2.3 Need for W as an Alternative Material

2.3.1 Low-Z Materials as Possible Material Choice

Low-Z based materials such as graphite, boron or beryllium are preferred as plasma facing materials (PFM) in present day devices, because the plasma performance is the most important aspect [23]. Their ions are fully stripped in the plasma core which leads to a negligible contribution of line radiation and energy is lost only by Bremsstrahlung, as discussed above. Be as armour material was only used in JET as a limiter [38] and divertor material [39]. In general, the characteristics of L- and H-mode plasmas with the Be-divertor were very similar to the one with CFC targets. The impurity content in the two cases was also similar and it is believed that carbon sputtered from plasma-facing components in the main chamber played a significant role in the beryllium target experiments. In a specific melt experiment designed to assess the behaviour of plasmas on molten and melted beryllium, little evidence of vapour shielding was found. On the other hand no major increase in radiation was observed. However, the low power handling capacity of Be and the high physical sputtering yield at low particle energies prohibits its use in the divertor of a reactor-type device. Recently, liquid metal surfaces have been reconsidered as plasma facing components (see for example liquid Li-limiter at CDX-U [40]). Besides serious concerns with the integrity of the surface of a conducting liquid under electro-magnetic forces, the erosion behaviour is not well understood yet and it seems to restrict the use of Li to a very narrow operation window [34]. A comparison of tokamak behaviour with low-Z PFMs (mostly carbon) with tungsten is given in [14].

2.3.2 Behaviour of Carbon Based Plasma Facing Components

Carbon based plasma facing components (PFC) are most commonly used in todays fusion devices. The reasons for this are the very advantageous thermo-mechanical properties [41], their availability and machinability, the low activation and the low radiation loss from C for the plasma temperatures achieved in the plasma core.
Present experiments show that the carbon impurity concentration in the plasma core decreases with density reaching levels well below 1% near the density limit. Figure 2.5 shows, for example, Z_{eff}-values in JET L-mode and H-mode discharges as a function of the line averaged density [42]. As a consequence, at high densities the fuel dilution and radiation losses from carbon are tolerable, even if they are extrapolated to ITER [10,43]. However, the carbon radiation can lower the critical density for a MARFE, an instability leading to a region of cold dense plasma mainly near the X-point region [44]. This provokes a localised reduction of plasma temperature, pressure and confinement and often ends in a disruption. On the other hand, the carbon radiation from the edge and inside the divertor can significantly reduce the peak power fluxes to the divertor strike

zones. A large contribution to the radiation level from the divertor volume requires a low-Z radiator such as carbon due to the low electron temperatures there. Experiments in ASDEX Upgrade have shown that a radiation level of 80% can be achieved independently of the input power and that about half of this is radiated within the divertor volume. The radiation shows a stabilising, feedback-like behaviour, with higher radiation when the power flux crossing the last closed flux surface (LCFS) is increased [45,46].

A great advantage of carbon based materials is that they do not melt under off-normal heat loads, but the biggest concern is related to erosion under normal operation. The physical sputtering of graphite by D impact reaches the 1% level at plasma temperatures above about 15 eV and is below about 10^{-3} only for plasma temperatures below about 5 eV. However, chemical erosion by hydrocarbon formation dominates the carbon erosion and influx for most of the plasma edge conditions (see Fig. 2.4). In most reactor relevant scenarios, the erosion rate lies above 1% and under unfavourable conditions it may even be in excess of 10% (see [14] and references therein).

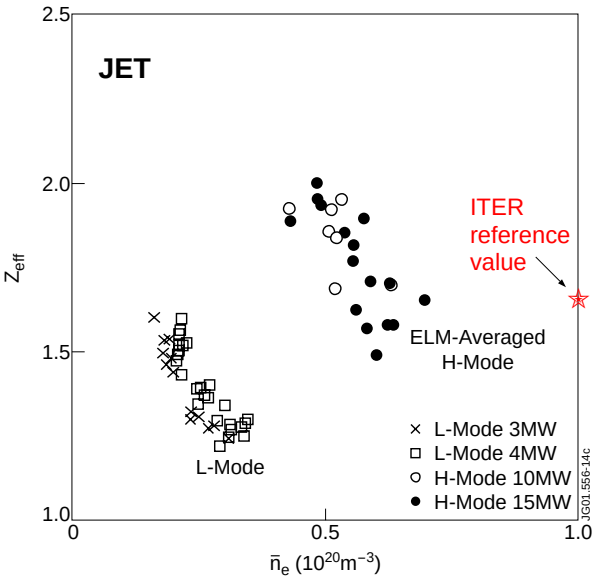

Figure 2.5: Z_{eff} for L-Mode and H-mode discharges at different heating powers as a function of the line averaged density (after [42])

The most serious consequence of such high erosion is given by the subsequent redeposition of C in remote locations. There, not only layers of C were found but also huge amounts of co-deposited hydrogen. Depending on the deposition conditions, so called soft or hard amorphous carbon films are formed. The soft layers are deposited by low energy C ions (< 50 eV) and a hydrogen content of H/C $\approx 0.8 - 1$ is reached [47]. The hard layers are formed for particle energies higher than 100 eV and contain hydrogen at a ratio of H/C ≈ 0.4, similar to carbon implanted to saturation by energetic H. However, unlike hydrogen implantation, where the thickness of the hydrogen containing zone is more or less restricted to the ion penetration depth, both kinds of film can grow virtually without limit, leading to accumulation of hydrogen, which increases linearly with exposure time. In ASDEX Upgrade both kind of layers are found below the divertor, and their continuous growth was observed throughout a campaign by quartz micro-balance measurements [48, 49]. Similar tritium rich deposits were also found after tritium experiments in JET and TFTR. They contained a substantial fraction of the total tritium fuel supplied to the machines (TFTR: $\approx 50\%$ [50], JET: $\approx 15\%$ [16]).

Extrapolation of the fuel retention to a steady state burning fusion plasma is difficult, but model calculations on the basis of the experimental observations reveal [51] that only 70 - 170 discharges would be possible [17–19] before exceeding the limit imposed by administration. This is illustrated in Fig. 2.6. The line which shows the strongest increase is given by a straight extrapolation of the JET results. These simulations clearly point to the fact that even under the the most benign circumstances the T co-deposition is not tolerable.

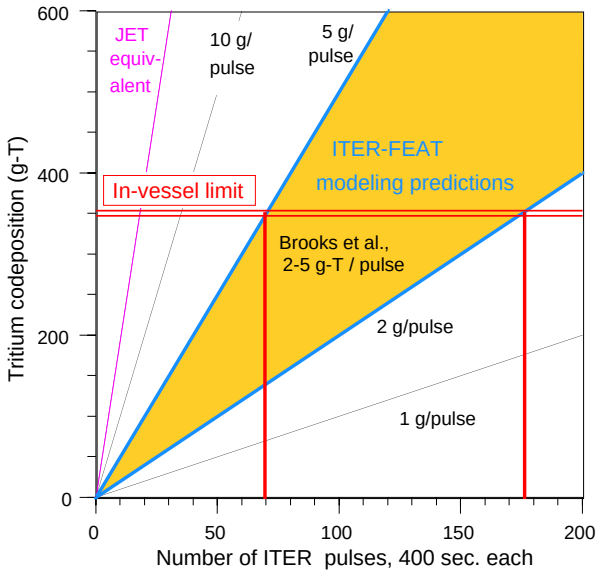

Figure 2.6: Calculated T co-deposition versus number of T-discharges in ITER. The limit of total releasable T inventory is given by administrative regulations due to radiation safety (after [19]).

Since it is not clear at the moment how to suppress it (although this is currently a matter of strong research efforts, see for example [52]), there are only two more solutions: Developing an efficient cleaning method for layer removal, or trying to omit carbon as PFM. The second approach would also be the suitable one for a future reactor, as the high C erosion itself is also not tolerable [53]. At the moment, the only material solutions for the first wall armour seem to be tungsten as a coating on low activation steel, or low activation steel alone (see also Sec. 7.2.1).

density	19.3 g/cm^3
melting point	3410° C
vapour pressure (@m.p.)	$1.3 \cdot 10^{-7}$ Pa
therm. conductivity (@r.t.)	145 W/mK
electr. resistivity (@r.t.)	$5 \cdot 10^{-8}$ Ωm
DBTT	$100° - 400°$ C
thermal expansion	$4 \cdot 10^{-6}$/K

Table 2.1: Properties of tungsten.

2.4 Boundary Conditions for W in Fusion Devices

The use of a material for a plasma facing component in a fusion reactor requires an integrated approach. In this sub-section, additional boundary conditions, which cannot be discussed in detail within this work, will be given. Some of the processes, as for example properties related to the behaviour in a nuclear device, cannot be studied experimentally at ASDEX Upgrade.
A general treatment of most of the processes relevant to PFCs is given in [54]. Reviews on the materials development and the evaluation of tungsten for fusion applications can be found under [20, 55].

2.4.1 Thermo-Mechanical Properties of Tungsten

Tungsten is a body centred cubic (bcc) refractory metal with a high melting point and a low vapour pressure at melting point. The thermal as well as the electrical conductivity do not decrease substantially with temperature.
A critical issue is the mechanical properties of tungsten. Although its strength is high, its tensile elongation at room temperature is almost zero, making it brittle. The ductile to brittle transition temperature (DBTT) is far above room temperature, depending on the details of the manufacturing. In order to improve the brittleness several kinds of W based alloys have been developed. Among them W-5 wt% Re, W-1 wt% La_2O_3 and W-Mo-Y-Ti (W-131) show much lower DBTT (even down to 50° C) and are nominated as a candidate material for ITER [56].
A critical issue for high heat flux components is the bonding between W armour and the heat sink. In the case of ITER copper alloys are proposed as the heat sink material. Copper exhibits a much smaller thermal expansion ($1.8 \cdot 10^{-6}$/K) than W and therefore castellated or 'brush'-like structures of W have been proposed (see Fig. 7.9). As joining techniques, plasma spray of Cu or Cu/W to W, casting of Cu to W or direct diffusion bonding of the W rods to the Cu substrate are considered.

In most present day devices inertial cooling is sufficient due to the short pulse durations. Also the particle fluencies and therefore the total amount of eroded material is low. This enables the use of W coatings on a graphite (or alternate) substrate. The coating techniques employed are chemical vapour deposition (CVD), physical vapour deposition (PVD), vacuum plasma spray (VPS) and inert gas plasma spray (IPS). These techniques result in different properties of the coatings. Whereas layers produced by CVD and PVD are homogeneous and dense as bulk tungsten, VPS and IPS coatings are porous and exhibit a reduced thermal conductivity [57]. More details on the coatings used in ASDEX Upgrade are found in Chap. 6.

2.4.2 Arcs, Melt Losses and Dust

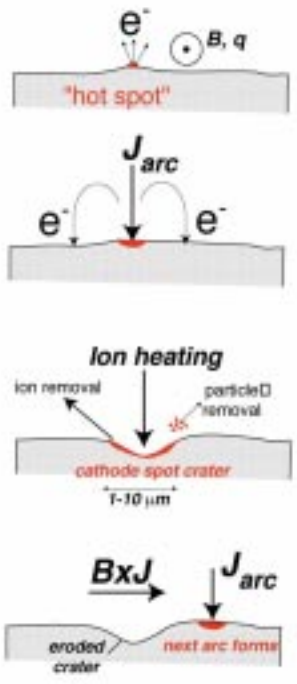

Figure 2.7: Schematic view of typical arc behaviour at plasma-facing components in a tokamak (from [54])

Electrical arcs are short duration (< 1 ms) high current density ($\leq 10^{11}$ A/m^2) discharges that occur between the plasma and a PFC. The PFM is evaporated and eroded quickly with depths larger than 1 μm, and the arc traces (tracks, scratches, pits) are even visible with the naked eye. To initiate an arc, the driving potential at the material surface must surpass the threshold $U_{arc} \approx 10 - 30$ eV, which is easily provided by the sheath potential of a 3-10 eV plasma [58]. These arcs are called 'unipolar' since they have only one solid electrode namely the wall acting as cathode. The other key element is an irregularity in the surface providing a hot spot, which is characterised by large local electric fields and reduced thermal conductivity leading to a faster heating up of the area and to thermal emission of electrons. The cathode spot is heated by ion impact and cooled by melting and evaporation, the source of the material erosion. By interacting with the external magnetic field via the Lorentz force, the arc moves across the surface, leading to the scratch-like signatures which are typically several mm long. The movement is opposite to $J \times B$ (retrograde motion) and its origin has not been completely resolved yet. Very recent observation of its dynamics [59] point to an ejection of plasma jets which in turn lead to the ignition of new arcs. The erosion rate of arcing is mainly given by the total current and most elements (including C and W) show a very similar ratio of eroded

ion current to total arc currents which amounts to 10%. This value may be enhanced by a factor of two through neutrals contributing to erosion in the form of clusters in μm size (dust), which are ejected by the high pressure vapour produced by the arc. The temporal evolution of a typical arc is shown in Fig. 2.7 which is taken from [54]. Typical dimensions of an arc are 10 μm in depth, 10-100 μm in width and 5-10 mm in length, resulting in 10^{17} - 10^{18} atoms of eroded material per arc event. Since the microscopic structure of the material surface in a fusion device is subject to continuous changes, the predictive modelling of arc erosion is very difficult. Experimental results during the experiments with the W central column in ASDEX Upgrade show that about 5-10 % of the eroded material is due to arcing [60, 61]. Figure 2.8 shows a SEM picture of the surface of a 300 nm thick W coating after one experimental campaign.

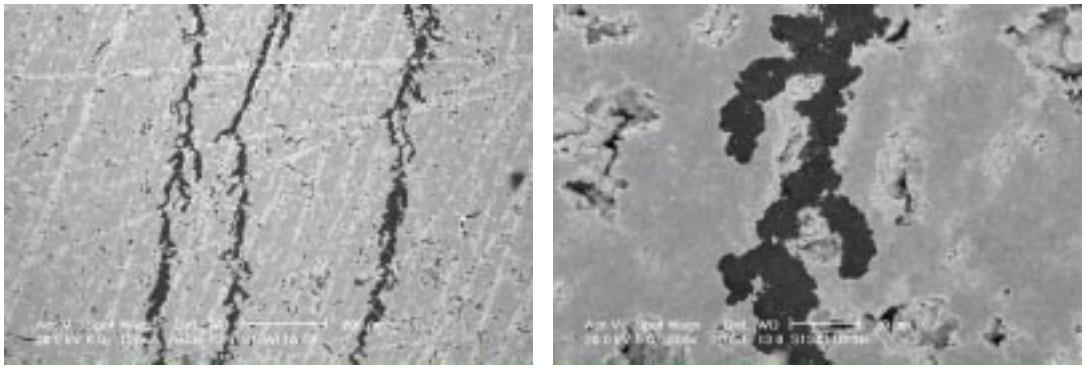

Figure 2.8: SEM picture (back scattered electrons) of the surface of a 300 μ nm W coated tile after one experimental campaign in ASDEX Upgrade [62].

The next step power producing device (see 7.2) will be of the tokamak type and will have an elongated plasma shape. Therefore, there is the inherent possibility of disruptions in conjunction with a vertical displacement event (VDE). During this process a major part of the stored energy will be deposited on the PFCs in about 1 ms leading to power densities in the order of 10 GWm^{-2}. Another reason for 'off normal events' with temporary high power loads are ELMs (edge localised modes) which are characteristic for the envisaged H-mode operation in a fusion reactor. Extrapolation from present day devices to ITER (see 7.2.1) show that a few percent of the core plasma thermal energy are deposited onto the divertor plate in a time of 0.1-1 ms leading to energy densities of about 1 MJm^{-2} and power densities above 1 GWm^{-2}, respectively [10]. Such large power densities can lead to melting and evaporisation of metallic surfaces. These melt layers are exposed to various forces such as electro-magnetism, surface tension, ablation recoil and so on [63]. The erosion rate during off normal events will be controlled and dominated by the evolution and hydrodynamics of these melt layers and vapour clouds. Detailed modelling of these processes reveal, that if the vapour cloud is confined above the exposed surface

it can shield the surface from further energy deposition and thereby reduce the erosion by evaporation by up to two orders of magnitude [64]. However, if the confinement for the vapour cloud is lost due to MHD instabilities the turbulent hot vapour may lead to even higher erosion by depositing its energy on nearby components [65]. Although much modelling work has been done on this issue, there is a lack of experimental confirmation since the present day devices do not have comparable power densities in off normal events. The simulation in other test devices is also difficult, due to the complex dynamics and its interplay with the strong magnetic field of a fusion device. The most relevant experiments are performed in plasma guns, which yield adequate energy densities (≈ 10 MJm^{-2}) but deposit the energy on too short a time scale ($\approx 50\mu$s) (see for example [66]). The melt and vapour losses are calculated to be higher by far than the erosion by ordinary plasma impact in the divertor of a future burning plasma experiment as long as 'off normal events' cannot be excluded. C based materials do not melt and therefore carbon-fibre compound (CFC) is envisaged as a material for the strike point position in ITER. Figure 2.9 shows the calculated lifetime of W and CFC at the strike point zone in ITER [19]. The lifetime of the W surface is mainly limited by melt losses during disruptions. However, as stated in 2.3, the use of carbon materials is very restricted due to its potential for strong co-deposition of tritium. Presently, for this reason, there are huge efforts undertaken, to control and mitigate the effect of off-normal events, which should finally allow the carbon based surfaces to be dropped.

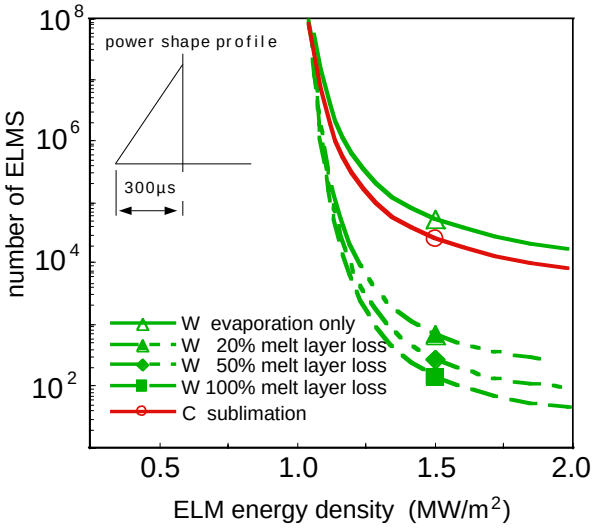

Figure 2.9: Calculated number of ELMs to erode 2 cm of C or 1 cm of W at the strike point zone in ITER [19]. For the ELM thermal loads a triangular power shape profile with a rise and fall time of 0.3 ms is assumed. The peak heat flux in between ELMs is taken to be 5 MW m^{-2} . For C, brittle destruction effects are not included. For W, results are shown assuming 0%, 20%, 50% and 100% loss of melt layer.

As a result of the erosion processes mentioned above dust will be produced. Although dust has not been a concern in magnetic fusion devices, its amount will scale up by 2-3 orders of magnitude along with the erosion and the discharge duration. Therefore, it has to be accounted for in accident scenarios because chemical reactions of fine dust with steam and air create potential explosions and dispersal of radioactivity hazards [67]. In the case of carbon PFC the radiation hazard is caused by a large amount of co-deposited tritium, whereas the

location	armour	particle flux 10^{20} $m^{-2}s^{-1}$	energy eV
main chamber			
first wall	Be	0.1 - 1	100 - 500
upper baffle	Be	0.1 - 1	100 - 500
lower baffle	W	1 - 10	100
divertor			
lower target	CFC	<10000	<5
sidewall	W	1 - 10	5 - 100
dome	W	1 - 10	5 - 100

Table 2.2: PFC materials and particle fluxes in ITER [17]

activated tungsten is a radiation safety issue in itself (see Sec. 2.4.4). Therefore, the maximum amount of W dust in ITER will be restricted to 100 kg [68]. Little is known about the details of production, properties and behaviour of dust in fusion devices and research on it has just begun [69]. Only recently first dust analyses were performed at ASDEX Upgrade [70].

2.4.3 Effects of Particle Loads

Plasma facing components are subject to high particle fluxes from the plasma background ions (H,D,T) as well as from intrinsic impurities (He, Be, C, O) and eventually seeded impurities as Ne, Ar or Kr for the operation with a radiating edge. The fluxes and energies of the particles expected in ITER are given in [17, 18]. The different character of the fluxes (see Table 2.2), together with the consideration of off-normal events, led to the present choice of PFMs in ITER.

Displacement damages

Charge exchange (CX) hydrogen neutrals with keV range energies can cause significant defects to accumulate in the tungsten lattice as demonstrated in experiments in the super conducting tokamak TRIAM-1M (see Sec. 7.1.2) [71]. According to laboratory experiments [72] the dislocation loops are formed above 3 keV but not below 2 keV, because the displacement threshold energy in W is 44 eV corresponding to a hydrogen ion energy of 2.05 keV. Dislocation loops, which form dislocation networks by interconnection have a negative impact on the structural integrity of the component. At the same time as interstitials, vacancies are formed by the knock-on damage, which can be saturated by implanted hydrogen. The micro-structural evolution of these dislocations/vacancies

depends on irradiation temperature and material purity. According to recent laboratory experiments even hydrogen bubbles in W are formed during large fluency irradiation [73–75]. These bubbles may increase the hydrogen retention described below and may give rise to an initial surface damage, which may then be increased by power load. The circumstances under which the growth of the bubbles is favoured, or how it may be hindered are not yet clear. Most recent investigations [76] lead to the conclusion that the observed blistering has to be attributed to the samples themselves, since it is only observed in cold rolled W foils, which are not relevant to reactor applications.

Hydrogen retention

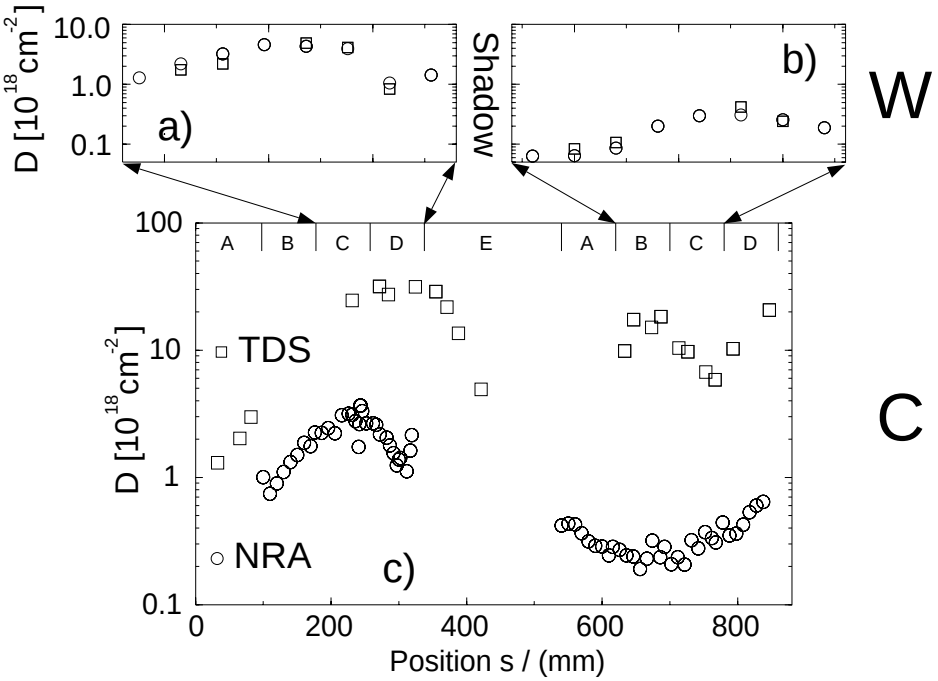

Figure 2.10: Near surface D-inventory measured by nuclear reaction analysis (NRA) and total D-inventory from thermal desorption spectroscopy (TDS) analysis across inner (a) and outer (b) tungsten tiles. For graphite (c), near-surface NRA data refer to the same experimental period (graphite thermography tiles). The corresponding TDS data were obtained from graphite tiles removed after the previous experimental campaign and refer to three subsequent campaigns (after [77]).

The H-retention by co-deposition in a-CH layers is the major concern which led to a minimisation of the carbon based PFC as described in 2.3.2. The hydrogen retention in tungsten depends on several factors, such as material grade, fabrication process (see for example [78]), temperature and ion energy. Laboratory experiments show that diffusion of hydrogen (D) in W is strong and that for fluencies $> 10^{22}$ D/m^2 the retained

amount is independent whether D is injected at sub or super threshold energies for displacement [79]. The retained D is highest for temperatures at 400-500 K and decreases with increasing temperature. From thermal desorption spectroscopy (TDS) at ASDEX Upgrade (see for example [80, 81]) one gets the following picture for H-retention: Some part of the hydrogen implanted in the sub-surface layer diffuses in the bulk and there it is trapped by natural traps with trapping energies of about 0.5 eV. If the ion incident energy is high enough to form radiation damage another part of the hydrogen is trapped by vacancies, bubbles and dislocations in the implantation zone. After the W divertor experiment, it was observed [82] that D diffused even through the plasma sprayed tungsten coating of 0.5 mm thickness in the substrate graphite. Nevertheless, the amount of retained deuterium was clearly governed by co-deposition in deposited surface carbon layers [77, 83, 84]. Fig. 2.10 shows the D-inventory measured by nuclear reaction analysis (NRA) and TDS across inner and outer tungsten (top) and graphite tiles (bottom). NRA probes only the near surface layers ($d \leq 2\mu$m) for D because of the limited range of the ^{3}He beam particles at 790 keV. This inventory equals the total amount of D in W, showing that the major fraction is retained at the surface. The difference between the outer and inner divertor can be explained by the fact that the inner divertor is deposition dominated due to the lower plasma temperatures existing there. In fact, Rutherford back scattering (RBS) and X-ray photo-electron spectroscopy (XPS) measurements revealed that these areas were covered with a low-Z layer (C, B and O) of a few μm thickness [85]. In contrast, the total D-inventory found in the graphite target tiles is much larger than the near-surface one. This is explained by diffusion out of the co-implanted/saturated zone deep into the tile and subsequent bonding at inherent trapping sites, which dominates the hydrogen retention [86]. As a consequence, the benefit of low hydrogen retention in W might be partially lost by simultaneous use of low-Z material for other PFCs leading to formation of hydrogen inventories by co-deposition at deposition dominated surfaces.

Helium bubble-formation

The helium produced in the DT-reaction is transported within the scarpe-off layer (SOL) from the bulk plasma towards the divertor. There it hits the target plates and gets neutralised. Depending on the plasma temperature it leads to additional sputtering (see below), or it can be implanted into the armour material. Very recent investigations show bubbles and holes in W specimens irradiated by He ions with fluxes of about 10^{23} m^{-2}s^{-1} (which are similar to those expected for ITER) and fluencies in the range of 10^{26} m^{-2}. They were not observed when the incident energy of the He was below 12 eV, pointing to a threshold due to a surface potential barrier for the penetration of He in W [87]. In contrast to this observation no blistering was observed in a similar experiment performed

with He particles at 100 eV but at lower sample temperatures ($\approx$ 900 K instead of 1850-2850 K) [88]. Whether this different behaviour is due to the different temperatures leading to different He diffusivities, as well as to a different vacancy concentration and mobility, or whether this is due to different W material grades has not been resolved yet. In light elements as Be (n, α)-reactions lead to the production of He within the bulk of the material. There He concentrations in the order of 10^{-3} per wall atom will be produced during a neutron load of 1 MWam^{-2} [89]. In the case of W this ratio will be in the range of 10^{-5} and it is therefore of less concern.

Sputtering

The low erosion yields by plasma particles are the driving force for the use of W. In a divertor device there is reduced plasma wall interaction in the main chamber and the plasma temperature in front of the divertor target plates can be de-coupled to some extend from the main plasma (see Sec. 5.1). In the foreseen 'semi-detached' operation in ITER, divertor plasma temperatures below 10 eV are envisaged. The sputtering thresholds for H, D and T on W are 447 eV, 209 eV and 136 eV, respectively, therefore the erosion by the background plasma during steady state phases will be negligible (see Fig. 2.4). However, as described earlier, it is not yet clear to what extent ELMs will appear. During these events the particle energy may be increased to values in the order of 1 keV. Another source of sputtering are impurities existent in the background plasma. These may be intrinsic impurities as W itself or light elements as C and O and seeded impurities (mostly noble gases) which are introduced to increase the edge plasma radiation and to cool the divertor plasma [90] (see also Secs. 6.1.2 and 7.1.2). These impurities will have the ionic charge of A^{Z+} with $Z \approx 3-4$, because on their way towards the divertor they will not recombine completely. Therefore, they gain additional energy in the sheath potential in front of the targets and the thermal energy distribution will be shifted by $3ZkT_e$ (T_e: electron temperature). Consequently, the effective sputtering yield will be much higher as from the background plasma alone.
In the main chamber the ion flux to the walls is much smaller but not negligible (see Sec. 6.2.2) as it was assumed in the simulation for ITER until recently. Additionally, hydrogen neutrals (CX) from charge exchange reactions will be present with energies far above the sputtering threshold [91]. For ITER-conditions W erosion between $10^{-4} - 10^{-3}$nm/s [18] is expected from these CX-particles alone. In the case of (the planned) Be-armour, the erosion by CX-particles is higher by 1-2 orders of magnitude.
Investigations on W erosion under fusion-relevant parameters comprises a large part of the W programme at ASDEX Upgrade. Two methods are used for its characterisation: Surface analysis techniques and spectroscopy. The results of the surface measurements will be briefly highlighted here and they are described in more detail in [61, 77, 92–97].

The spectroscopic results will be dealt with in Secs. 4 and 6.

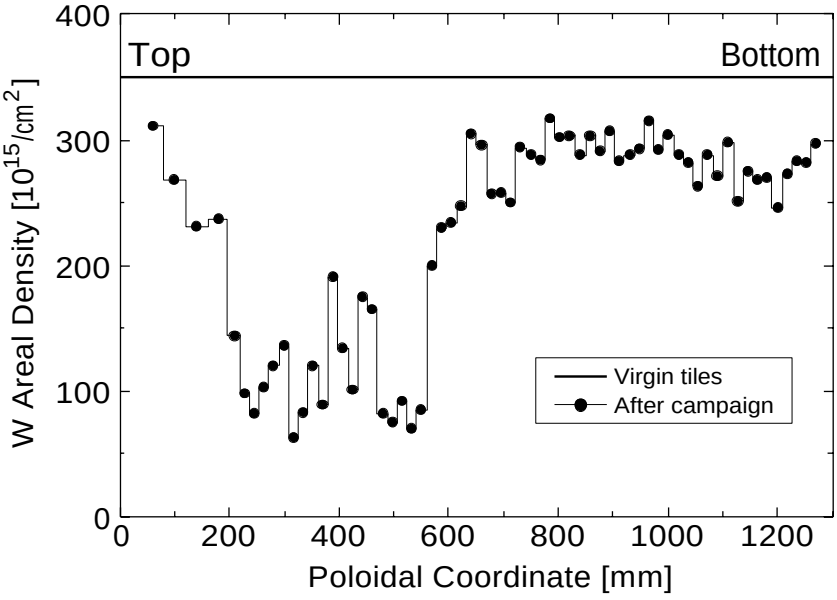

Figure 2.11: W erosion measured on 60 nm W test tiles along a vertical line. They were installed at the central column of ASDEX Upgrade during the experimental campaign in the year 2001. They were exposed to about 300 plasma discharges. The erosion is observed only at the top side (200 - 600 mm) because of their geometry and the topology of the impinging field lines [61].

A common problem of surface analysis techniques is that they have no temporal resolution. Mostly the measurements integrate over a whole experimental campaign and the samples are analysed post mortem. The problem can be alleviated by using erosion probes mounted on retractable manipulators. The investigations complement the spectroscopic measurements and yield the net erosion instead of the gross erosion deduced from spectroscopy. Here a difference by a factor of 10 was found under low temperature high density conditions in the ASDEX Upgrade W divertor experiment [98, 99]. This much lower net erosion is attributed to 'prompt redeposition' as it was already observed in the W marker experiments [92]: For high-Z materials the gyro-radius in the external field may be larger than the ionisation length, which can lead to deposition of the eroded particle directly after its erosion, as will be explained in Sec. 5.1.1.
During the experiments with W coated tiles at the central column of ASDEX Upgrade a complete column of test tiles with a W layer thickness of 60 nm was installed to allow a sensitive measurement of a poloidal erosion profile. The analysis showed W erosion on all tiles and the maximum of the poloidal W erosion profile was found above the midplane (see Fig. 2.11). It exceeds the expected values from erosion by CX particles

by at least one order of magnitude. Considering the observed two-dimensional variation and the magnitude of the tungsten erosion flux, it became evident that the predominant erosion channel is due to ion impact. This is mostly attributed to the direct plasma contact during plasma ramp-up and ramp-down, when the central column is used as a limiter consistent with spectroscopic and Langmuir probe measurements.
In the case of a 'mixed-material' device, i.e. a device which uses different plasma facing materials, the reduction of erosion by deposition of other materials also has to be taken into account. Code simulations have shown, that for carbon as a second impurity there is a delicate balance between enhanced W erosion and C deposition depending on the C concentration and the plasma temperature in front of the W PFC [100]. During the W divertor experiment as well as during the ongoing W investigations (see Chap. 6) deposition as well as erosion dominated zones could be identified [61, 83, 85, 101].

2.4.4 Effects of Neutron Irradiation

Neutron irradiation leads to activation and to changes in the mechanical properties of the material. Reviews of the effects relevant for fusion applications are given in [102, 103]. The 1998 ITER design foresees a 0.4 MWa/m^2 ($\approx 2 \cdot 10^{21}$ n/cm^2) fluency for tungsten armour used in the divertor region [104]. This is equivalent to damage of 0.3-0.5 dpa (displacements per atom) [102]. For this moderate neutron fluency no critical deterioration of the performance of W as an armour material is foreseen. However, for the application of W in a DEMO or commercial reactor further R & D is required.

Activation

The high energy of the DT-fusion neutrons (see A.1.1) opens up a broad class of nuclear reactions, as there are (n,γ), (n,p), (n,2n), (n,d) and (n,α). The relevant reaction chains are highlighted in [105] for the case of ^{186}W. In all W isotopes (0.135% ^{180}W, 26.4% ^{182}W, 14.4% ^{183}W, 30.6% ^{184}W, 28,4% ^{186}W) the main reactions (also secondary and further step reactions) are (n,γ) and (n,2n), where the latter dominates above 1 MeV neutron energy. However, since the integrated cross section of (n,γ) is higher than that of (n,2n), W transmutes to Re followed by Os. During the lifetime of the tungsten plasma facing components an inventory of solid transmutants is built up. For the neutron fluency stated above, the transmutation reactions lead to 4800 atomic parts per million (appm) of Re, 170 appm of Ta and 75 appm of Os. These contaminants have a strong influence on the mechanical behaviour as described in the next section. The other critical issue is the decommissioning and waste. In general safety evaluations as [106, 107] the armour material is still kept open (Be or W). Although W has a much larger potential for the production of activation products, the two different choices do not show up strongly in the general accounting of the radioactive inventory due to the comparable

small masses involved. For ITER 'Radioactive Materials, Decommissioning and Waste' are dealt within the 'ITER Generic Site Safety Report (GSSR) Vol. V' [104]. Besides reactions on the tungsten isotopes themselves activation products of alloying materials and contaminants have to be considered. From the viewpoint of decommissioning and waste treatment the retained tritium is also important. Following [108] the radiotoxity contained in the tungsten components leads to a clearance index of 1100 after 30 years, 220 after 100 years and reaches values around one after 10^5 years after shutdown. As a consequence the tungsten divertor structures have to be clearly treated as radioactive waste, but due to the rather small amount which is produced during the lifetime of ITER (95 tons) it is not considered a major drawback. The numbers also have to be compared to the waste from the other divertor structure materials, which will be produced irrespective of the plasma facing components: steel 330 tons, copper 90 tons. In total the tungsten will contribute about 13% of the total mass of the in vessel waste (750 t) and about 5% of its total volume (180 m^3). Comparing the clearance indices of the tungsten PFC's to values of the projected Be first wall, one finds that for the tungsten divertor plasma facing components they are already lower after 3 years and also decrease faster in time on a longer time scale, showing that there is no strong qualitative difference between the low-Z armour material of the main chamber and the high-Z material in the divertor.

Change of thermo-mechanical properties

Thermal conductivity:
No data on the effect of n-irradiation is available for thermal conductivity. However, an increase of electrical resistance of 24% was measured in pure W after irradiation to about 4 dpa [102]. In accordance with the Wiedemann-Franz law, the electrical conductivity of metals is proportional to the thermal conductivity, so the latter should change accordingly. Since significant generation of Re is expected, the thermal conductivity should also be reduced during the lifetime of the component.

Swelling:
The maximum reported swelling was 1.7% at 9.7 dpa and 800° C [102]. However, there is a significant change of the microstructure, which may have an impact on the T-retention in the W bulk material.

Mechanical properties:
W becomes brittle after neutron irradiation due to radiation hardening and loss of strength at grain boundaries which lead to an increase in the ductile to brittle transition temperature (DBTT) [102]. The embrittlement depends mainly on the temperature during irradiation and there is some hope that for temperature above 900° C the DBTT remains unchanged or that doping of W with TiC makes it more radiation resistant [103].

In any case, it is proposed to use W armour material without structural function and to optimise the geometry of the components to avoid crack initiation.

3. Experimental Tools

3.1 Spectroscopic Systems

3.1.1 Visible Spectroscopy

The boundary layer spectrometer (BLS) at ASDEX Upgrade is equipped with a visible and a vacuum ultra-violet (VUV) spectrometer [109]. A movable mirror is mounted at the upper outer plasma boundary. The area of observation can be positioned onto a defined spot or scanned over a distinct region of interest. The mirror can be rotated poloidally and toroidally to allow observations in the divertor and the central column. Typically the line of sight is swept with a frequency of 1 to 2 Hz over the inner and outer divertor plates during a plasma discharge. At every sampling time point the position of the line of sight is protocolled and a spectrum is recorded. Thus, for stable plasma conditions a spatial emission profile can be recorded. During the tungsten divertor experiment there are also several fixed lines of sight tangential to the target plates (DIV) using fibre guides [110], providing a measurement of the height distributions of line intensities. During the experiments with the tungsten coated central column additional fibre guides with fixed lines of sight almost perpendicular to the surface were used. The tungsten erosion was measured by observing a W I spectral emission line at 400.8 nm. A spectral overview performed at the Plasma-SImulater (PSI) in Berlin identified this line as the most prominent of the neutral tungsten spectrum [111] as can be judged from Fig. 4.1. The absolutely calibrated 1 m visible spectrometer recorded a full spectrum every 22 ms with an exposure time of 9 ms. Under typical divertor plasma conditions the W I line was very weak ($\approx 10^{-2}$ $\mathrm{Wm^{-2}sr^{-1}}$), and lowering the exposure time would have made an intensity measurement impossible. Therefore, events and processes on a shorter time scale, like ELMs, could only be observed in a time averaged manner.

3.1.2 VUV Spectroscopy

The Grazing Incidence Spectrometer

The radiation in the EUV-region from 4 nm to 30 nm was observed with a 2.2 m grazing incidence spectrometer manufactured by McPherson. This instrument is described in more detail in [112]. The line of sight of the spectrometer looks almost horizontally through the plasma centre of ASDEX Upgrade. The plasma radiation is diffracted and focused by a 600 grooves/mm grating and observed by means of a multi channel plate (MCP) system, consisting of a single MCP, a phosphor screen, a fibre guide and a photo diode array. At about 5 nm a wavelength range of 3 nm can be viewed simultaneously with a time resolution of Δt=5 ms and a wavelength resolution of about $\lambda/\Delta\lambda \approx 150$. By shifting the MCP along the Rowland circle the spectral range can be tuned from 4 nm up to 60 nm. The line of sight is given in Fig. 6.22.

The calibration of the grazing incidence spectrometer was done by means of a double branching ratio method. The transitions used are

1. $2s^2 3s\ ^2S_{1/2} - 2s^2\ (^1S)3p\ ^2P_{1/2}$ (CII, $\lambda \approx 658$ nm) $\Leftrightarrow$
$2s2p^2\ ^2S_{1/2} - 2s^2\ (^1S)3p\ ^2P_{1/2}$ (CII,$\lambda \approx 237$ nm)
2. $1s2s\ ^3S_1 - 1s2p\ ^3P_1$ (BIV,$\lambda \approx 282.6$ nm) $\Leftrightarrow$
$1s^2\ ^1S_0 - 1s2p\ ^3P_1$ (BIV, $\lambda \approx 6.1088$ nm)

With the assumptions that the emission is homogeneous from the point of view of the spectrometers used and toroidally symmetric, a UV/visible spectrometer with the same line of sight as the grazing incidence spectrometer (but other toroidal location) was calibrated at $\lambda \approx 237$ nm. In a second step the grazing incidence spectrometer was calibrated by means of the second line pair and compared with the UV spectrometer.

The SPRED Spectrometer

For the monitoring of a broader wavelength region a so called SPRED spectrometer (survey, poor resolution, extended domain) was used [113]. This spectrometer offers the possibility to observe simultaneously the whole spectral range from 10 nm to 140 nm with the reduced resolution of $\Delta\lambda \approx 0.3$ nm. The detector consists of an open multi channel plate (MCP) system with a phosphor screen which is coupled by a glass flange to a programmable CCD camera. Typically the temporal resolution is 10 ms.

3.1.3 Soft X-Ray Spectroscopy

The soft X-ray spectrometers at ASDEX Upgrade use crystals in reflection geometry. X-rays with wavelength λ are only reflected, if the glancing angle ϑ fulfils the Bragg equation

$$n \cdot \lambda = 2d \cdot \sin \vartheta \tag{3.1}$$

with n being the reflection order and d the layer spacing of the crystal. Two types of spectrometers are installed at ASDEX Upgrade: An ordinary Bragg spectrometer using flat crystals and a Johann type spectrometer with a curved crystal in a Rowland configuration.

The Bragg Spectrometer

In the case of the Bragg spectrometer the X-rays have to be collimated to form a parallel beam. A spectrum is created by rotating the crystal and the detector during a plasma discharge and detecting the reflected radiation (scanning mode). This implies that not a whole spectrum, but only one wavelength at any point of time can be observed. The crystal can be rotated with an angular velocity of up to $\omega = 16.7\ ^{o}/\mathrm{s}$. This results in one full spectrum during 4 s ($\approx$ 2 spectra per discharge). The time resolution of the spectrometer is determined by the sampling rate of the acquisition system and the maximum countrate. For a sufficient counting statistics a sampling rate of 1 kHz is used, leading to about 6 data points per *fwhm*, which is adequate for the spectroscopical applications. In the monitoring mode the crystal and the detector are kept fixed to measure the temporal evolution of the radiation at a constant wavelength.

Two similar Bragg crystal spectrometers exist, which are placed in a common vacuum housing. They observe the plasma in a radial direction along an almost identical horizontal line of sight (separated toroidally 9 cm) 14 cm above the mid plane almost through the plasma centre. The spectrometers, the preamplifiers and the power supplies are situated in a large concrete housing for shielding from neutron and gamma radiation. The schematic setup is shown in figure 3.1. X-rays emitted from the plasma first pass a multigrid collimator [114] and an entrance slit 40 mm high and 0–50 mm wide used for the adjustment of the incoming photon fluxes. For detection a Multi Strip Gaseous Chamber (MSGC) is used [115], which allows single photon counting with count rates above 1 MHz [116].

The dimensions of the detector (sensitive area: $30 \times 40\ mm^2$) were optimised to detect all the reflected photons also in the case of the small excursions of the detector from its optimal position. The depth of the detector volume (9 mm) is chosen to insure the absorption of photons in the used energy range, but simultaneously to minimise the absorption of high energy photons with energies above 15 keV which are responsible for the background signal. As a window towards the spectrometer vacuum a 2 μm thick Mylar

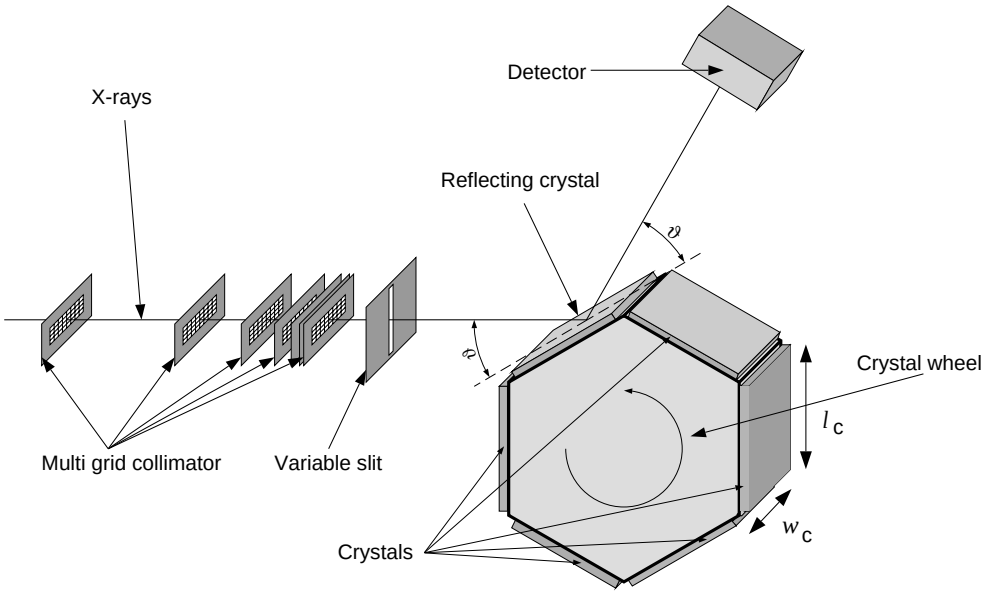

Figure 3.1: Experimental setup of one Bragg crystal spectrometer at ASDEX Upgrade. X-rays emitted from the plasma enter the spectrometer from the left.

Nr.	System A			System B		
	Crystal	$2d$ (nm)	measurement range (nm)	Crystal	$2d$ (nm)	measurement range (nm)
1	Topaz (303)	0.2712	0.047 - 0.270	Topaz (303)	0.2712	0.047 - 0.270
2	Silicon (111)	0.6271	0.109 - 0.625	Silicon (111)	0.6271	0.109 - 0.625
3	ADP (101)	1.0640	0.185 - 1.061	ADP (101)	1.0640	0.185 - 1.061
4	KAP (100)	2.6579	0.460 - 2.647	KAP (100)	26.579	4.60 - 26.47
5	Lead stearate	10.04	1.70 - 10.00	Lead stearate	10.04	1.70 - 10.00
6	Multilayer	9.65	1.68 - 9.61	LiF (220)	0.2848	0.047 - 0.280

Table 3.1: Available crystals for both Bragg crystal spectrometers at ASDEX Upgrade. The wavelength range for all crystals is given for Bragg angles between 9° and 80°.

(Polyethylenterephtalate) foil covered by an 80 nm thick aluminium layer is used. Since the thin window is not completely vacuum tight, a counting gas mixture (Ar (83.25 %), methane (9.25 %) and butane (7.5 %)) is kept continously flowing through the counter at atmospheric pressure. A second MSGC, which has the same dimensions and electronics as the X-ray counting detector, measures the background due to neutron induced gamma radiation. The relative sensitivity of both detectors was determined during plasma discharges with high neutron rate and closed spectrometer entrance.

The crystals have the size 100×50 mm^2 and are mounted on a revolver. Each revolver

consists of six crystals allowing the selection of one between two subsequent discharges without breaking the vacuum. In table 3.1 all available crystals are listed together with their wavelength range, for the usable crystal angles ranging from 9° to 80°. Together they cover the wavelength range between 0.047 nm and 10.0 nm.
Depending on the crystal used, spectral resolutions of $\Delta\lambda/\lambda = 100 - 2000$ are achieved. The wavelength calibration is gained from reference lines of intrinsic impurities and the errors in the wavelength measurement are due to the jitter in the rotation which is found to be about 0.03°. This gives a relative error of about $\pm 2.8 \times 10^{-3}$ to $\pm 1 \times 10^{-4}$, depending on the Bragg angle. The absolute intensity calibration is gained from ab initio calculations using the properties of the single components, as well as from comparison with measurements of a Si-semiconductor detector [117, 118] and of an absolutely calibrated X-ray monochromator [116]. The absolute calibration, as well as the technical components of the spectrometer, are described in more detail in [119].

The Johann - Spectrometer

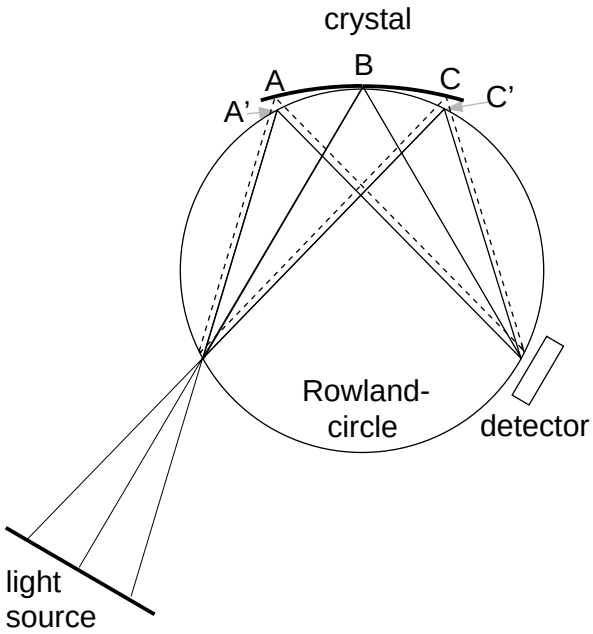

Figure 3.2: Schematic view of the arrangement of a Johann spectrometer.

The Johann spectrometer uses a bent crystal in Rowland geometry [120, 121], where the bending radius is twice the radius of the Rowland circle. Combined with a position sensitive detector, high resolution spectra can be gained. For a homogeneous light source (as the plasma in ASDEX Upgrade) it allows the operation without slit, yielding an increased sensitivity which makes it ideal to monitor the weak lines of W. The geometry of the arrangement is sketched in Fig. 3.2. As can be concluded from the figure, the reflections from the points A and C are shifted backwards compared to A' and C' which would lie on the circle. This leads to a shift towards larger angles for both reflection points, resulting in a degradation of the resolution on the low wavelength side of a spectral line. The maximum achievable resolution is therefore given by the geometry and the Bragg angle to

$$\frac{\lambda}{\Delta\lambda_{Joh}} = 32(\frac{R}{s})^2 \tan^2 \Theta_B, \tag{3.2}$$

with R radius of the Rowland circle, s crystal length and Θ_B Bragg angle.

crystal	$2d$ (nm)	λ_{min}	λ_{max}
Quartz 206	0.16559	0.106	0.151
Quartz 106	0.17626	0.110	0.160
Quartz 403	0.1832	0.117	0.167
Quartz 203	0.2749	0.176	0.250
Quartz 211	0.3082	0.197	0.280
Quartz 200	0.42548	0.272	0.387
Quartz $11\bar{2}0$	0.4913	0.314	0.447
LiF 220	0.2848	0.182	0.259
LiF 200	0.4027	0.258	0.366
Topaz 303	0.2712	0.174	0.247
Ge 220	0.4000	0.256	0.364
Si 111	0.6284	0.402	0.574
EDDT 020	0.8808	0.564	0.802
Beryl $10\bar{1}0$	1.5954	1.019	1.462
KAP 001	2.6579	1.701	2.419

Table 3.2: List of available crystals for the Johann spectrometer at ASDEX Upgrade. The usable wavelength range $(\lambda_{min}, \lambda_{max})$ is given by the tunable angle range and twice the lattice spacing $(2d)$. An overview on crystals useful for X-ray spectroscopy is found in [122, 123].

To overcome this, the crystal could be ground in such a way that its surface falls on the Rowland circle leading to the Johannson spectrometer [124].
For the Johann spectrometer at ASDEX Upgrade the bending radius of the crystal is 1.5 m. The resolution $\lambda/\Delta\lambda$ ranges from 1000 - 4000 and is given by the geometry (see eq. 3.2), the individual properties of the used crystal and the spatial resolution of the detector. In table 3.2 the crystals available at ASDEX Upgrade are given. As can be concluded from the table, the wavelength ranges from 0.1 to 2.4 nm. The best resolution is with quartz crystals, whereas organic crystals usually show broader lines. The detector is mounted on an arm with movable bellows, to allow the adjustment of the focal length under different Bragg angles. The arm itself is attached to the crystal chamber via a relocatable stainless steel sheet which is pressed to Viton seals and pumped differentially. The crystal mount is fixed to a rotatable vacuum feed-through, thereby allowing the system to be adjusted to a given Bragg angle in between two discharges without breaking the vacuum. However, unlike the Bragg system a vent is needed to change crystals. The scattered X-rays are detected by a closed MCP-CCD image intensifier system supplied by PROSCAN [125]. They produce visible light on a phosphor coated fibre taper, which reduces the spectra in size by 5:3, to match the camera dimensions. The taper also acts as vacuum window to which the closed (vacuum sealed) image intensifier is attached.

There the light produces electrons on the photo cathode of the MCP, which multiplies the number of electrons and acts as a fast shutter during the read out of the camera. The electrons produce an intensified picture on a second phosphor screen which is observed by the CCD. The arrangement allows the detection of low energy X-rays down to the Lyman-α radiation of O VIII at 1.897 nm [126] and an easy adjustment of the camera without breaking the vacuum. During the investigations on tungsten the Ni-like line at 0.792 nm is monitored using the EDDT crystal ($2d = 0.802$ nm).

3.2 Systems for Impurity Injection

There are four common methods for the injection of external impurities into fusion plasmas, namely pellet injection, laser ablation, erosion probes and gas puffing. Each of these methods has its own advantages and disadvantages concerning the energy, amount and temporal behaviour of the injected particles. In the following, the ones which were specially developed and adapted for the high-Z investigations at ASDEX Upgrade for use during spectroscopic investigations will be presented.

3.2.1 Laser Ablation

The injection of impurities by laser-ablation (see [127, 128] and [129] for further references) into fusion devices is a common method of studying atomic processes [130–134], the transport of impurities and their effect on the plasma discharge [135–142]. Additionally, plasma temperatures and densities can be measured with high spatial resolution at the plasma edge [143, 144] and in-situ investigations of surface deposition layers were performed [145]. Recently the the edge cooling effect of the injected impurities has been used for the study of electron heat transport [146–152].
The laser blow-off (LBO) system at ASDEX Upgrade consists of a 0.6J Nd-YAG laser with a pulse-length of 8 ns and a wavelength of 1064 nm. The ablation efficiency in the infrared is somewhat lower than in the visible or in the UV, however, there is the advantage that the fraction of ions in the ablated particles is lower [129]. Additionally, the Nd-YAG laser is a robust system for multi-pulse operation, this means ablations in single pulse operation or in pulse series with a repetition rate of up to 20 Hz are possible. For pulse series the laser beam has to be focused onto virgin parts of the target, which is attained by deflecting the laser beam by a combination of a movable lense and fixed mirrors. The advantages of this system are that they allow a fast movement without complex vacuum feed-throughs and minimise the power load in the vacuum windows by using different regions for every laser pulse. The targets are mounted on a carriage which can be moved from a target lock, where they can be changed towards the plasma. In the ablation position they are only about 0.5 m away from the plasma, which means that only very few ablated particles are lost on their way to the plasma.
The individual targets have the size of about 50×50 mm^2, and 4 different targets can be mounted simultaneously. They are made of 0.3 μm - 2.0 μm metallic films evaporated on a thin glass substrate or by deposited layers of powder ($\approx$ 1.5 mg/cm^2 of C and Si) and are irradiated from the back side. The injected amount of particles is estimated from the ablation spot size. Depending on the target thickness and the spot size, the amount of injected particles is varied from about 5×10^{16}, typically used in the case of W injections, up to a few 10^{18} particles in the case of C. This arrangement allows about

30 injections during one plasma discharge. Since the impurity transport time in most discharges is larger than 50 ms [153], the injections result in an almost constant impurity inventory in the plasma discharge over 1-2 seconds.
By minor modifications it is also possible to focus the laser beam onto the inner wall of ASDEX Upgrade. An area with the diameter of about 300 mm at the central column can be scanned. This allows us to investigate deposited layers [154] (as already described in [145]) or to monitor the status of an initial surface coating and to probe the impurity penetration from the high field side as it will be described later (see Sec. 5.1.4). Additionally, this offers the very simple possibility of supplying an almost inexhaustible ablation target.

3.2.2 Sublimation Probe

A variation of the gas puffing method is the so called sublimation probe. This probe was first developed at ASDEX Upgrade [155] in order to investigate the transport behaviour in the edge plasma. It can be exposed to the plasma via manipulator systems [93] in the divertor and the midplane of the ASDEX Upgrade tokamak. The probe sublimates suitable materials, which then are puffed into the plasma through a valve which can be opened during the discharge. The advantage over an erosion probe is the externally controllable sublimation, making the amount of injected material independent of the plasma parameters in front of the probe. The advantage over gas puffing is the wider range of available substances containing high-Z materials like W.
The probe consists of a heatable cavity (see Fig. 3.3) made of a copper-bronze alloy (CuAlNi) with a volume 1 cm^3. The plasma facing surfaces of the probe are covered with a carbon-fibre compound (CFC) which are flush with the front of the divertor tiles in exposure position to avoid excessive heat loads by plasma impact at leading edges. Additionally, a heat shield is used to protect the cavity from the plasma heat flux. The rear end is cooled actively by a heat bridge to the divertor tile cooling system. The maximum heat flux onto the probe tiles in divertor II according to thermography measurements in our experiments was 0.5 MWm^{-2}. Measurements performed with a similar probe equipped with an internal thermocouple show that the system can be safely operated at much higher heat loads. The

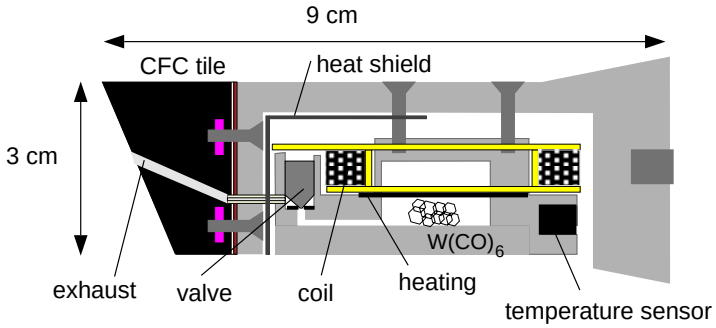

Figure 3.3: Schematic view of the sublimation probe with the CFC front cap for use in divertor II [155].

means for heat protection are so efficient that the maximum deviation from the preset temperature during a discharge could be kept below 1° C. For the exposure of probe 2 to the midplane edge plasma, a graphite shield with a front cap made of CFC is used.

The heating system consists of a heating wire around the upper part of the cavity. The probes can be operated in a temperature range from about 50° C up to 150° C. The minimum temperature is determined by the heat load on the divertor tiles during a plasma discharge. For $W(CO)_6$ sublimation the probes were operated at 70° C.

For the temperature measurement a sensor is used which encodes the detected temperature into a rectangular signal with a duty cycle proportional to the temperature. The opening mechanism acts via the toroidal magnetic field (1.3 T - 3.2 T) of ASDEX Upgrade due to the magnetic moment caused by the current flowing through the coil attached to the valve.

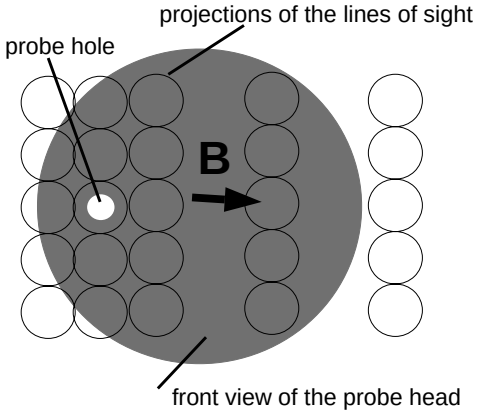

Figure 3.4: Projection of the viewing chords onto the probe head.

An array of glass fibres was built into the divertor dome for the direct spectroscopic observation of the probe surface. It consists of 25 optical quartz fibres, the viewing chords of which are projected onto the front of the probe tile by concave mirrors ($f = 60$ mm), as seen in Fig. 3.4. The distance of the viewing chords is increased in $\vec{B}$-direction to account for the cloud spread due to the plasma flow in front of the probe. Due to the setup with optical fibres and an optical switchboard, the system can be used with various spectrometers of different spectral and temporal resolutions. Normally a 1 m Czerny Turner spectrometer with a slow-scan CCD camera is used. More details of the probe can be found in [155–157].

4. Spectroscopic Investigations

Spectral lines from highly charged tungsten ions have been found in the VUV at least since the use of a W limiter in PLT and ORMAK (see Sec. 7.1.1, [21, 158, 159]). However, concentrations of W in fusion plasmas were mostly calculated from the radiation loss parameter from an average ion model [24,25] (see for ex. [160]). Of course this is only feasible if the radiation from intrinsic tungsten accounts for the major part of the total radiation, or if the radiation from the plasma background and other impurities can be quantified, as in trace experiments, where W is injected artificially and the background radiation can be subtracted under the assumption that there is no change of the target plasma during the injection. During the experiments performed in ASDEX Upgrade tungsten contributed only a minor fraction of the total radiation excluding the traditional method cited above. In contrary, if the tungsten radiation had been dominant, W would not be used in future devices and also ASDEX Upgrade would have stopped its investigations on W.
Additionally, one ought to be careful using the radiation loss parameter, because detailed investigations of the ionisation equilibria of Mo ions in the tokamaks Alcator C-Mod [161] and FTU [162] revealed strong deviations from the conventional coronal equilibrium predictions [163] due to the effect of excitation-autoionisation (EA), which also changes in the radiation power across the plasma.
In summary, this means that performing a tungsten programme in a fusion device requires a lot of effort to achieve sensitive diagnostic systems for tungsten influx and content.

4.1 Visible Spectral Range

The visible spectrum of neutral W exhibits a huge amount of spectral lines, which finally leads to rather weak individual transitions. For the monitoring of the W influx one has to concentrate on the ones which appear predominantly under the conditions of a fusion edge plasma. Therefore, an investigation was initiated at the Berlin Plasma Simulator (PSI-1) at the IPP in order to identify the best suited lines [111] in the range of 350-540 nm. In this experiment a tungsten plate was used as a target in an He plasma with

$n_e = 7 \cdot 10^{17}$ m^{-3} and $T_e = 10$ eV, measured by Langmuir probes. In order to yield higher sputtering and light yield, the target was biased up to -210V. Fig. 4.1 shows a detail of the measured spectra containing the strongest line found in this experiment at 400.8 nm resulting from the $^7S_3 - {}^7P_4^o$ transition. This finding is in line with early measurements of Laun and Corliss [164] and more recent determinations of oscillator strengths [165, 166]. In order to use this transition as a quantitative measure for the tungsten influx, the

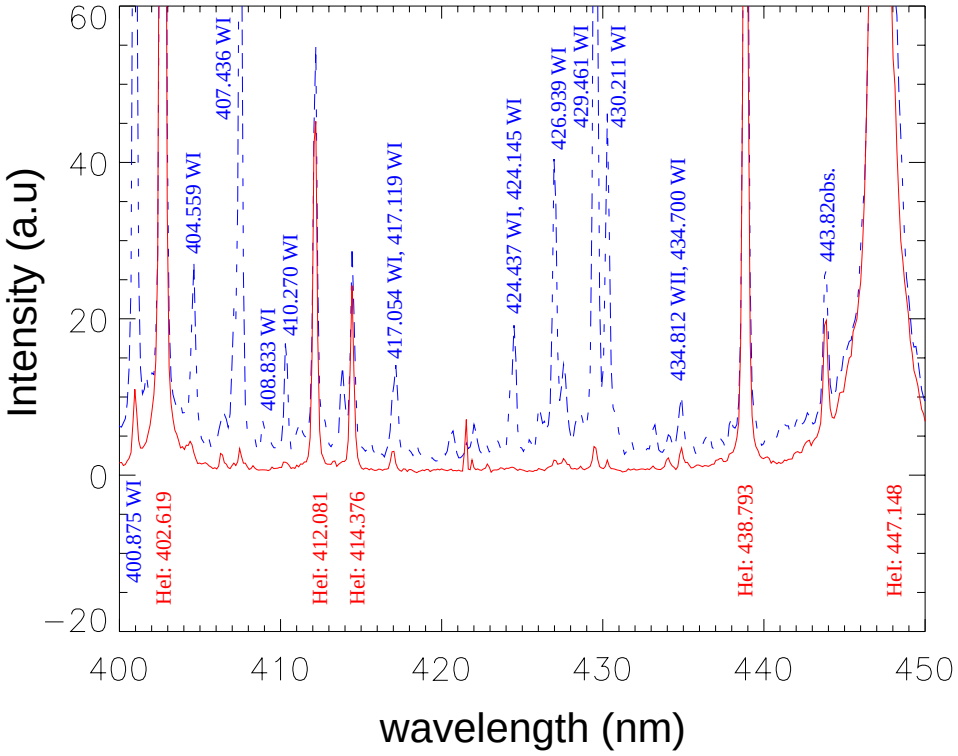

Figure 4.1: Tungsten spectrum (dashed line) around 425 nm measured at the PSI in Berlin using a He plasma [111]. For comparison the pure He spectrum (solid line, without W target) is shown.

adequate rate coefficients have to be known. If recombination can be neglected, the influx can be determined without detailed knowledge of the local electron density as described by Behringer et al. [167]. Integrating along a line of sight the particle influx Γ_{in}^Z from a material surface is given by

$$\Gamma_{in}^Z = \int_0^R dl\, n_e \sum_\sigma S_\sigma^{(Z,Z+1)} n_\sigma^Z, \tag{4.1}$$

where $S_\sigma^{(Z,Z+1)}$ denotes the ionisation rate coefficient for ionisation from charge state Z to $Z+1$. The index σ denotes metastable states within one charge state.
In the coronal equilibrium, which is mostly valid for low density fusion plasmas, the collisional electron excitation is balanced by spontaneous emission

$$\sum_{f<i} A_{if} n_i^Z = n_e X_{\sigma \to i} n_\sigma^Z, \tag{4.2}$$

with the Einstein coefficients A_{if} and the rate-coefficient $X_{\sigma\to i}$ for the collisional electron excitation. Thereby one gets for the spectral emissivity $\varepsilon_{Ph,i\to j}$ (photons per volume unit)

$$\varepsilon_{Ph,i\to j} = B_{\sigma,i\to f} n_e X_{\sigma\to i} n_\sigma, \tag{4.3}$$

with the branching ratio $B_{\sigma,i\to f}$ defined as

$$B_{\sigma,i\to f} = \frac{A_{i,j}}{\sum_f A_{i,f}}. \tag{4.4}$$

Integrating $\varepsilon_{Ph,i\to j}$ over the line of sight yields the photon flux $\Gamma_{ph,i\to j}$ for the observed transition:

$$\Gamma_{ph,i\to j} = B_{\sigma,i\to f} \int_0^R dl\; n_e X_{\sigma\to i} n_\sigma. \tag{4.5}$$

By dividing eq. 4.1 through eq. 4.5 one ends up with

$$\frac{\Gamma^Z_{in}}{\Gamma_{ph,i\to j}} = \frac{\int_0^R dl\; n_e \sum_\sigma S^{(Z,Z+1)}_\sigma n^Z_\sigma}{B_{\sigma,i\to f} \int_0^R dl\; n_e X_{\sigma\to i} n^Z_\sigma}. \tag{4.6}$$

Since $S^{(Z,Z+1)}_\sigma$ and $X_{\sigma\to i}$ behave in a very similar way along the line of sight l (similar temperature dependence) and the ion (or atom) with charge Z exists only in a narrow temperature range, one can make the following approximation:

$$\Gamma^Z_{in} = \sum_\sigma \frac{S^{(Z,Z+1)}_\sigma}{B_{\sigma,i\to f} X_{\sigma\to i}} \Gamma_{ph,i\to j} \tag{4.7}$$

Therefore, the so called inverse photon efficency S/XB directly connects the particle flux to the measured photon flux. S/XB is a function of the plasma temperature and under typical conditions (influx of particles against a temperature gradient) $T_e \approx 1/3 E^Z_{ion}$, with E^Z_{ion} ionisation potential of the ion with charge Z has to be taken. The spectroscopic measurement has to be performed in the direction of the impurity influx and for a laterally non-isotropic particle source the whole emission cloud has to be observed.

The sum in equation 4.7 can also be written in the form

$$\left.\frac{S}{XB}\right|_{eff} = \frac{1}{f_\sigma} \left.\frac{S}{XB}\right|_\sigma \tag{4.8}$$

introducing an effective S/XB ratio $S/XB|_{eff}$ where the f_σ are the fractional abundances of the respective metastables.

By means of the sublimation probe described in Sec. 3.2.2, the $S/XB|_{eff}$ ratio of the 400.9 nm line of W I was determined. This was accomplished by the simultaneous observation of the 397.3 nm line of O II. Fig. 4.2 presents the lateral intensity distribution during the injection of $W(CO)_6$ in the divertor of ASDEX Upgrade. The usage of the spectral line of singly ionised oxygen helps to avoid uncertainties due to the unknown dissociation process of $W(CO)_6$ since the direct formation of more than singly ionised

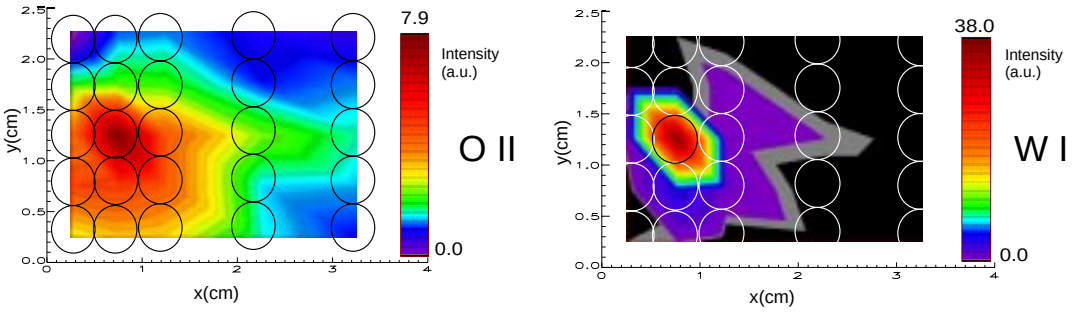

Figure 4.2: Spatial distribution of the emitted radiation after $W(CO)_6$ injection [157]. The projections of the viewing chords are indicated as black/white rings.

oxygen is very unlikely (see eg. [168,169]). As expected, the O II emission is much larger than the W I emission. O II as well as W I have several metastable electron configurations [167], so that for both influxes relation 4.8 has to be used. Thus taking into account the stoichiometric relation of tungsten and oxygen in $W(CO)_6$ one gets the equation

$$\left.\frac{S}{XB}\right|_{WI,eff} = \frac{1}{6}\left.\frac{S}{XB}\right|_{OII,eff}\frac{I_{OII}}{I_{W,I}}. \tag{4.9}$$

The ratio for the observed oxygen line can be calculated with the data for $S/XB|_{OII,397.3nm}$ and f_σ given in [167] and [170] as $S/XB|_{OII,eff} = 9.7$ for a temperature of 12 eV and an electron density of 10^{20} m^{-3} in the divertor as measured by Langmuir probes. From equation 4.9 one sees that for the determination of the S/XB ratio only the relative intensities of the observed lines are necessary. Since both lines lie together closely enough to assure that there is no difference in detection sensitivity, no absolute calibration of the spectrometer was necessary.

The value one obtains for the effective S/XB ratio for the 400.9 nm line of W I from the ratio of integrated intensities is $\left.\frac{S}{XB}\right|_{WI,eff} = 16 \pm 10$ for an electron temperature of 12 eV taken from Langmuir probe measurements. This value is in good agreement with measurements performed at the Berlin Plasma Simulator (PSI) cited earlier [111] and confirms these findings under reactor relevant divertor plasma conditions (see Fig. 4.3).

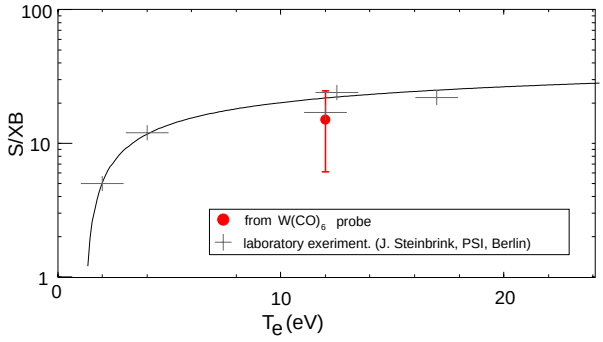

Figure 4.3: Effective inverse photon efficiency S/XB for the W I spectral line at 400.9 nm from [111] and [157]

Following these preparatory experiments a spectral scan was performed during the W divertor experiment at ASDEX Up-

grade. Again, the W I line at 400.9 nm was found to be the brightest, whereas no W II emission could be detected except in the case of disruptions. Therefore, the W I at 400.9 nm was used for all W influx measurements in ASDEX Upgrade (see [99, 171] and Chap. 6) and it has been adopted in other W experiments within fusion devices as well (see for example [172–174]).

4.2 Vacuum Ultra Violet Spectral Range

A diagnostic tool for the investigation of the W behaviour in plasma discharges was vital for the W experiments at ASDEX Upgrade. Therefore, investigations on W spectroscopy by W injection using laser ablation were initiated well before the installation of W coated tiles. As a starting point the tungsten radiation in the VUV spectral range was investigated. There, the W quasi-continuum around 5 nm was already well known from the early tungsten experiments at PLT or ORMAK [21,159,175,176] (see Sec. 7.1). It originates from tungsten ions with open 4d and 4f sub-shells around W^{28+} (see Fig. 4.4). The large number of coupling possibilities of the bound electrons leads to a large number of energy levels with similar energies, resulting in an array of lines. Furthermore the arrays of different tungsten ions overlap in the same wavelength region. The emission from these ions has been studied by Finkenthal et al. [175] and Mandelbaum et al. [176] using the 'Unresolved Transition Array' formalism.

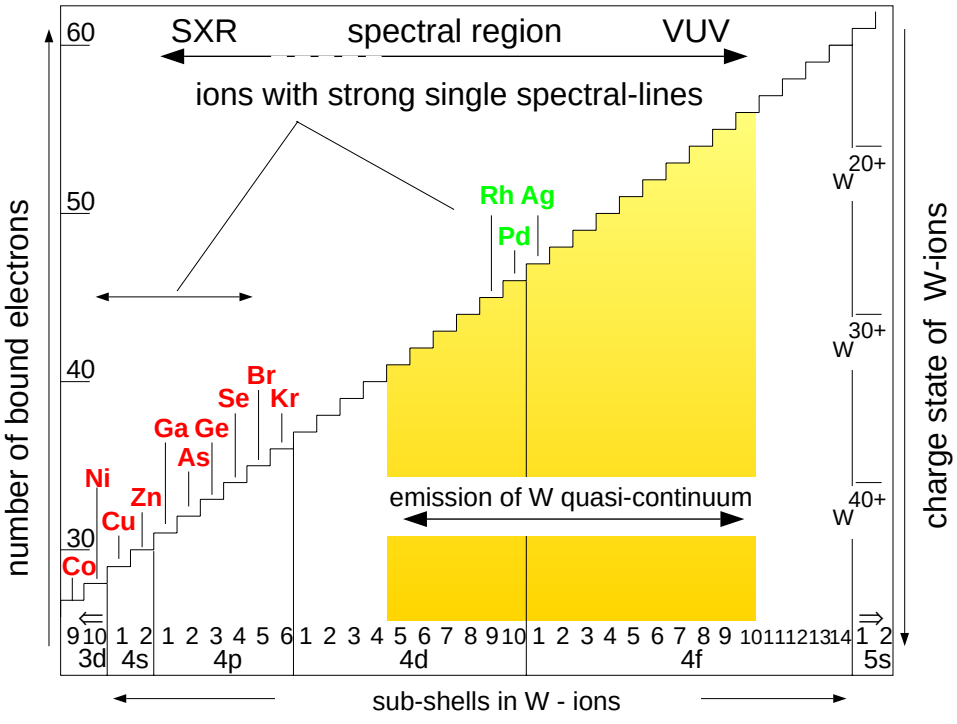

Figure 4.4: Schematic view of the electronic configuration of highly charged W ions.

4.2.1 The Tungsten Quasi-Continuum

During ohmic discharges in ASDEX Upgrade only the known quasi-continuum structure of tungsten at about 5 nm was observed in the EUV and VUV region (4 nm to 140 nm). The main contribution to the quasi-continuum is emitted from W ions around the Pd-like W^{28+} ion [177–179]. This is confirmed by the dependence of the quasi-continuum

intensity on the plasma temperature [180]: After normalising the intensity for the W concentration and the background plasma density a broad maximum is found for central temperatures around 1.2 keV with a weak decrease towards the higher central temperatures indicating the reduced radial width of the corresponding ionisation shells. The strong decrease of the intensity towards lower temperatures can be explained by the fact that a certain minimum temperature is needed to produce the quasi-continuum emitting tungsten ions. Very recent investigations at the Berlin EBIT [181, 182] allowed a very precise resolution of the charge states contributing to the quasi-continuum, corroborated by the above observations. However, at the same time it could be shown that for the electron densities present in the EBIT, the quasi-continuum of single ion species fuses to a narrow band around 5 nm with decreasing wavelengths for increasing charge number. The collisional radiative calculations described in [182] revealed a strongly density dependent level population leading to non-Boltzmann distributions at the low densities ($n_e \leq 10^{19}\mathrm{m}^{-3}$) as existent in the EBIT. They result in a much larger number of transitions, already at $n_e \geq 10^{20}\mathrm{m}^{-3}$, as observed for the quasi-continuum at ASDEX Upgrade. In a few discharges an accumulation of tungsten in the central plasma after laser ablation occurred, which offered a second test for the identification of the source of the quasi-continuum radiation. The resulting high tungsten radiation losses in these accumulation discharges led to flat or almost hollow temperature profiles. An example of the temporal evolution of W spectra during accumulation is shown in Fig. 4.5, where the tungsten remains in the plasma longer than 500 ms ($\tau_{decay} > 1000$ ms). After injecting

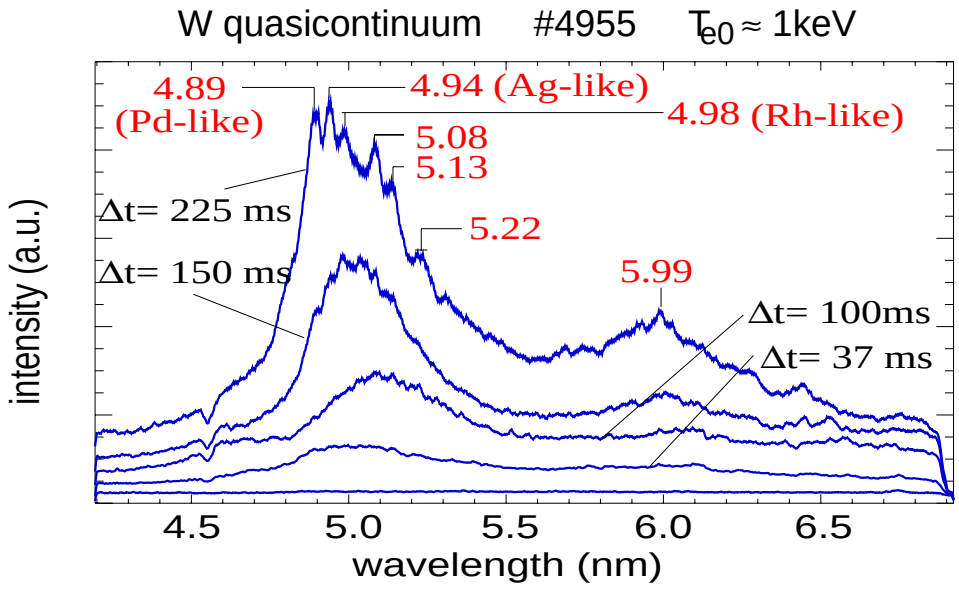

Figure 4.5: Temporal evolution of measured tungsten spectra around 5 nm in a low temperature plasma after W laser blow-off ($P_{NBI} = 2.5$ MW, $I_p = 1$ MA, $\bar{n}_e = 6.5 \cdot 10^{19}$ m^{-3}).

W into the plasma at 3 s, the usual quasi-continuum structure is observed (Δt= 35 and 100 ms). The large additional radiation losses due to tungsten of about 1 MW in the main plasma cause a temperature drop from $T_{e0} \approx 2.5$ keV to about 900 eV, resulting in a hollow temperature profile. The distributions of the Ag-, Pd- and Rh-like ions (W^{27+},W^{28+}, and W^{29+}, respectively) get broader, the intensity of the lines emitted by these ions increases ($\Delta t \geq 150$ ms) and isolated lines can be distinguished from the rest of the quasi-continuum. Table 4.1 gives the identification of the lines according to [178]. Other lines in the spectrum could not be identified, because the resolution of the grazing incidence spectrometer was insufficient.

Ion	transition	λ_{obs} (nm)	λ_{SKR} (nm)
W^{27+} (Ag–like)	$4d^{10}4f\ {}^2F_{5/2}$ – $4d^{10}4f(^1P)4f\ {}^2D_{3/2}$ $4d^{10}4f\ {}^2F_{7/2}$ – $4d^{10}4f(^1P)4f\ {}^2D_{5/2}$	4.94	4.9403
W^{28+} (Pd–like)	$4d^{10}\ {}^1S_0$ – $4d^9 4f\ {}^1P^\circ_0$	4.89	4.8948
W^{29+} (Rh–like)	$4d^9\ {}^2D_{5/2}$ – $4d^8(^3F)4f\ {}^2F_{7/2}$	4.98	4.9785

Table 4.1: Observed transitions of tungsten ions around W^{28+} in the $\lambda \approx 5$ nm wavelength region. These spectral lines were measured after tungsten laser ablation in a discharge (#4955) with $T_{e0} = 0.9$ keV. The values for λ_{SKR} were taken from [177–179].

4.2.2 Isolated Spectral Lines of Higher Ionised Tungsten

In hot plasmas with temperatures above 2 keV, isolated tungsten lines can be observed in the wavelength region from 4 nm to 15 nm. In the region above 15 nm no lines were found. The region from 4 nm to 7 nm was monitored routinely, because it made the simultaneous detection of the quasi-continuum structure and the line features possible. Therefore, it was used for monitoring the W concentration (see Sec. 4.2.4). Figure 4.6 shows the temporal evolution of the spectrum of the grazing incidence spectrometer in a discharge with 7 MW NBI additional heating power (#4896, $\bar{n}_e \approx 8 \cdot 10^{19}$ m^{-3}, $T_{e0} \approx 2.4$ keV, $I_p = 1$ MA). Immediately after tungsten ablation the quasi-continuum rises and reaches a maximum after about 20 ms. As the tungsten ions penetrate deeper into the plasma they reach regions with higher temperatures. Ions with larger charge numbers occur and radiate strong isolated lines (see also Fig. 4.4). A characteristic of these additional lines is the temporal evolution of their intensities. The sawtooth-shaped behaviour indicates that they are emitted from the hot core plasma by highly ionised tungsten ions. The variation in intensity is a result of the internal sawtooth–instability, which periodically ejects particles and energy out of the central plasma. Because of the lowered T_e the tungsten ions recombine and become less ionised. Along with recombination in the cooler plasma, the tungsten is distributed over a larger plasma volume that cannot

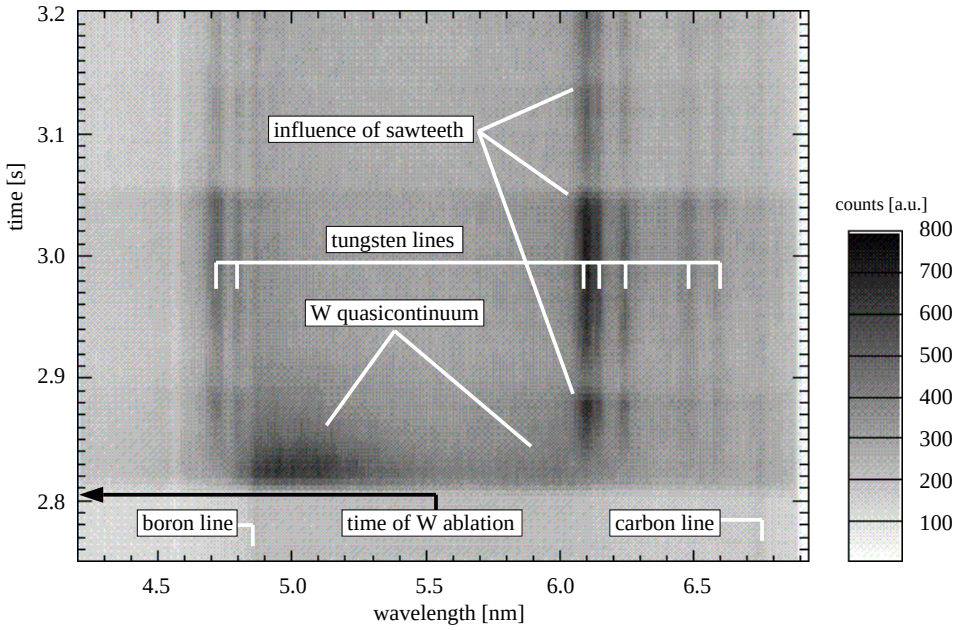

Figure 4.6: Temporal evolution of the spectrum of the grazing incidence spectrometer at 5.5 nm in a discharge with 7 MW NBI additional heating power (#4896, $\bar{n}_e \approx 8 \cdot 10^{19}$ m^{-3}, $T_{e0} \approx 2.4$ keV, $I_p = 1$ MA). The influence of the sawteeth on the intensities of single lines is clearly visible.

be completely observed by the grazing incidence spectrometer. Both effects lead to a reduction of the observed intensity of the isolated tungsten lines. After the sawtooth–crash W accumulates again in the central plasma, and the cycle starts over again.

A spectrum of the lines 200 ms after the W injection of the same discharge is shown in Fig. 4.7. The total exposure time was 100 ms, and the background radiation was subtracted. The upper spectrum (a) in Fig. 4.7 was detected before the injection of W and served for the wavelength calibration. It shows lines of He-like boron (B IV: 1s^2 – 1s2p), H-like boron (BV: 1s –2p) and H-like carbon (2.order C VI:1s – 2p) [183]. The error of the peak position of isolated lines is estimated to be 0.01 nm. The identification of the W lines was performed by comparison with observations in [184–186] and with the help of HULLAC-code calculations by J.M. Laming [180] shown in the lower part of the figure (c). Each calculated spectrum of a single W ion has to be shifted by an amount of up to 0.03 nm to longer wavelengths, to fit the observed lines. Table 4.2 lists the fitted wavelengths and relative intensities of the observed spectrum. Furthermore, the table shows the probable composition of the line patterns from calculated lines which are given in Table 4.3 (transitions, theoretical wavelengths and intensities). Strong lines are radiated by tungsten ions isoelectronic to Cu, Zn, and Ga and because of their relatively simple electron configuration, there are only a few resonant transitions in each ion. In the investigations at the Berlin EBIT [182] these transitions and their identification could

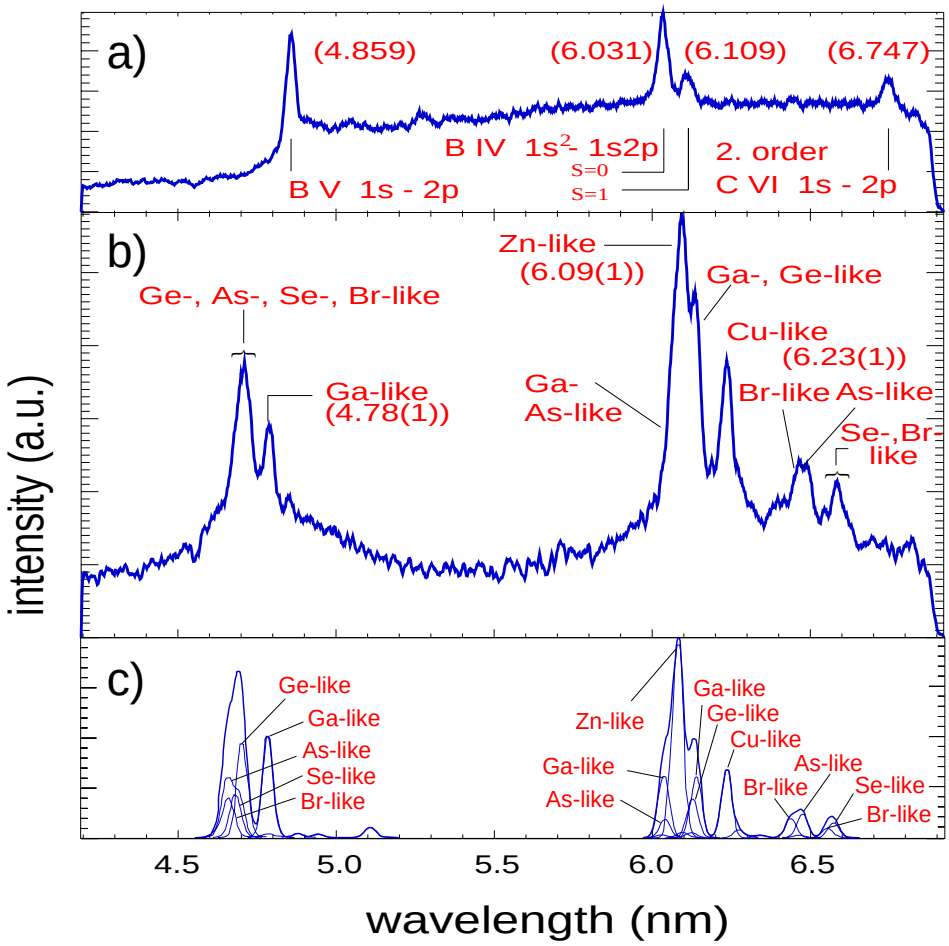

Figure 4.7: a) Spectrum of light intrinsic impurities around 5 nm. b) Spectrum of $4s-4p$ and $4p-4d$ transitions in Br-like to Cu-like W observed in discharge #4896. c) Simulated spectra from atomic physics calculations with the HULLAC code [180].

be confirmed.

Other lines of the same ions were observed for the first time in the wavelength region from 12 to 14 nm, whereas in the region from 7 to 12 nm no lines were evident. Tungsten was injected in discharge #7470 ($I_p = 1$ MA), in both, an ohmic ($\bar{n}_e \approx 4 \cdot 10^{19}$ m^{-3}, $T_{e0} \approx 1$ keV) and an additional heated phase ($P_{NBI} = 5$ MW, $\bar{n}_e \approx 6 \cdot 10^{19}$ m^{-3}, $T_{e0} \approx 2.6$ keV). In the ohmic phase (not shown) no tungsten lines were found in the 7 nm to 14 nm region, whereas during the neutral beam injection, with higher T_{e0}, isolated lines occurred after laser ablation. Figure 4.8 shows the temporal behaviour of the grazing incidence spectra (top), the time-averaged spectrum (integration period 60 ms, 150 ms after W ablation, (centre), and the result of RELAC-Code calculations (bottom) [180]. Due to the lack of calibration lines in this spectral range the measured wavelengths are more uncertain than in the 4–7 nm region. The overall maximum shift of the measured spectra is estimated to be $\Delta\lambda_{shift} \leq 0.2$ nm whereas the relative position of two spectral lines should be

λ_{obs}	λ_{ref}	rel. meas. int.	transition
4.69		45	W^{41+},W^{40+},W^{39+} (I.10,11,16,17,22,24)
4.72		42	W^{42+}(I.7)
4.79		40	W^{43+}(I.4)
6.06		47	W^{43+}, W^{41+}(I.5,12)
6.09	6.096 [184]; 6.0883 [186]	100	W^{44+}(I.2)
6.14		81	W^{43+}, W^{42+} (I.6,8)
6.23	6.2386 [187]; 6.2304 [186]	55	W^{45+}(I.1)
6.46		10	W^{39+}(I.26)
6.49		18	W^{41+}(I.13)
6.58		15	W^{40+}, W^{39+} (I.20,27)

Table 4.2: Observed transitions of Br- to Cu-like W ions in the $\lambda \approx 5$ nm wavelength region. The spectral lines were measured after tungsten laser ablation in the discharge (#4896) with $T_{e0} = 2.4$ keV. The uncertainty of the observed wavelengths is around 0.01 nm. The numbers in brackets in the fourth column denote the corresponding transitions in Table 4.3.

better than $\Delta(\lambda_1 - \lambda_2) \leq 0.02$ nm. The sawtooth–like temporal behaviour of the line intensities and the high T_{e0} suggests, that these lines are emitted by similar ion stages as the spectral lines in the 5 nm–region. The measurements in the soft X-ray region at 0.7 nm under comparable plasma conditions (see Sec. 4.3), also reveal spectral lines from transitions ($\Delta n = 1$) in Br-like to Ni-like tungsten ions, making this tentative assignment very plausible.

Table 4.4 lists the wavelengths and probable transitions of the measured spectral lines resulting from a comparison with the predicted ones. The lines II.1–II.4 are 2nd order diffractions of the lines around 6 nm. Many of the lines in the spectrum of Fig. 4.8 are electric dipole (E1) forbidden (see Table 4.4) and the high intensity of a magnetic dipole (M1) or electric quadrupole (E2) line must be due to the high population in its upper state making collisional-radiative calculations necessary [188]. However, there the same fractional abundance is used for all ions and so the relative line intensities are strictly valid only in the same charge state. The calculated wavelength of the Zn-like W^{44+} line observed at 13.35 nm, which had not been observed before, is very sensitive to configuration interaction (CI) in the energy level calculation [189]. Other calculations [188, 190] that account for CI between the ground level of the Zn-like ion ($4s^2\ ^1S_0$) and doubly excited levels from configurations such as $4p^2$, $4d^2$ and $4p4f$ produce wavelengths shorter than that reported in Table 4.4. In the presented calculations CI is not taken into account.

no.	Ion	transition	λ_{calc} (nm)	calc. int.†
I.1	W^{45+} (Cu–like)	$4s^2S_{1/2}$ – $4p\ ^2P_{3/2}$	6.2128	8.6
I.2	W^{44+}	$4s^2\ ^1S_0$ – $4s4p\ ^1P_1$	6.0643	19.6
I.3	(Zn–like)	$4s4p^1P_1$ – $4s4d\ ^3D_1$	7.3186	1.52
I.4	W^{43+}	$4s^24p\ ^2P_{1/2}$ – $4s^24d\ ^2D_{3/2}$	4.7594	9.89
I.5	(Ga–like)	$4s^24p\ ^2P_{1/2}$ – $4s4p^2\ ^2P_{1/2}$	6.0161	6.22
I.6		$4s^24p\ ^2P_{1/2}$ – $4s4p^2\ ^2P_{3/2}$	6.1159	6.14
I.7	W^{42+}	$4s^24p^2\ ^3P_0$ – $4s^24p4d\ ^3D_1$	4.6861	19.0
I.8	(Ge–like)	$4s^24p^2\ ^3P_0$ – $4s4p^3\ ^3D_1$	6.1123	7.77
I.9	W^{41+}	$4s^24p^3\ ^4S_{3/2}$ – $4s^24p^24d\ J=1/2$	4.6587	2.89
I.10	(As–like)	$4s^24p^3\ ^4S_{3/2}$ – $4s^24p^24d\ J=3/2$	4.6621	7.76
I.11		$4s^24p^3\ ^4S_{3/2}$ – $4s^24p^24d\ J=5/2$	4.6976	7.99
I.12		$4s^24p^3\ ^4S_{3/2}$ – $4s4p^4\ ^4P_{3/2}$	6.0497	3.7
I.13		$4s^24p^3\ ^4S_{3/2}$ – $4s4p^4\ ^4P_{5/2}$	6.4853	4.67
I.14		$4s^24p^3\ ^4S_{3/2}$ – $4s^24p^24d\ J=5/2$	7.0440	1.05
I.15	W^{40+}	$4s^24p^4\ ^3P_2$ – $4s^24p^34d\ J=1$	4.6402	3.88
I.16	(Se–like)	$4s^24p^4\ ^3P_2$ – $4s^24p^34d\ J=2$	4.6518	6.92
I.17		$4s^24p^4\ ^3P_2$ – $4s^24p^34d\ J=2$	4.6543	8.92
I.18		$4s^24p^4\ ^3P_0$ – $4s^24p^34d\ J=1$	4.6598	3.19
I.19		$4s^24p^4\ ^3P_2$ – $4s4p^5\ ^3P_2$	6.2498	3.93
		(blended with: $4s^24p^4\ ^3P_0$ – $4s4p^5\ ^3P_1$)		
I.20		$4s^24p^4\ ^3P_2$ – $4s^24p^34d\ J=3$	6.5480	7.36
I.21	W^{39+}	$4s^24p^5\ ^3P_{3/2}$ – $4s^24p^44d\ J=5/2$	4.5886	1.41
I.22	(Br–like)	$4s^24p^5\ ^3P_{3/2}$ – $4s^24p^44d\ J=1/2$	4.6195	4.88
I.23		$4s^24p^5\ ^3P_{3/2}$ – $4s^24p^44d\ J=3/2$	4.6313	1.00
I.24		$4s^24p^5\ ^3P_{3/2}$ – $4s^24p^44d\ J=5/2$	4.6336	5.67
I.25		$4s^24p^5\ ^3P_{3/2}$ – $4s4p^6\ ^2S_{1/2}$	6.0688	2.65
I.26		$4s^24p^5\ ^3P_{3/2}$ – $4s^24p^44d\ J=5/2$	6.4145	9.40
I.27		$4s^24p^5\ ^3P_{3/2}$ – $4s^24p^44d\ J=3/2$	6.5293	4.72

Table 4.3: Calculated transitions of Br- to Cu-like W ions in the $\lambda \approx 5$ nm region. The intensities (10^4 photons/ion/s) were calculated taking $T_e = 2000$ eV, $n_e = 10^{20}$ m^{-3} [180].

4.2.3 Fractional Abundance of W Ions

The relative abundances of the W ions and the radial extension of the corresponding plasma shells were calculated by means of the ADPAK-package [24] and the transport code STRAHL. The required rates for ionisation, radiative and dielectronic recombination are included in the ADPAK-package. A comparison of observed tungsten spectra in different types of discharges with theoretical W ion distributions allowed these rates to be checked.

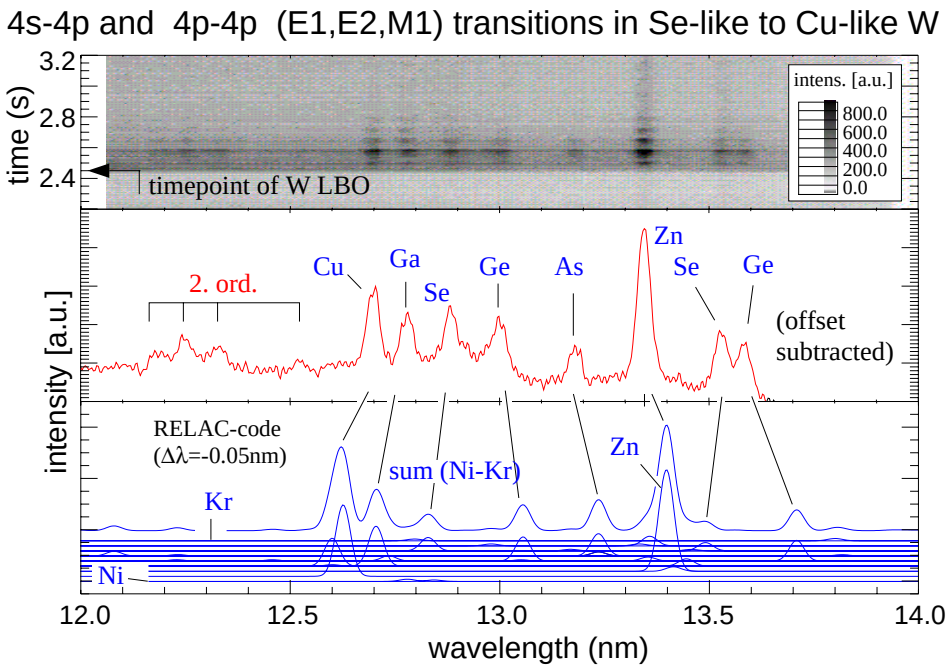

Figure 4.8: Spectral lines of highly ionised tungsten in the 13 nm region. Top: Temporal behaviour of the lines as observed by the grazing incidence spectrometer after a W injection at 2.5 s. The horizontal lines show the influence of the central sawtooth activity (see Fig. 4.6). Centre: Time integrated spectra (t_{integ} = 100 ms, 200 ms after injection). Bottom: Calculated spectra (RELAC-Code) [180], showing the total intensity and the individual contributions of the Kr- to Ni-like W ions (with different vertical offsets).

Whereas the dependence of the intensity of the W quasi-continuum on T_e is consistent with the calculated distribution of Ag- to Pd-like W ions (see [180]), the observation of Cu-like tungsten in additionally heated plasmas with T_e ≈2.3 keV cannot be explained by the original ADPAK rates. To get agreement between spectroscopic observations and STRAHL predictions, the ionisation rates for W ions with charge numbers larger than 30 had to be increased by a factor of up to 3. The same result could have been obtained by decreasing the recombination rates by the same factor. Calculations by Mitnik et al. [191, 192] explain the increase of the ionisation rates by excitation autoionisation. The importance of the excitation autoionisation has already been pointed out by Rice et al. [161] in the case of the molybdenum ionisation equilibrium in Alcator C-Mod discharges.

Trans. No.	λ_{obs} (nm)	λ_{calc} (nm)	λ_{pred} (nm)	Isoel. Seq.	Transition	Type	Rel. Meas. Intensity
II.1	12.19				2nd ord. 6.06 nm (Tab. 4.2)		10
II.2	12.25				2nd ord. 6.09 nm (Tab. 4.2)		19
II.3	12.33				2nd ord. 6.14 nm (Tab. 4.2)		14
II.4	12.52				2nd ord. 6.23 nm (Tab. 4.2)		8
II.5	12.70	12.627		Cu	$4s\ ^2S_{1/2} - 4p\ ^2S_{1/2}$	E1	52
II.6	12.78	12.706		Ga	$4s^24p\ ^2P_{1/2} - 4s4p^2\ ^4P_{1/2}$	E1	34
II.7	12.89	12.830		Se	$4s^24p^4\ ^3P_2 - 4s^24p^4\ ^1D_2$	M1	33
II.8	13.00	13.057		Ge	$4s^24p^2\ ^3P_0 - 4s^24p^2\ ^3P_2$	E2	31
II.9	13.18	13.237		As	$4s^24p^3\ ^4S_{3/2} - 4s^24p^3\ ^2D_{5/2}$	M1	20
II.10	13.35	13.399	13.2824	Zn	$4s^2\ ^1S_0 - 4s4p\ ^3P_1$	E1	100
II.11	13.53	13.492		Se	$4s^24p^4\ ^3P_2 - 4s^24p^4\ ^3P_1$	M1	40
II.12	13.59	13.710		Ge	$4s^24p^2\ ^3P_0 - 4s^24p^2\ ^3P_1$	M1	35

Table 4.4: Observed and calculated transitions in the wavelength region from 12 nm to 14 nm. The spectral lines were measured after tungsten laser ablation in a plasma discharge (#7470) with $T_{e0} = 2.6$ keV. The wavelengths λ_{calc} were calculated by means of the HULLAC-code. (Note: Agreement between the wavelength of lines with the corresponding 1st order wavelengths of Table 4.2 can be obtained by shifting the measured wavelengths of II.1–II.4 by 0.058 nm to shorter wavelengths and division by two. The same wavelength shift also leads to an agreement between λ_{obs} and λ_{pred} of II.10 [190].)

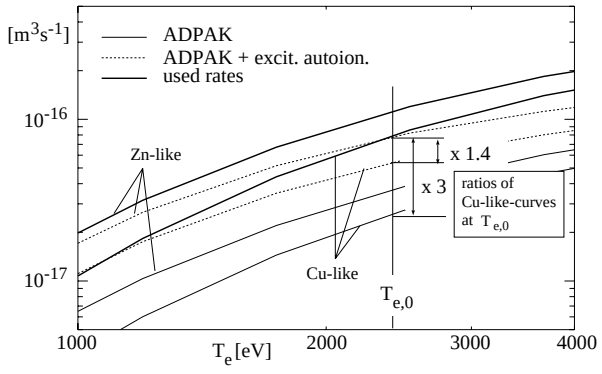

Figure 4.9: Ionisation rate coefficients for Zn- and Cu-like tungsten ions. The thick solid lines represent the ionisation rates ultimately used, the dashed lines are the sum of ADPAK-rates (shown as thin solid lines) and excitation autoionisation rates [191].

A comparison of the different ionisation rate coefficients for Zn- and Cu-like tungsten ions is given in Fig. 4.9. Thick solid lines are the ionisation rates ultimately used in STRAHL, thin solid lines represent unmodified ionisation rates from ADPAK, and the dashed lines are the sum of ADPAK- and excitation autoionisation rates. By inclusion of excitation autoionisation the difference between the theoretical total ionisation rate and the ionisation rate needed to reproduce the measurements is reduced from a factor of 3 to a factor of 1.4, i.e. good agreement within the uncertainties of the modification factors. Figure 4.10 shows the relative abundances of some W ions, calculated with differ-

ent ionisation rates for a typical ASDEX Upgrade discharge with NBI-heating ($n_{e0} = 8 \cdot 10^{19}$ m^{-3}, $T_{e0} = 2.6$ keV; pure diffusive transport with a smoothly varying diffusion-profile: $D(\rho_{pol} = 0) = 0.5$ m^{2}s^{-1}, $D(\rho_{pol} = 0.8) = 2.5$ m^{2}s^{-1} [193]). Thin short dashed lines represent the results from unmodified ADPAK rates for ionisation and recombination. In this case the maximum charge state of tungsten is about 42, which is insufficient to explain the occurrence of lines of Cu- and Zn-like W ions. Thick solid lines indicate the calculations with modified rates of ionisation. The ion distribution calculated for a coronal ionisation equilibrium without transport can be seen from the thin dashed lines. The influence of the transport on the distribution is very small, and thus is excluded as a possible explanation for the observation of the lines of W^{45+}.

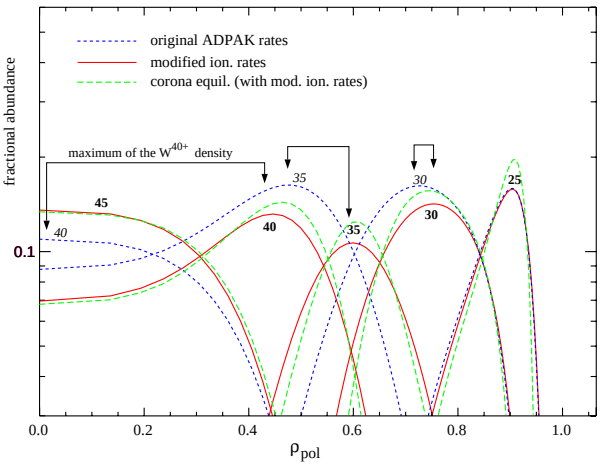

Figure 4.10: Fractional abundances of selected W ions, calculated with different ionisation rates with (see text) and without transport for a typical ASDEX Upgrade discharge with NBI-heating ($n_{e0} = 8 \cdot 10^{19}$ m^{-3}, $T_{e0} = 2.6$ keV).

In Fig. 4.11 the distribution of all W ionisation states is shown (determined with the modified ADPAK-rates). In discharges with central temperatures $T_{e0} \geq 2.3$ keV tungsten ions with simple electron configurations (Kr- to Cu-like tungsten, $4s^2 4p^m$ or $4s^n$) can be found in the plasma centre (see also Fig. 4.4). Tungsten ions with charge numbers similar to Ag-like tungsten (W^{27+}), which emit the quasi-continuum structure at about 5 nm, are located at the outer half of the plasma ($\rho_{pol} \approx 0.7$). In ohmic discharges only ionisation states up to $\approx W^{30+}$ can be found in the plasma, because of of the lower electron temperatures. These calculated distributions of the W ionisation states are in qualitative agreement with calculations of the ionisation equilibrium given in [163], although it is not evident from the reference, how such a shift in the ionisation equilibrium is gained. The (modified) rate coefficients for ionisation (and recombination) used throughout are given in the appendix of [180].

4.2.4 W Concentration from VUV Measurements

The primary aim of the spectroscopic investigations in the VUV was the preparation of a basis for evaluation of W inventories in discharges during the W experiments at ASDEX Upgrade. However, it is rather evident that such complex spectroscopic structures as the W quasi-continuum are not easily handled with spectroscopic *ab initio* calculations. In

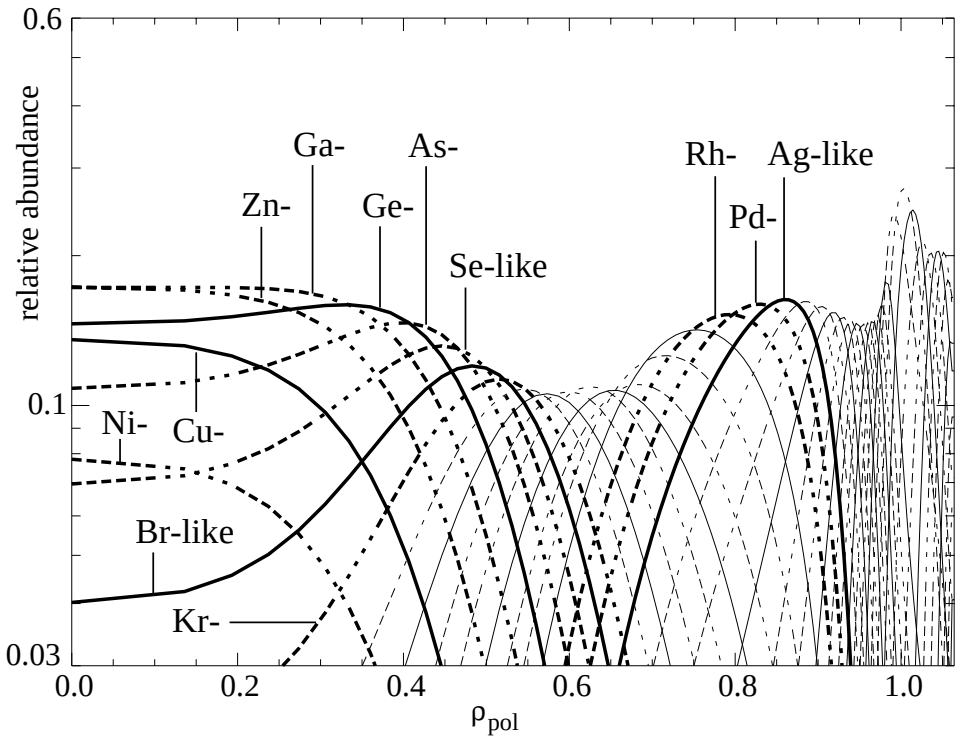

Figure 4.11: Radial distribution of the fractional abundances in coronal equilibrium of W ions in a typical additionally heated plasma ($T_{e0} \approx 2.6$ keV) calculated with the modified ADPAK rates. Bromine- to nickel-like W ions exist in the plasma centre. Tungsten ions around the charge state $Z = 28+$, which emit the quasi-continuum radiation around 5 nm, exist in the outer half of the main plasma.

the case of the observed single lines the situation was somewhat alleviated, but there the accuracy of the calculated photon emission coefficients was not clear from the beginning and a more pragmatic way had to be followed. As described in Sec. 2.1, the main influence of the W contamination on a fusion plasma is given by the central loss of energy by its radiation. Therefore, the additional tungsten radiation after laser ablation was taken as a basis for the determination of the tungsten concentration in the main plasma of ASDEX Upgrade. The spatial distribution of the radiation is obtained from a deconvolution of the line of sight intensities of the bolometer camera channels. Averaging this radiation over magnetic flux surfaces gives the radial radiation profiles. With the assumption that the tungsten injection does not modify the background radiation (the amount of ablated tungsten has to be small enough), a subtraction of the radiation immediately before the tungsten laser ablation from all following profiles yields radial tungsten radiation profiles.

Assuming an ionisation equilibrium near to coronal ionisation equilibrium for the tung-

sten ions in the main plasma, the inversion of

$$P_W = n_e(r,t) \cdot n_W(r,t) \cdot p_W(r,t) \tag{4.10}$$

yields the tungsten density n_W and concentration $c_W = n_W/n_e$ as a function of time and the minor plasma radius. In this equation P_W is the radiation loss due to tungsten, $n_e(r)$ the electron density profile, and $p_W(T_e(r,t))$ the radiation loss parameter (or radiation potential) of tungsten (cf. Fig. 2.1), taken from [24, 25]. No alterations due to the shift of the ionisation rates were performed, because the major contribution to the radiation originates from W ions where no changes in the ionisation rates were needed. The tungsten concentration $c_{W,bolo}$ determined by means of this method was then taken to cross calibrate the measured intensities of the spectroscopic signatures. The magnitude of the error of c_W is determined by the validity of the coronal ionisation equilibrium, the uncertainties of the deconvolution algorithm, the error of the profiles of electron temperature and density, and the error in the radiation loss parameter $p_W(T_e)$. Since the later is also used to estimate the allowed concentrations in a reactor, an error there will hamper the comparison of the cross calibrated data with spectroscopic *ab initio* calculations, but the results of this work would be consistent with the general calculations. The overall relative error of $c_{W,bolo}$ was estimated in [180] to be $\leq 80\%$. To check the determined c_W the maximum inventory of tungsten after laser ablation inside the confined plasma $N_W = \int n_W(\rho) dV$ was compared with the injected amount of tungsten. In the majority of the discharges the maximum inventory inside ρ=0.6 is found to be 4% to 14% of the ablated amount of W [180], consistent with other investigations of laser ablation experiments [194].

The detection limit of this method is given by the need to subtract the background radiation of the plasma and the deconvolution errors. In the case of a W injection, the background radiation can be rather easily subtracted and concentrations down to $c_W \approx 10^{-5}$ can be extracted because there is a clear temporal distinction. However, in the case of a continuous W source, as in the W experiments at ASDEX Upgrade, the errors of this method are found to be too large to give reliable results below $c_W \approx 10^{-4}$.

An alternative signal to the total radiation is the intensity of the quasi-continuum structure of tungsten measured by the grazing incidence spectrometer. Besides the fact, that the spectroscopic signal is much easier to discriminate from the background, it is an advantage of this line structure that it is emitted by tungsten ions of comparatively low ionisation state, i.e. it can be observed in both ohmic and additional heated plasmas. However, it is a rather broad spectroscopic structure composed of the spectra of many ions, which renders the determination of its intensity more difficult. Simply monitoring the peak intensity at 5 nm may lead to incorrect results due to the additional radiation background especially in neutral beam heated discharges. To get a quantitative measure for the quasi-continuum intensity it is essential to use the whole feature to achieve a sen-

sitive detection limit. A linear regression was used to fit the grazing incidence spectrum in the wavelength region from 4 to 7 nm (averaged over 50 ms) by means of a set of sample spectra. Two of the spectra represented the quasi-continuum structure and the isolated lines of tungsten, respectively, three more spectra represented the lines of boron and carbon, which usually dominate the isolated lines in the observed wavelength region, and three additional spectra were used to model the changing background radiation of the plasma. The intensities of the spectra representing the W quasi-continuum structure and the isolated W lines will be denoted in the following $I_{W,qc}$ and $I_{W,il}$, respectively. The samples for the characteristic tungsten radiation were taken from the discharges #4955 and #4896 (see Figs. 4.5 and 4.7), where the tungsten radiation could be well separated from the background radiation. A comparison between fitted and measured spectra for #8195 is shown in Fig. 4.12. In this discharge the tungsten was not injected by means of laser ablation but was intrinsic, originating from the tungsten divertor plates in ASDEX Upgrade. The lower part of the figure shows the sample spectra, the upper part the ob-

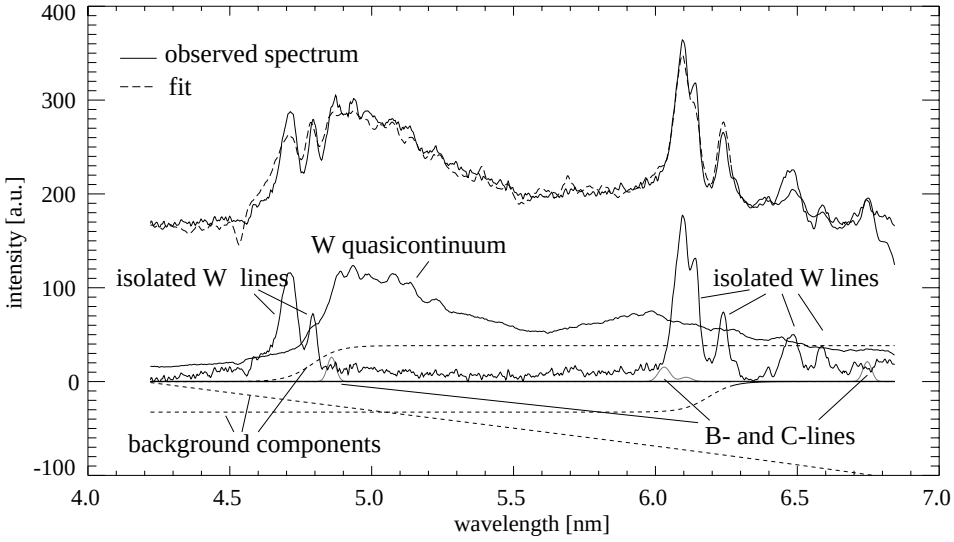

Figure 4.12: Comparison of the fitted spectrum and the measured spectrum (top) in discharge #8195. The sample spectra (W quasi-continuum, isolated W lines, B and C spectral lines, background spectra) used for the regression are shown in the lower part.

served and the fitted spectrum. A high particle confinement of the tungsten ions in the main plasma led to a grazing incidence spectrum, in which both the isolated lines and the quasi-continuum structure can be seen. To derive the tungsten concentration $c_{W,qc}$ from the spectroscopic measurements the quasi-continuum intensity was compared with the values of the tungsten concentrations derived by means of the bolometer measurements in W injection experiments described above. In contrast to the bolometer method, the analysis of the grazing incidence spectrum cannot deliver $c_W(\rho) = n_W(\rho)/n_e(\rho)$-profiles but only a mean concentration $c_W(\rho_{L,qc}) = c_{W,qc}$ for the plasma layer where the quasi-

continuum-emitting ions exist. Assuming that this layer has an effective thickness Δl, a constant emissivity of the quasi-continuum structure and a constant c_W, the intensity of the quasi-continuum can be written as

$$I_{W,qc} = \int d\lambda \int dl n_e(l) c_W(l) n_e(l) \eta_{qc}(l,\lambda) C_{GI}^{cal}(\lambda) \quad (4.11)$$

$$= n_e(\rho_{L,qc})^2 c_{W,qc} C_{GI,qc}^{cal} \bar{\eta}_{qc} \Delta l(\rho_{L,qc}) \quad (4.12)$$

$I_{W,qc}$ is the intensity of the quasi-continuum extracted by means of linear regression to the spectrum observed by the grazing incidence spectrometer in the wavelength region from from 4.5 nm to 7.0 nm in (counts/s). The sensitivity of the instrument is given by $C_{GI}^{cal}(\lambda)$ and $\eta_{qc}(l,\lambda)$ summarises the excitation and branching ratios of all transitions of the quasi-continuum in this wavelength region. The integration with respect to λ and l leads to an equation with mean values $C_{GI,qc}^{cal}$, $\bar{\eta}_{qc}$, $n_e^2(\rho_{L,qc})$, and $c_{W,qc}$ of the plasma layer located at ρ_L with a thickness of $\Delta l(\rho_{L,qc})$. This thickness varies slightly with the central temperature because the ionisation shells are shifted outwards with increasing temperature in the core plasma. This dependence was approximated with the help of the simple model of the temperature dependence described in [180]. The calibration factor $C_{qc,rel}^{cal} = C_{GI,qc}^{cal} \bar{\eta}_{qc} \Delta l(\rho_{L,qc})$ was obtained by comparing

$$c_{W,qc} = \frac{I_{W,qc}}{C_{qc,rel}^{cal} n_e^2(\rho_{L,qc})} \quad (4.13)$$

after W laser ablation with the tungsten concentration $c_{W,bolo}$ obtained with the help of the bolometer method for several discharges. n_e was approximated by the line averaged electron density $\bar{n}_e$ of the central DCN-interferometer channel (H-1). The difference between the actual density profile and $\bar{n}_e$ has only a small influence on c_W, because in ohmic discharges (with more peaked n_e profiles) the quasi-continuum is emitted in the central plasma and in H–mode discharges the electron profiles are usually flat.

Figure 4.13 shows the relation between $c_{W,qc}$ and $c_{W,bolo}$. The data points of almost all discharges are in a region defined by the two dashed lines indicating a 50% deviation from perfect agreement of the two concentration measurement methods (solid line). Larger deviations occur in H-mode-discharges in which the concentrations measurements can be disturbed by higher temperatures in the plasma centre (strong decrease of p_W for $T_{e0} \geq 1.5$ keV) or hollow temperatures profiles (anomalous increase of Δl). The relative error of $c_{W,qc}$ can be conservatively approximated by $\delta c_{W,qc} \approx \delta(n_e^2) + \delta l + \delta I_{W,qc} + \delta C_{qc,rel}^{cal} \approx 1.3$. Additionally to this estimated errors, a detection limit was adopted which results from the signal-to-noise-ratio of the grazing incidence spectrometer and therefore is also valid for a continuous W source. From a comparison of several discharges with W laser ablation it was found to be $(5 \cdot 10^{-6} \times (4 \cdot 10^{19} \mathrm{m}^{-3}/\bar{n}_e)^2$, i.e. concentrations $c_{W,qc}$ below this detection limit were not expected to be reliable.

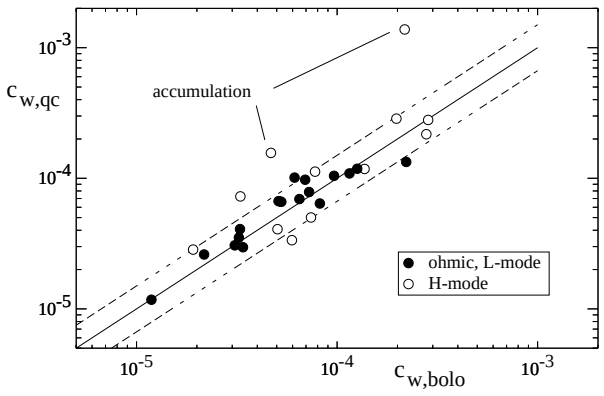

Figure 4.13: Tungsten concentrations calculated from the intensity of the W quasi-continuum versus the tungsten concentration determined from bolometer measurements in discharges with W laser injection. The dotted curves show the 50% deviation from ideal agreement.

In order to detect W in the centre of hot, additionally heated plasmas, the isolated lines of Br- to Cu-like tungsten, which are observed in the same λ region as the quasi-continuum, are better suited. The intensity of the single lines can be compared to the theoretical intensity from transport calculations using the temperature dependent excitation rate from the collisional-radiative model [188]. For a fast automatic evaluation for every time point of the discharge this elaborate procedure was substituted by an alternative method, replacing the necessary line integral by a simple product of mean values similar to eq. 4.12: The intensity $I_{W^{45+}}$ at 6.23 nm emitted by Cu-like tungsten can then be approximated by

$$I_{W^{45+}} = C^{cal}_{6nm}\eta_{W^{45+}} n_e^2(\rho_{W^{45+}})\Delta l(\rho_{W^{45+}})c_{W^{45+}}(\rho_{W^{45+}}) \tag{4.14}$$

with $\rho_{W^{45+}}$ the position of the maximum of the density of the copper like W ions, $\Delta l(\rho_{W^{45+}})$ the thickness of the corresponding plasma layer, $c_{W^{45+}}$ the concentration of the Cu-like W ions, and $\eta_{W^{45+}}$ the theoretical emissivity for the line at 6.23 nm calculated by the HULLAC code. Using the fractional abundance of these ions ($f_{W^{45+}} = c_{W^{45+}}/c_W$) (see Sec. 4.2.3), the total tungsten density is

$$c_W(\rho_{W^{45+}}) = \frac{I_{W^{45+}}}{C^{cal}_{6nm}\eta_{W^{45+}} n_e^2(\rho_{W^{45+}}\Delta l(\rho_{W^{45+}})f_{W^{45+}}} \tag{4.15}$$

To check the calibration factor C^{cal}_{6nm}, which was obtained by means of a double branching ratio method (cf. Sec. 3.1.2), an alternative calibration was performed which uses the intensity of the quasi-continuum structure. It is assumed that all radiation of the tungsten ions in the plasma region with $T_e \approx 0.8 - 1.$ keV is emitted in the quasi-continuum structure and that about 3/4 of this radiation is emitted into the 5 nm region (cf. [158]). With the help of the radiative potential p_W another calibration factor C^{cal}_{bolo} of the grazing incidence spectrometer in the 4.5 nm–7.0 nm region can be deduced from a comparison of the observed intensity $I_{W,qc}$ and the de-convoluted bolometer measurements. Both calibration factors, C^{cal}_{6nm} and C^{cal}_{bolo}, agree within 20%. The total relative error for the determination of $c_W(\rho_{W^{45+}})$ is estimated in a similar way as for the quasi-continuum to be $\delta c_W(\rho_{W^{45+}}) \approx 2$.

Finally, the intensity $I_{W,il}$ of the sample of isolated W lines (cf. previous section), was

then calibrated by means of $c_W(\rho_{W^{45+}})$. This was done by comparison of $c_W(\rho_{W^{45+}})$ with $I_{W,il}$ during t=2.25 s–2.75 s in the discharge #8195. The resulting $c_{W,il}$ is an average value of the tungsten concentration c_W in the centre of the plasma ($T_e \approx 2 - 2.5$ keV). Due to the inclusion of a larger number of lines and a larger wavelength region this value turned out to be less sensitive to perturbations (e.g. blending of the Cu-like line with boron lines) than $c_W(\rho_{W^{45+}})$, which is determined by means of one single line and was therefore used throughout the experiments.

4.3 Soft X-Ray Spectral Range

The investigations in the VUV spectral range are hampered by the rather complex structure of the quasi-continuum structure originating from $\Delta n = 0$ transitions as already mentioned in Sec. 4.2. The spectra of the individual ionisation states become simpler by going to shorter wavelengths and therefore to $\Delta n = 1$ transitions. Additionally, experimental arrangements with higher spectral resolving power can be used and also a separation of the diagnostic from the vacuum of the fusion device is possible in principle. This might be necessary in a future fusion device, which will use tritium as the working gas.

There are several publications on observations of soft X-ray spectral lines of highly charged ions of W from laser produced plasmas in the range from 0.34 to 0.45 nm [195, 196], from 0.67 to 0.73 nm [197, 198] and above 1 nm [186]. Recently, high resolution measurements of spectral lines from Ni-like W at 0.717 nm were reported from an electron beam ion trap (EBIT) experiment [199].

The identification of the spectra and the calculation of the line emissivities were performed in close collaboration with K.B. Fournier from Lawrence Livermore National Laboratory who was running HULLAC (Hebrew University Lawrence Livermore Atomic Codes) and performed the collisional radiative model calculations [188, 200–202].

4.3.1 Predictions from *ab initio* calculations

Atomic structure

The atomic structure part of HULLAC includes the graphical angular momentum coupling code ANGLAR [203] to generate fine structure levels in a jj-coupling scheme for a set of user-specified electron configuration. The fully relativistic parametric potential code RELAC of Klapisch et al. [189, 204] determines the ionic potential in an analytic form by minimising the average energy of a configuration of a group of configurations. To accomplish this, the Dirac Hamiltonian is divided into a spherical zero'th order contribution and a perturbation:

$$H_D \approx H_0 + H_1 + higher\ order\ terms. \tag{4.16}$$

H_0 contains the sum over all N electrons of the Dirac kinetic energy, the electron-nuclear interaction and the interaction between an electron and a spherically averaged potential arising from all other electrons:

$$H_0 = \sum_i^N [h_i^D + \frac{Z}{r_i} + V(r_i)]. \tag{4.17}$$

The perturbation includes only the difference between exact electrostatic interaction and the interaction between the electrons and the spherically symmetric potential:

$$H_1 = \sum_{i<j}^{N} \frac{1}{r_{ij}} - V(r_i). \tag{4.18}$$

The potential V represents the potential due to the superposition of a point nuclear charge Z and a radial electron charge density given by a sum of nodeless Slater-type wavefunctions.

The physical state of some ionic energy level can contain contributions from many

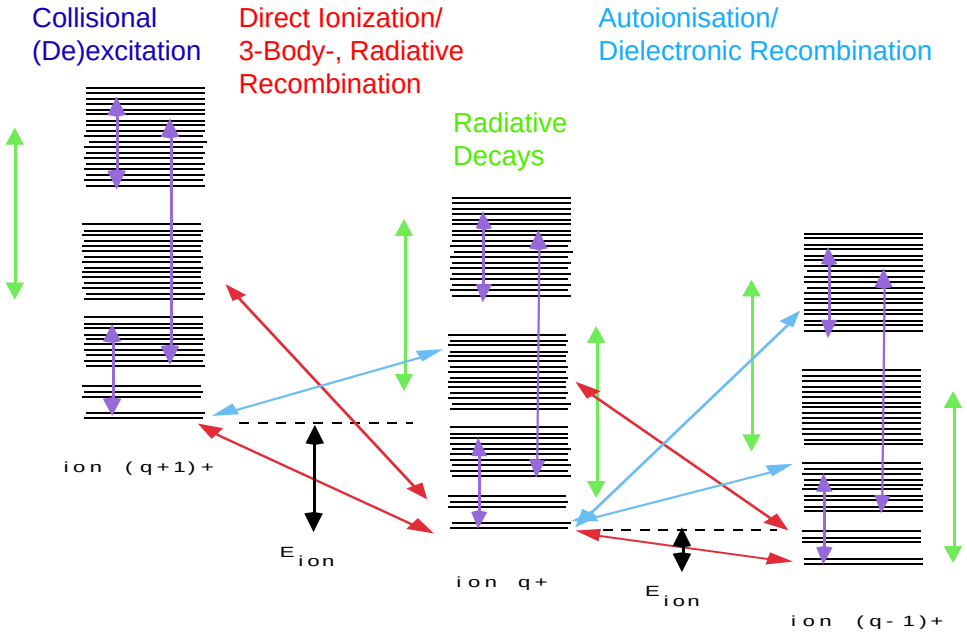

Figure 4.14: Schematic view of the elementary processes considered in the collisional radiative model used to determine the photon emission coefficients in highly charged W [201].

components of a pure basis representation. Since the Coulomb operator is a two electron operator, it can have non-vanishing elements when evaluated between configurations that differ by one or two electron orbitals. Therefore, the energy calculation for the levels of a given configuration can be perturbed by 'mixing' (or configuration interaction (CI)) with levels of a different configuration. The calculation of the CI contribution to a level's energy depends on an (infinite) number of contributions from all states with the same parity and total J-value, including states in the continuum. The more widely separated in energy two levels are, the weaker the interaction between them will be. CI effects on the level structure giving rise to X-ray spectra in highly charged, high-Z ions are mainly due to 'accidental' level crossings. Consequences of the multiple basis components in the physical states of energy levels, which are manifested in collisional radiative (CR)

emissivities, are perturbations of energy eigenvalues and redistribution of transition oscillator strengths (see for example [134]). Another consequence of CI is an enabling of 'forbidden' transitions corresponding to two electron jumps [205]. Its effect on transition arrays may be more pronounced than for cases of individual transitions between well separated levels [206].
Finally, the Breit interaction energy, vacuum polarisation and electron self energy corrections are added to a level's energy. The nuclear charge is treated as a point charge, since a finite charge distribution would only have an effect for $s_{1/2}$-states equal or less in magnitude to the above mentioned higher order terms.

Transition rates

Radiative transition rates can be calculated within RELAC for any multipole operator according to the formalism given in [207] using the full multi-configuration wavefunctions. The calculations include autoionisation decays from excited levels in the continuum to all accessible levels in the next ion state. This process may strongly affect the branching ratio for radiative decays of X-ray lines as already found for Ne-like ions [133] and as demonstrated in Fig. 4.17 for transitions in Br-like W ions. The autoionisation rates are determined by evaluating the two-electron Coulomb interaction between multi-configuration states of the ions with charge Z and $Z + 1$ and a free, outgoing electron [208]. The factorisation technique of [209] is used to split the matrix elements into an angular part depending only on the bound electrons and an interpolation scheme to compute the radial integrals on a grid of free electron energies. The contributions to line emissions from stabilising transitions for dielectronic recombination are deduced by finding the rate of radiationless capture assuming detailed balance with the rates of autoionisation from a given ion.

Impact excitation

The CROSS suite of codes [203] completes the HULLAC package. It uses RELAC's wavefunctions to compute the cross section for electron impact excitation from energy level i to level j of a given ion in the distorted wave approximation. This procedure represents a good tool for the treatment of highly charged, high-Z ions, however, it misses resonance contributions to the excitation cross section which may be significant at low electron temperatures (see for example [210]). The two-electron Coulomb-operator is evaluated between multi-configuration states of an ion and a free outgoing electron. The levels of all singly and doubly excited configurations have been allowed to mix with each target level. Finally, the rate coefficients for the electron impact excitation are calculated by integrating them over the Maxwellian distribution of free electron velocities.

Collisional radiative model

The level to level transition rates, including autoionisation rates from highly excited levels into all accessible levels of the next ion, as well as direct impact ionisation (DI) are used to construct the collisional-radiative rate matrix

$$\begin{aligned}\frac{dn_j}{dt} &= \sum_{i>j} n_i A_{i,j} + n_e\Big(\sum_{i\neq j} n_i Q_{i\to j} + \sum_{i\in Z-1} n_i I_{i\to j} + \sum_{i\in Z+1} n_i R_{i\to j}\Big) \\ &\quad -n_j\Big(\sum_{i<j} A_{j,i} + n_e\Big(\sum_{i\neq j} Q_{j\to i} + \sum_{i\in Z+1} I_{j\to i} + \sum_{i\in Z-1} R_{j\to i}\Big)\Big) \qquad (4.19)\end{aligned}$$

where n_j, n_i are the populations in level j and i respectively, and A, Q, I, R denote the radiative decay rates, the collisional excitation/de-excitation rates, the ionisation rates and the recombination rates, respectively. A sketch of the processes considered is given in Fig. 4.14. The contribution of DI from both valence and inner-shell orbitals to the total ionisation rate is evaluated using the Lotz-formula [211, 212] and a relativistic calculation of subshell binding energies [189]. The inverse of each of the ionisation processes, namely dielectric recombination and three body recombination have been determined according to the principle of detailed balance.

The majority of the line emission in the 0.5 to 1.0 nm region is composed of $3l \to 4l'$ transitions, whereas in the spectral region from 1.0 to 2.0 nm $4l \to 5l'$ transitions are dominant.

In the case of E1 emission features, there is a correlation between oscillator strength and the predicted emissivity [161, 213]; in this case, the lines with the strongest E1 oscillator strengths will have the brightest emissivities, and the RELAC calculations alone are adequate to the job at hand. Other multipole transitions (M1, E2 and M2) have small oscillator strengths, but when they originate from highly populated (metastable) levels they can be quite bright. In this case, the full collisional-radiative prediction of transition emissivity is required to classify spectral features. For example, the influence of the inner shell ionisation on the emissivities of the spectral lines of W46+ is shown in Fig. 4.15. The spectral line predicted at 0.794 nm is a ΔJ=2, $3d \to 4s$, $E2$-decay. It is rather bright and

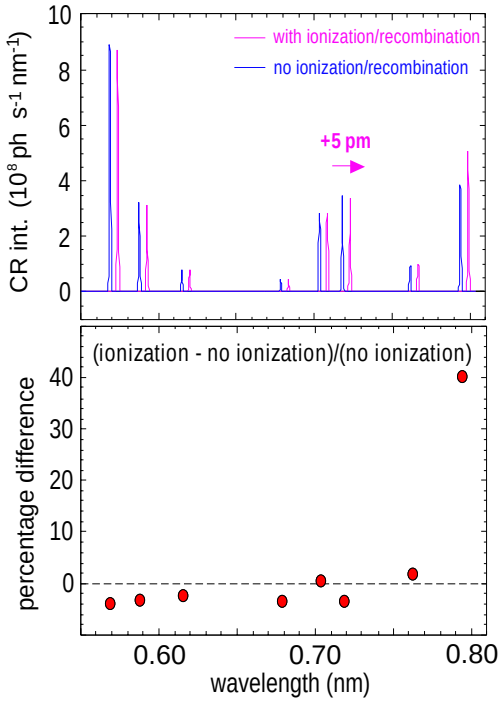

Figure 4.15: Influence of the inner shell ionisation on the emissivities of the spectral lines of Ni-like tungsten.

is strongly fed by inner shell ionisation from the $3d^{10}4s$ configuration in Cu-like W^{45+}.

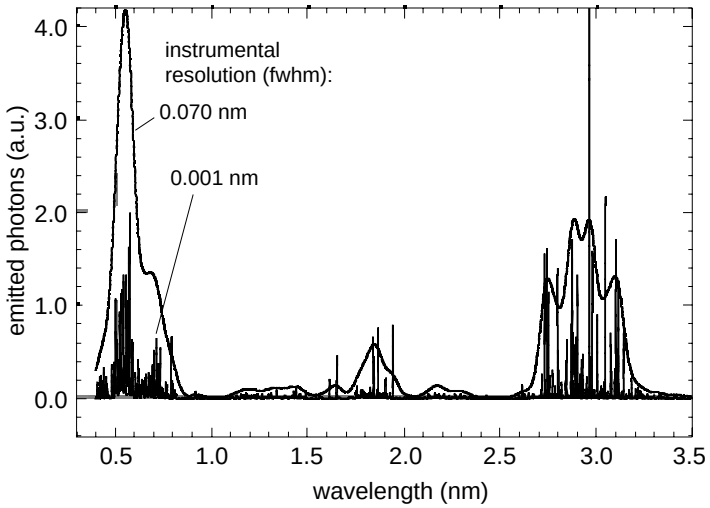

Figure 4.16: Synthetic blended spectra for Zn-like W^{44+} to Ca-like W^{54+} showing the $\Delta n = 0$ and $\Delta n = 1$ M-shell transitions.

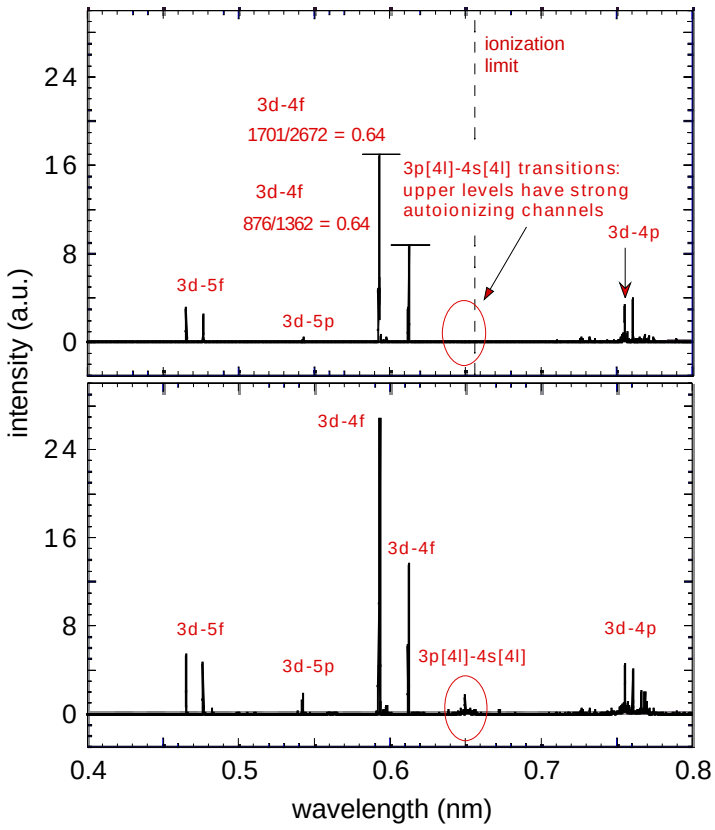

Figure 4.17: Influence of the excitation autoionisation on the emissivities of the spectral lines of Br-like tungsten.

For the correct population distribution amongst the levels of the ground configurations in each ion, M1, E2 and M2 decays are essential, which are visible in the related VUV spectra of each ion (see Sec. 4.2). In the case of the Cu- to Kr-like W ions dielectronic recombination has also been taken into account in the calculation of the PECs. More detailed information on the calculations and a complete tabulation of X-ray (and VUV) transitions in tungsten charge states between W^{37+} and Co-like W^{47+} are presented in Ref. [188]. For the present work these calculations were extended to ionisation states up to Ca-like W^{54+} to also cover plasma discharges with electron temperatures in the range of 5 keV [201, 202, 214].

Fig. 4.16 shows the transitions calculated by the HULLAC code with intensities deduced from a collisional radiative model. Excitation-autoionisation (EA) already found in [161, 162] and also observed by the shift of the ionisation equilibrium (see Sec. 4.2.3) was taken into account. EA reduces the intensities of spectral lines especially from $3p4l - 4s4l$ transitions for ionisation states up to Ga-like tungsten. As an example a comparison of calculated intensities from

the collisional radiative model with and without EA is shown in Fig. 4.17 for Br-like tungsten. It is clearly visible that the lines around 0.65 nm are quenched almost completely and also the intensity of the strong $3d-4f$ transitions is reduced to 64%. The collisional radiative (CR) models also show a quenching of the spectral lines in the 1.7 nm range originating more highly charged ions (as for example Co-like) due to configuration interaction in favour of a strong (still unobserved) transition array between 2.5 and 3.0 nm see Fig. 4.16.

In order to use the observed spectral lines for the deduction of W densities, temperature and density dependent photon emission coefficients (PECs) for over 2000 transitions were extracted from the collisional radiative model [201] and are now available in ADAS [215] data sets at ASDEX Upgrade, from where they can be easily retrieved by impurity transport codes as for example STRAHL. Figure 4.18 shows the photon emission coefficients for several transitions in Ni-like W versus the electron temperature for $n_e = 10^{20}\mathrm{m}^{-3}$.

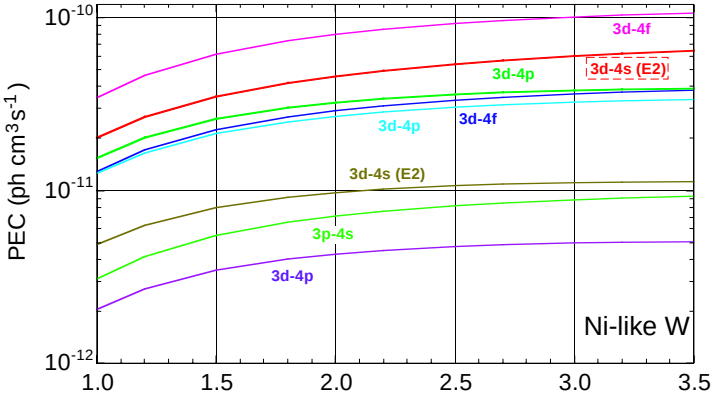

Figure 4.18: Photon emission coefficients for transitions in Ni-like tungsten calculated at $n_e = 10^{20}\mathrm{m}^{-3}$.

4.3.2 W Concentration from SXR-Measurements

Unlike the method in the case of the W quasi-continuum, the extraction of the W concentration from the SXR spectral lines was more straightforward. Again the W injections were performed and the induced total radiation was compared to the increase in the line integrals of spectral lines, as described in Sec. 4.2.4. This allowed the cross calibration of the Johann-spectrometer with the Bragg-spectrometer (see Sec. 3.1.3) and the extraction of the W concentrations without absolute calibration. However, since the observed single transitions were much easier to be identified, their dependence on the plasma temperature could be directly quantified from the ionisation equilibrium and the theoretical PEC. Therefore c_W was extracted from

$$c_W = \frac{I^{SXR}_{W^{+x},line}}{C^{cal}_{SXR} \int_\ell f_{W^{+x}} n_e^2 X_W ds} \ , \tag{4.20}$$

with the calibration factor C^{cal}_{SXR} from the comparison with the total radiation, the profiles of the electron density n_e, the corresponding PEC X_W from the *ab initio* calculations

and the corresponding fractional abundance $f_{W^{+x}}$ of the ion W^{+x}, which was taken from the coronal equilibrium or calculated using the transport code STRAHL. Since the transport in the centre is usually small, and the extracted concentration is only taken in the radial range of the emission of the spectral line the difference between both methods is negligible. For routine investigations of the behaviour of the central c_W the above method was applied, using the E2 transition in Ni-like W^{46+} (for the corresponding PEC, see Fig. 4.18), measured by the Johann spectrometer. The temporal behaviour of the brightness of this spectral line is shown in Fig. 4.19 (right side) together with the the one of the W I line (left side) measured in the visible spectrum during a radial shift of the plasma towards the tungsten coated tiles (for details see Sec. 6.2.4).

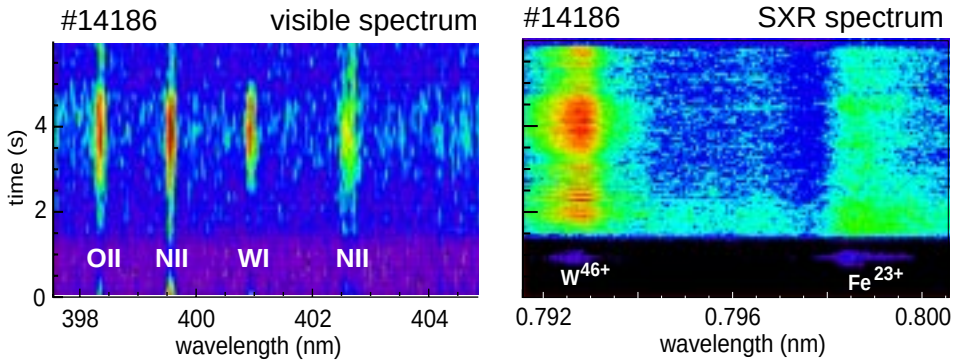

Figure 4.19: Behaviour of the spectral lines in the visible (W I at 400.8 nm) and the SXR spectral range (W^{46+} at 0.793 nm) during the radial shift of the plasma towards the central column in discharge #14186 (I_p = 1 MA, B_t = −2.3 T, P_{NBI} = 5 MW, $\delta = 0.15$).

The spectral line at 0.793 nm has been chosen for several reasons. The Ni-like W^{46+} is rather abundant due to its filled shell configuration (in highly charged ions the $3d$ shell is filled before the $4s$). For this reason the spectra are also rather simple and the radiation is concentrated into a few strong lines. Its ionisation potential of 4065 eV leads to central emission in typical H-mode plasmas in ASDEX Upgrade.
In the case of the absolute calibrated Bragg spectrometer the theoretical and the experimental brightness can be compared directly. In this case the extraction of c_W is similar to eq. 4.20 but instead of C^{cal}_{SXR} simply the factor $\frac{1}{4\pi}$ has to be used. Depending on the spectral line to be used, both methods agree with a factor of 2-3, demonstrating their consistency, but also giving room for future refinement of either the PEC or the the radiation loss parameter. More details on the comparison will be given in the next section.

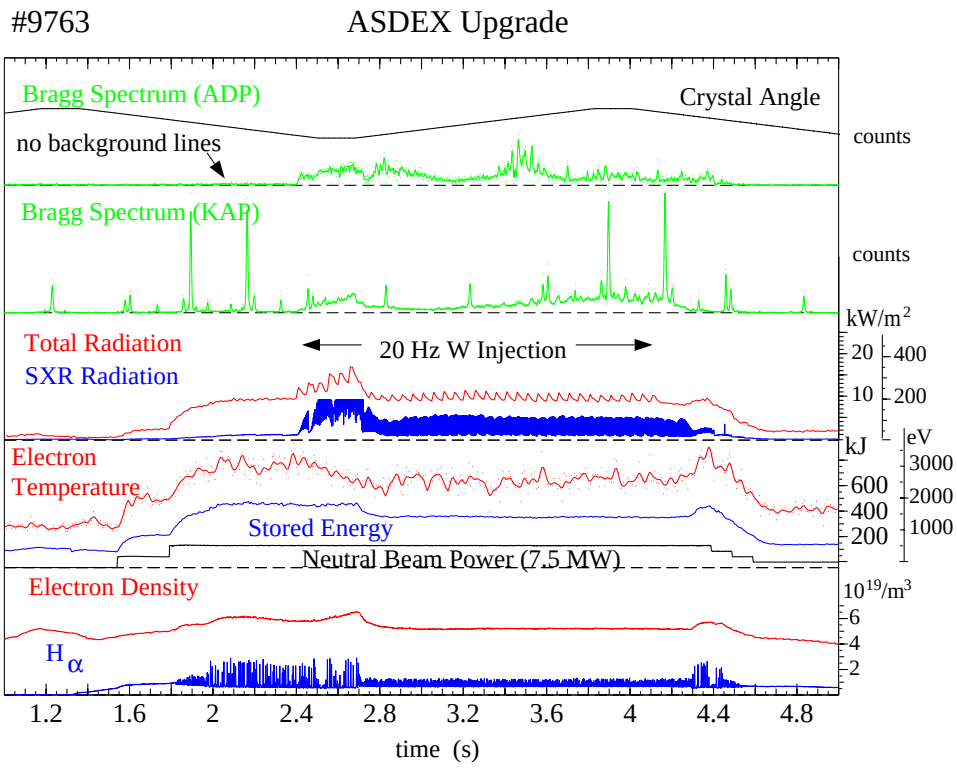

Figure 4.20: X-ray spectra and the corresponding crystal angle (ADP) for the discharge #9763 with 20Hz W injection together with (in descending order) the temporal behaviour of a central line of sight integrated bolometric measurement of the total plasma radiation and of the soft X-ray radiation ($E_{rad} \geq 1$ keV), the central electron temperature T_{e0}, the total stored energy and the neutral beam heating power (7.5MW), as well as the line averaged electron density and the edge H_α emission.

4.3.3 Experimental Tungsten X-ray Spectra

During this work, spectra were recorded in the wavelength range from 0.4 - 2.0 nm, mostly with the Bragg spectrometer at ASDEX Upgrade (see Sec. 3.1.3) using the KAP (2d=2.6579 nm), ADP (2d= 1.064 nm) and the Silicon crystal (2d=0.6271 nm). They were measured in discharges with electron temperatures from 1 to 5 keV, line averaged electron densities around $\bar{n}_e = 6 \cdot 10^{19}/\mathrm{m}^3$ and additional heating through NBI up to 14 MW. For a clear identification of the W lines it was necessary to inject tungsten in discharges with no (or low) W content. Therefore, most of these experiments were performed in-between the W divertor experiment (see Sec. 6.1) and the experiments with W coated column (see Sec. 6.2). In most of the cases spectra are recorded several times during the discharges with and without W injection to look for the contribution of spectral lines from intrinsic impurities. Identification of the W line features is achieved by comparison of the observed spectra with the *ab initio* atomic structure calculations

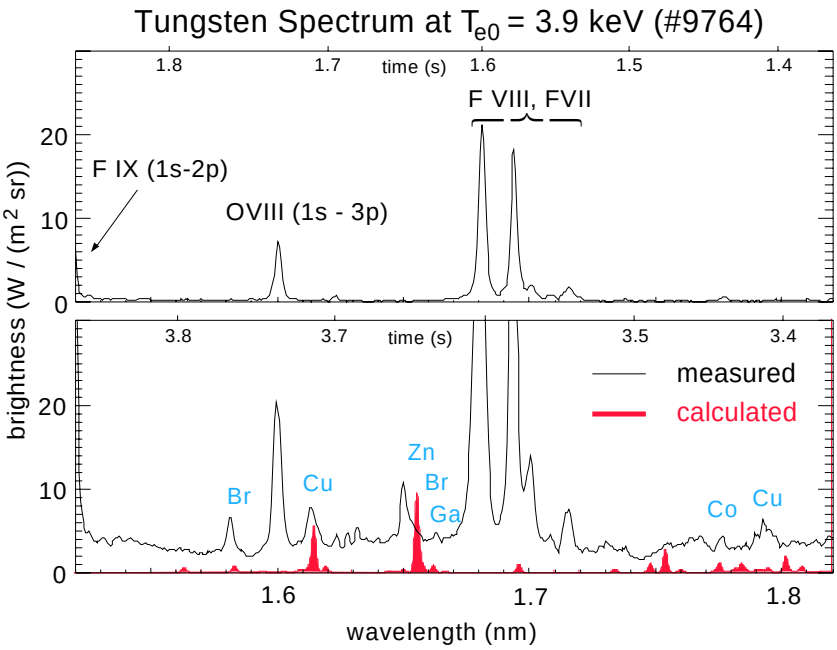

Figure 4.21: X-ray spectra in the range from 1.52 to 1.82 nm measured with a KAP crystal (discharge #9764, $T_{e0} \approx 3.9$ keV during W injection) without (upper part) and with tungsten injection (lower part) together with the theoretical predictions.

and predictions of the collisional-radiative line emissivities described above. Since the recording of the spectra is sequential in time (see Sec. 3.1.3), the plasma parameters have to be kept constant. The temporal behaviour of the plasma parameters of one of the discharges with 20 Hz tungsten laser blow-off injection from 2.4 s – 4.1 s is presented in Fig. 4.20. The traces on the top show the spectrum measured during the rotation of the ADP crystal and the monitored crystal angle (Θ_C) that translates to the wavelength. The second row shows the spectrum measured with the second spectrometer using KAP crystal. The third row shows a line of sight integral of the total radiation (P_{rad}), where every tungsten injection could be identified as a spike. The central soft X-ray radiation (P_{SXR}, $E_{rad} \geq 1$ keV) exhibits strong variations due to sawtooth instabilities and central MHD-modes. The time averaged central temperature and the stored energy (fourth row), as well as the line averaged central density and the behaviour of the H_α (fifth row) stayed constant throughout the tungsten measurement.

Long wavelength range

In the long wavelength region (1.2 - 2.0 nm) a lot of spectral lines of intrinsic He-like and H-like fluorine and oxygen are present (see Fig 4.21). These were used for wavelength calibration in the individual spectra. In this spectral region however, the sensitivity of the spectrometer is rather low and the lines emitted by W appear to

be rather weak, especially compared to the ones of the intrinsic impurities. Figure 4.21 shows the recorded spectrum from discharge #9764 with an central electron temperature of about 3.9 keV. Although contributions from W could clearly be identified comparing the spectra with and without W injection, the identification of single spectral lines from a single spectrum is somewhat ambiguous. The situation is improved by comparing spectra with W injections into several discharges with different central temperatures. At higher plasma temperatures contributions from Zn-like to Co-like W dominate the spectra. However, transitions from Br-like W always appear to be rather strong. The extracted W concentrations are consistent with those obtained at shorter wavelength (see below), but due to the low signal to noise ratio the spectral lines were not used further. Table 4.5 summarises the result of the measurements at the longer wavelength. Obviously, the predicted wavelengths are less accurate than in the short wavelength range and therefore the identification of the observed lines is sometimes ambiguous.

Short wavelength range

The situation is improved in the short wavelength range. Here, almost no spectral lines from intrinsic impurities were observed – except for the ones from He- and H-like silicon – and the sensitivity of the spectrometer is much higher. (Sometimes during the measurements below 0.5 nm spectral lines from He- and H-like sulfur and chlorine were present.) Individual lines of most ionisation states were identified and the measurements and the calculations show very good wavelength agreement. Figure 4.24 shows three tungsten spectra recorded with the ADP-crystal #9763, #9764 and with the KAP-crystal #11635 during W injection (solid line) for the central electron temperatures of 3 keV, 3.9 keV and 5.0 keV, respectively. Calculated spectra using the PECs from [201, 202] are also plotted (dashed line). The spectral lines are denoted by the element symbol, which equals the charge state of W. A clear shift towards shorter

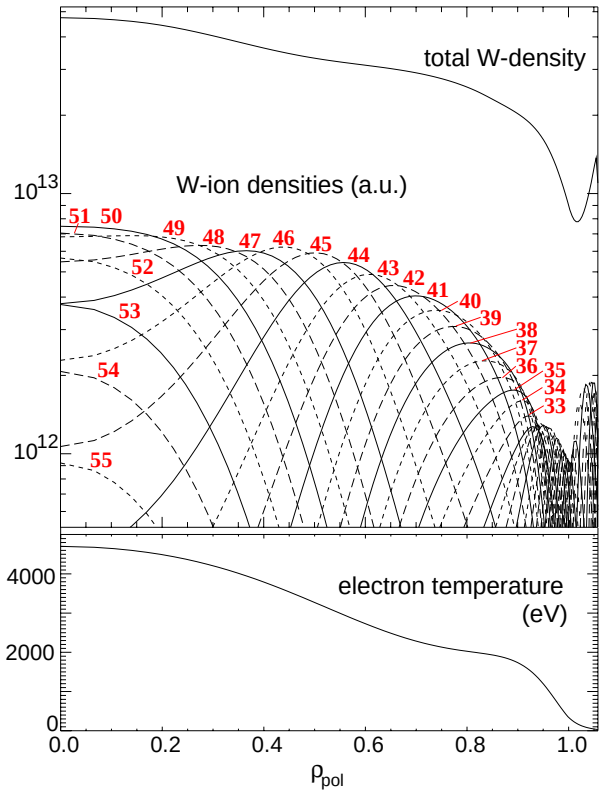

Figure 4.22: Electron temperature profile of discharge #11635 (bottom) used in the calculation of the tungsten ion density profiles (top). The numbers denote the tungsten ion charges.

wavelength is observed at higher temperatures for the experimental as well as for the synthetic spectra. It is obvious that the calculated intensity of the spectral lines at 0.75 nm of Kr-like to As-like W is much too low in the case of #9763, suggesting that the central temperature is measured too high. However, using for example $T_{e0} = 2.3$ keV for the calculation of the ionisation equilibrium, the predicted brightness of this feature is enhanced only by a factor of two. It is also unlikely that transport processes in the plasma would enrich these ions in such a strong selective way. Looking at spectra taken in other discharges with a lower central temperature, it also suggests that the transitions of Br-like to As-like at 0.75 nm may be underestimated by the CR calculations.
In discharges with higher central temperatures the agreement is improved, since the transitions in the lower ionisation states do not play a significant role anymore. This is demonstrated in spectrum of #9764 taken at $T_{e0} = 3.9$ keV and even more for #11635 where $T_{e0} = 5.0$ keV. Fig. 4.22 shows the electron temperature profile of discharge #11635 (bottom) used in the calculation of the tungsten ion density profiles (top). The numbers denote the tungsten ion charges. For this central temperature the ionisation states around Ni-like W^{46+} exist in broad radial region and even the abundance of Ti-like W^{52+} is still relatively high. Indeed, at the highest temperature the spectrum is dominated by spectral lines from Zn-like to Ni-like W and hints for contributions of Co- to Mn-like W are seen. The agreement of the measured and the synthetic spectra is good in this case. Only the brightness of the very strong E2 transition in W^{46+} at 0.793 nm and the broad structure at 0.63 nm cannot be reproduced. The latter is also found in #9764 but not in lower temperature discharges, which points to the fact, that it should be emitted from ions around Ni-like W^{46+}. The W concentrations were deduced from the absolute value of the measured spectral lines and the brightness calculated following the procedure described in Sec. 4.3.2. In the case of discharge #9763, $6 \cdot 10^{-5}$ was found, disregarding the spectral lines at 0.75 nm. For discharge #11635 the single transitions yield much more uniform concentrations and a mean value of $5 \cdot 10^{-5}$ could be extracted. In the course of the extension in of the W surfaces as PFCs in ASDEX Upgrade, intrinsic tungsten could be quite abundant in special discharge scenarios as will be described in the next chapter. Fig. 4.25 shows a spectrum from 0.40 nm to 0.82 nm taken during a QH-Mode discharge (#16111) with a central electron temperature $T_{e0} \approx 4.5$ keV. As it is denoted at the top of frames, it took from 1.8 s to 3.5 s to record the whole spectrum. During this time period c_W was almost constant as it could be deduced from the monitoring of the spectral line of W^{46+} at 0.793 nm which was performed with the Johann spectrometer. From this measurement $c_W \approx 2 - 3 \cdot 10^{-4}$ could be extracted whereas an almost radially constant $c_W = 5 \cdot 10^{-4}$ was used for the STRAHL calculation of the spectrum also shown in the figure. Again, the spectrum is well reproduced and only a few line features differ by a maximum factor of 2. The use of independently measured electron temperature (ECE or Thomson scattering, see Appendix B.2) allowed us to as-

sign the spectral lines to the theoretical calculations to a high degree of confidence, since the information from ionisation equilibria as well as from the PECs could be used. Table 4.3.3 summarises the results in the short wavelength region, for the plasma discharges with different central electron temperatures ranging from 2.5 - 5.0 keV. The wavelength calibration usually is performed by using spectral lines of H- or He-like intrinsic mid-Z impurities as Si, S, Cl and Ar. As an example Fig. 4.25 shows the $1s - 2p$ doublet of H-like Si. The linearity of the scan as well as the $2d$ of the crystals was checked in other discharges showing more spectral lines originating from mid-Z impurities.
Generally, there is a good agreement between the wavelength from the *ab initio* calculations and the experiment as well as with the wavelength from earlier measurements using laser produced plasmas [195–198]. However, in some cases the earlier identification of the lines differ from the one presented here, but due to the superior diagnostics of the tokamak plasma the later has to be preferred, at least for the low density plasmas investigated here. The exceptions to this overall accordance, are the spectral lines originating from $J = 2$ transitions Ni-like W presented by Wyart et al. [216]. At the given wavelengths of 0.5028 nm and 0.5054 neither spectral lines from Ni-like W appear nor any other lines are found in the present investigations.

Similarily to the procedure in the VUV, W investigations have been initiated at the

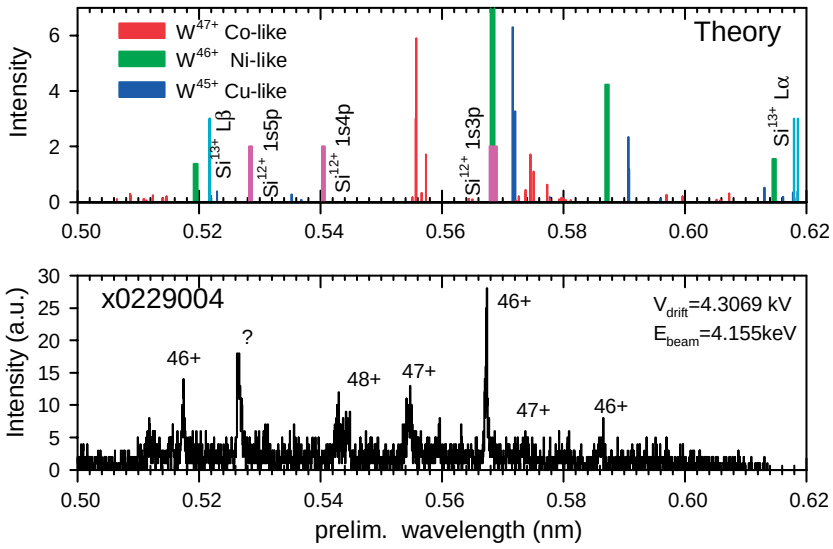

Figure 4.23: Soft X-ray spectrum of W measured at the Berlin EBIT [217] (bottom). The beam energy was adjusted to yield ions around W^{46+}. The result of collisional radiative calculations is shown at the top.

Berlin EBIT in the SXR spectral region, in order to allow a detailed analysis of the individual tungsten ionisation states [217]. Fig. 4.23 presents the first measurements for the ionisation states around Ni-like W.

4.4 Conclusions from Spectroscopic Investigations

The source and the transport of an impurity species determine its abundance in the plasma, as described in Chap. 5. In order to quantify the source, spectroscopic signitures from neutral or low ionisation states of W have to be used. In a survey performed at the PSI-1 in Berlin [111] the $^7S_3 - -^7P_4^o$ transition in neutral W was identified to be strongest under the conditions which are predominant in the plasma edge. In the same work the inverse photon efficiency S/XB was determined as a function of electron temperature, which allowed the gross erosion in a large number of discharges to be quantified, as described in the next chapter. With the help of a sublimation probe inserted into the divertor of ASDEX Upgrade, the S/XB-value could be confirmed under fusion reactor conditions. The W I spectral line has developed the character of a standard for W influx measurements and is also used in other laboratories (see Sec. 7.1).
In the VUV and the SXR spectral region the emission of tungsten was investigated by W injection using laser ablation into plasma discharges. In low temperature discharges ($T_{e0} \leq 1.5$ keV) only the W quasi-continuum around 5 nm, which was already well known from the early tungsten experiments as PLT or ORMAK (see Sec. 7.1) could be identified. With increasing T_{e0} several single lines emerge from the continuum structure originating from resonant transitions ($4s - 4p$ or $4p - 4d$) in Br-like (W^{39+}) to Cu-like (W^{45+}) W ions exhibiting much simplier configurations than the ions around W^{28+} which are responsible for the quasi-continuum. The identification of these lines was performed by means of HULLAC-code calculations. Besides spectral lines in the wavelength region from 4.5–7.0 nm, lines around 13 nm were observed for the first time.
The radial distribution of the W ions was calculated with the help of ionisation and recombination rates of the ADPAK-package and the transport code STRAHL. It turned out that the ionisation rates for Br- to Cu-like ions had to be increased by a factor of up to 3 in order to obtain agreement with the appearance of the corresponding spectral lines. This increase was explained by the effect of excitation autoionization.
Rich spectra from W^{39+} and higher ions were recorded in the soft X-ray spectral range from 0.4 -1.9 nm. Most of the spectral lines were measured for the first time and they were identified with *ab initio* atomic physics calculations. The extensive measurements of the SXR spectra allowed us to benchmark these calculations for a large range of ionisation states of W. In general, the agreement of predicted and observed wavelengths is very good. By taking into account processes as inner shell ionisation and excitation-autoionisation within the collisional radiative calculations a statisfactory description of the spectra is also achieved.
All of the investigations profitted strongly from the close collaboration with the dedicated

devices PSI-1 and EBIT available at the Plasma Diagnostic Department of the MPI für Plasmaphysik which is situated in Berlin. In the case of the visible spectral range the work at the PSI-1 laid the foundation for the influx measurements at ASDEX Upgrade, whereas in the VUV- and SXR-spectral range the regions of interest were defined from the experimental experiences at ASDEX Upgrade. At the same time it turned out, that despite the technically superior measurements at dedicated devices such as the EBIT, investigations within tokamak plasmas are necessary due to the specific plasma parameters which exist there. This became especially evident in the case of the transitions contributing to the W quasi-continuum. As described in [182] there is a strong density dependence in the level population leading to non-Boltzmann distributions at low densities ($n_e \leq 10^{19}$ m^{-3}) as existent in the EBIT. The collisional radiative calculations described in [182] result in much richer line spectra already at $n_e \leq 10^{20}$ m^{-3}, which are relevant in tokamaks.

The measurement of the W emission from different ionisation states allowed the extraction of the tungsten concentration c_W at different locations in the plasma. Using the spectroscopic signatures considerably lowered the detection limit for W in the plasma compared to the common method of using the total radiation and the radiation loss parameter alone. Therefore, the spectroscopic investigations represent the back-bone of the tungsten programme at ASDEX Upgrade. Statements on the W behaviour and its influence on the plasma discharges only became possible, due the preparation of the tools for the quantification of the W influx and the W concentration.

Stimulated by the work at ASDEX Upgrade as well as by the need for future fusion devices, experimental as well as theoretical investigations on high-Z material were initiated at JET as well as within the ADAS collaboration [219].

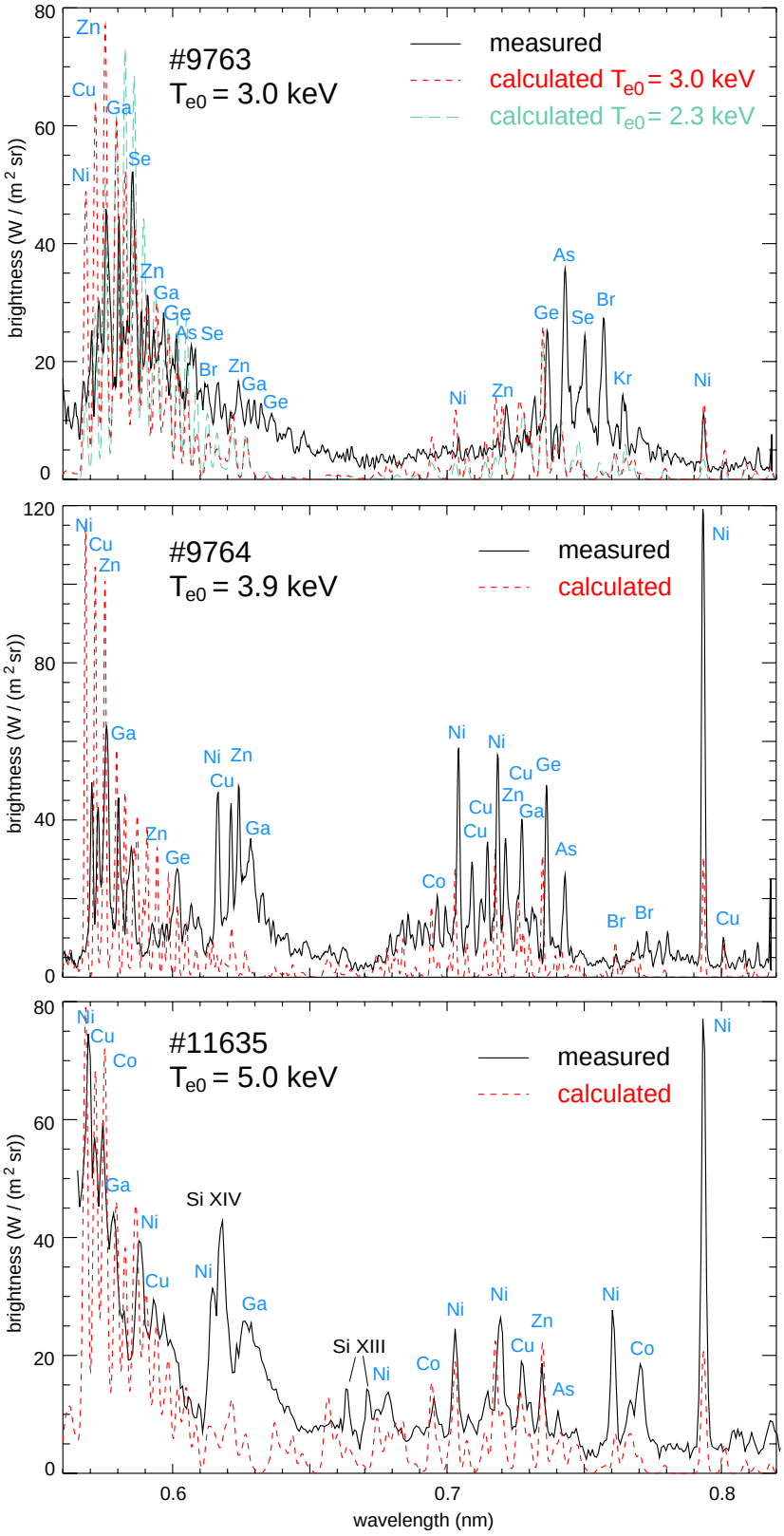

Figure 4.24: Tungsten spectra measured at ASDEX Upgrade during discharges with different central temperatures T_{e0} (solid line). Calculated spectra using the PECs from [201, 202] are also plotted (dashed line). The spectral lines are denoted by the element symbol, which equals the charge state of W.

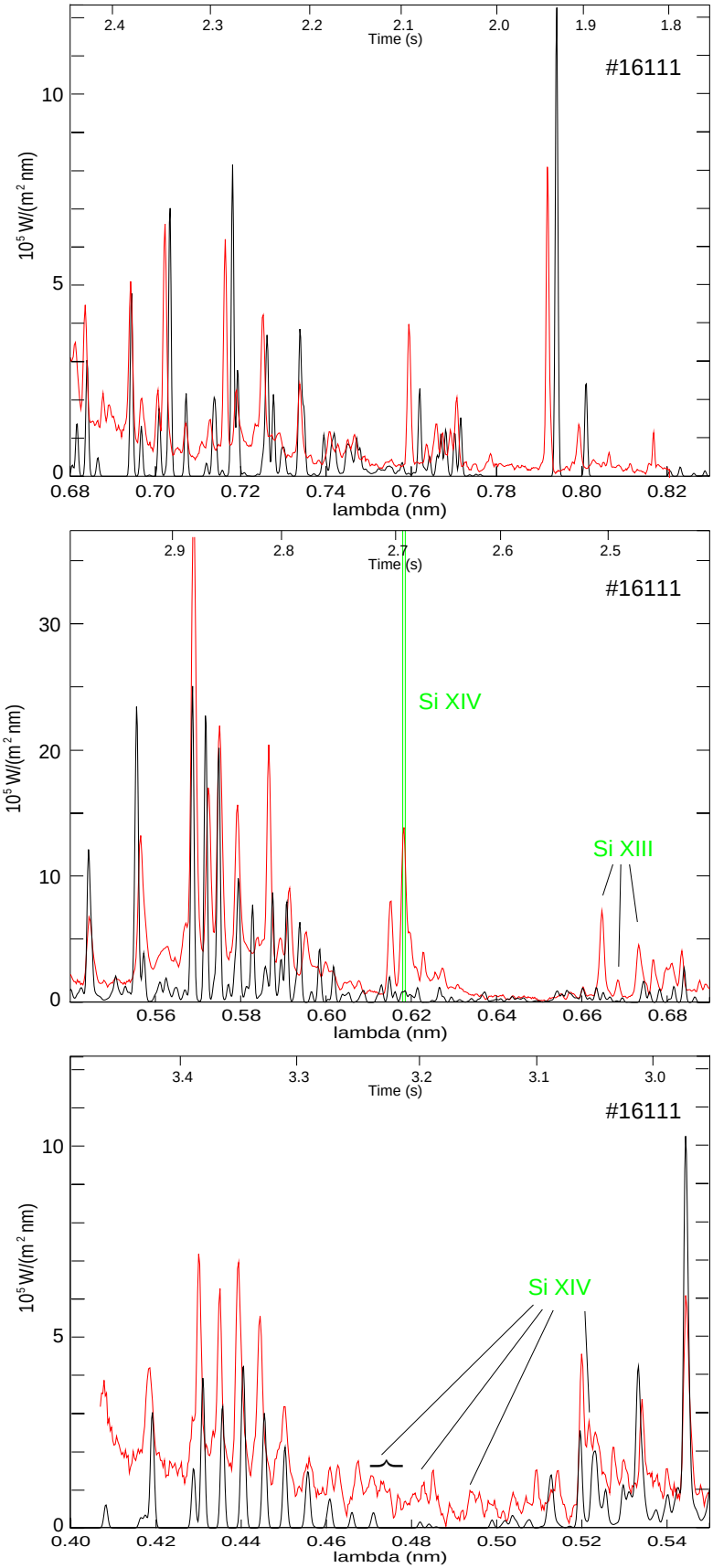

Figure 4.25: Tungsten spectrum measured at ASDEX Upgrade during discharge #16111 with a central temperature $T_{e0} \approx 4.5$ keV (red line). Calculated spectra using the PECs from [201, 202] are also plotted (black line). The resonance lines of H-like Si at 0.6180 nm and 0.6186 nm were used for wavelength calibration.

Ion	transition	λ_{th} (nm)	λ_{exp} (nm)	$\lambda_{exp.}^{ref}$ (nm)
$W^{?+}$			1.532	
W^{46+}	$(3p)^6(3d\text{-})^4(3d\text{+})^5(4p\text{+})^1$ J =2 – $(3p\text{-})^2(3p\text{+})^3(3d)^{10}(4f\text{+})^1$ J =2	1.563	1.564	
W^{46+}	$(3p)^6(3d\text{-})^4(3d\text{+})^5(4p\text{+})^1$ J =2 – $(3p)^6(3d\text{-})^4(3d\text{+})^5(5s\text{+})^1$ J =2	1.565		
W^{39+}	$(4s)^2(4p\text{-})^2(4p\text{+})^2(4d\text{-})^1$ J =7/2 – $(4s)^2(4p\text{-})^2(4p\text{+})^2(5f\text{-})^1$ J =9/2	1.583	1.582	
W^{39+}	$(4s)^2(4p\text{-})^2(4p\text{+})^3$ J =3/2 – $(4s)^2(4p\text{-})^1(4p\text{+})^3(5s\text{+})^1$ J =5/2	1.584	1.585	
	$(4s)^2(4p\text{-})^1(4p\text{+})^3(4d\text{-})^1$ J =5/2 – $(4s)^2(4p\text{-})^1(4p\text{+})^3(5f\text{-})^1$ J =7/2	1.584		
	$(4s)^2(4p\text{-})^2(4p\text{+})^2(4d\text{-})^1$ J =7/2 – $(4s)^2(4p\text{-})^2(4p\text{+})^2(5f\text{-})^1$ J =7/2	1.584		
$W^{?+}$			1.587	
W^{39+}	$(4s)^2(4p\text{-})^2(4p\text{+})^2(4d\text{+})^1$ J =7/2 – $(4s)^2(4p\text{-})^2(4p\text{+})^2(5f\text{+})^1$ J =7/2	1.609	1.609	
W^{39+}	$(4s)^2(4p\text{-})^2(4p\text{+})^2(4d\text{-})^1$ J =1/2 – $(4s)^2(4p\text{-})^2(4p\text{+})^2(5f\text{+})^1$ J =3/2	1.611	1.611	
W^{39+}	$(4s)^2(4p\text{-})^1(4p\text{+})^3(4d\text{+})^1$ J =3/2 – $(4s)^2(4p\text{-})^1(4p\text{+})^3(5f\text{-})^1$ J =3/2	1.611		
W^{39+}	$(4s)^2(4p\text{-})^2(4p\text{+})^2(4d\text{+})^1$ J =7/2 – $(4s)^2(4p\text{-})^2(4p\text{+})^2(5f\text{+})^1$ J =9/2	1.611		
W^{39+}	$(4s)^2(4p\text{-})^1(4p\text{+})^3(4d\text{+})^1$ J =9/2 – $(4s)^2(4p\text{-})^1(4p\text{+})^3(5f\text{+})^1$ J =11/2	1.612		
W^{39+}	$(4s)^2(4p\text{-})^2(4p\text{+})^2(4d\text{+})^1$ J =9/2 – $(4s)^2(4p\text{-})^2(4p\text{+})^2(5f\text{+})^1$ J =11/2	1.612	1.613	
W^{38+}	$(4s)^2(4p\text{-})^2(4p\text{+})^3(4d\text{-})^1$ J =2 – $(4s)^2(4p\text{-})^2(4p\text{+})^3(5f\text{-})^1$ J =3	1.614		
W^{38+}	$(4s)^2(4p\text{-})^2(4p\text{+})^3(4d\text{-})^1$ J =3 – $(4s)^2(4p\text{-})^2(4p\text{+})^3(5f\text{-})^1$ J =4	1.615	1.614	
W^{45+}	$(3p)^6(3d)^{10}(4p\text{+})^1$ J =3/2 – $(3p)^6(3d)^{10}(5s\text{+})^1$ J =1/2	1.615		1.614
W^{39+}	$(4s)^2(4p\text{-})^1(4p\text{+})^3(4d\text{-})^1$ J =1/2 – $(4s)^2(4p\text{-})^1(4p\text{+})^3(5f\text{-})^1$ J =3/2	1.619	1.620	
W^{39+}	$(4s)^2(4p\text{-})^2(4p\text{+})^2(4d\text{+})^1$ J =5/2 – $(4s)^2(4p\text{-})^2(4p\text{+})^2(5f\text{+})^1$ J =7/2	1.620		
$W^{?+}$			1.624	
W^{39+}	$(4s)^2(4p\text{-})^1(4p\text{+})^3(4d\text{-})^1$ J =5/2 – $(4s)^2(4p\text{-})^1(4p\text{+})^3(5f\text{-})^1$ J =7/2	1.626	1.628	
$W^{?+}$			1.630	
$W^{?+}$			1.632	
W^{37+}	$(4p)^6(4d\text{-})^1$ J =3/2 – $(4p)^6(5f\text{-})^1$ J =5/2	1.647	1.647	
W^{44+}	$(3p)^6(3d)^{10}(4s\text{+})^1(4p\text{+})^1$ J =1 – $(3p)^6(3d)^{10}(4s\text{+})^1(5s\text{+})^1$ J =0	1.652	1.652	
W^{39+}	$(4s)^2(4p\text{-})^2(4p\text{+})^2(4d\text{+})^1$ J =5/2 – $(4s)^2(4p\text{-})^2(4p\text{+})^2(5f\text{+})^1$ J =5/2	1.657	1.658	
W^{39+}	$(4s)^2(4p\text{-})^2(4p\text{+})^2(4d\text{+})^1$ J =5/2 – $(4s)^2(4p\text{-})^2(4p\text{+})^2(5f\text{+})^1$ J =7/2	1.658		
W^{43+}	$(3p)^6(3d)^{10}(4s)^2(4p\text{+})^1$ J =3/2 – $(3p)^6(3d)^{10}(4s)^2(5s\text{+})^1$ J =1/2	1.662	1.662	
W^{38+}	$(4s\text{+})^1(4p)^6(4d\text{+})^1$ J =2 – $(4s\text{+})^1(4p)^6(5f\text{+})^1$ J =3	1.667	1.665	
$W^{?+}$			1.672	
W^{45+}	$((4f)^1$ J=7/2 - $(5g)^1$ J=9/2 [186])		1.725	1.724
W^{47+}	$(3p)^6(3d\text{-})^3(3d\text{+})^5(4p\text{-})^1$ J =5/2 – $(3p\text{-})^1(3p\text{+})^4(3d\text{-})^4(3d\text{+})^5(4p\text{-})^1$ J =5/2	1.734	1.731	
W^{44+}	$(3p)^6(3d\text{-})^3(3d\text{+})^6(4s\text{+})^2(4p\text{-})^1$ J =1 – $(3p\text{-})^1(3p\text{+})^4(3d)^{10}(4s)^2(4p\text{-})^1$ J =0	1.748	1.748	
W^{45+}	$(3p)^6(3d\text{-})^3(3d\text{+})^6(4s\text{+})^1(4p\text{-})^1$ J =3/2 – $(3p\text{-})^1(3p\text{+})^4(3d)^{10}(4s\text{+})^1(4p\text{-})^1$ J =1/2	1.752	1.752	
W^{46+}	$(3p)^6(3d\text{-})^3(3d\text{+})^6(4p\text{-})^1$ J =1 – $(3p\text{-})^1(3p\text{+})^4(3d)^{10}(4p\text{-})^1$ J =0	1.754	1.754	
W^{45+}	$(3p)^6(3d\text{-})^3(3d\text{+})^6(4s\text{+})^1(4p\text{-})^1$ J =1/2 – $(3p\text{-})^1(3p\text{+})^4(3d)^{10}(4s\text{+})^1(4p\text{-})^1$ J =1/2	1.755		
$W^{?+}$			1.758	

continued

Ion	transition	λ_{th} (nm)	λ_{exp} (nm)	$\lambda_{exp.}^{ref}$ (nm)
W^{43+}	$(3p)^6(3d\text{-})^3(3d\text{+})^6(4s)^2(4p\text{-})^2$ J =3/2 – $(3p\text{-})^1(3p\text{+})^4(3d)^{10}(4s)^2(4p\text{-})^2$ J =1/2	1.762	1.764	
$W^{?+}$			1.767	
W^{47+}	$(3p)^6(3d\text{-})^3(3d\text{+})^5(4p\text{-})^1$ J =7/2 – $(3p\text{-})^1(3p\text{+})^4(3d\text{-})^4(3d\text{+})^5(4p\text{-})^1$ J =5/2	1.775	1.777	
W^{47+}	$(3p)^6(3d\text{-})^3(3d\text{+})^6$ J =3/2 – $(3p\text{-})^1(3p\text{+})^4(3d)^{10}$ J =1/2	1.790	1.789	
W^{45+}	$(3p)^6(3d)^{10}(4d\text{+})^1$ J =5/2 – $(3p)^6(3d)^{10}(5p\text{+})^1$ J =3/2	1.795	1.793	
W^{43+}	$(3p)^6(3d)^{10}(4s\text{+})^1(4p\text{-})^1(4p\text{+})^1$ J =3/2 – $(3p)^6(3d)^{10}(4s)^2(5p\text{-})^1$ J =1/2	1.795	1.797	1.797
W^{39+}	$(4s)^2(4p\text{-})^2(4p\text{+})^3$ J =3/2 – $(4s)^2(4p\text{-})^2(4p\text{+})^2(5s\text{+})^1$ J =3/2	1.802	1.804	
W^{39+}	$(4s)^2(4p\text{-})^2(4p\text{+})^3$ J =3/2 – $(4s)^2(4p\text{-})^2(4p\text{+})^2(5s\text{+})^1$ J =5/2	1.808	1.809	
$W^{?+}$			1.835	
$W^{?+}$			1.837	
W^{38+}	$(4s)^2(4p)^6$ J =0 – $(4s)^2(4p\text{-})^2(4p\text{+})^3(5s\text{+})^1$ J =1	1.840	1.841	
W^{44+}	$(3p)^6(3d)^{10}(4s\text{+})^1(4d\text{+})^1$ J =2 – $(3p)^6(3d)^{10}(4s\text{+})^1(5p\text{+})^1$ J =1	1.842		
W^{37+}	$(4p)^6(4d\text{+})^1$ J =5/2 – $(4p\text{-})^2(4p\text{+})^3(4d\text{+})^1(5s\text{+})^1$ J =5/2	1.863	1.863	
$W^{?+}$			1.927	
$W^{?+}$			1.948	
$W^{?+}$			1.950	
W^{43+}	$(3p)^6(3d)^{10}(4s)^2(4d\text{-})^1$ J =3/2 – $(3d)^{10}(4s)^2(5p\text{-})^1$ J =1/2	1.955	1.956	
W^{39+}	$(4s\text{+})^1(4p)^6$ J =1/2 – $(4s)^2(4p\text{-})^1(4p\text{+})^3(5p\text{-})^1$ J =3/2	1.964	1.966	
W^{39+}	$(4s)^2(4p\text{-})^2(4p\text{+})^2(4d\text{-})^1$ J =1/2 – $(4s)^2(4p\text{-})^2(4p\text{+})^2(5p\text{+})^1$ J =3/2	1.970	1.972	

Table 4.5: Observed and calculated transitions in the wavelength region from 1.5 nm to 2.0 nm. The spectral lines were measured after tungsten laser ablation in several plasma discharges with different T_{e0}. The value for $\lambda_{exp.}^{ref}$ are taken from [186].

Ion	transition	$\lambda_{th.}$ (nm)	$\lambda_{exp.}$ (nm)	$\lambda_{exp.}^{ref}$ (nm)
W^{47+}	$(3d)^9$ J=5/2 – $(3d\text{-})^3(3d\text{+})^5(5f\text{-})^1$ J=3/2,5/2,7/2	0.419	0.418	0.417[a]
W^{47+}	$(3d)^9$ J=5/2 – $(3d\text{-})^4(3d\text{+})^4(5f\text{+})^1$ J=5/2,7/2	0.429	0.429	
	$(3d)^9$ J=5/2 – $(3d\text{-})^4(3d\text{+})^4(5f\text{+})^1$ J=5/2,7/2	0.430		
W^{46+}	$(3d)^{10}$ J=0 – $(3d\text{-})^3(3d\text{+})^6(5f\text{-})^1$ J=1	0.431	0.430	0.431[a,b]
W^{46+}			0.433	0.433[b]
W^{45+}	$(3d)^{10}(4s\text{+})^1$ J=1/2 – $(3d\text{-})^3(3d\text{+})^6(4s\text{+})^1(5f\text{-})^1$ J=1/2,3/2	0.436	0.435	0.436[a,b]
W^{44+}	$(3d)^{10}(4s)^2$ J=0 – $(3d\text{-})^3(3d\text{+})^6(4s)^2(5f\text{-})^1$ J=1	0.440	0.439	
W^{46+}	$(3d)^{10}$ J=0 – $(3d\text{-})^4(3d\text{+})^5(5f\text{+})^1$ J=1	0.441	0.443	0.441[a,b]
W^{45+}	$(3d)^{10}(4s\text{+})^1$ J=1/2 – $(3d\text{-})^4(3d\text{+})^5(4s\text{+})^1(5f\text{+})^1$ J=1/2,3/2	0.445	0.445	0.446[a,b]
W^{43+}	$(3d)^{10}(4s)^2(4p\text{-})^1$ J=1/2 –	0.446		
	$(3d\text{-})^3(3d\text{+})^6(4s)^2(4p\text{-})^1(5f\text{-})^1$ J=1/2,3/2			
W^{44+}	$(3d)^{10}(4s)^2$ J=0 – $(3d\text{-})^4(3d\text{+})^5(4s)^2(5f\text{+})^1$ J=1	0.450	0.449	0.449[a,b]
W^{42+}	$(3d)^{10}(4s)^2(4p\text{-})^2$ J=0 –	0.450	0.450	0.451[a,b]
	$(3d\text{-})^3(3d\text{+})^6(4s)^2(4p\text{-})^2(5f\text{-})^1$ J=1			
W^{41+}	$(3d)^{10}(4s)^2(4p\text{-})^2(4p\text{+})^1$ J=3/2 –	0.455	0.456	0.456[a,b]
	$(3d\text{-})^3(3d\text{+})^6(4s)^2(4p\text{-})^2(4p\text{+})^1(5f\text{-})^1$ J=1/2,3/2			
	$(3d)^{10}(4s)^2(4p\text{-})^2(4p\text{+})^1$ J=3/2 –	0.455		
	$(3d\text{-})^4(3d\text{+})^5(4s)^2(4p\text{-})^2(4p\text{+})^1(5f\text{-})^1$ J=5/2			
	$(3d)^{10}(4s)^2(4p\text{-})^2(4p\text{+})^1$ J=3/2 –	0.455		
	$(3p\text{-})^2(3p\text{+})^3(3d)^{10}(4s)^2(4p\text{-})^1(4p\text{+})^2(4d\text{-})^1$ J=3/2			
W^{43+}	$(3d)^{10}(4s)^2(4p\text{-})^1$ J=1/2 –	0.456		
	$(3d\text{-})^4(3d\text{+})^5(4s)^2(4p\text{-})^1(5f\text{+})^1$ J=1/2,3/2			
W^{40+}	$(3d)^{10}(4s)^2(4p\text{-})^2(4p\text{+})^2$ J=2 –	0.460	0.461	0.462[b]
	$(3d\text{-})^3(3d\text{+})^6(4s)^2(4p\text{-})^2(4p\text{+})^2(5f\text{-})^1$ J=1,3			
	$(3d)^{10}(4s)^2(4p\text{-})^2(4p\text{+})^2$ J=0 –	0.461		
	$(3d\text{-})^3(3d\text{+})^6(4s)^2(4p\text{-})^2(4p\text{+})^2(5f\text{-})^1$ J=1			
W^{42+}	$(3d)^{10}(4s)^2(4p\text{-})^2$ J=0 – $(3d\text{-})^4(3d\text{+})^5(4s)^2(4p\text{-})^2(5f\text{+})^1$ J=1	0.461	0.463	
W^{41+}	$(3d)^{10}(4s)^2(4p\text{-})^2(4p\text{+})^1$ J=3/2 –	0.466	0.467	0.468[b]
	$(3d\text{-})^3(3d\text{+})^6(4s)^2(4p\text{+})^3(5f\text{-})^1$ J=5/2			
	$(3d)^{10}(4s)^2(4p\text{-})^2(4p\text{+})^1$ J=3/2 –	0.466		
	$(3d\text{-})^4(3d\text{+})^5(4s)^2(4p\text{-})^2(4p\text{+})^1(5f\text{+})^1$ J=1/2,3/2			
W^{38+}	$(3d)^{10}(4s)^2(4p)^6$ J=0 – $(3d\text{-})^3(3d\text{+})^6(4s)^2(4p)^6(5f\text{-})^1$ J=1	0.471	0.471	0.471[b]
W^{40+}	$(3d)^{10}(4s)^2(4p\text{-})^2(4p\text{+})^2$ J=2 –	0.471		
	$(3d\text{-})^4(3d\text{+})^5(4s)^2(4p\text{-})^2(4p\text{+})^2(5f\text{-})^1$ J=3			
	$(3d)^{10}(4s)^2(4p\text{-})^2(4p\text{+})^2$ J=2 –	0.471		
	$(3d\text{-})^4(3d\text{+})^5(4s)^2(4p\text{-})^2(4p\text{+})^2(5f\text{+})^1$ J=1,2,3			
	$(3d)^{10}(4s)^2(4p\text{-})^2(4p\text{+})^2$ J=0 –	0.471		
	$(3d\text{-})^4(3d\text{+})^5(4s)^2(4p\text{-})^2(4p\text{+})^2(5f\text{+})^1$ J=1			
W^{38+}	$(3d)^{10}(4s)^2(4p)^6$ J=0 – $(3d\text{-})^4(3d\text{+})^5(4s)^2(4p)^6(5f\text{+})^1$ J=1	0.482	0.483	
W^{46+}	$(3p^6 3d^{10} - 3p^5_{3/2} 3d^{10} 4f^1_{7/2})^b$	0.485[b]	0.485	0.486[b]
W^{47+}	$(3p)^6(3d)^9$ J=5/2 –	0.509	0.509	0.510[b]
	$(3p\text{-})^2(3p\text{+})^3(3d\text{-})^4(3d\text{+})^5(4d\text{+})^1$ J=5/2,7/2			
W^{47+}	$(3p)^6(3d)^9$ J=5/2 –	0.513	0.513	0.511[b]
	$(3p\text{-})^2(3p\text{+})^3(3d\text{-})^4(3d\text{+})^5(4d\text{+})^1$ J=7/2			
	continued			

Ion	transition	$\lambda_{th.}$ (nm)	$\lambda_{exp.}$ (nm)	$\lambda_{exp.}^{ref}$ (nm)
W^{47+}	$(3p)^6(3d)^9$ J=5/2 – $(3p\text{-})^2(3p\text{+})^3(3d\text{-})^4(3d\text{+})^5(4d\text{+})^1$ J=3/2	0.514		0.514[b]
	$(3p)^6(3d)^9$ J=5/2 – $(3p\text{-})^2(3p\text{+})^3(3d\text{-})^4(3d\text{+})^5(4d\text{+})^1$ J=5/2	0.515	0.515	
W^{46+}	$(3p)^6(3d)^{10}$ J=0 – $(3p\text{-})^2(3p\text{+})^3(3d)^{10}(4d\text{+})^1$ J= 1	0.520	0.520	0.520[b]
W^{45+}	$(3d)^{10}(4s\text{+})^1$ J=1/2 – $(3p\text{-})^2(3p\text{+})^3(3d)^{10}(4s\text{+})^1(5d\text{+})^1$ J=1/2	0.522	0.522	
W^{45+}	$(3d)^{10}(4s\text{+})^1$ J=1/2 – $(3p\text{-})^2(3p\text{+})^3(3d)^{10}(4s\text{+})^1(5d\text{+})^1$ J=3/2	0.523	0.523	
W^{44+}	$(3d)^{10}(4s)^2$ J=0 – $(3p\text{-})^2(3p\text{+})^3(3d)^{10}(4s)^2(4d\text{+})^1$ J=1	0.526	0.527	0.526[b]
W^{43+}	$(3d)^{10}(4s)^2(4p\text{-})^1$ J=1/2 – $(3p\text{-})^2(3p\text{+})^3(3d)^{10}(4s)^2(4p\text{-})^1(4d\text{+})^1$ J=1/2,3/2	0.530	0.530	
W^{49+}	$(3d\text{-})^4(3d\text{+})^3$ J=9/2 – $(3d\text{-})^3(3d\text{+})^3(4f\text{-})^1$ J=11/2	0.532	0.531	
	$(3d\text{-})^4(3d\text{+})^3$ J=9/2 – $(3d\text{-})^3(3d\text{+})^3(4f\text{+})^1$ J=11/2	0.533		
	$(3d\text{-})^4(3d\text{+})^3$ J=5/2 – $(3d\text{-})^3(3d\text{+})^3(4f\text{-})^1$ J=3/2,5/2,7/2	0.533		
	$(3d\text{-})^4(3d\text{+})^3$ J=5/2 – $(3d\text{-})^3(3d\text{+})^3(4f\text{+})^1$ J=7/2	0.533		
	$(3d\text{-})^4(3d\text{+})^3$ J=3/2 – $(3d\text{-})^3(3d\text{+})^3(4f\text{-})^1$ J=1/2,3/2,5/2	0.533		
	$(3d\text{-})^4(3d\text{+})^3$ J=3/2 – $(3d\text{-})^3(3d\text{+})^3(4f\text{+})^1$ J=5/2	0.533		
W^{49+}	$(3d\text{-})^4(3d\text{+})^3$ J=9/2 – $(3d\text{-})^3(3d\text{+})^3(4f\text{-})^1$ J=7/2,9/2,11/2	0.534	0.534	
	$(3d\text{-})^4(3d\text{+})^3$ J=5/2 – $(3d\text{-})^3(3d\text{+})^3(4f\text{+})^1$ J=5/2	0.534		
W^{40+}	$(3d)^{10}(4s)^2(4p\text{-})^2(4p\text{+})^2$ J=2 – $(3p\text{-})^2(3p\text{+})^3(3d)^{10}(4s)^2(4p\text{-})^2(4p\text{+})^2(4d\text{+})^1$ J=3	0.540	0.540	
W^{48+}	$(3d\text{-})^4(3d\text{+})^4$ J=4 – $(3d\text{-})^3(3d\text{+})^4(4f\text{-})^1$ J=4,5	0.544	0.545	
	$(3d\text{-})^4(3d\text{+})^4$ J=2 – $(3d\text{-})^3(3d\text{+})^4(4f\text{-})^1$ J=3	0.544		
	$(3d\text{-})^4(3d\text{+})^4$ J=0 – $(3d\text{-})^3(3d\text{+})^4(4f\text{-})^1$ J=1	0.544		
W^{48+}	$(3d\text{-})^4(3d\text{+})^4$ J=4 – $(3d\text{-})^3(3d\text{+})^4(4f\text{+})^1$ J=4	0.545	0.546	
	$(3d\text{-})^4(3d\text{+})^4$ J=4 – $(3d\text{-})^3(3d\text{+})^4(4f\text{-})^1$ J=3	0.545		
	$(3d\text{-})^4(3d\text{+})^4$ J=2 – $(3d\text{-})^3(3d\text{+})^4(4f\text{+})^1$ J=2	0.545		
W^{47+}	$(3d)^9$ J=5/2 – $(3d\text{-})^3(3d\text{+})^5(4f\text{-})^1$ J=5/2,7/2	0.556	0.556	0.556[c]
W^{48+}	$(3d\text{-})^4(3d\text{+})^4$ J=2 – $(3d\text{-})^4(3d\text{+})^3(4f\text{+})^1$ J=3	0.561	0.561	
	$(3d\text{-})^4(3d\text{+})^4$ J=4 – $(3d\text{-})^4(3d\text{+})^3(4f\text{+})^1$ J=4,5	0.562	0.562	
	$(3d\text{-})^4(3d\text{+})^4$ J=4 – $(3d\text{-})^4(3d\text{+})^3(4f\text{-})^1$ J=4	0.563	0.563	
	$(3d\text{-})^4(3d\text{+})^4$ J=2 – $(3d\text{-})^4(3d\text{+})^3(4f\text{+})^1$ J=2	0.564		
	$(3d\text{-})^4(3d\text{+})^4$ J=4 – $(3d\text{-})^4(3d\text{+})^3(4f\text{+})^1$ J=4	0.565		
W^{48+}	$(3d\text{-})^4(3d\text{+})^4$ J=2 – $(3d\text{-})^4(3d\text{+})^3(4f\text{+})^1$ J=2	0.565		
	$(3d\text{-})^4(3d\text{+})^4$ J=0 – $(3d\text{-})^4(3d\text{+})^3(4f\text{+})^1$ J=1	0.565		
	$(3d\text{-})^4(3d\text{+})^4$ J=2 – $(3d\text{-})^4(3d\text{+})^3(4f\text{+})^1$ J=1	0.566		
	$(3d\text{-})^4(3d\text{+})^4$ J=4 – $(3d\text{-})^4(3d\text{+})^3(4f\text{+})^1$ J=5,3	0.567	0.567	
	$(3p\text{-})^2(3p\text{+})^3(3d\text{-})^4(3d\text{+})^5$ J=4 – $(3p\text{-})^1(3p\text{+})^4(3d\text{-})^3(3d\text{+})^5(4f\text{-})^1$ J=4	0.567		
	$(3p\text{-})^2(3p\text{+})^3(3d\text{-})^4(3d\text{+})^5$ J=4 – $(3p\text{-})^2(3p\text{+})^3(3d\text{-})^4(3d\text{+})^4(4f\text{+})^1$ J=5	0.568		
W^{46+}	$(3d)^{10}$ J=0 – $(3d\text{-})^3(3d\text{+})^6(4f\text{-})^1$ J=1	0.569	0.569	0.569[d]
W^{45+}	$(3d)^{10}(4s\text{+})^1$ J=1/2 – $(3d)^9(4s\text{+})^1(4f\text{-})^1$ J=1/2,3/2	0.572	0.572	
W^{47+}	$(3d)^9$ J=5/2 – $(3d\text{-})^4(3d\text{+})^4(4f\text{+})^1$ J=7/2	0.574	0.575	
	$(3d)^9$ J=5/2 – $(3d\text{-})^4(3d\text{+})^4(4f\text{+})^1$ J=5/2	0.575		
	continued			

Ion	transition	$\lambda_{th.}$ (nm)	$\lambda_{exp.}$ (nm)	$\lambda_{exp.}^{ref}$ (nm)
W^{44+}	$(3d)^{10}(4s)^2$ J=0 – $(3d\text{-})^3(3d+)^6(4s)^2(4f\text{-})^1$ J=1	0.575	0.575	
W^{43+}	$(3d)^{10}(4s)^2(4p\text{-})^1$ J=1/2 – J=1/2,3/2	0.579	0.579	
	$(3d\text{-})^3(3d+)^6(4s)^2(4p\text{-})^1(4f\text{-})^1$ J=1/2,3/2			
	$(3d)^{10}(4s)^2(4p\text{-})^1$ J=1/2 –	0.579		
	$(3d\text{-})^4(3d+)^5(4s)^2(4p+)^1(4f\text{-})^1$ J=1/2,3/2			
W^{42+}	$(3d)^{10}(4s)^2(4p\text{-})^2$ J=0 – $(3d\text{-})^3(3d+)^6(4s)^2(4p\text{-})^2(4f\text{-})^1$ J=1	0.583	0.583	
	$(3d)^{10}(4s)^2(4p\text{-})^2$ J=0 – $(3d\text{-})^4(3d+)^5(4s)^2(4p\text{-})^1(4p+)^1(4f\text{-})^1$ J=1	0.583		
W^{46+}	$(3d)^{10}$ J=0 – $(3d\text{-})^4(3d+)^5(4f+)^1$ J=1	0.587	0.587	0.587[d]
W^{40+}	$(3d)^{10}(4s)^2(4p\text{-})^2(4p+)^2$ J=2 –	0.589	0.589	
	$(3d\text{-})^4(3d+)^5(4s)^2(4p\text{-})^1(4p+)^3(4f\text{-})^1$ J=3			
	$(3d)^{10}(4s)^2(4p\text{-})^2(4p+)^2$ J=2 –	0.590		
	$(3d\text{-})^3(3d+)^6(4s)^2(4p\text{-})^2(4p+)^2(4f\text{-})^1$ J=1,2			
W^{45+}	$(3d)^{10}(4s+)^1$ J=1/2 – $(3d\text{-})^4(3d+)^5(4s+)^1(4f+)^1$ J=1/2, 3/2	0.591	0.591	
W^{44+}	$(3d)^{10}(4s)^2$ J=0 – $(3d\text{-})^4(3d+)^5(4s)^2(4f+)^1$ J=1	0.594	0.595	
W^{43+}	$(3d)^{10}(4s)^2(4p\text{-})^1$ J=1/2 –	0.599	0.598	0.596[d]
	$(3d\text{-})^4(3d+)^5(4s)^2(4p\text{-})^1(4f+)^1$ J=1/2,3/2			
W^{42+}	$(3d)^{10}(4s)^2(4p\text{-})^2$ J=0 – $(3d\text{-})^4(3d+)^5(4s)^2(4p\text{-})^2(4f+)^1$ J=1	0.602	0.601	
W^{41+}	$(3d)^{10}(4s)^2(4p\text{-})^2(4p+)^1$ J=3/2 –	0.605	0.604	
	$(3d\text{-})^3(3d+)^6(4s)^2(4p+)^3(4f\text{-})^1$ J=5/2			
	$(3d)^{10}(4s)^2(4p\text{-})^2(4p+)^1$ J=3/2 –	0.605	0.606	
	$(3d\text{-})^4(3d+)^5(4s)^2(4p\text{-})^2(4p+)^1(4f+)^1$ J=3/2			
W^{40+}	$(3d)^{10}(4s)^2(4p\text{-})^2(4p+)^2$ J=2,0 –	0.609	0.608	
	$(3d\text{-})^4(3d+)^5(4s)^2(4p\text{-})^2(4p+)^2(4f+)^1$ J=1			
W^{39+}	$(3d)^{10}(4s)^2(4p\text{-})^2(4p+)^3$ J=3/2 –	0.612	0.612	
	$(3d\text{-})^4(3d+)^5(4s)^2(4p\text{-})^2(4p+)^3(4f+)^1$ J=3/2			
	$(3d)^{10}(4s)^2(4p\text{-})^2(4p+)^3$ J=3/2 –	0.613		
	$(3d\text{-})^4(3d+)^5(4s)^2(4p\text{-})^2(4p+)^3(4f+)^1$ J=1/2,5/2			
W^{45+}	$(3p)^6(3d)^{10}(4f\text{-})^1$ J=5/2 –	0.613		
	$(3p\text{-})^2(3p+)^3(3d)^{10}(4s+)^1(4f+)^1$ J=5/2			
W^{46+}	$(3p)^6(3d)^{10}$ J=0 – $(3p\text{-})^2(3p+)^3(3d)^{10}(4s+)^1$ J=1	0.615	0.615	0.615[d]
W^{45+}	$(3p)^6(3d)^{10}(4f+)^1$ J=7/2 –	0.618	0.618	
	$(3p\text{-})^2(3p+)^3(3d)^{10}(4s+)^1(4f+)^1$ J=5/2			
W^{45+}	$(3p)^6(3d)^{10}(4d+)^1$ J=5/2 –	0.619	0.620	
	$(3p\text{-})^2(3p+)^3(3d)^{10}(4s+)^1(4d+)^1$ J=3/2			
	$(3p)^6(3d)^{10}(4p+)^1$ J=3/2 –	0.620		
	$(3p\text{-})^2(3p+)^3(3d)^{10}(4s+)^1(4p+)^1$ J=1/2			
W^{44+}	$(3p)^6(3d)^{10}(4s+)^1(4p+)^1$ J=1 –	0.622		
	$(3p\text{-})^2(3p+)^3(3d)^{10}(4s)^2(4p+)^1$ J=0			
	$(3p)^6(3d)^{10}(4s+)^1(4f+)^1$ J=3 –	0.623	0.623	
	$(3p\text{-})^2(3p+)^3(3d)^{10}(4s+)^2(4f+)^1$ J=2			
	continued			

Ion	transition	$\lambda_{th.}$ (nm)	$\lambda_{exp.}$ (nm)	$\lambda_{exp.}^{ref}$ (nm)
W^{43+}	$(3p)^6(3d)^{10}(4s+)^1(4p-)^1(4p+)^1$ J=1/2,3/2 – $(3p-)^2(3p+)^3(3d)^{10}(4s)^2(4p-)^1(4p+)^1$ J=1/2	0.627	0.627	
	$(3p)^6(3d)^{10}(4s+)^1(4p-)^1(4f+)^1$ J=5/2 – $(3p-)^2(3p+)^3(3d)^{10}(4s)^2(4p-)^1(4f+)^1$ J=3/2	0.629		
	$(3p)^6(3d)^{10}(4s+)^1(4p-)^1(4f+)^1$ J=7/2 – $(3p-)^2(3p+)^3(3d)^{10}(4s)^2(4p-)^1(4f+)^1$ J=5/2	0.629		
W^{42+}	$(3p)^6(3d)^{10}(4s+)^1(4p-)^2(4p+)^1$ J=1 – $(3p-)^2(3p+)^3(3d)^{10}(4s)^2(4p-)^2(4p+)^1$ J=0	0.631	0.631	
	$(3p)^6(3d)^{10}(4s+)^1(4p-)^2(4f+)^1$ J=3 – $(3p-)^2(3p+)^3(3d)^{10}(4s)^2(4p-)^2(4f+)^1$ J=2	0.634	0.635	
W^{48+}	$(3d-)^4(3d+)^4$ J=4 – $(3d-)^4(3d+)^3(4p+)^1$ J=4	0.657	0.657	
W^{46+}	$(3d)^{10}$ J=0 – $(3d-)^3(3d+)^6(4p+)^1$ J=1	0.678	0.677	0.678[d,e]
W^{45+}	$(3d)^{10}(4s+)^1$ J=1/2 – $(3d-)^3(3d+)^6(4s+)^1(4p+)^1$ J=1/2, 3/2	0.689	0.689	0.688[e]
W^{47+}	$(3d-)^4(3d+)^5$ J=5/2 – $(3d-)^3(3d+)^5(4p-)^1$ J=7/2	0.694	0.694	0.695[e]
	$(3d-)^4(3d+)^5$ J=5/2 – $(3d-)^3(3d+)^5(4p-)^1$ J=3/2	0.695		
	$(3d-)^4(3d+)^5$ J=5/2 – $(3d-)^3(3d+)^5(4p-)^1$ J=3/2, 5/2	0.697	0.697	
	$(3d-)^4(3d+)^5$ J=5/2 – $(3d-)^3(3d+)^5(4p-)^1$ J=5/2, 7/2	0.701	0.701	
W^{46+}	$(3d)^{10}$ J=0 – $(3d-)^4(3d+)^5(4p+)^1$ J=1	0.703	0.702	0.703[e]
W^{45+}	$(3d)^{10}(4s+)^1$ J=1/2 – $(3d-)^4(3d+)^5(4s+)^1(4p+)^1$ J=3/2	0.707	0.707	0.708[e]
W^{48+}	$(3d-)^4(3d+)^4$ J=4 – $(3d-)^3(3d+)^4(4s+)^1$ J=6	0.712	0.711	0.711[e]
W^{45+}	$(3d)^{10}(4s+)^1$ J=1/2 – $(3d-)^4(3d+)^5(4s+)^1(4p+)^1$ J=1/2	0.714	0.713	0.714[e]
W^{46+}	$(3d)^{10}$ J=0 – $(3d-)^3(3d+)^6(4p-)^1$ J=1	0.718	0.716	0.717[d,e]
W^{44+}	$(3d)^{10}(4s)^2$ J=0 – $(3d-)^4(3d+)^5(4s)^2(4p+)^1$ J=1	0.719	0.719	0.719[e]
W^{45+}	$(3d)^{10}(4s+)^1$ J=1/2 – $(3d-)^3(3d+)^6(4s+)^1(4p-)^1$ J=1/2,3/2	0.726	0.725	0.724[e]
W^{43+}	$(3d)^{10}(4s)^2(4p-)^1$ J=1/2 – $(3d-)^4(3d+)^5(4s)^2(4p-)^1(4p+)^1$ J=1/2,3/2	0.728	0.727	0.727[e]
W^{42+}	$(3d)^{10}(4s)^2(4p-)^2$ J=0 – $(3d-)^4(3d+)^5(4s)^2(4p-)^2(4p+)^1$ J=1	0.735	0.732	0.732[e]
W^{44+}	$(3d)^{10}(4s)^2$ J=0 – $(3d-)^3(3d+)^6(4s)^2(4p-)^1$ J=1	0.734	0.734	0.734[e]
W^{41+}	$(3d)^{10}(4s)^2(4p-)^2(4p+)^1$ J=3/2 – $(3d-)^4(3d+)^5(4s)^2(4p-)^2(4p+)^2$ J=3/2,5/2	0.741	0.741	
W^{43+}	$(3d)^{10}(4s)^2(4p+)^1$ J=3/2 – $(3d-)^3(3d+)^6(4s)^2(4p-)^1(4p+)^1$ J=5/2	0.742		
	$(3d)^{10}(4s)^2(4d-)^1$ J=3/2 – $(3d-)^3(3d+)^6(4s)^2(4p-)^1(4d-)^1$ J=1/2	0.745	0.745	
W^{42+}	$(3d)^{10}(4s)^2(4p-)^1(4p+)^1J$=1 – $(3d-)^3(3d+)^6(4s)^2(4p-)^2(4p+)^1$ J=1	0.746		
W^{48+}	$(3d-)^4(3d+)^4$ J=4 – $(3d-)^4(3d+)^3(4s+)^1$ J=5	0.747	0.747	
W^{40+}	$(3d)^{10}(4s)^2(4p-)^2(4p+)^2$ J=2 – $(3d-)^4(3d+)^5(4s)^2(4p)^5$ J=2,3	0.748	0.748	
W^{40+}	$(3d)^{10}(4s)^2(4p-)^2(4p+)^2$ J=0 – $(3d-)^4(3d+)^5(4s)^2(4p-)^2(4p+)^3$ J=1	0.750	0.750	
W^{39+}	$(3d)^{10}(4s)^2(4p)^5$ J=3/2 – $(3d-)^4(3d+)^5(4s)^2(4p-)^2(4p+)^4$ J=5/2	0.756	0.757	
W^{46+}	$(3d)^{10}$ J=0 – $(3d-)^3(3d+)^6(4s+)^1$ J=2	0.762	0.759	
	continued			

Ion	transition	$\lambda_{th.}$ (nm)	$\lambda_{exp.}$ (nm)	$\lambda_{exp.}^{ref}$ nm)
W^{39+}	$(3d)^{10}(4s)^2(4p\text{-})^1(4p+)^3(4d\text{-})^1$ J=1/2,3/2,5/2 – $(3d\text{-})^3(3d+)^6(4s)^2(4p)^5(4d\text{-})^1$ J=3/2	0.761	0.762	
W^{38+}	$(3d)^{10}(4s)^2(4p\text{-})^1(4p+)^4(4d\text{-})^1$ J=1 – $(3d\text{-})^3(3d+)^6(4s)^2(4p)^6(4d\text{-})^1$ J=0	0.765	0.764	
W^{47+}	$(3d\text{-})^4(3d+)^5$ J=5/2 – $(3d\text{-})^4(3d+)^4(4s+)^1$ J=3/2	0.766	0.766	
	$(3d\text{-})^4(3d+)^5$ J=5/2 – $(3d\text{-})^4(3d+)^4(4s+)^1$ J=5/2	0.767		
W^{42+}	$(3d)^{10}(4s)^2(4p\text{-})^1(4d\text{-})^1$ J=1 – $(3d\text{-})^4(3d+)^5(4s)^2(4p\text{-})^2(4d+)^1$ J=0	0.767	0.767	
W^{45+}	$(3d)^{10}(4s+)^1$ J=1/2 – $(3d\text{-})^3(3d+)^6(4s+)^2$ J=3/2	0.768	0.769	
W^{39+}	$(3d)^{10}(4s)^2(4p\text{-})^1(4p+)^3(4d+)^1$ J=1/2 – $(3d\text{-})^3(3d+)^6(4s)^2(4p)^5(4d+)^1$ J=3/2	0.769	0.770	
W^{47+}	$(3d\text{-})^4(3d+)^5$ J=5/2 – $(3d\text{-})^4(3d+)^4(4s+)^1$ J=7/2	0.770	0.771	
	$(3d\text{-})^4(3d+)^5$ J=5/2 – $(3d\text{-})^4(3d+)^4(4s+)^1$ J=9/2	0.772		
W^{43+}	$(3d)^{10}(4s)^2(4p+)^1$ J=3/2 – $(3d\text{-})^4(3d+)^5(4s)^2(4p\text{-})^1(4p+)^1$ J=5/2	0.772	0.773	
W^{42+}	$(3d)^{10}(4s)^2(4p\text{-})^1(4p+)^1$ J=2 – $(3d\text{-})^4(3d+)^5(4s)^2(4p\text{-})^2(4p+)^1$ J=3	0.778	0.777	
	$(3d)^{10}(4s)^2(4p\text{-})^1(4p+)^1$ J=2 – $(3d\text{-})^4(3d+)^5(4s)^2(4p\text{-})^2(4p+)^1$ J=2	0.780	0.780	
W^{46+}	$(3d)^{10}$ J=0 – $(3d\text{-})^4(3d+)^5(4s+)^1$ J=2	0.794	0.793	
W^{45+}	$(3d)^{10}(4s+)^1$ J=1/2 – $(3d\text{-})^4(3d+)^5(4s+)^2$ J=5/2	0.801	0.800	
	$(3d)^{10}(4p\text{-})^1$ J=1/2 – $(3d\text{-})^4(3d+)^5(4s+)^1(4p\text{-})^1$ J=5/2	0.808	0.807	
W^{44+}	$(3d)^{10}(4s+)^1(4p+)^1$ J=2 – $(3d\text{-})^4(3d+)^5(4s)^2(4p+)^1$ J=4	0.809	0.809	
	$(3d)^{10}(4s+)^1(4p\text{-})^1$ J=0 – $(3d\text{-})^4(3d+)^5(4s)^2(4p\text{-})^1$ J=2	0.809		
	$(3d)^{10}(4s+)^1(4p\text{-})^1$ J=1 – $(3d\text{-})^4(3d+)^5(4s)^2(4p\text{-})^1$ J=3	0.812	0.812	
W^{45+}	$(3d)^{10}(4p\text{-})^1$ J=1/2 – $(3d\text{-})^3(3d+)^6(4s+)^2$ J=3/2	0.818	0.817	
W^{43+}	$(3d)^{10}(4s+)^1(4p\text{-})^2$ J=1/2 – $(3d)^9(4s)^2(4p\text{-})^2$ J=5/2	0.823	0.823	
$W^{?+}$			0.833	
W^{45+}	$(3d)^{10}(4p+)^1$ J=3/2 – $(3d)^9(4s)^2$ J=5/2	0.919	0.918	

Table 4.6: Observed and calculated transitions in the wavelength region from 0.42 nm to 0.92 nm. The spectral lines were measured in several plasma discharges with different T_{e0}. The experimental values in column $\lambda_{exp.}^{ref}$ are taken from a : [195], b : [196], c : [218], d : [197], e : [198].

5. Description of Impurity Transport

Energy losses from the core plasma by radiation and dilution are the negative consequences from finite impurity densities. The central impurity concentrations are the result of a complex sometimes non-linear interplay between the background plasma and the impurity sources and their transport into and within the plasma. Fig. 5.1 presents some of the major processes involved in the build-up of the central impurity content. The impurity-path starts with the release at a plasma facing component, it continues with the transport within the scrape of layer (SOL) and the penetration through the last closed flux surface (LCFS) towards the core plasma. The radial transport, which leads to movement of the charged particles perpendicular to the magnetic flux tubes is set up through different components. Some are governed by binary collisions, others are due to macroscopic turbulent phenomena. Since only very recently could some light be shed on the physics of the turbulent transport, it is called anomalous. Under most plasma conditions it is larger than the collisional transport, which is on a firm basis, called neoclassical theory. Especially in the plasma edge, the transport is mostly anomalous and the neoclassical theory breaks down due to the strong gradients. The following sections will highlight the nature of the the most important processes, however for an in-depth discussion the reader should refer to the given references.

5.1 Divertor and Scrape Off Layer Transport

In a limiter as well as in the divertor configuration the confined plasma is separated by the last closed flux surface (LCFS). Closely inside the LCFS, strong gradients can appear due to reduced radial transport in the high confinement mode (H-Mode). The region radially outboard of the LCFS is called the scrape-off layer (SOL). All the flux surfaces in the SOL are open, which means that they end on the material surfaces of the limiter, or the divertor. Therefore, cross field *and* parallel velocities have to be considered in order to describe transport phenomena. Plasma edge and boundary physics are extensively developed in a book of P.C. Stangeby [220] and in a report by R. Schneider [221]. Experimental divertor physics is reviewed in [222].

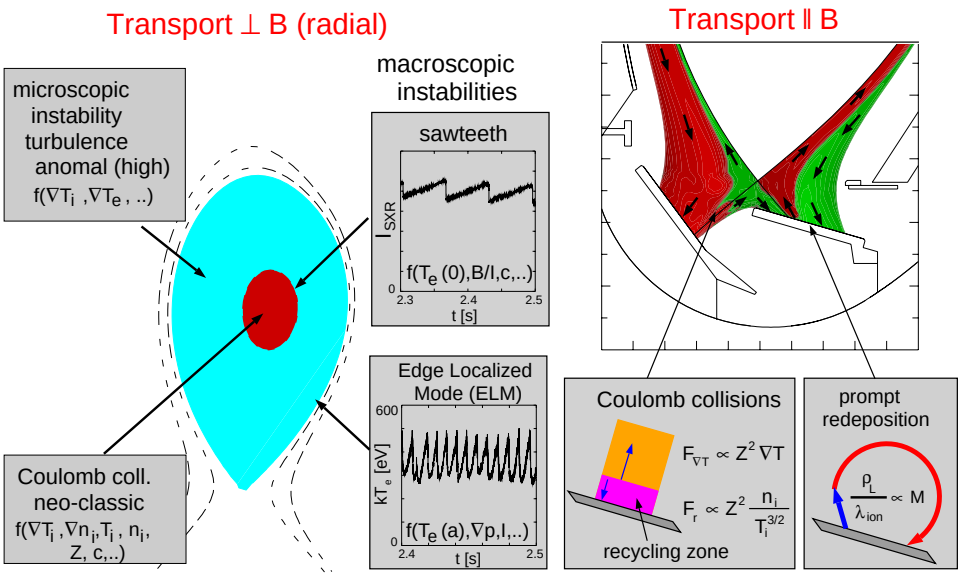

Figure 5.1: Transport processes relevant in the core (left side) and the divertor (right side)

5.1.1 Prompt Re-deposition

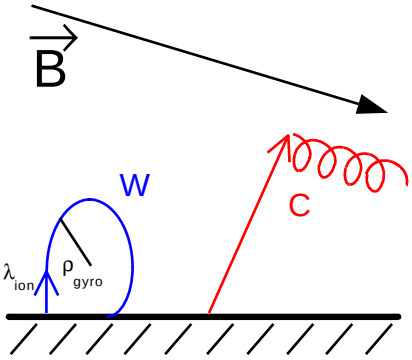

Figure 5.2: Schematic view of the motion of W and C atoms and ions after erosion in a plasma with an oblique magnetic field.

In the divertor as well as at a limiter the magnetic field lines of the SOL impinge on the material surfaces under a very shallow angle. Eroded atoms, which are predominantly released as neutrals, may be re-deposited on the target plate after ionisation during the first gyration. This process is called 'prompt re-deposition'. It is governed by the ratio p of ionisation length λ_{ion} and gyro-radius r_L,

$$p = \frac{\lambda_{ion}}{r_L} \sim \frac{B}{m_Z S_Z n_e} \tag{5.1}$$

where B denotes the local magnetic field, m_Z the ion mass and S_Z the ionisation rate coefficient. Note that p is independent of the particle velocity but inversely proportional to its mass. Fig. 5.2 illustrates the effect for ions with strongly different mass as W and C. All sputtered particles become ionised on the hemisphere of radius λ_{ion}. On the assumption of a $\cos\theta$ distribution, the fraction f_r of promptly re-deposited particles can be calculated by integration to [223]

$$f_r = \frac{1}{2}\left[1 + \frac{(1-p^2)}{(1+p^2)}\right]. \tag{5.2}$$

For typical plasma parameters as $T_e = 20$ eV, $n_e = 5 \cdot 10^{19}$ m^{-3} and $B = 2$ T one obtains $p \approx 7$ for C and $p \approx 0.1$ for W leading to $f_r = 0.02$ for C and $f_r = 0.99$ for W, respectively.
A more adequate description has to include the distribution of the ionisation length, multiple ionisation and the sheath potential, which are considered in the Monte Carlo code ERO [224]. These calculations result in an increased re-deposition in the case of C ($f_r = 0.1$) and only a slight decrease in the case of W [92, 223]. A comparison to spectroscopic measurements in the divertor of ASDEX Upgrade [171] is shown in Fig. 5.3. A very good agreement with the height distribution of the W I brightness is found when taking into account prompt re-deposition.

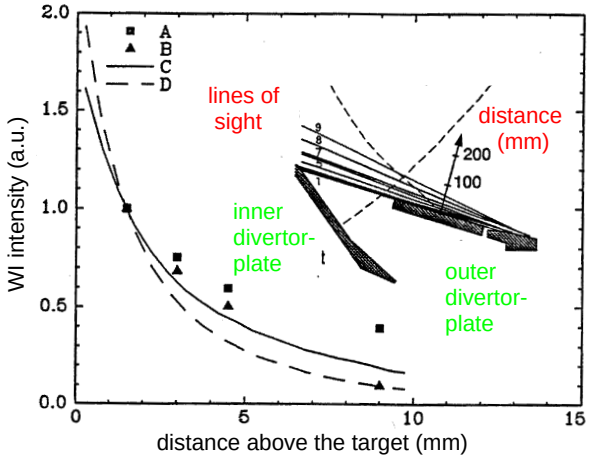

Figure 5.3: Height distribution of the brightness of the W I line above the DIV I W target plates. Experimental values for two different plasma densities (A: $\bar{n}_e = 1.7 \cdot 10^{19}$ m^{-3} , B: $\bar{n}_e = 2.0 \cdot 10^{19}$ m^{-3}) and results from ERO code calculations (C,D) taking prompt re-deposition of W into account are shown (after [92]). The insert presents a schematic view of the experimental arrangement.

5.1.2 Force Balance in the Divertor

On a longer timescale than the gyro-motion, the impurity ion is subject to different forces resulting from the interaction with the plasma background. Essentially, the force parallel to $\vec{B}$ on an ion with charge Z is given as [220, 221]:

$$F_Z = -\frac{1}{n_z}\frac{dp_Z}{ds} + m_Z\frac{v_i - v_Z}{\tau_s} + ZeE + \alpha_e\frac{d((kT_e)}{ds} + \beta_i\frac{d((kT_i)}{ds} + ... \qquad (5.3)$$

where s is the co-ordinate along the magnetic field pointing away from the target and the subscript i marks the quantities related to the background ions. The individual forces can be described as follows:

- $-\frac{1}{n_z}\frac{dp_Z}{ds}$ is the force resulting from the impurity pressure gradient
- $m_Z\frac{v_i - v_Z}{\tau_s}$ is the friction force on the impurity ion moving with v_Z in the plasma background which has the fluid velocity v_i. τ_s describes the time for momentum exchange between impurities and background, leading to an increase of the force proportional to Z^2

- ZeE is the electrostatic force due to the parallel electric field in the SOL
- $\alpha_e \frac{d((kT_e)}{ds}$ is the electron temperature gradient force, and
- $\alpha_e \frac{d((kT_i)}{ds}$ is the ion temperature gradient force.

The coefficients of the last two forces are proportional to Z^2. These forces are due to collisions with the background ions. Because of the underlying Coulomb force, the collision frequency decreases proportional to $Z^2/T^{3/2}$. As a result, both terms push the impurity towards the higher temperature plasma regions.
In practise, the resulting force is mainly governed by the friction force and the ion temperature gradient force, both being proportional to Z^2. Since the friction force decreases with plasma temperature $\sim 1/T^{3/2}$ and the temperature gradient force may increase (due to larger gradients) the impurities will be pushed more strongly towards the plasma and the divertor leakage will increase with increasing plasma temperature. This leads to the criterion of low plasma temperatures in the divertor, which is also consistent with the demand for low erosion rates, also strongly depending on T_i (see Sec. 2.2). Simultaneously to the parallel transport, the impurities undergo perpendicular transport mainly due to fluctuations as will be described below. These processes are usually treated with a diffusive ansatz similar to the one of eq. 5.21.

5.1.3 Simulation of SOL Transport

In the SOL, the plasma parameters vary perpendicularly as well as along the flux tubes. It this therefore inevitable that simulations are performed in a 2D geometry. In addition to the thermal motion, drifts may also play a strong role in the streaming of the background plasma. Experimental investigations at several tokamaks show that drifts with substantial Mach numbers ($|M| \leq 1$) can be present [225–227]. A further complication originates from the fact that background neutrals are important in the plasma edge and have to be treated by a sophisticated neutral particle code. A code package that deals with the edge/divertor plasma in a consistent way is B2-EIRENE [228]. However, this code consumes a huge amount of CPU-power, especially in the case of the treatment of multiple ionisation states, as in the case of tungsten. In order to keep the problem treatable, a different approach has been started recently: A background plasma is self-consistently setup by the B2-EIRENE code taking into account experimental boundary conditions as the power flux or measured edge profiles. This background plasma is introduced in the DIVIMP code [229] which calculates the transport of trace impurities in the plasma edge. Initially DIVIMP was designed to model erosion and transport in the divertor region and the SOL of tokamaks. Therefore in most versions of the code the plasma-wall interaction is restricted to two areas, the inner and outer divertor. During the ongoing W experiments at ASDEX Upgrade tungsten is used as a plasma facing

material in the central column (see Sec. 6.2). Erosion at the main chamber wall can only be calculated with neutral hydrogen fluxes taken from EIRENE simulations. For the calculation of the erosion source term at the central column, a simple plasma model was implemented, where the plasma parameters are extrapolated from the outermost grid ring to corresponding points of the wall assuming an exponential decay of n_e, T_e and T_i, with a decay length λ [230,231]. The decay length λ was taken from Thomson scattering measurements at ASDEX Upgrade [232] at the low-field side plasma boundary mapped to the high-field side.

For the modelling of the W erosion source only physical sputtering needs to be taken into account. The sputtering data were taken from measurements during the W divertor experiment (see 6.1.2), which accounts for the erosion caused by carbon impurities in the background plasma. The sputtered tungsten is then fed back into the appropriate outer grid cells analogous to the case of wall erosion by EIRENE generated neutrals. Due to the distance between grid and wall, prompt re-deposition which might contribute significantly to the small SOL penetration probabilities is not included. Up to now only an L-mode hydrogen discharge has been modelled because of its good edge diagnostic and the thorough B2/EIRENE background plasma. A poloidal cross section showing the distribution of the resulting density of some ionisation states is shown in Fig. 5.4. While the lower ionisation states are more concentrated around the source location and also in the divertor, the higher ionisation stages are located more at the top of the plasma and within the separatrix.

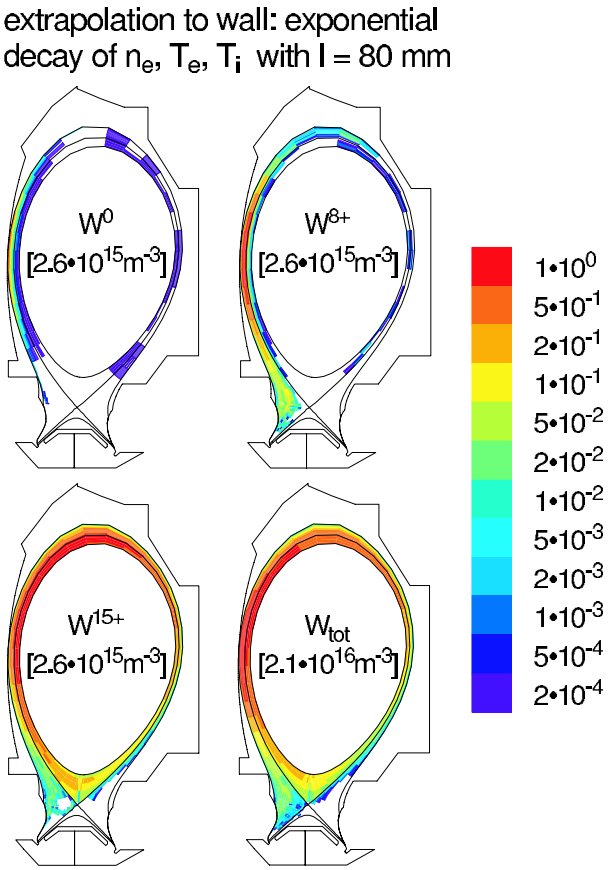

Figure 5.4: Two-dimensional distribution of the density of some ionisation states. The densities corresponding to the colours can be found by multiplying the maximum density in brackets with the corresponding number on the colour bar (after [230]).

For the W source region as present during PHASE I (see Sec. 6.2) the W migration pattern has been determined on the basis of the model discharge described above. The overall distribution of the modelled deposition agrees quite well with the measured deposition pattern, however with significant discrepancies in the small scale details [230].

Nevertheless, the strong deposition at the inner baffle and the inner strike point are well reproduced. This behaviour might be a consequence of the strong drag force on the W particles towards the divertor caused by friction with the plasma background, due to the plasma flow in front of the heat shield. Another consequence of these drag forces is the fast decay of the W deposition towards the top of the heat shield, which is also seen in the experiment. However, the deposition at the outer divertor described in Sec. 6.2.2 could not be reproduced with the code.

5.1.4 Experimental Approach

The application of simulation codes is the most reliable way to extrapolate results gained at a present device towards a future fusion reactor. First attempts have been made to model the erosion and transport of W in ITER in a similar way as described above by using the B2-EIRENE as well as the DIVIMP code [19]. On the other hand, there are also some ambiguities in the simulation due to weaknesses in the underlying models or lack of experimental input data, which cannot be resolved at the moment. This situation justifies simplified approaches in order to get at least a rough picture of the processes involved. Therefore trace impurities have been injected at various locations to disentangle the role of impurity sources in the main chamber and in the divertor and the result of these experiments has been analysed in a simplified way, described below.

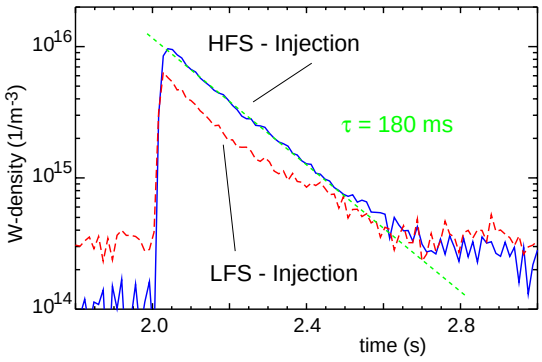

Figure 5.5: Temporal evolution of the tungsten density after W ablation from central column (solid line) and from a W target at the low field side (dashed line, scaled to the same amount of ablated W). The values for the W densities before the injection are below the detection limit.

An experimental approach was performed to get an estimate for the particle confinement time τ_p for W originating from the central column. For this purpose the laser of the LBO system was focused on the W coating at the central column. The layer could be ablated with one single laser pulse and the number of ablated particles was calculated from the thickness of the coating and the spot-size. The tungsten penetrating into the plasma was analysed with the spectroscopic means described in Chap. 4. The relation between a source flux Φ and a concentration c in the confined plasma can be established via the expression

$$c = p\frac{\Phi\tau_t}{n_e V}, \tag{5.4}$$

where τ_t is the particle transport time and p the so called penetration probability, e.g. in the case of impurities injected in the main chamber p is their probability to penetrate

through the SOL into the main plasma. This penetration probability depends on the impurity species and its energy when it interacts with the SOL as well as on the local properties of the SOL which can vary for different discharge types but also for different spatial locations inside the tokamak. From the comparison of the total amount of ablated W atoms and the maximum number of W ions in the plasma, a penetration factor of $p = 0.04$ was calculated. Performing the same experiment with a W target of comparable thickness at the low field side (LFS) of the torus (classical laser ablation), a value of $p = 0.03$ is found for the penetration of the W. This result is illustrated in Fig. 5.5 where the temporal evolution of the W density is shown.

The W sublimation probe described in Sec. 3.2.2 has been used in the divertor and in the midplane of ASDEX Upgrade for the measurement of the divertor retention R [157]. For R the definition

$$R = \frac{\Phi_{div}}{\Phi_{SOL}} \tag{5.5}$$

is used, where Φ_{div} and Φ_{SOL} are the impurity fluxes into the plasma from the divertor and the SOL respectively. Taking the formal impurity residence time $\tau_p = p\tau_t$ the definition R is identical to the expression given for R in [233]. By a combination of central spectroscopy and deposition measurements it was possible to shed light on the W transport path. In order to use deposition probes for a sensible measurement of the amount of tungsten in the main plasma, one has to assure, that there is no direct flux of injected particles between the sublimation- and the deposition probe. However, this is very unlikely since a magnetic field line starting at the sublimation probe opening intersects a horizontal plane at the position of the deposition probe at a point that is toroidally 135° away after two toroidal revolutions. Moreover the radial electric field, due to $\vec{E} \times \vec{B}$ forces, leads to a significant deviation of the drift trajectory from the magnetic field line, also away from the deposition probe. The third mechanism preventing a direct connection is the large magnetic shear in the region around the X-point which leads to a large toroidal and poloidal spread of the puffed cloud once it reaches the main chamber. For the determination of the respective fluxes in the SOL and the concentrations in the main plasma the knowledge of the decay lengths and penetration probabilities p is necessary. The values obtained for p from the sublimation probe range from 2 % to 11 % with an average of 5 % are in good agreement with the LBO results. In addition, the decay length of the W flux in the limiter shadow was obtained by the measurement of the deposited tungsten on the probe graphite housing. This flux decay length in the limiter shadow ($\lambda_{lim} = 22$ mm) is in good agreement with earlier findings during the tungsten divertor experiment [95]. The respective decay length λ_{SOL} in the SOL can be obtained using the relation assuming purely diffusive transport in the SOL

$$\frac{\lambda_{SOL}}{\lambda_{lim}} \approx \sqrt{\frac{L_{SOL}}{L_{lim}}} \tag{5.6}$$

with the connection lengths L_{lim} and L_{SOL} in the limiter shadow and the SOL. The

decay length of approximately 8 cm found in the SOL is compatible with the background plasma determined experimentally in the outer, cold SOL by Thomson scattering [232]. The shorter decay length measured in the hot SOL close to the separatrix would lead to an even higher tungsten concentration in the main plasma for a measured areal W density on the deposition probe.
The relation between the perpendicular W flux density $\Gamma_\perp(x)$ in the limiter shadow and the areal density σ_W of W deposited on the probe head is

$$\Gamma_\perp(x) = \frac{\lambda_{lim}\sigma_{W,l}}{tL/2} \exp\left(-\frac{x - x_l}{\lambda_{lim}}\right). \tag{5.7}$$

Here the index l refers to the innermost measured position, L is the connection length between the probe and the next limiter in plasma streaming direction. λ_{lim} is the decay length of the W flux in the limiter shadow, x is the large plasma radius and t the exposure time of the deposition probe. For the derivation of this equation it was assumed that half of the W entering the limiter shadow flows in the direction of the probe. For the propagation of W from the divertor into the main plasma, there are two possible paths, as indicated in figure 5.6. Firstly, a propagation directly from the divertor into the confined central plasma and from there across the separatrix into the SOL and onto the deposition probe (Fig. 5.6a). In this case one gets the relation

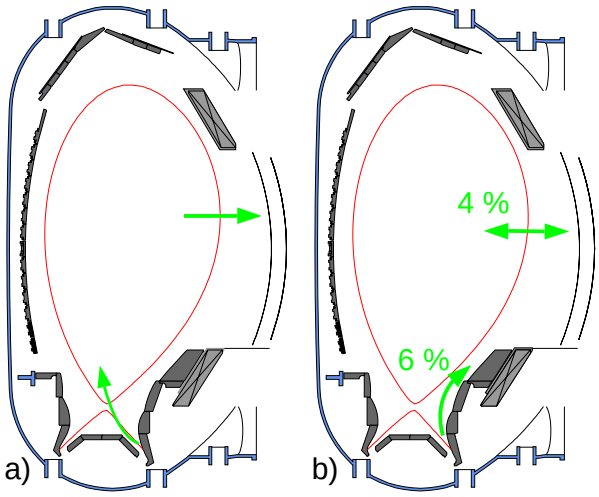

Figure 5.6: *Possible paths of the tungsten injected in the divertor into the main plasma of ASDEX Upgrade. The final values found for r and p are depicted on the right side.*

$$\Phi_{SOL} = \frac{c_W n_e V}{\tau_t} \tag{5.8}$$

for the central W concentration c_W and the particle transport time τ_t. Φ_{SOL} is the flux across the separatrix into the SOL in the main chamber. The relation to the measured W on the deposition probe was established using equations 5.6 and 5.7 assuming a poloidally constant flux across the separatrix with a surface of 42 m^2 at ASDEX Upgrade. The SOL width was 5 cm taken from equilibrium reconstruction. The obtained value $c_W = 3 \cdot 10^{-6}$ lies clearly above the spectroscopic detection limit, but no W was detected in the main chamber and thus this propagation path can be excluded. As already mentioned above, c_W in the central plasma would be even higher, taking into account the smaller decay length in the SOL close to the separatrix.

The second possibility is a propagation from the divertor into the SOL and from there into the main plasma (Fig. 5.6b). In this case one gets the relation

$$\Phi_{SOL} = \frac{1}{p}\frac{c_W n_e V}{\tau_t} \tag{5.9}$$

between the Φ_{SOL} and c_W. For the flux in the divertor Φ_{div} and c_W the relation

$$\Phi_{div} = \frac{1}{rp}\frac{c_W n_e V}{\tau_t} \tag{5.10}$$

where r is the probability of a W particle to escape from the divertor into the main chamber SOL. In this case all restrictions imposed from detection limits are satisfied. From the definition of R in equation 5.5 it follows, that $R = 1/r$ is the reciprocal probability of a particle to escape from the divertor. Φ_{div} is the measured flux out of the probe while Φ_{SOL} is determined from the deposition probe measurement using equation 5.7, taking only the outboard surface area of the plasma since there should be no flux across the stagnation points at the top and the bottom of the plasma column. Thereby, the value $R = 17$ is obtained. This means that $r = 1/R \approx 6$ % of the injected tungsten actually reaches the SOL in the mainchamber. The product $rp \approx 3 \cdot 10^{-3}$, i.e. the total probability of a particle originating from the divertor to reach the confined plasma is in good agreement with investigations during the tungsten divertor experiment. There a value of $rp = 2 \cdot 10^{-3}$ could be extracted [77, 234] and a linear dependence between the eroded W in the divertor and the W measured on midplane deposition probes was experimentally observed [95].

5.2 Central Impurity Transport

Once the impurities have crossed the separatrix towards the plasma core the problem of impurity transport gets essentially one dimensional and only the *radial* transport has to be considered further. The impurity transport depends on the plasma parameters and may influence them through the power loss by impurity radiation. In extreme cases, as they can be observed especially for high-Z impurities, this in turn can lead to a non-linear behaviour as described later (see Sec. 6.2.5). A short introduction to the *radial* transport equation in the plasma bulk and the definition of the transport parameters that have been used, will be given below.

5.2.1 Ionisation Equilibria

Neglecting plasma transport, the ionisation equilibrium in the core of a fusion plasma is usually well described by the coronal approximation due to the high temperatures and the rather low densities involved. There, the total ionisation rate is dominated by direct electron ionisation

$$X^{Z+} + e \longrightarrow X^{(Z+1)+} + 2e \tag{5.11}$$

and contributions from autoionisation of inner shell excited states

$$X^{(Z+)**} \longrightarrow X^{(Z+1)+*} + e. \tag{5.12}$$

The rate coefficient for direct ionisation S_{DI} is usually calculated by integration of the semiempirical formula given by Lotz [211,235], whereas the rate coefficient for excitation-autoionisation S_{EA} depends critically on the individual configuration of the ion which has to be assessed specifically (see Chap. 4).
The total recombination rate is mainly given by radiative recombination

$$X^{Z+} + e \longrightarrow X^{(Z-1)+*} + h\nu \tag{5.13}$$

which is most important for highly charged ions with only few electrons remaining. It can be calculated following [236]. In the process of dielectronic recombination,

$$X^{Z+} + e \longrightarrow X^{(Z-1)+**} + h\nu \tag{5.14}$$

the energy of the electron is transfered to the recombining ion leading to double excitation, which is stabilised by a radiative transition. Usually, the stabilisation process is more likely than the autoionisation process for highly charged ions, since the relaxation rates increase with Z^4. An approximation formula to calculate the rate coefficients is given in [24, 236]. Their calculation is complicated by the fact that they are density depended because de-excitation by electron collision has to be considered. Due to the high actual importance of W in fusion plasmas all the necessary rates are presently revisited

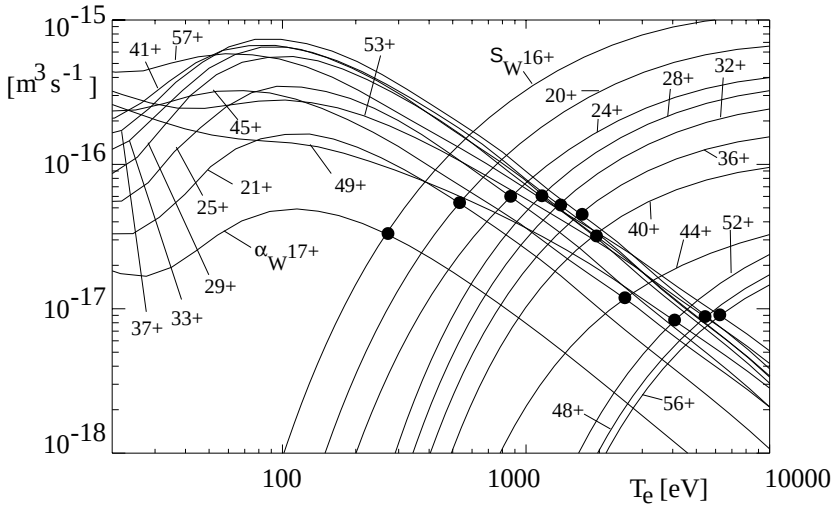

Figure 5.7: Ionisation rates and recombination rates for W from [238] (even charge states: ionisation, odd charge states: recombination)

and recalculated [237] within the framework of the ADAS database [215].
Summarising, the coronal equilibrium can be written as a set of Z equations of the form:

$$\frac{d}{dt}n_Z = n_e(n_{Z-1}S_{Z-1} + n_{Z+1}\alpha_{Z+1} - n_Z S_Z + n_Z\alpha_Z) \tag{5.15}$$

where S_Z denote the total rate coefficients for ionisation and α_Z the ones for recombination. In steady state this simply reduces to

$$\frac{n_Z}{n_{Z+1}} = \frac{S_{Z-1}}{\alpha_Z}. \tag{5.16}$$

Figure 5.7 shows the rate coefficients for ionisation and recombination of W without taking into account excitation autoionisation [238].

5.2.2 Formal Description of Radial Transport

Inside the separatrix, the law of particle conservation for the total impurity density n_I of all ionised stages (neglecting ionisation and recombination to neutrals) can be integrated over the volume V inside a flux surface which leads to

$$\frac{\partial}{\partial t}\int n_I dV = -\oint \mathbf{\Gamma} d\mathbf{S} = -\oint \Gamma^\rho \frac{dS}{|\nabla\rho|} \tag{5.17}$$

where ρ is a flux surface label and Γ^ρ is the *radial* contravariant component of the particle flux density $\Gamma^\rho = \mathbf{\Gamma}\nabla\rho$. Using the flux surface average (following [239])

$$\langle A\rangle = \left(\frac{\partial V}{\partial\rho}\right)^{-1}\oint A\frac{dS}{|\nabla\rho|} \tag{5.18}$$

and

$$\int n_I dV = \int_0^\rho d\rho \frac{\partial V}{\partial \rho} \langle n_I \rangle \tag{5.19}$$

the continuity equation 5.17 can be differentiated with respect to ρ.

$$\frac{\partial \langle n_I \rangle}{\partial t} = -\Big(\frac{\partial V}{\partial \rho}\Big)^{-1} \frac{\partial}{\partial \rho}\Big(\frac{\partial V}{\partial \rho}\langle \Gamma^\rho \rangle\Big) \tag{5.20}$$

The impurity density is assumed to be constant on a flux surface $\langle n_I \rangle = n_I$ and for $\mathbf{\Gamma}$ an ansatz with a diffusive and a convective part is used.

$$\mathbf{\Gamma} = -D\nabla n_I + v n_I \tag{5.21}$$

$$\langle \Gamma^\rho \rangle = -\langle D|\nabla\rho|^2\rangle \frac{\partial n_I}{\partial \rho} + \langle v|\nabla\rho|\rangle n_I \tag{5.22}$$

By using the flux surface label $r = \sqrt{V/(2\pi^2 R_0)}$ (R_0 is the major radius of the magnetic axis) equations 5.20 and 5.22 yield the radial transport equation that looks similar to the more familiar equation in cylindrical geometry.

$$\frac{\partial n_I}{\partial t} = \frac{1}{r}\frac{\partial}{\partial r} r\Big(D^* \frac{\partial n_I}{\partial r} - v^* n_I\Big) \tag{5.23}$$

with $D^* = \langle D|\nabla r|^2\rangle$ and $v^* = \langle v|\nabla r|\rangle$. In the centre the flux surface averages of ∇r are close to 1. In the following, D^* and v^* will be determined from the measurements. These quantities include the geometry factors and depend on the choice of the flux surface label which in our case is r. The superscript $*$ will be omitted from now on. For charge state resolved transport calculation as they are necessary for the interpretation of spectroscopic measurements, Z coupled equations of the form 5.23 have to be solved taking the sources and sinks from ionisation and recombination from the neighbouring charge states into account. This is done numerically using the transport code STRAHL [240, 241].

5.2.3 Neoclassical Transport

In the neoclassical transport theory the transport parameters are calculated from binary collisions of different species of particles existent in the plasma. The theory is summarised in [242] as well as in [243, 244]. The neoclassical transport parameters are the sum of a classical (CL), a Pfirsch-Schlüter (PS) and a banana-plateau (BP) term.

The classical diffusion coefficient and drift velocity result from displacements during the gyro-motion (with gyro-radius r_L) of the particles. They are given by

$$D^{CL} = \frac{1}{(\partial\Psi/\partial r)^2}\Big\langle \frac{R^2 B_p^2}{B^2}\Big\rangle \quad \frac{m_I k T \nu_{ID}}{e^2 Z^2} \tag{5.24}$$

$$v^{CL} = D^{CL} Z\Big[\frac{d\ln n_D}{dr} - \frac{1}{2}\frac{d\ln T}{dr}\Big] \tag{5.25}$$

Here Ψ is the poloidal magnetic flux, B_p is the poloidal magnetic field and ν_{ID} is the binary collision frequency of impurity and main ion. The brackets $\langle\rangle$ denote a flux surface average as defined in equation 5.18. The product of the first two terms in equation 5.24 reduces to $1/B_0^2$ for the large aspect ratio circular cross section case (B_0 is the vacuum toroidal field on axis).

In a toroidal device (with a radial gradient of the magnetic field) there exist particles which are trapped on so called banana orbits (see Fig. 5.8). These particles are reflected at some radius larger than the inner plasma boundary if for their parallel velocity $v_\parallel$ the mirror condition holds:

$$|v_\parallel| < |v_\perp|\sqrt{2\varepsilon}, \tag{5.26}$$

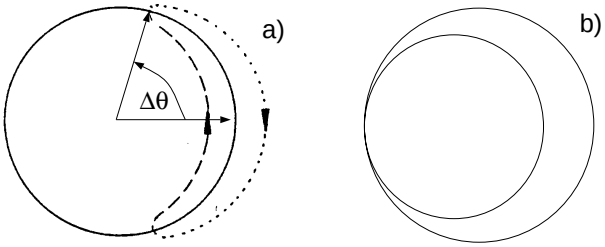

Figure 5.8: Projections of banana orbits in the poloidal plane. $\Delta\theta$ gives the poloidal angle of the reflection point (a). Particles which are reflected only at the inner plasma radius show the maximum banana width (b).

with $v_\perp$ denoting the perpendicular velocity and $\varepsilon = r/R$, (r: small radius, R: large radius) the inverse aspect ratio of the device. The maximum width w_B of the bananas can be estimated to

$$w_B \approx r_L \frac{q}{\sqrt{\varepsilon}} \tag{5.27}$$

(q: safety factor) indicating a much larger transport than the classical one. In a detailed derivation the collision frequency during the banana motion (collisionality ν^*) has to be considered. For $\nu^* > 1$ the particles undergo many collisions during a banana-orbit, here one gets the so called Pfirsch-Schlüter coefficients:

$$\begin{aligned} D^{PS} &= \frac{\langle RB_T\rangle^2}{(\partial\Psi/\partial r)^2}(\langle B^{-2}\rangle - \langle B^2\rangle^{-1}) \\ &\times \quad K^{PS}\ \frac{m_I k T \nu_{ID}}{e^2 Z^2} \end{aligned} \tag{5.28}$$

$$v^{PS} = D^{PS} Z\Big[\frac{d\ln n_D}{dr} + \frac{H^{PS}}{K^{PS}}\frac{d\ln T}{dr}\Big] \tag{5.29}$$

where the term in the first row reduces to $2q^2/B_0^2$ in the case of large aspect ratio and circular geometry. The factors K^{PS} and H^{PS} are functions of the impurity strength parameter $\alpha = n_I Z_I^2/n_D$ and the main ion collisionality $\nu_D^* = \nu_D R_0 q/(v_{th}\varepsilon^{3/2})$.

$$\begin{aligned} K^{PS} &= 1 - \frac{0.52\alpha}{0.59 + \alpha + 1.34(\varepsilon^{3/2}\nu_D^*)^{-2}} \\ H^{PS} &= -\frac{1}{2} + \frac{0.29 + 0.68\alpha}{0.59 + \alpha + 1.34(\varepsilon^{3/2}\nu_D^*)^{-2}} \end{aligned} \tag{5.30}$$

For $\nu^* \leq 1$ the collision frequency is in the order of the frequency for the banana orbits or much smaller, here the transport is dominated by the banana-plateau coefficients, which are

$$D^{BP} = \frac{\langle RB_T \rangle^2}{(\partial\Psi/\partial r)^2 \langle B^2 \rangle} \frac{kT\mu^*_{ID}}{e^2 Z^2 n_I} \tag{5.31}$$

$$v^{BP} = D^{BP} Z \Big[\frac{d \ln n_D}{dr} + H^{BP} \frac{d \ln T}{dr} \Big] \tag{5.32}$$

where the term with the flux surface averages reduces to $q^2/(\varepsilon^2 B_0^2)$ in the case of large aspect ratio and circular geometry (ε is the inverse aspect ratio). μ^*_{ID} is the weighted viscosity coefficient μ_{00} of impurity and main ion.

$$\mu^*_{ID} = \frac{m_D n_D \mu_{D00} \cdot m_I n_I \mu_{I00}}{m_D n_D \mu_{D00} + m_I n_I \mu_{I00}} \tag{5.33}$$

The factor H^{BP} in the drift term is connected to the ratio of the viscosity coefficients μ_{01}/μ_{00} of impurity and main ion.

$$H^{BP} = (1 - \frac{\mu_{D01}}{\mu_{D00}}) - \frac{1}{Z}(1 - \frac{\mu_{I01}}{\mu_{I00}}) \tag{5.34}$$

The viscosity coefficients were calculated using the expressions given by Kim [245]. For the poloidal plasma cross section of ASDEX Upgrade with elongation $\kappa = 1.6$ and average triangularity $\delta = 0.2$ the ratios of the true geometry factor and the large aspect ratio circular geometry approximation are 1.1/1.3 at ρ_{pol} =0.3/0.9 for the CL term, 0.75/0.42 for the PS term, and 0.75/0.44 for the BP term [246]. In addition to these analytical approximations which are directly implemented in STRAHL, the neoclassical code package NEOART [247] can also be coupled to STRAHL [246]. There, the neoclassical transport coefficients are calculated numerically by solving the set of linear coupled equations for the parallel velocities in arbitrary toroidally symmetric geometry for all collision regimes in a reduced charge state formalism. The equations for the banana plateau contribution are equal to that used by Houlberg [248]. The Pfirsch-Schlüter contribution is calculated from the coupled equations (6.1-2) and (6.14-15) of Hirshman and Sigmar [242], as described in Ref. [247]. The package allows the simultaneous consideration of multiple impurities species, which is important for high impurity densities exceeding the trace limit [249].

In both approaches (analytical and numerical) toroidal rotation of the plasma is not taken into account and equal temperatures of main ion D and impurity I ($T_D = T_I = T$) are assumed. A comparison of both methods for an Ar test-case revealed that the Pfirsch-Schlüter contributions agree very well, whereas differences are observed for D^{BP} due to an improved calculation of the viscosity coefficients in NEOART [246].

5.2.4 Anomalous Transport

Anomalous transport is attributed to electrostatic and magnetic fluctuations. They can lead to drift-waves or to a stochastisation of the magnetic flux surfaces by error currents, respectively. For the central plasma there exist several theory based models which predict the heat transport for given boundary conditions. Most of them are based on ion temperature gradient (ITG) and trapped electron mode (TEM) physics: the IFS/PPPL [250], Weiland [251] and GLF23 [252] models. The IFS/PPPL and the Weiland model reproduce qualitatively and quantitatively the experimental ion temperature profiles of ASDEX Upgrade as demonstrated by Tardini et al. [253]. Common to these models is a critical value for the gradient length $L_{T_{cr}} = |T_i/\nabla T_i|_{cr}$ below which the transport strongly increases with $1/L_{T_i}$. As a consequence, the $\nabla T_i/T_i$ profile tends to stay very close to a critical profile (profile stiffness). Using an ad hoc model, where the particle transport reacts similarly to the energy transport ($D \sim \chi$) [254, 255] a good description of the background density profiles and their temporal evolution was possible. For discharge scenarios where the critical temperature gradient is not reached, this has the consequence that the particle transport behaves almost neoclassically. On the other hand, it is also possible to enhance the particle transport by increased local heating and to prevent the plasma from neoclassical accumulation effects as will be described in Sec. 6.2.5. Experiments in ASDEX Upgrade (see below) did not indicate that there is a Z dependence of the anomalous transport and following [244] there are also theoretical arguments which support the independence from Z. Macroscopic instabilities as the central sawtooth events [256] or edge localised modes (ELMs) [257] effectively increase the anomalous transport [246, 258].

5.2.5 Consequences of Mixed Transport

In [193, 259] the (low-Z) impurity transport was measured in ASDEX Upgrade using charge exchange spectroscopy measurements following He and Ne puffs. In these investigations the transport coefficients were time averaged over sawteeth and very similar central diffusion coefficients ($D = 0.3 - 0.6$ m^{2}s^{-1}) for both species could be extracted in H-modes as well as in L-modes, showing a parameter dependence very similar to that of the energy transport. The Z-dependence of the impurity-transport was studied by puffing trace amounts of noble gases Ne, Ar, Kr, Xe in virtually identical plasmas [246]. There, the transport coefficients of the different impurity species were deduced from the temporal evolution of the impurity density profiles in-between sawtooth crashes. The impurity density profiles were calculated from the emissivity profiles of the soft X-ray radiation yielding a very good temporal and spatial resolution. Figure 5.9 compares the deduced central transport parameters with the neoclassical predictions. For Ne and Ar there is good agreement between neoclassical theory and experiment,

but for the species with higher Z, both the experimental values of D and v are larger than the neoclassical ones. However, the discrepancies are less pronounced in the case of v/D the value of which gives the shape of the impurity density profile (see below).

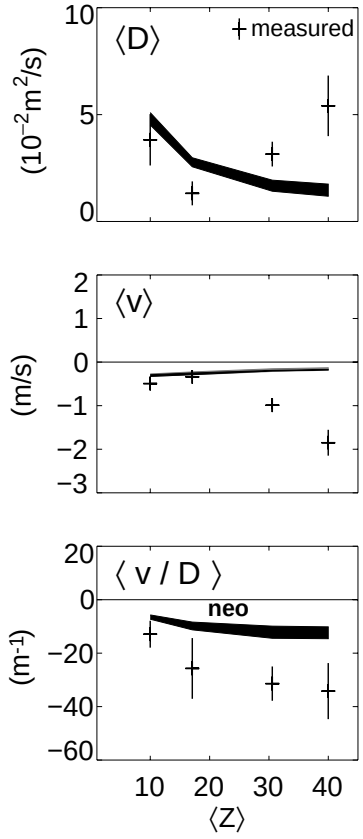

Figure 5.9: Measured central transport parameters together with the neoclassical predictions (line averaged over $0.1 < \rho_{pol} < 0.3$) as a function of the mean atomic charge [246]. The bands represent calculation with/without contributions from collisions with C and 0 also present in the background plasma.

The deviations may be caused by the strong rotation observed in the plasma. Assuming equal toroidal speed for impurities, toroidal Mach numbers $M_{tor} = v_{tor}/v_{th} > 2$ are deduced for Xe. These high velocities cause a poloidal gradient of the impurity density due to the centrifugal force, which are not included in the neoclassical treatment as described above.

Under steady state conditions the transport equation (eq. 5.23) leads, in the source free region, to

$$\frac{1}{n_I^{eq}}\frac{dn_I^{eq}}{dr} = \frac{d\ln n_I^{eq}}{dr} = \frac{v}{D}. \tag{5.35}$$

Guided by the experiments described above one can assume for the diffusion coefficient $D = D_{an} + D_{neo} = D_{an} + D^{CL} + D^{PS} + D^{BP}$ and for the convective contribution $v = v_{neo} = v^{CL} + v^{PS} + v^{BP}$. Considering only collisions of impurity and main ions, one gets

$$\frac{d\ln n_I^{eq}}{dr} = \frac{d\ln n_D}{dr}\frac{Z_I}{Z_D}\frac{D_{neo}}{D_{neo}+D_{an}}\Big(1 - H\eta_D\Big) \tag{5.36}$$

for the normalised impurity density gradient in a hydrogen plasma, where Z_I is the charges of the impurity ions and $H \approx 0.2 - 0.5$ is a sum of all the coefficients in eqs. 5.25,5.29,5.32 and represents the so called impurity screening, which depends on the collisional regime, as discussed above. $\eta_D = (\frac{d\ln n_D}{dr})/(\frac{d\ln T_D}{dr})$ is the ratio of the normalised temperature gradient to the normalised density gradient of the background ions. From these equations one can easily see that a necessary ingredient for impurity accumulation is a density gradient (density peaking) of the main ions. This gradient is amplified by $\frac{Z_I}{Z_D}$, pointing out that high-Z impurities are more prone to central accumulation: Typically, low-Z elements are fully ionised in the centre of fusion plasmas yielding $Z_C = 6$ or $Z_O = 8$ for carbon or oxygen, respectively. W exists in charge states around 40-50 in ASDEX Upgrade plasmas and will be $Z_W \approx 70$ in a burning plasma. The impurity gradient is diminished through the anomalous diffusion and the term in parenthesis. This term appears critical because it may vary from small positive numbers to small negative numbers: typically the

normalised temperature gradient is significantly larger than the density gradient in the confinement region and hence the product $H\eta_D$ is in the order of one.
Density peaking of the background plasma due to an anomalous inward pinch (not considered here) would not be a concern for impurity accumulation as long as $D_{an}(\not{Z}) \gg D_{neo}$ and $v_{an} = v_{an}(\not{Z})$. In such a case the peaking of the density profiles given by v/D would be almost independent of Z and consequently the impurity concentrations would be constant over the plasma radius.

6. Tungsten-Experiments at ASDEX Upgrade

Since 1993 a tungsten programme has been run at ASDEX Upgrade, leading to the installation of a complete W divertor in 1995 followed by one year of operation. From 1998 onwards an increasing area of tungsten coated tiles has been installed at the central column of ASDEX Upgrade, reaching an area of 7.1 m^2 in 2001/2002 representing about 85% of the total area of the central column. The programme comprises not only the operation with large area W coatings but also the qualification and testing of the coated tiles, W erosion and migration investigations, development of spectroscopic diagnostics and interpretation of the observed W behaviour by impurity transport calculations. The stages of the W programme in ASDEX Upgrade are summarised in Table 6.1 and details of the investigations will be presented in the forthcoming sections.

6.1 The W Divertor Experiment

During the experimental campaign 1995/1996 a tungsten divertor was installed in ASDEX Upgrade. It was the first time that W was used as a plasma facing component

location	campaign	coating	remark	references
divertor	1993/1994	PVD, massive W	markers, inlays	[92, 260]
	1994/1995	VPS, 0.1-0.5 mm	test tiles	[261]
	1995/1996	VPS, 0.5 mm	W divertor experiment	[77, 234, 262, 263]
	1997	installation and exploitation of CFC- Divertor II		
	1998	first siliconisation in ASDEX Upgrade		[12, 264]
central column	1998/1999	PVD, 8 nm	test tiles	[265]
	1999/2000	PVD, 0.5 - 1.5 μm	PHASE I, 2 rows, 1.2 m^2	[96, 264, 266]
	2001	arc-dep. 1 μm	PHASE II, $\approx$ 10 rows, 5.5 m^2	[267, 268]
	2001/2002	arc-dep. 1 μm	PHASE III, startup lim., 7.1 m^2	[61, 269]

Table 6.1: Stages of the tungsten programme at ASDEX Upgrade. In 1996/1997 Divertor I was replaced by the closed Divertor II with optimised power load and pumping characteristics. Siliconisation was performed as a pre-experiment to the W coating of the central column. (PVD: physical vapour deposition, VPS: vacuum plasma spray)

under reactor relevant plasma conditions.

6.1.1 The tungsten coating

The tungsten-coated divertor in ASDEX Upgrade consisted of a toroidal belt of tungsten tiles on the inner and outer target plate at the position of the strike zone (Fig. 6.1). There were only a few graphite tiles left for Langmuir probes and thermography, representing less then 10% of the total area. Figure 6.2a shows the poloidal cross section of the divertor region in Divertor I (DIV I) configuration and Fig. 6.2b a perpendicular view of one of the divertor segments. In the toroidal direction the tiles were slightly tilted to achieve shadowed edges. The tiles consist of a fine-grain graphite substrate coated by vacuum plasma spray (VPS) with a 0.5 mm thick layer of tungsten. A 20 μm W/Re-multilayer prevented the formation of carbides within the main tungsten layer and thus inhibited its embrittlement. Prototypes of the tiles were extensively tested by electron and ion beam irradiation. Both the structure of the coatings and the tests of the tungsten tiles were described in detail in [261]. As a consequence of these tests the time averaged heat load on the tiles was initially limited to 7 $\mathrm{MWm^{-2}}$.

Figure 6.1: The tungsten divertor in ASDEX Upgrade. The tungsten coated tiles were mounted on a toroidal ring at the outer and the inner strike zones of Divertor I (DIV I). They are clearly visible as light grey rings.

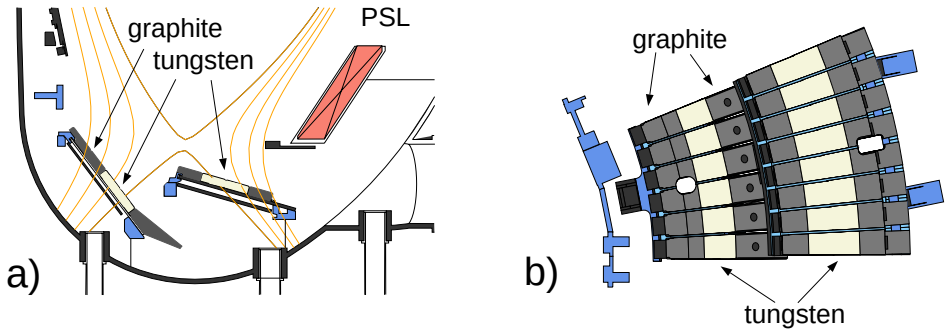

Figure 6.2: Schematic view of the tungsten divertor: a) poloidal cross section of the divertor region, b) perpendicular view on one section of the divertor (1/16 of the circumference). Only the target plates at the strike point regions were covered with tungsten.

6.1.2 Tungsten sputtering and influx

The tungsten flux in the divertor was monitored spectroscopically by the W I line at 400.8 nm using the BLS spectrometer-system (see Sec. 3.1.1) viewing almost perpendicularly onto the target plates [99]. The strike zones on the outer and inner target plates can be scanned several times during a discharge, which allows the spatial profile across the target plates to be recorded .

The evaluation of the gross tungsten influx was performed using the S/XB-values as described in Sec. 4.1. The local plasma parameters were evaluated from flush mounted target Langmuir probes [270], which were located at different radial positions in the target plates (see Fig. 6.1). These measurements were complemented by thermographic measurements using a sheath transmission factor of 7. The divertor plasma temperatures ranged from below 2 eV up to 60 eV. During an ELM the electron temperature and the particle flux to the target plates can be much higher, however due to the low duty cycle their influence on the time averaged emission should be low. Figure 6.3 shows typical time traces of various plasma parameters during an ohmically heated discharge. As the plasma current is increased to 800 kA the line averaged electron density in the main plasma is also raised to the pre-programmed value of $2.5{\cdot}10^{19}$ m^{-3}. In the third row the power load onto the outer divertor target plate from thermography is shown. Furthermore, the deflection angle of the boundary layer spectrometer is overlayed with the strike point calculated from magnetic reconstruction. As the line of sight scans over the position of the strikepoint the tungsten emission is observed as shown in the next row. The bottom trace shows the electron temperature derived from Langmuir probes close to the strikepoint. The figure demonstrates that during the first phase of the discharge (1-1.5 s), the W I is significantly higher due to the much higher energy of the impacting plasma particles. At later times in the discharge the temperature drops from 60 eV to about 20 eV but the higher particle influx to the target plates still yields a measurable tungsten erosion. These time traces already reflect the influence of the

temperature and particle flux to the erosion of tungsten. The particle flux to the target plates in the divertor shows a strong variation over the radial position. It is very low in the private flux region (PFR, the region inside the separatrix in the divertor) but rises rapidly at the strike point and decays in the plasma boundary. The resulting profile of the erosion could be determined by spatially resolved measurements of the tungsten emission. Fig. 6.4 demonstrates the mapping of the time traces in Fig. 6.3 to a profile of the W I line emission at the outer target in a steady state phase of the discharge. The tungsten emission profile is overlayed with the electron temperature and the particle flux to the target plates which are derived from the data of the Langmuir probes. As one can see, the tungsten emission drops rapidly at the edge of the tungsten tiles, and there is no large radial migration of the tungsten atoms which would also cause a W I signal on the carbon tiles. As an interesting feature one can see two distinct maxima in the tungsten emission profile. This can be explained by the overlaid flux parameters. The maximum close to the strikepoint is caused by the electron temperature, while the right hand maximum is due to the maximum of the particle flux. In general the tungsten emission profile reflects the radial flux and temperature variation in the divertor. The results of probe erosion measurements show a radial erosion pattern which correlates with the particle flux [94]. Figure 6.5 shows the variation of the spatial profile under different plasma conditions. The neutral beam heating power was 5 and 7.5 MW, respectively. During the ohmic phase of the discharge there is only low erosion of tungsten, which is localised in the scrape off layer. With additional heating the power load on the target plates rises strongly, and the strike point moves inward as a result of the plasma position control reacting on the higher plasma pressure. This is reflected in the profiles of the W I emission by a significant increase of the intensity and a shift of the emission maximum by the same quantity as the strike

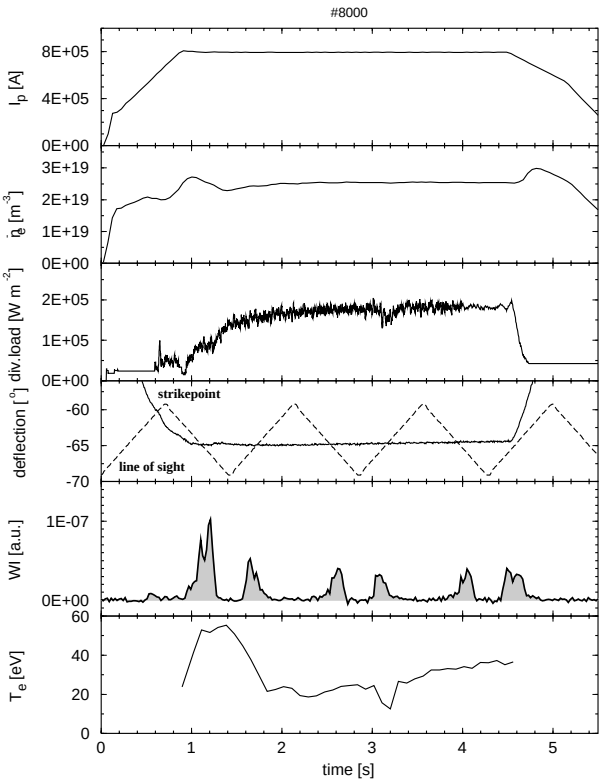

Figure 6.3: Typical time traces for an ohmic plasma discharge, showing from top to bottom [99]: plasma current (I_p), line averaged electron density ($\bar{n}_e$) in the midplane, power load on the target plates, strikepoint and observation position, W I brightness, electron temperature (T_e) close to the strikepoint. W I emission is detected as the spatial scan crosses the strikepoint position.

point. The erosion signals in the ohmic phase before and after the NBI-heating are identical, which leads to the conclusion, that the sputtering is caused by the flux and not changed by the surface temperature, which increases from 310 K during the first ohmic phase of the discharge to 480 K at the end of the discharge.

The dependence of the tungsten influx on the plasma temperature can easily be observed in a density limit discharge. As the plasma density is raised, the temperature of the divertor plasma drops dramatically and ends up in the detachment of the plasma where the divertor plasma is cooler than 2 eV. The W I emission follows this trend and starts in the beginning transient phase at a high intensity which drops continuously below the detection limit as the detachment begins.

This behaviour is also found in an evaluation over a series of plasma discharges with very different divertor plasma conditions. While the observed W I intensity maximum rises exponentially for temperatures up to 25 eV, it decreases for higher electron temperatures. The drop with higher temperature reflects the operational limitation of the maximum power flux on the targets. This means that it is not possible to maintain high divertor plasma temperatures at very high deuterium fluxes. Of course, the temperature and the flux can reach very high values during an ELM, but as mentioned already in Sec. 3.1.1, all measurements were interpreted in a time averaged manner because the W I emission could not be monitored sufficiently fast. Looking at the tungsten influx versus deuterium/hydrogen flux under steady state plasma conditions one can see a linear dependence, which holds for two orders of magnitude for constant divertor electron

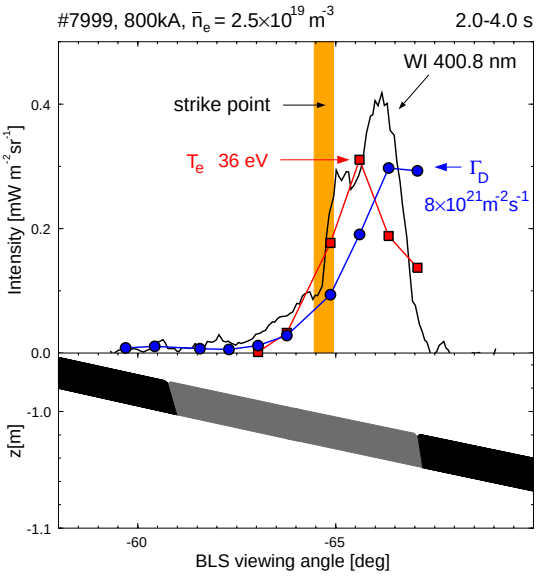

Figure 6.4: Spatial profiles of the W I brightness, the electron temperature (T_e) and the particle flux (Γ_D) to the outer target plate [99].

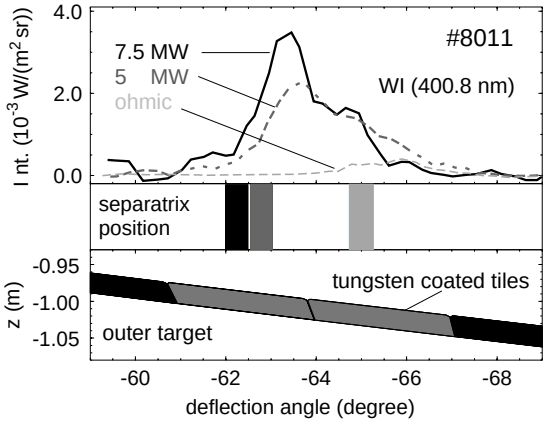

Figure 6.5: Tungsten erosion profiles at the outer target plate at different additional heating powers (P_{NBI}). With increasing power load the W I emission rises and shifts by the same amount as the strikepoint moves inward.

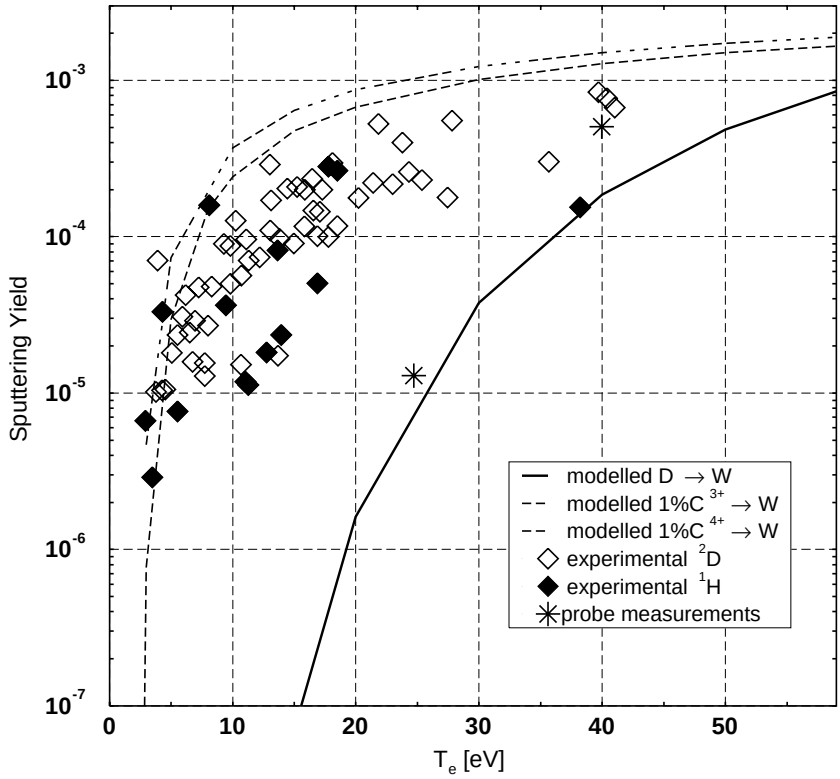

Figure 6.6: Measured effective sputtering yield of tungsten [99]. The W erosion is derived from the spectroscopic measurements of W I and the deuterium/hydrogen flux from thermographic and Langmuir probe measurements. The lines represent results from calculations assuming different carbon impurity charge states and the expected sputtering yield for pure deuterium sputtering [94]. There are also two points of net erosion from probe measurements (asterisks) [93,94], from which the prompt re-deposition fraction of tungsten can be evaluated.

temperatures. The plasma typically contains about 0.5 to 2 % of carbon for all different operational regimes. Normalising the tungsten influx by the hydrogen/deuterium influx gives the temperature dependent sputtering yield. Figure 6.6 shows the results for very different divertor plasma conditions. About 60% of the shown points are measured in H-mode. The discharges in hydrogen do not vary significantly from the deuterium discharges. The lines in Fig. 6.6 represent the results from TRIM sputtering simulations, based on ion beam measurements and taking into account the energy and angular distribution of an isotropic Maxwellian distribution accelerated in the sheath potential [94, 100]. Comparison of the modelled data for a pure deuterium plasma with the experimental results shows a significantly higher erosion of tungsten than would be expected for pure deuterium sputtering. Simulations are also done for plasmas with 1% C^{+3} or 1% C^{+4}. These ionisation states can be found in the shown temperature range. As already discussed in Sec. 2.4.3, the higher mass of carbon leads to a higher sputtering yield and the carbon ions also gain additional impact energy

in the range of $E_{C^{+z},acc} \approx Z \cdot 3kT_e$ in the sheath potential of $\approx 3kT_e$. The simulations containing carbon are in much better agreement with the experimental data. The low temperature onset of the sputtering yield is shifted to temperatures below 5 eV. The lowering of the threshold temperature has also been found for molybdenum target plates during argon puffing [271]. In summary the experimental results can be modelled by a divertor plasma with about 1% charged light impurities which leads to the conclusion that the sputtering of tungsten is clearly dominated by the plasma impurities. Recent investigations [77,272] showed an even better agreement with the experimental data by taking into account deposition of carbon out of the plasma.

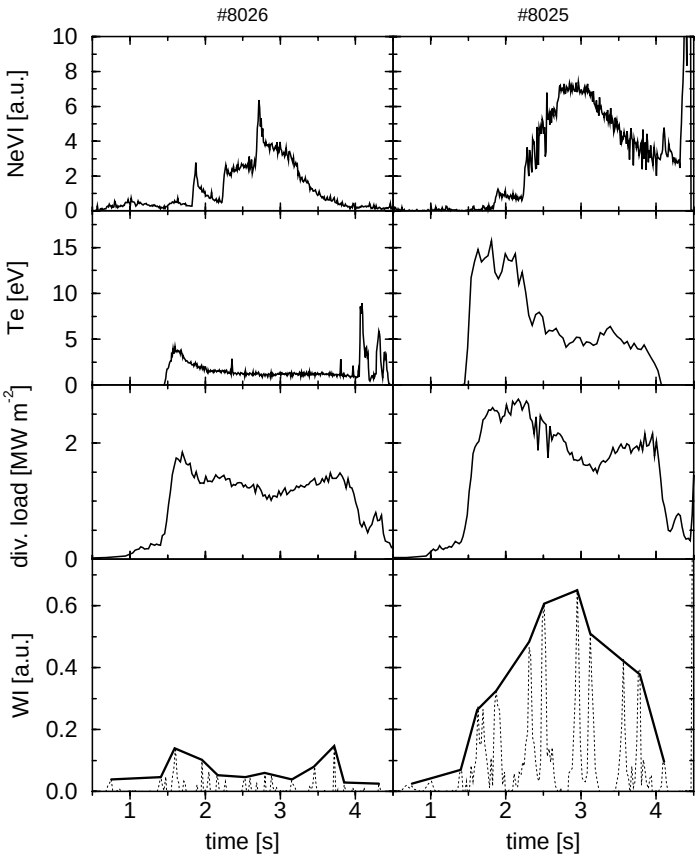

Figure 6.7: Attached ELMy H-mode plasma discharges ($I_P = 1$ MA, $B_t = -2.5$ T, $P_{NBI} = 7.5$ MW) with Neon puffs. #8026 ($\bar{n}_e = 9{\cdot}10^{19}$ m^{-3}) represents a typical discharge with a low electron temperature in the divertor whereas in #8025 ($\bar{n}_e = 8 \cdot 10^{19}$ m^{-3}) the divertor electron temperature remains above 5 eV during the neon puff.

The injection of additional impurities into the plasma has two effects on the sputtering yield. On the one hand increased radiative losses lead to lower electron temperatures and thus to much lower sputtering yields. On the other hand the additional fraction of impurities with a higher net charge and a higher mass, causes erosion with higher impact energies and leads to lower sputtering thresholds. In ASDEX Upgrade neon is usually injected in radiative cooling scenarios. For example, figure 6.7 shows the measurements of two different attached discharges with neon puffs in the main chamber. The Ne VI signal in the midplane gives an estimate of the time dependence of the neon concentration in the edge. One discharge (#8026) shows a low divertor electron temperature, in the other (#8025) the neon gas puff did not lower the electron temperature below 5 eV, because the initial edge electron density was not high enough to yield sufficient radiation cooling. In the cold divertor plasma of discharge #8026 the additional neon concentration did

not lead to a tungsten influx above the detection limit. In contrast to this observation the time dependence of the tungsten influx of discharge #8025 clearly follows the time dependence of the Ne VI emission. The tungsten erosion increases with the additional neon despite the drop in temperature and divertor power load. This leads to the conclusion that the increased erosion is caused by the additional neon. These observations are consistent with the rapid drop of the sputtering yield of tungsten impacted by Ne^{+3}, which reaches a value of $2 \cdot 10^{-1}$ for plasma temperatures above 20 eV and less than 10^{-4} below 4 eV [92]. Similar behaviour, but to a far smaller extent, is also found in limiter experiments with additional neon puffs [273,274] (see Sec. 7.1.2). In typical neon puff experiments at ASDEX Upgrade the effect of the lowered temperature by radiative loss dominates by far the more effective erosion by additional impurities, so that the W I signal typically vanishes. In detached plasmas, like the CDH-mode [275], the W I emission drops below the background noise level.
Puffing helium into the discharge has no measurable effect on the tungsten erosion because the carbon ions still dominate the sputtering. Even if the complete plasma gas is helium, there is no major increase of the sputtering yield compared with similar deuterium discharges.
As neutral tungsten atoms are released from the surface they will be ionised by the divertor plasma. The ionised tungsten atoms are exposed to the electric field in the sheath potential and perform a gyration in the local magnetic field and they may undergo prompt re-deposition, as discussed in Sec. 5.1.1. Additionally to the spectroscopically

$T_{e,div}$ [eV]	$n_{e,div}$ [m^{-3}]	measured f_{red} [%]	$\frac{r_{ion}}{r_{gyro}}$ [92]	predicted f_{red} [%]
25	$1{\cdot}10^{20}$	≥ 95	0.05	≥ 95
40	$7{\cdot}10^{18}$	≈ 50	0.6	60

Table 6.2: Comparison of the measured and predicted re-deposition of tungsten. The predicted re-deposition fraction takes the electric field of the sheath potential into account [92].

measured yield for the tungsten erosion, Fig. 6.6 shows results for the net erosion. It is determined by measuring the tungsten loss from probes [93, 94], which were inserted into selected plasma discharges. As expected, the determined net sputtering yield lies below the overall tungsten erosion. The difference in this quantity can be interpreted as prompt re-deposition. For the high temperature point at 40 eV the net erosion is about 50 % of the initially eroded tungsten. The prompt re-deposition at lower temperatures is at least 95%. This temperature dependence can be explained by a rather simple argument. As already mentioned, the high divertor electron temperature ($T_{e,div}$) in steady state discharges can only be achieved at low electron densities. In this case the average electron density in the divertor ($n_{e,div}$) drops from $1{\cdot}10^{20}$ m^{-3} at 25 eV down

to $7{\cdot}10^{18}$ m^{-3} at 40 eV. This change in the electron density by more then one order of magnitude is reflected in the change of the ionisation length (r_{ion}). The temperature dependence of the ionisation rate is small. Therefore the ratio of ionisation length to the effective gyration radius (r_{gyro}) changes drastically. This leads to a significant loss in the re-deposition fraction (f_{red}) as illustrated in table 6.2.

Generally, prompt re-deposition in the order of 90% can be reached in divertor arrangements. Under conditions typical for limiter experiments, an increase of the prompt re-deposition with higher plasma densities is also found [276], but typical values are in the range of 50% [14]. As the plasma typically contains about 0.5 to 2 % carbon there is a continuous flux of carbon atoms to the tungsten target plates. The carbon increases the sputtering yield as shown previously, but it is simultaneously deposited on the tungsten tiles. Post mortem analyses of the divertor target tiles show [77,277] that on the inner tiles a layer of low-Z material (38% – 76% carbon) up to several μm is deposited, whereas at the more erosion dominated outer divertor tiles only small amounts of low-Z deposits (close to the initial ones) are found.

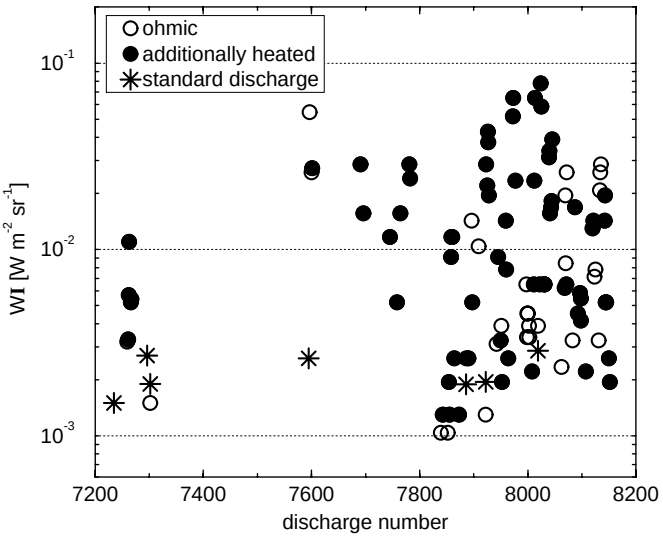

Figure 6.8: Long term observation of the W I emission in the outer divertor [99]. The tungsten erosion remains stable over the whole experimental campaign for comparable discharges (standard discharge: I_p=600 kA, n_e=$3{\cdot}10^{19}$ m^{-3}, ohmically heated).

This observation is reflected by a measurable carbon influx from the tungsten tiles. To obtain the chemical carbon erosion on the tungsten tiles the CD molecular band emission was measured. The carbon influx caused by chemical erosion is nearly identical for graphite and tungsten surfaces. Only at the strike point positions, the chemical erosion seems to be reduced by about 10 % for tungsten tiles. In a separate gas puff experiment in the divertor, it was verified that the CD emission is strongly (≤ 2 cm) localised to the CD_4 gas inlet. Furthermore, a new tungsten tile immediately showed CD emission as it was exposed to the divertor plasma for the first time. Similar instantaneous behaviour was found in metal limiter experiments, but the intensity of the CD emission from tungsten and molybdenum surfaces was reported to be one order of magnitude reduced [173, 278] in comparison to copper or stainless steel limiters [278]. This might be caused by the differences in limiter and divertor plasmas.

As figure 6.8 illustrates, the W I signal varied by two orders of magnitude for the different discharges. For comparable discharges (so called ohmic standard discharges) there is no change in the tungsten erosion at the outer divertor plate over a period of more then 500 plasma discharges. This can be explained by a constant carbon content in the scrape off layer for these comparable discharges. This long term stability of the tungsten erosion is in line with the post mortem analyses cited above and also shows that the carbon coverage is not reaching a value where the tile is completely coated with carbon. From the observation of a slightly reduced CD emission close to the strike point one can conclude that this zone is cleaned by the plasma fan itself.

6.1.3 Behaviour of tungsten in plasma discharges

The tungsten in the plasma centre was monitored mainly by the grazing incidence spectrometer observing the quasi-continuum at 5 nm emitted by ionisation states around W^{27+}, which was cross calibrated against the total radiated power following the procedure described in Sec. 4.2. Over 800 discharges with the tungsten divertor had been performed, about 400 of them with substantial auxiliary heating ($P_{aux} \geq 2$ MW). The discharges comprised almost the full operational space in regard to plasma current (0.6 MA $\leq I_P \leq$ 1.2 MA), density ($2 \cdot 10^{19}$ m$^{-3} \leq \bar{n}_e \leq 15 \cdot 10^{19}$ m^{-3}) and auxiliary heating power ($P_{aux} \leq 10$ MW). The power load on the target plates was deduced routinely from tile temperature measurements using a thermography camera [279]. The time-averaged power load reached up to 6 MWm^{-2} in a 7.5 MW neutral beam heated discharge. During ELMs the power load reached up to 20 MWm^{-2} in low density high power discharges.

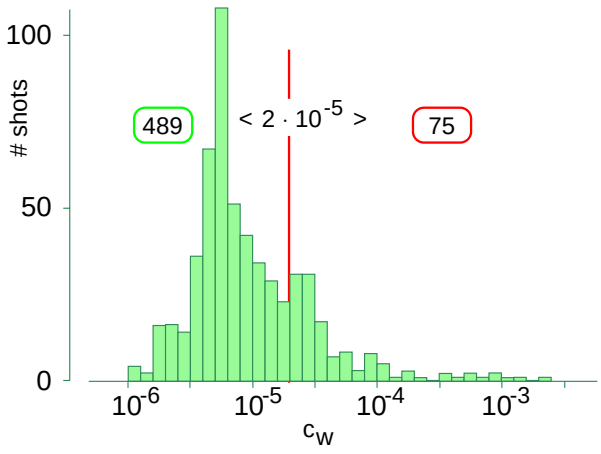

Figure 6.9: Frequency distribution of tungsten concentration (c_W) in H-mode discharges [263].

About 85% of all investigated plasmas show tungsten concentrations below $2 \cdot 10^{-5}$ (75% below $1 \cdot 10^{-5}$) [263] as demonstrated in Fig. 6.9. c_W almost never reached values which influenced the chosen discharge programme. Only in very few discharges with special parameters ('counter'-injection, low voltage of the neutral beam heating, improved confinement regimes after switch-off of NBI sources) c_W was higher and the radiation was sometimes strong enough to cause hollow T_e-profiles (see Sec. 6.1.4).

First analyses of the statistical behaviour of the tungsten concentration hinted at a decrease with heating power, similar to the well known power degradation of the con-

finement. However the high power discharges were preferentially run at higher densities leading to shorter ionisations lengths for W and therefore better shielding of the influx. On the other hand there was also no direct relation found between the W influx and central concentrations. This can be judged from Fig. 6.11, where W densities are plotted versus the effective W influx derived from W I line intensities and the adequate photon efficiency, corrected for the prompt re-deposition. The plasma regime is indicated by different symbols. Although a weak dependence of the concentration seems to exist, there are also large differences in the concentrations for identical normalised influxes indicating the strong influence of the W transport.

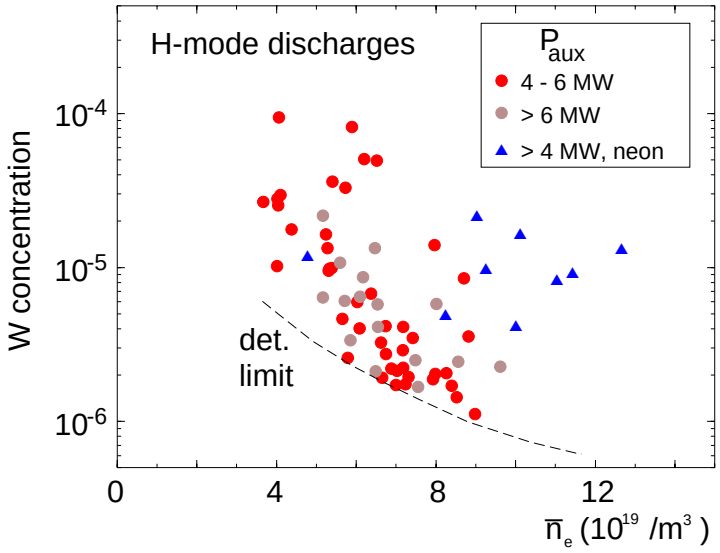

Figure 6.10: Tungsten concentration (c_W) in H-mode discharges deduced from the W quasi-continuum versus the line averaged density. The auxiliary heating power is marked by different colours and the triangles represent neon seeded discharges [263].

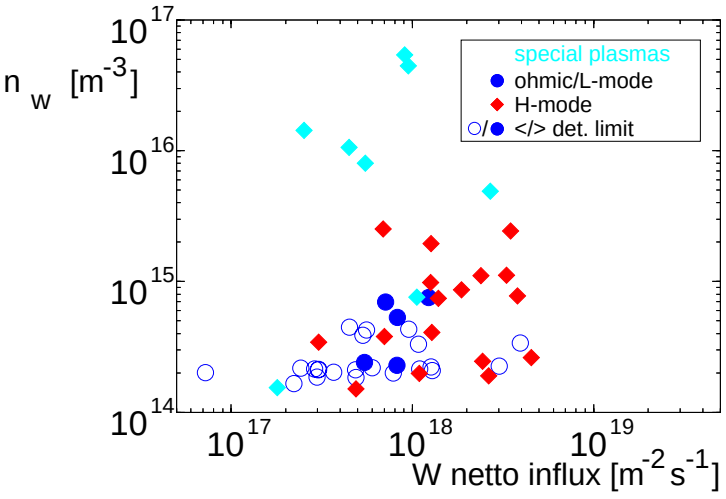

Figure 6.11: W densities n_W versus the effective tungsten influx Γ_W. The concentrations in ohmic and L-Mode discharges are shown as circles, H-mode discharges as diamonds. The light blue diamonds indicate exceptional discharge scenarios [263].

Recently, an elaborate statistical analysis on the behaviour of the W concentration of ELMy H-Mode discharges in the W divertor experiment has been performed [126]. In this investigation the influence of 19 different parameters on the W concentrations has been evaluated. Besides the standard method of 'multiple least squares' (MLS), principle component approximation (PCA) has been used. The latter method allows the errors of the dependent as well as of the independent data to be treated equally. In addition to global plasma parameters as the toroidal field or the plasma cur-

rent, local parameters as the W influx or the divertor electron temperatures were also incorporated. In both methods the same independent parameters showed a significant influence on the W concentration – in none of the analyses was a significant dependence on the W influx found. The best description of the experimental data within the PCA was achieved with the following scaling [126]:

$$c_W \sim Z_{eff}^{3.77\pm0.52} n_{Div}^{-2.23\pm0.32} B_t^{-3.46\pm0.70} \gamma_{ne}^{6.12\pm2.08} \beta_{pol}^{1.62\pm0.44} \tag{6.1}$$

with Z_{eff} as defined in eq. 2.2, the divertor neutral density n_{div} in m^{-3}, the toroidal field B_t in T, the density peaking γ_{ne} (ratio of a central and a peripheral interferometer chord, see Fig. B.1) and the plasma pressure normalised to the poloidal field (defined similarly as eq. A.14). In Fig. 6.12 the experimental values and the scaling are compared. The dataset extends over two orders of magnitude. The scaling reflects the intuitive impression that the W concentration is mainly governed by transport as elucidated by the strong dependence on the density peaking. Even the negative dependence on n_{div} may support this picture, since high n_{div} are reached by strong gas puffing which usually degrades edge confinement, and at the same time no significant dependence on T_{div} is found. The fact that transport is the main driver for the central c_W was illustrated even more clearly during the experiments with the W coated central column as will be discussed in Sec. 6.2.

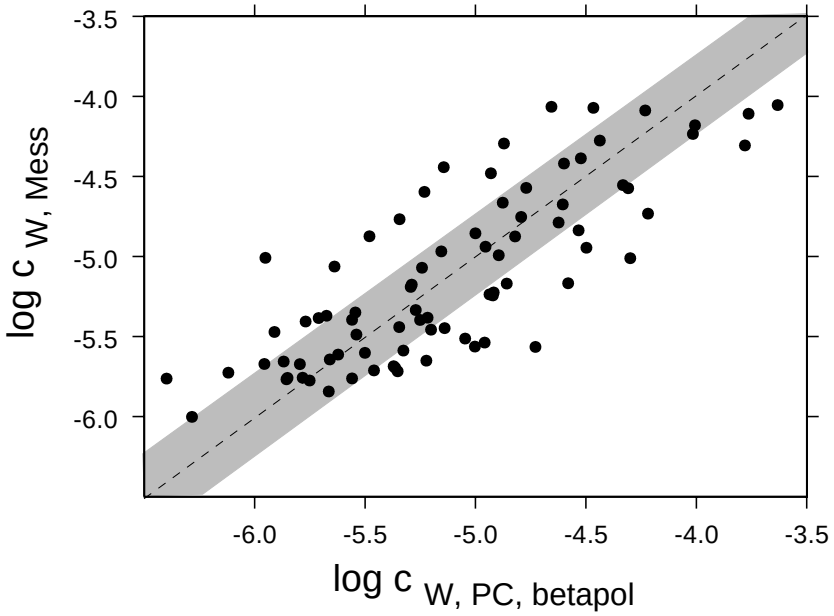

Figure 6.12: Comparison of the results from the principle component approximation (see eq. 6.1) and the experimental W concentrations in ELMy H-Mode discharges during the W divertor experiment. The grey band represents one standard deviation (after [126]).

6.1.4 Special discharge scenarios

It is known from literature (see for example [244, 280] and references therein) that discharge scenarios exist which are prone to impurity accumulation. A common phenomenon of these scenarios is the peaking of the background plasma density often combined with good confinement, which leads to an amplification of the impurity peaking, according to the equations discussed in Sec. 5.2. During preparatory experiments (W-LBO, [92, 238]), as well as during the W divertor experiment (intrinsic W and W-LBO), it was also observed that the accumulation occurs preferentially at central electron temperatures around 1 keV (see also Fig. 6.14b). This might be an indication for the thermal instability discussed by Tokar et al. [281]. The scenarios with the most pronounced accumulation were 'low energy' NBI and 'counter'-NBI. Fig. 6.13 shows a comparison of two almost identical 600 kA H-Mode discharges with low auxiliary heating power ($P_{NBI} \approx 2$ MW). In #8114 the beam heating was performed at 35 keV ('low' energy case), whereas in #8115 beam heating with 60 keV was applied. They had the same pre-programmed density waveform but in the case of the 'low energy' NBI, the control on the density is lost, although the edge behaviour is very similar as can be judged from the H_α time trace. The MHD-activity indicates, that for the standard case regular sawteeth exist, whereas they are absent in the discharge with 'low energy' NBI. In this case the central tungsten concentrations rapidly rise to values more than a factor of ten higher than in the reference case. The effect becomes even clearer when looking at the tungsten spectra themselves and the soft X-ray emission. These are shown in Fig. 6.14. Here two almost identical 600kA H-Mode discharges with low auxiliary heating power ($P_{aux} \approx 1.5$ MW,

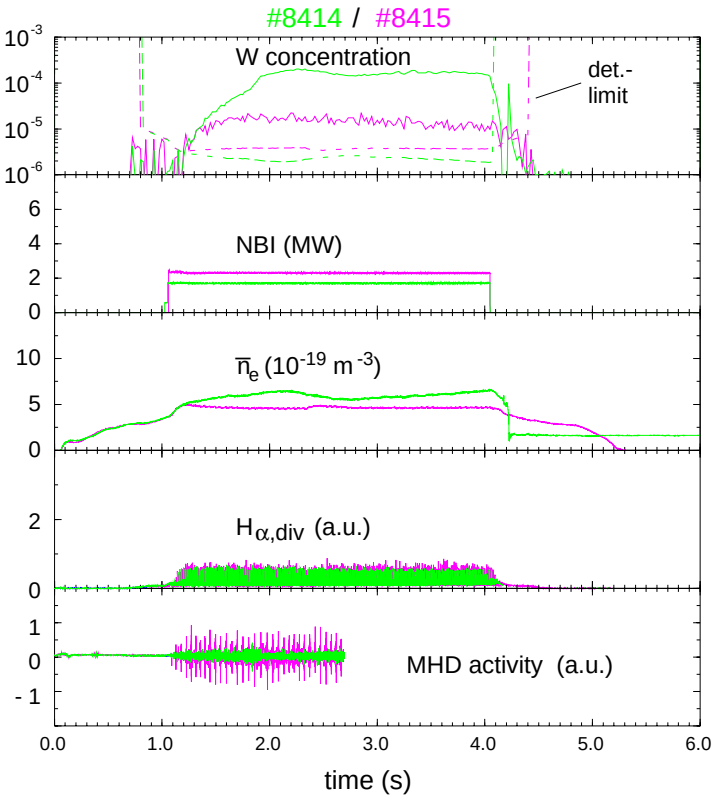

Figure 6.13: Comparison of plasma parameters for two almost identical H-Mode discharges ($I_p = 600$ kA, $B_t = -1.51$ T) with 60 keV (pink, #8415) and 32 keV (green, #8414) NBI

both similar to #8414) are compared. Whereas in discharge #8102 W accumulates after the disappearance of the sawteeth to concentrations of about $5 \cdot 10^{-4}$, the sawteeth activity continues in discharge #7560 keeping the W concentration at $\approx 10^{-4}$. The electron density and temperature profiles of discharge #8102 are shown in Fig. 6.14b for time points before and during the accumulation. This second example demonstrates the beneficial influence of the sawtooth activity on the stability of the discharge and it highlights the nonlinear behaviour of the strong high-Z accumulation.

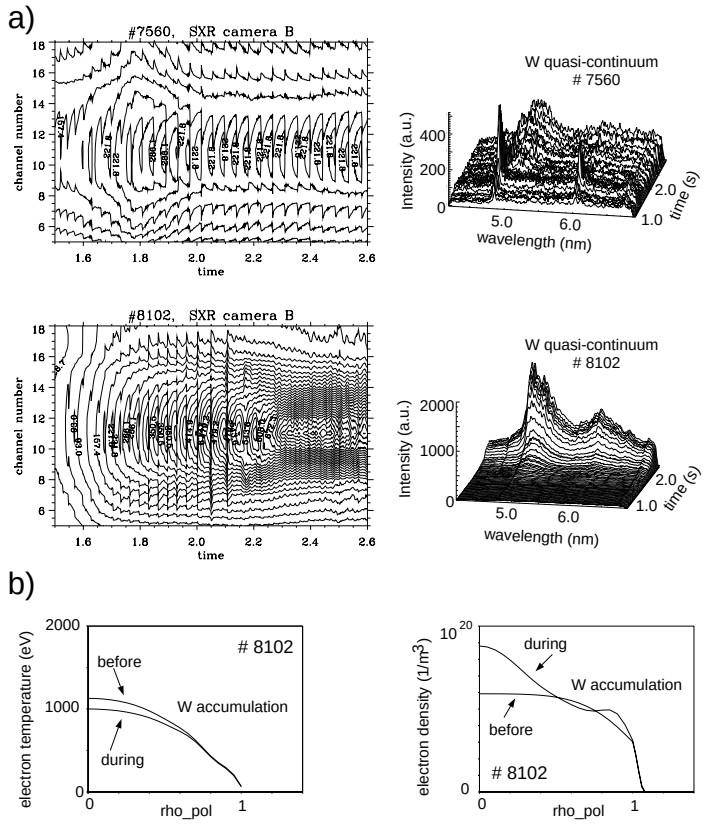

Figure 6.14: a) Temporal behaviour of the SXR radiation and the W quasi-continuum at 5 nm during two almost identical discharges #7560 and #8102 ($I_P = 600$ kA, $\bar{n}_e \approx 6 \times 10^{19}\mathrm{m}^{-3}$, $P_{NBI} \approx 1.5$ MW). The brightness of the SXR-radiation is shown as a contour plot (channels 10 – 12 look through the plasma centre). Note the different scales for the W quasi-continuum radiation. b) Electron temperature and density profiles of discharge #8102 before and during the W accumulation.

The other scenario exhibiting strong accumulation during the W divertor experiment was 'counter'-NBI. Here, the direction of the plasma current is such that the poloidal magnetic field leads to drift surfaces of the injected particles which are directed outward after ionisation. This leads to a strong modification of the power deposition (see Fig. 6.35). Fig. 6.15 shows the temporal behaviour of some plasma parameters for a discharge with about 5 MW of 'counter'-NBI. Tungsten concentrations of up to 10^{-3} (the highest during the W divertor experiment) were observed. At the same time, there is a strong MHD activity. The spikes in the H_α light, as well as the abrupt decreases in the stored energy indicate internal disruptions. Although both scenarios described above showed a very similar phenomenology the common underlying mechanism was only clarified during the experiments with the W central column, as will be described in Sec. 6.2. The absence of sawteeth (or fishbones) seems to be a necessary condition (see also Fig. 6.39) but it seems to be not sufficient as shown during

recent experiments (see Fig. 6.40).

The influence of the sawteeth on the impurity transport was nicely demonstrated in [246] by the injection of trace impurities. In the case of W, their impact was studied on the occasion of the occurrence of 'snakes' [92, 153, 238]. The 'snakes' were interpreted as strong $(m, n = 1, 1)$-MHD modes with a rotating island, which exhibit a better particle confinement also seen for the background plasma particles [92]. Therefore, their structure and temporal behaviour could be observed in the light of the soft X-ray, as shown in Fig. 6.16. From a tomographic reconstruction the size of the island in #4955 could be deduced to about 5 - 15 cm depending on the position in the poloidal plane. From the difference in brightness at the high and the low field side the influence of the the centrifugal force could also be estimated [238]. Sawteeth lead to a strong degradation of the central impurity confinement which obviously also acts on the (1,1)-mode. This is demonstrated in Fig. 6.17. After the W-LBO the radiation (and the tungsten) contracts to a narrow region in the centre stopped by the first sawtooth at $t \approx 3.22$ s, where W is expelled. The next cycle, starting right after the sawtooth elucidates this process. During each sawtooth a fraction of W is transported to the edge and lost from the confined plasma, leading to a decay of the central W density in time. The right side of the figure shows a blown-up section of the overview, which highlights the snake-like behaviour of the central radiation.

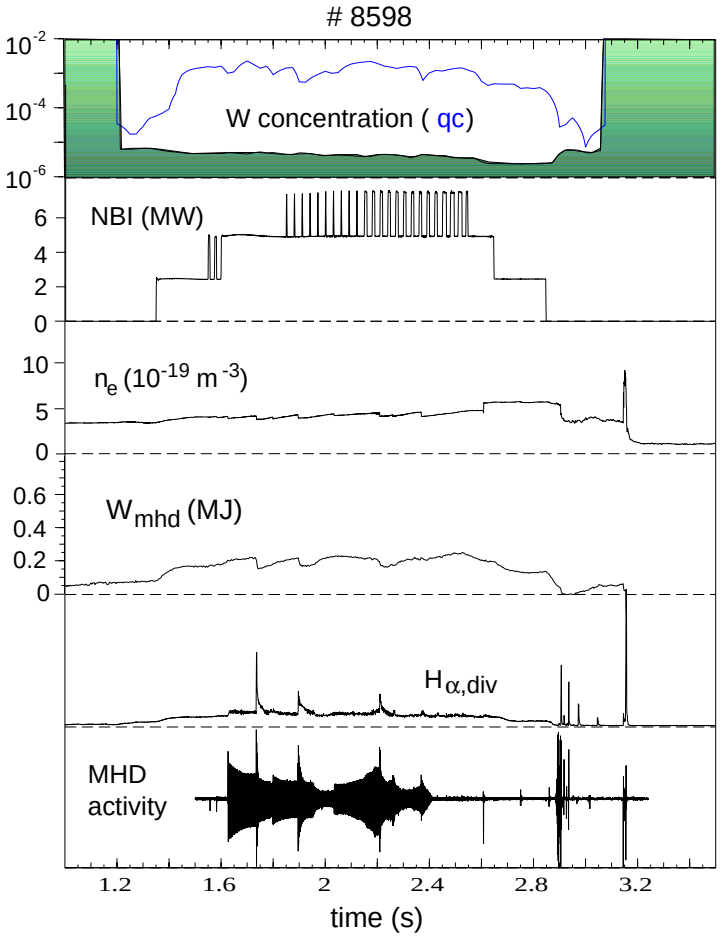

Figure 6.15: Plasma parameters of discharge #8598 ($I_p = -1.0$ MA, $B_t = 2.97$ T) with 'counter'-NBI.

6.1.5 Plasma Performance

Besides the specific tungsten programme, the influence of the tungsten divertor on the other intrinsic impurities and on the global plasma behaviour was evaluated. In all the

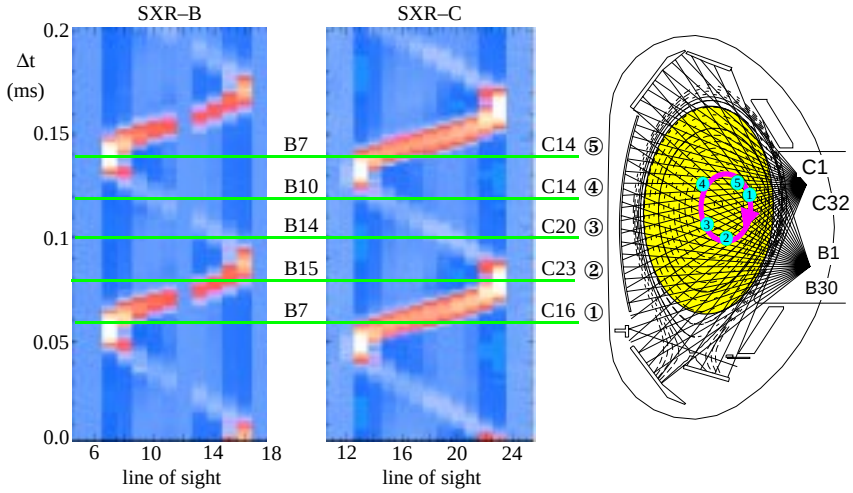

Figure 6.16: Illustration of the spatial and temporal behaviour of the soft X-ray radiation in discharge #4955 with a strong (1,1)-mode.

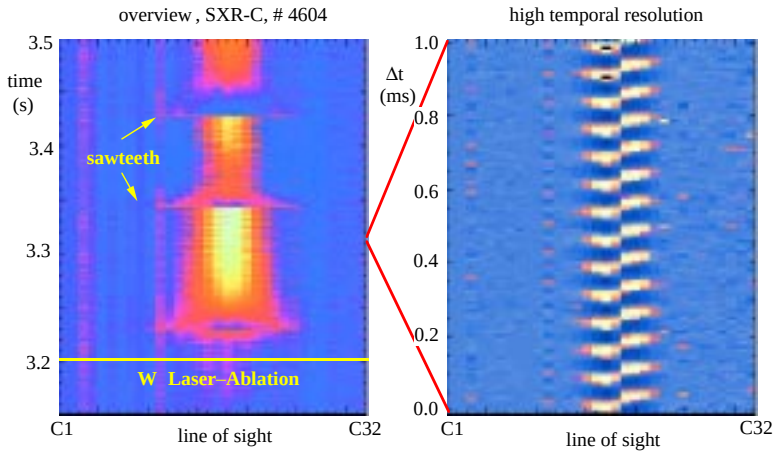

Figure 6.17: Temporal behaviour of the soft X-ray radiation after W-LBO in #4604 (after [92]). The line of sight represents the spatial co-ordinate as illustrated in Fig.6.16.

discharges without tungsten accumulation, the influence on the main plasma parameters was negligible. The carbon and oxygen content was monitored routinely by two crystal monochromators [116]. The intensities of the Lyman-α spectral lines of the H-like ions in ohmic standard discharges ($I_P = 600$ kA, $\bar{n}_e = 2 \cdot 10^{19}\mathrm{m}^{-3}$) were comparable to the discharges of the preceding experimental campaign (Fig. 6.18). A strong reduction especially of the oxygen radiation was found, as usual, in both periods after boronisation of the vessel. By taking into account the electron density and the temperature profiles, the C and O concentrations could be extracted [116]. Typical concentrations were about 0.5% for carbon and about 0.1% for oxygen.

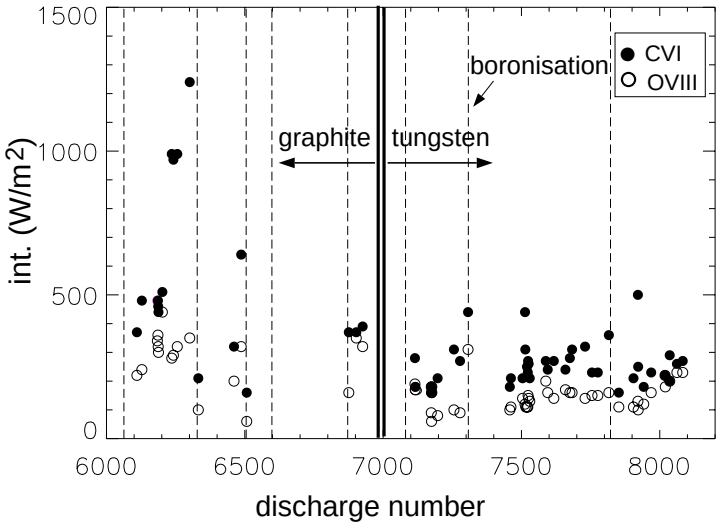

Figure 6.18: Brightness of the C VI (black dots) and O VIII (open circles) Lyman-α spectral lines from ohmic standard discharges ($I_P = 600$ kA). The broad vertical bar marks the change from graphite to tungsten divertor, whereas the dashed vertical lines represent the vessel conditioning by boronisation.

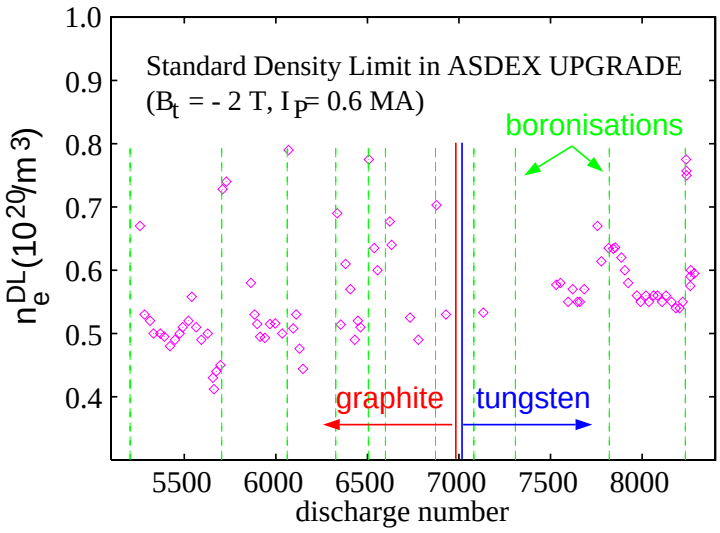

Figure 6.19: Maximum line averaged electron densities during ohmic standard density limit discharges ($I_P = 600$ kA). The broad vertical bar marks the change from graphite to tungsten tiles in the divertor, whereas the dashed vertical lines represent the vessel conditioning by boronisation.

In NBI heated discharges the impurity profiles of carbon and oxygen were measured by charge exchange recombination spectroscopy. Here, also no distinct difference to discharges with the graphite divertor could be found. These results are in line with former observations at ASDEX Upgrade, where it was shown that a large amount of the C impurity is produced by chemical erosion at the inner graphite heat shield [282] and not by physical sputtering from the divertor. Similarly, the experiments with a Be-divertor at JET revealed, that carbon was still the dominant impurity [283].

Density limit discharges ($I_P = 600$ kA) were performed at the beginning of every day of operation. Figure 6.19 shows the maximum value of $\bar{n}_e$ reached in these ohmic discharges. Again, the strong influence of the boronisation procedure was found but no significant change in the density limit due to the W divertor was observed. This reflects the weak influence of W on the intrinsic impurities and suggests that there is also no deleterious tungsten radiation. The sudden drops in the density limits were caused by accidental vacuum leaks, impurity events, or flooding with nitrogen for diagnostics calibration. In a se-

ries of discharges, the characteristics of the density limit in H and L-mode were investigated [284]. None of the discharges showed enlarged W concentrations.

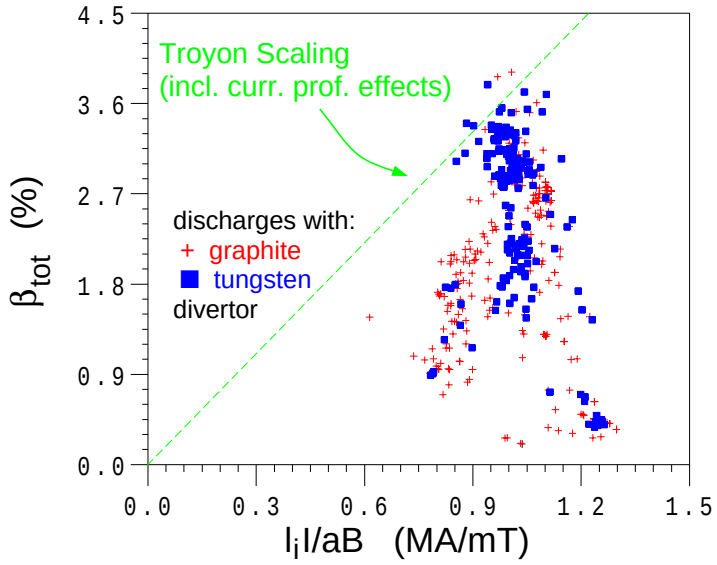

Figure 6.20: β_{tot}-values in % for discharges with graphite (crosses) and tungsten divertor (squares).

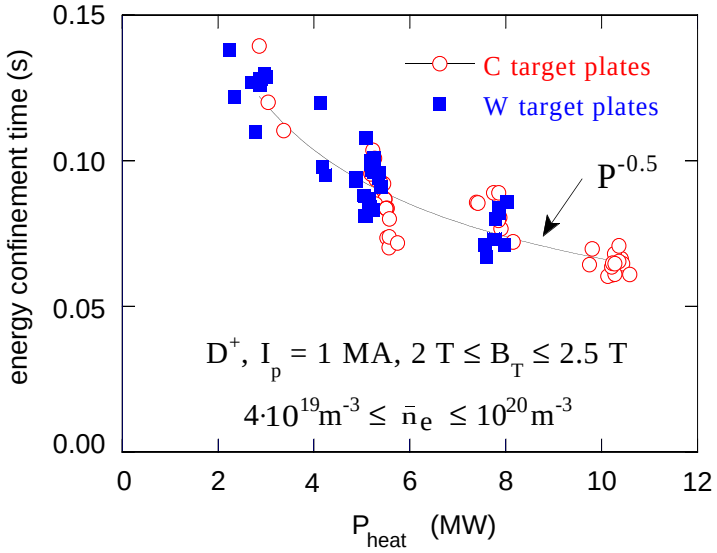

Figure 6.21: Energy confinement time in 1 MA discharges with graphite (dots) and tungsten divertor (squares).

β-limit discharges were performed with low plasma density and high heating power and therefore imposed high power loads on the target plates. Nevertheless, no increased W concentrations were found for these discharges. Values of β_N of up to 3.3 (during plasma current flat-top) and over 4.5 (during current ramp down) were found [285]. These values were in line with former investigations [286], indicating that there is also no negative influence of W on the MHD stability. A compilation of all β_{tot}-values with the graphite (crosses) as well as the tungsten divertor (squares) is shown in Fig. 6.20.

The different energy and particle reflecting coefficient of tungsten compared to graphite could have had an influence on the parameters at the boundary [287] and therefore might change the H-mode threshold. Detailed investigations of the H-Mode threshold [288] showed no difference to previous campaigns with the graphite divertor [289]. The comparison of the energy confinement time of $I_P = 1$ MA discharges (Fig. 6.21) also revealed no differences for the different divertor materials, again showing that there is no enhanced central radiation.

Investigations on radiating boundary scenarios have also been carried out during the W divertor campaign [290, 291]. In contrast to the findings at TEXTOR [292], only

slightly enhanced W concentrations were found in these discharges (see Fig. 6.10), reflecting the more effective reduction of the W source in the divertor (see Sec. 6.1.2). Additionally, no influence on the neon behaviour is found despite the expected difference in recycling of Ne at W and graphite surfaces.

6.2 Experiments with W coated central column

Although the plasma material interaction is strongly concentrated in the divertor region, it has become rather evident in recent years that in all divertor devices with large areas of carbon based wall components the carbon impurity content is strongly influenced by the main chamber carbon source. This was observed spectroscopically in ASDEX Upgrade [282,293] as well as in JET [42,283]. Further confirmation for the important role of main chamber erosion followed from the JET Be-divertor experiment, where C still was the dominant impurity [283], as well as from the ASDEX Upgrade W divertor experiment, where no influence on the carbon concentration in the plasma bulk was observed and strong carbon deposits on the inner strike point modules were found after the campaign [77]. Taking these observations into account, the questions which arise when a metallic central column is used can be formulated as follows: How does the wall material itself influence plasma operation and performance and can the amount of migrating carbon be reduced by a significant factor? In order to address the questions raised above, the central column of ASDEX Upgrade was covered with tungsten coated graphite tiles in a step by step approach, starting with the experimental campaign 1999/2000 (PHASE I), where 1.2 m^2 of the lower part of the central column was coated by tungsten [266]. Regarding the erosion by CX particles, this region corresponds to the divertor baffles of ITER-FEAT, where the present design uses tungsten [294]. During PHASE II (campaign April 2001 to July 2001) a total tungsten coverage of the central column was applied, except for regions, which may be hit directly by the shine through of the neutral beam injection (NBI) or which are used as a limiter. Finally, the limiter region was also coated for the campaign 2001/2002 (PHASE III). Fig. 6.22 shows the different positions of the W tiles during PHASE I-III together with the lines of sight of the main spectroscopic diagnostic used for the W investigations. An overview of the stages of the W programme for the central column is given in Table 6.1.

6.2.1 The tungsten coating

For PHASE I, the shape of the tungsten coated tiles was changed from the original rectangular design to a trapezoidal one in order to reduce edge erosion. The tiles were polished to reduce the surface roughness to values in the range of the thickness of the coating [264]. The W layer was applied by PVD at 150°C with a thickness of about 500 nm, which was calculated from the weight of the deposited W on special monitor samples. This thickness minimises the mechanical stress on the coating and is sufficiently large for the erosion expected at this position. Several tiles were additionally characterised by SEM and RBS analyses [295]. The W thickness extracted from the RBS measurements was quite similar to the results from the coating procedure itself, whereas the SEM

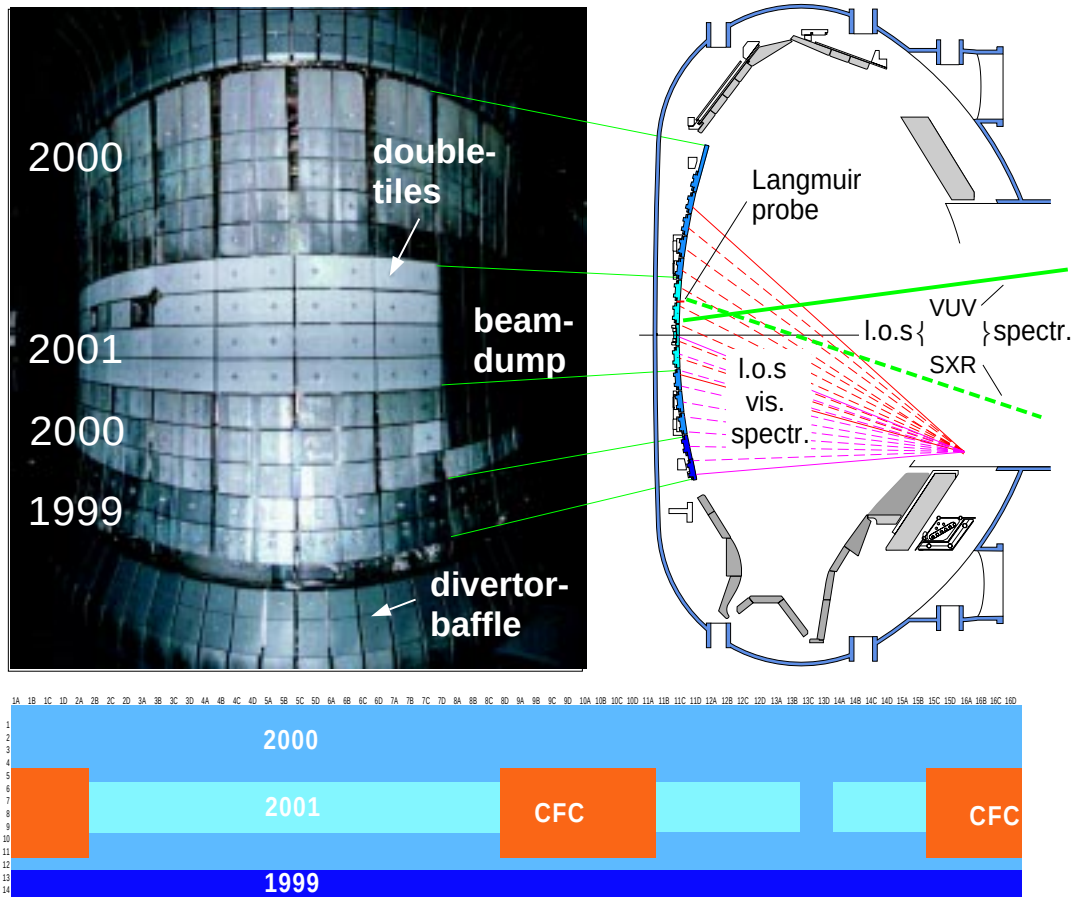

Figure 6.22: Left: The central column of ASDEX Upgrade with the tungsten coated tiles. The four rows in the equatorial plane are used as limiter during plasma start up and in dedicated limiter discharges. The numbers denote the year of installation of the W tiles.
Right: Poloidal cross section, showing the line of sights of the main diagnostics for the W influx and the central W radiation, as well as Langmuir probe tips installed at the central column.
Bottom: Schematic view of the unrolled central column showing the different phases of the W programme: PHASE I: dark blue, PHASE II: blue, PHASE III: pale blue. The brown areas are manufactured from CFC because of potential shine through of the NBI.

analysis yielded 40% larger values. This can be explained by the contamination with C and O, which is deduced from XPS to be about 10% C and O and from the fact that the density of the coating may be somewhat lower than that of solid W [295].
The increasingly larger surface area of tungsten coated tiles from PHASE II onward and the intention to use them at time as a limiter, necessitated the identification of an industrial scale technique for coating several hundred tiles with a tungsten film of a thickness in the order of 1μm. The coating was chosen to be as thin as possible to

keep mechanical stresses low, but also thick enough for the expected erosion and for a complete coverage of the substrate. For this purpose sample coatings on fine grain graphite obtained by magnetron sputtering and arc deposition were investigated [295]. The main parameters for evaluating the coatings were their adhesive properties especially under thermal loading conditions, their content of light impurities and the degree of surface coverage of these thin films on relatively rough fine grain graphite surfaces. The film thicknesses considered were in the range from 0.5 μm to 10 μm. Two types of graphite substrates were used (SGL Carbon R6710 and Schunk FU4206).

The samples were pre-treated mechanically to achieve an average surface roughness of 1-1.5 μm for all substrates. Tungsten film thicknesses were determined gravimetrically in all cases and for some samples cross-calibrated by Rutherford Backscattering Spectroscopy. The surface coverage was excellent, even at film thicknesses below the average substrate roughness. The contents of light impurities measured by X-ray photo-electron spectroscopy in combination with sputter depth profiling was around 5-10 at.% for carbon and at or below the detection threshold of 1 at.% for oxygen. While the arc-deposited films showed no signs of delamination at any thickness and independent of the substrate material, it turned out to be impossible to deposit films with a thickness exceeding 3 μm by the sputtering method: Delamination occurred in the form of small flakes with diameters up to the mm range. Thermal loading caused no failure up to the melting condition of the films, except for one case of a sputter deposited coating, which delaminated at a load of 11 MW/m^2. As a result of these investigations it was decided to choose 1 μm thick arc deposited W coatings from Plansee AG. More details about the procedures and results can be found in [295, 296].

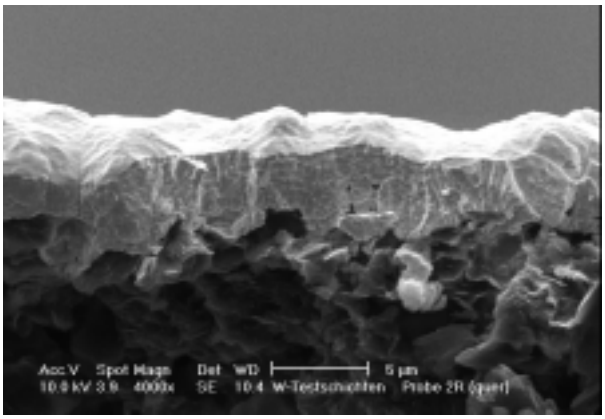

Figure 6.23: SEM cross sectional imaging of the 4 μm thick plasma-arc W coating of the the type used during PHASE II and PHASE III [295].

For the 2001 campaign (5.5 m^2 W coating, PHASE II), the tiles were shaped similarly to those used during PHASE I. For PHASE III (2001/2002) most of the start up limiter region (equatorial ring at the central column) was also tungsten coated with so called 'double-tiles' (see Fig. 6.22). These tiles diminish the number of leading edges and reduce the evolution of misalignment due to movement of the sub-structure after power load. Thermal screening tests for these complete tiles also indicated the possibility to use them at the position of the NBI dumps. During these tests the coated tiles were subject to power loads above 30 MW/m^2 during 0.3 s from the ion beam test facility

MARION at FZ Jülich [297]. No macroscopic damage of the coatings was observed and it was only after inspection with an SEM that microcracks in the order of 100 nm became evident. However, due to their very small extension and since no signs of exfoliation were visible, it was decided that their use in ASDEX Upgrade was feasible. During the plasma operation no signs of 'peeling-off' of the W layers (neither the PVD deposited ones, nor the arc deposited ones) was observed. These findings were confirmed by an optical inspection at the end of the corresponding experimental campaigns.

6.2.2 W Erosion and Migration

As in the case of the divertor experiment, the behaviour of tungsten in plasma discharges was mainly monitored by spectroscopical means. Again, the influx was determined from the brightness of the W I line at 400.8 nm employing both, the BLS spectrometer system with the movable mirror, which allowed the whole central column (see [293]) to be scanned, and an array of 20 fibre guides which was specially dedicated to the long term observation of the W tiles (see Fig. 6.22).

In most of the divertor discharges, no significant signal for the W I line was found. Therefore only an upper limit for the influx could be estimated. Using the photon efficiency S/XB as described in Sec. 4.1, one gets the value of $1.2 \cdot 10^{18}\mathrm{m}^{-2}\mathrm{s}^{-1}$. From an experiment where the plasma column was shifted towards the heat shield (see Sec 6.2.4), an even lower value for the influx could be estimated. Besides the W influx, the C-influx from the W tiles was monitored. This was originally done to trace the successive deposition of carbon. In Fig. 6.24 the intensity of a C III spectral line at 465 nm is plotted against the intensity of the O VIII Lyman-α spectral line (1.897 nm), which is a measure for the oxygen edge density. Already starting with the first discharge, a strong C III signal was visible, which decreased with an increasing number of discharges and rose again after venting the vacuum vessel. Finally it dropped by a factor of 2 after siliconisation. This behaviour implies that a thin carbon layer is built up rather quickly which is in a dynamic equilibrium with the impurity content in the plasma, as already observed from metallic surfaces in ASDEX Upgrade and TEXTOR [99,278]. Because no surface coating was performed at the start of the campaign high levels of O were observed, which slowly decreased from discharge

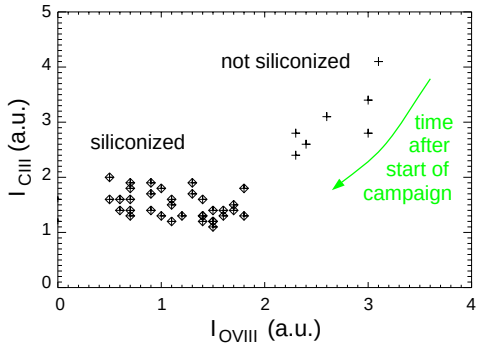

Figure 6.24: Carbon influx (C III line intensity) from the tungsten tiles in discharges with $I_P = 1$ MA, $\bar{n}_e \approx 6 \cdot 10^{19}$ m^{-3} and $P_{NBI} = 5$ MW, plotted versus the oxygen edge density (O VIII line intensity). For high levels of O a strong correlation of both signals is found.

to discharge and finally reached very low levels after the siliconisation. The correlation with the oxygen density for high levels of O clearly demonstrates the role of oxygen in the C recycling by the production of CO. For lower O density, as after the siliconisation, other effects, such as chemical erosion and local deposition may take over at a reduced level. However, in principal this behaviour could also explained by the fact that the initial C content of the W coating ($\approx 10\%$) is depleted through plasma-operation [298]. Through venting a carbon layer could also have been reformed but the details of the observations make this explanation somewhat more unlikely.

To complement the spectroscopic measurements during PHASE I, deposition probes were exposed to special discharge series in the first phase of the campaign [266, 299]. The evaluation of the divertor probes showed average W fluxes from 0.5 to 2.8 $\times 10^{17}$ atoms $m^{-2}s^{-1}$. The deposited amount is largest in H-Mode discharges with very low electron densities, and in H-mode discharges at intermediate density and higher triangularity. Whereas in the first case this is expected because of the higher erosion by CX-particles [300], there is no obvious explanation for the second observation. However, the different plasma shape may have a strong influence on the W transport in the SOL.

The midplane probe showed no W deposition above the detection limit of 10^{17} atoms m^{-2}. This observation is consistent with the observations in the divertor, because the W deposition is concentrated in the small strikepoint region due to the much faster parallel transport in the scrape-off layer. Additionally, this also leads to a larger integral deposition in the divertor as already shown in [93]. Assuming that the deposited W can only reach the outer midplane and the divertor through the main plasma, the divertor probe measurements can be compared to spectroscopic measurements. The out-flux of W can be estimated by taking the transport time of W inside the plasma ($\tau = 180$ ms, see Sec. 5.1.4), the average W concentration ($c_W \leq 10^{-5}$) and the particle content ($N_e \approx 6 \cdot 10^{21}$) to

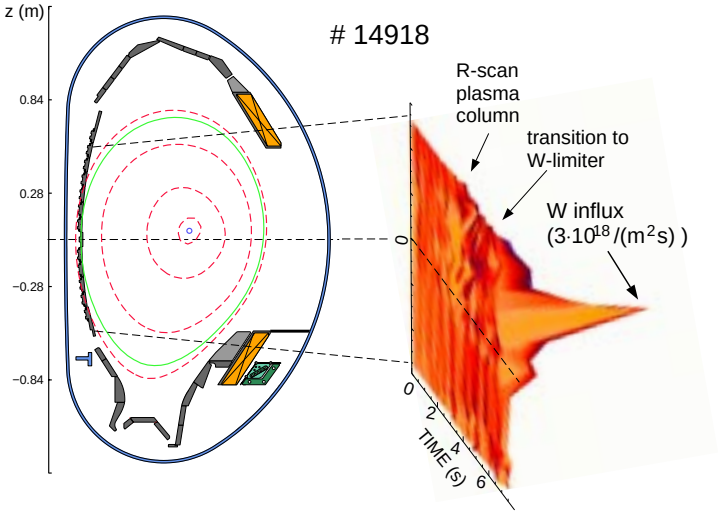

Figure 6.25: Spatial distribution of the W I-brightness as a function of time during a plasma discharge with a radial shift towards the central column.

$$\Gamma_W = \frac{c_W \cdot N_e}{\tau} \leq 10^{15}\ \mathrm{s}^{-1} \tag{6.2}$$

In Ref. [93] it is found, that about one third of the W from the main plasma is deposited

in the outer divertor. Together with a deposition zone of about 1/3 m^{-2} this leads to expected particle fluxes of $\approx 10^{15}$ atoms $m^{-2}s^{-1}$, which is in strong contradiction to the measured deposition rates. However, assuming that there is also a direct transport channel not involving the bulk plasma, all observations (including the detection limit for the influx measurements) are consistent. (It should be noted that in investigations at JET fluxes in the opposite direction were found [226].)

The strong W erosion observed in the post mortem surface analyses is dominated by the current ramp-up and ramp-down phase, when the central column is used as a limiter. This can be concluded from spectroscopic measurements of the W influx during PHASE II and PHASE III, as well as recent Langmuir probe measurements at the central column [301] as shown in the next figures. Fig. 6.25 shows the W I-brightness as a function of time during a plasma discharge, with a radial shift towards the central column. The maximum W influx is detected during the limiter phase of the plasma ramp down, whereas the increase of the W I-brightness during the radial shift (still in divertor configuration) is rather moderate. In Fig. 6.26 the temporal behaviour of T_e and n_e at the central column is presented for a discharge similar to the one presented in Fig. 6.29. As in almost all discharge scenarios currently run at ASDEX Upgrade there is 2.5 MW of neutral beam heating during the ramp-down. Whereas T_e is highest during the plasma ramp-up (probably related to the strong edge heating by the induced current) the deduced erosion is highest during ramp-down due to the high particle fluxes. During the flat-top phase the temperatures are similar as during ramp-down, but due to densities, which are lower by at least three orders of magnitude, the erosion is almost negligible there.

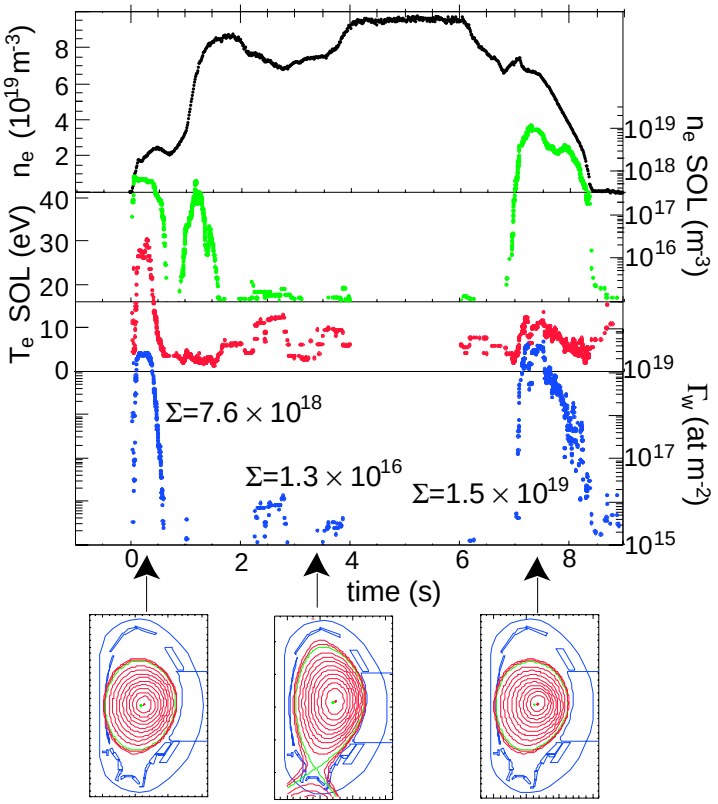

Figure 6.26: T_e and n_e at the central column derived from Langmuir probe measurements for a typical H-mode discharge. Using the effective W sputtering yields from [99] the erosion can be estimated (integral values for plasma ramp-up, flattop and ramp-down). At the bottom, the corresponding magnetic configurations for these three phases are shown (after [301]).

Phase	w/o cond.	boronised	siliconised
no W		X	X
I	X		X
II	X	X	
III		X	

Table 6.3: Phases of different wall conditioning before and during the experiments with W coating at the central column. He glow discharge cleaning after vents was performed in all phases.

Due to the trapezoidal cross-section of the tiles, there are also areas, which are shadowed from the incident field lines. There AES analysis revealed a deposited layer consisting mainly of carbon, oxygen and silicon with a thickness of 20-30 nm on top of the tungsten coating [60]. Details on the post mortem analyses of tiles are presented in [61].
The migration of tungsten was investigated by the measurement of the deposition on graphite and CFC tiles [61, 299]: Only about 10% of the eroded material is found in the divertor. This may be attributed to the fact that the main erosion is during the limited phase of the discharges, where no parallel transport to the divertor is possible. Additionally, the analyses of graphite tiles in the main chamber reveal that W is very locally re-deposited. In order to understand the W transport mechanisms in the SOL, calculations with the DIVIMP 2D Monte-Carlo impurity transport code [229] (see Sec. 5.1) have been started [230, 231] recently.

6.2.3 Operation with W Startup Limiter

During PHASE III, special emphasis has been given to the analysis of the start-up phase at the tungsten startup limiter. As deduced from the limiter experiments in PHASE II a higher W contamination during start-up (and ramp-down) was expected. This led to the questions whether this higher W content would deteriorate the build-up of the plasma current and whether the initially high W concentration would decay strongly enough when switching to divertor operation. An important parameter for operation of the device is the status of the wall conditioning. The start-up was investigated in all experimental phases (summarised in Table 6.3). Fig. 6.27 shows the behaviour of several parameters in 'standard H-Modes' (see Fig. 6.29) versus the discharge number. The first row of Fig. 6.27 clearly indicates, that the increase of the ohmic transformer flux consumption with W limiter is below 5% and is even weaker than after siliconisation. Moreover the plasma current ramp is not hampered in any way. From the erosion measurements cited above, it can also be excluded that deposited layers (boron from boronisation, carbon from deposition) mask the effect of W, because at least half the

W area is found to be erosion dominated. A long term decrease in the C VI brightness is visible, especially since the regular application of the siliconisation. Although no siliconisation was applied during PHASE II and PHASE III and large areas of new graphite surfaces were introduced before PHASE II (installation of the new divertor IIb, see [302]) I_{CVI} is at the lower end of the observed range right from the start of PHASE II, pointing to some carbon reduction due to the increased area of W coating. The tungsten concentration is evaluated at its maximum during the limiter phase ($t = 0.6$ s). Going from PHASE II to PHASE III an increase in c_W by about a factor of two during the early startup phase was observed, but the effect of the boronisations was even larger. Especially after the boronisation around #15500 a clear reduction of c_W by a factor 5 was observed. After the boronisation the W concentration recovers faster than the total radiation and the radiation from oxygen. This leads to the conclusions that the boron layer is quickly eroded at the positions of strong plasma wall interaction and that W contributes only a minor part to the radiation during the startup.

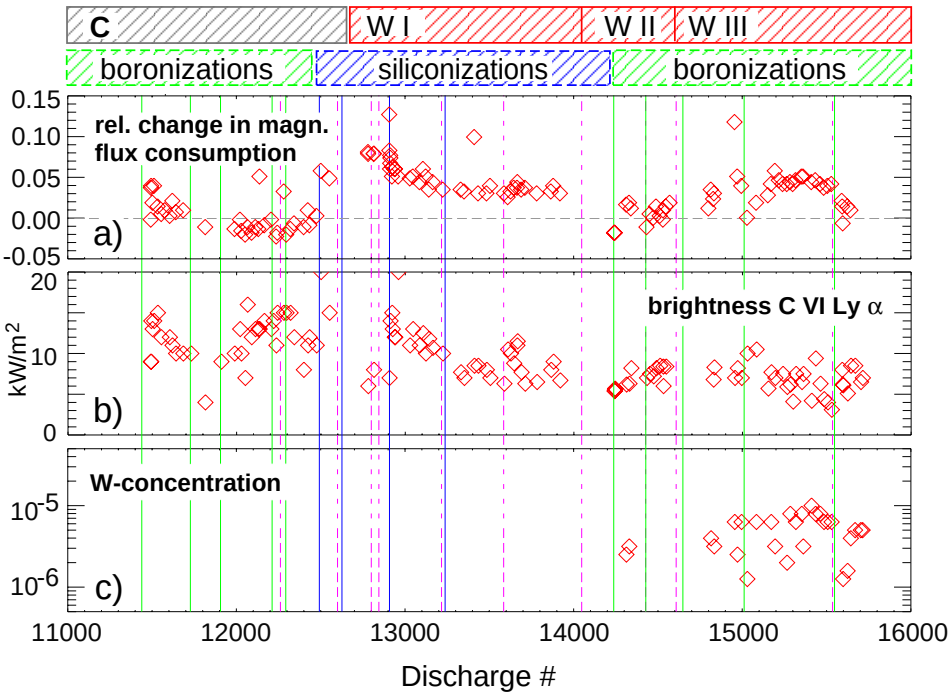

Figure 6.27: Behaviour of ohmic transformer current, C VI radiation and W concentrations during phases of different wall conditioning in 'standard H-mode discharges'. Boronisations/siliconisations are represented by solid lines and vents by dashed lines :
a) Relative change of the magnetic flux consumption at the end of the current ramp up phase, normalised to the mean value during operation with boronised graphite tiles (neg. values represent lower consumption of the magnetic flux).
b) C VI Lyman-α brightness during the high density phase ($t = 6.5$ s).
c) W concentration during the limiter phase of the current ramp up ($t = 0.6$ s).

6.2.4 Behaviour of tungsten in different discharge scenarios

The experimental campaigns of PHASE I + II were started without wall conditioning by coating of the vacuum vessel. This allowed the measurement of the W erosion and the W concentration with an almost pure tungsten surface exposed to the plasma in all major plasma regimes. During this initial period the total radiation and the Z_{eff} were higher than for a good conditioned machine, but this was attributed to the high oxygen content (few percent).
The tungsten concentration (c_W), which is relevant for the fusion performance, was determined using the two different spectral signatures described in Sec. 4. Using the spectra from ions with such different charge states guarantees a sensitive measurement of the central W concentration for the usual range of central T_e in ASDEX Upgrade (1 - 5 keV). For $T_e > 2.5$ keV it even allows the extraction of some profile information of c_W. The detection limits were established by W-LBO to be $\approx 5 \cdot 10^{-6}$ for the VUV and $\approx 10^{-6}$ for the SXR in discharges with intermediate densities.

Divertor discharges

Conventional H-Mode

The H-mode regime comprises by far the largest operational space in ASDEX Upgrade, since it is achieved at low densities ($\bar{n}_e \approx 4 \cdot 10^{19}$ m^{-3}) and intermediate toroidal fields $B_t \approx 2$ T for additional heating powers just above 1 MW [302, 303]. Therefore, most of the experimental data is gathered in the H-mode at low ($\delta \approx 0.15$) to intermediate ($\delta \leq 0.45$) triangularities. For low δ tungsten concentrations around 10^{-6} or below were observed. A typical example at intermediate density and heating power is shown in Fig. 6.28, performed during PHASE II still in the un-boronised machine. The discharge shows very regular type I ELMs and sawteeth visible on T_{e0} and the soft X-ray brightness. All parameters, including c_W, quickly reach their steady state values and stay constant up to the pre-programmed discharge termination. The spikes on the central tungsten concentration, which are correlated to the sawtooth crashes are artefacts. They are due the evaluation method which instantaneously changes the ionisation equilibrium with the temperature without taking into account finite recombination times. Although higher than with a boronised vessel – as mentioned above – the main chamber radiation is rather low (30%) and the confinement is good ($H_{ITER92Py} \approx 1$). Performing the same discharge at a higher density ($\bar{n}_e = 9 \cdot 10^{19}$ m^{-3}, $\bar{n}_e/n_{gw} = 0.75$) a fast decrease of c_W is observed during the density ramp until it falls below the detection limit [267]. This is also demonstrated in the 'standard H-Mode' discharge (see Fig. 6.29) which is run almost every day of operation [303]. It is designed to check the heating and the diagnostic systems and to document the conditioning of the device. After the measurement of the

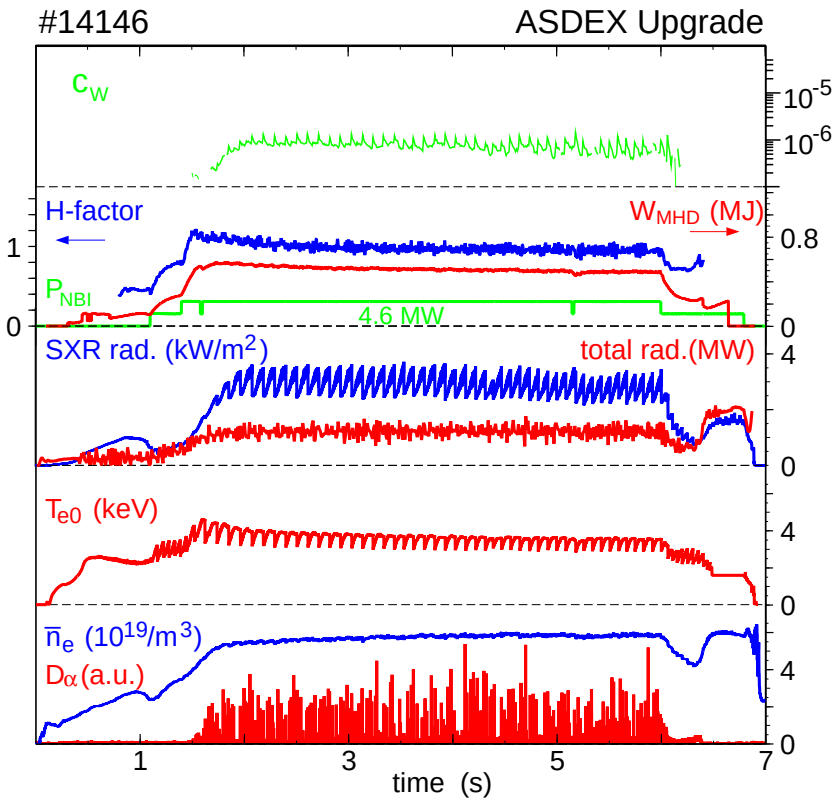

Figure 6.28: Typical H-mode discharge at 1 MA and intermediate density and heating power, performed before boronisation. The H-factor is calculated according to the ITER92P ELMy H-mode scaling and the tungsten concentration (c_W) is extracted from the central line emission of W^{46+}.

L-H threshold (power ramp by chopping one NBI source) a first phase at natural H-mode density with a second power ramp (performed by ICRH) to $P_{aux}^{heat} \approx 5$ MW follows. In the second part a density plateau at 80% of the Greenwald density limit ($\bar{n}_e = 10^{20}$ m^{-3}) is run. During the initial phase with one NBI source only, the particle confinement is rather high, as indicated by the strong increase of the natural density. Adding the ICRH power, the natural density is quickly reduced and it slightly increases when switching from ICRH to the second beam source. Throughout the discharge the main chamber radiation is very low. This general behaviour is reflected in the W concentration, which reaches its highest value just at the beginning of the H-Mode phase. By comparison of the concentration extracted from the W quasi-continuum (emitted from regions with $T_e \approx 1$ keV) with the one extracted from the W^{46+} (central emission) a peaking of the W concentration profile at $t = 2.5$ s becomes evident. This peaking is inverted during the ICRH phase and after switching to NBI only, the c_W-profile flattens at a value of $(2-3)\times 10^{-6}$. During the high density phase no W signal is detected in the SXR. This is due to the fact that the temperature is too low for the existence of W^{46+} and to a further

decrease of the W concentration as it is deduced from the measurements in the VUV. The value of $c_W = 10^{-6}$ (from the VUV measurement) during the high density phase has to be seen as an upper limit, since the complexity of the quasi-continuum radiation makes the distinction from the background radiation very difficult. During the start-up phase of the discharge ($t = 0.5 - 0.8$ s), with a direct plasma contact to the tungsten surface, an increased W concentration is observed, which decays quickly after the evolution of the X-point in the plasma. A similar process can be observed during current ramp-down (from $t = 7.8$ s on) as the increase of total radiation indicates. Measurements of the W quasi-continuum in other discharges show that the tungsten concentration there reaches values even around 10^{-4}. This is due to the fact that the auxiliary heating ($P_{NBI} = 2.5$ MW) leads to higher W sputtering than during the ohmic current ramp-up, consistent with the Langmuir probe measurements, described in the previous section.

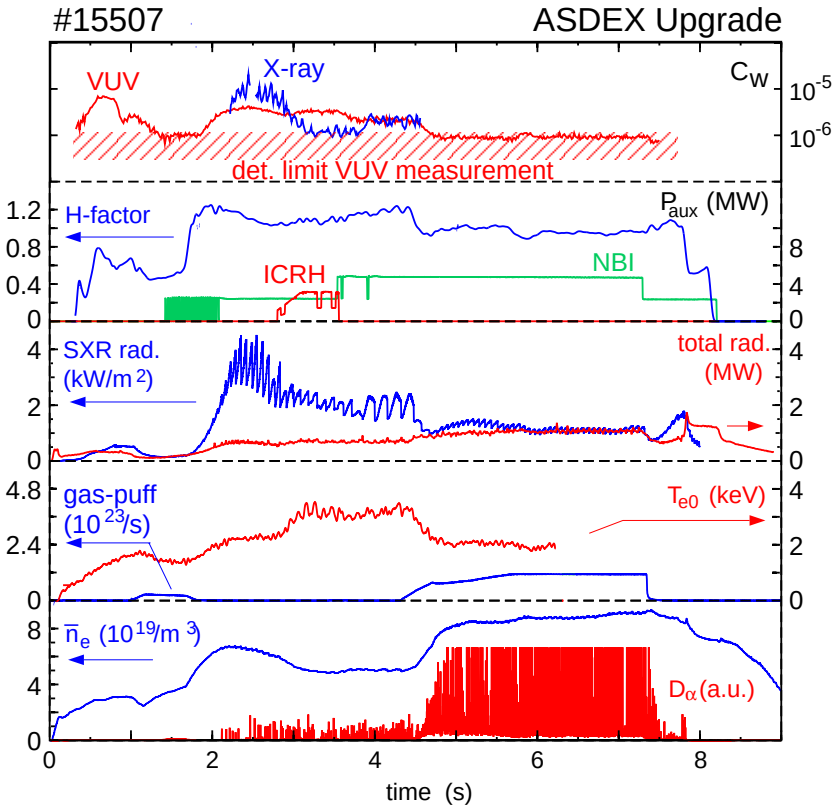

Figure 6.29: Temporal behaviour of a 'standard' H-Mode discharge in ASDEX Upgrade ($I_p = 1$ MA, $B_t = -2.0$ T, $q_{95} = 3.2$ and $\delta = 0.15$). The H-factor is calculated according to the ITER98P ELMy H-mode scaling.

In discharges with $\delta \approx 0.4$ the tungsten concentrations were higher by about a factor of five, reflecting the generally better particle confinement also seen for the natural density at a given current and heating power. Performing these kinds of discharges with moderate constant gas-puffing at intermediate heating powers from NBI ($P_{NBI} \leq 7.5$

MW) yield a very high energy and particle confinement at densities around or above the Greenwald limit (see Fig. 6.30). The reason for this seems to be a reduction of energy/particle transport in cases where the heating is applied further off axis as proposed by Stober et al. [304]. A further ingredient of these discharges is the slowly evolving density peaking of the background ions which can be explained by a very small inward velocity of the order of the neoclassical Ware-pinch [304]. Density peaking accompanied by a weak temperature gradient is the natural prerequisite for neoclassical impurity accumulation, which amplifies the density peaking proportional to the charge of the impurities [243]. Therefore these discharges were prone to higher c_W reaching values above 10^{-5}, increasing during the whole discharge. To study this behaviour further, specially designed discharges were performed. From the tungsten divertor experiment the tendency of tungsten accumulation for 'low' energy NBI, i.e. off axis heated discharges was known (see Sec. 6.1.4). Therefore, the NBI energy was reduced from 60 keV to $35 - 40$ keV, to shift the heating profile further off-axis. In these discharges the tungsten concentration rose after switching on the beams, until the sawteeth were lost and extremely peaked electron density profiles were observed, finally leading to central tungsten concentrations of up to $4 \cdot 10^{-5}$ [267]. Performing the same discharge with full beam voltage, i.e. more central heating, c_W stays around 10^{-6}, similar to the experiences with the W divertor. An even clearer experimental proof is provided using central ECRH: switching on the ECRH during the evolving accumulation, a fast suppression is found [267]. The effect is even clarified after switching off the ECRH heating, when the tungsten concentration rises again. The experiment was also performed by an exact replacement of beam power against ECRH power, to exclude the confinement degradation by additional heating power. This discharge showed the same beneficial behaviour [255]. The mechanism appears to be a complex interplay of the anomalous transport of the background ions and the anomalous and neoclassical transport of tungsten, as investigated further in Sec. 6.2.5.

As stated earlier, a significant amount of tungsten influx was only measured during plasma start-up and ramp-down and in specially designed discharges, which had low clearance with respect to the tungsten tiles (or when using the tungsten tiles as limiter, described later in this section). Fig. 6.31 shows the behaviour of the W influx (Γ_W) and the W concentration (c_W) during a radial shift of the plasma towards the central column in discharge #14186 ($I_p = 1$ MA, $B_t = -2.3$ T, $P_{NBI} = 5$ MW, $\delta = 0.15$). As can be judged from the top traces on the left ($\bar{n}_e, T_{e0}$), the main plasma parameters remained constant during the shift. The temporal evolution of the spectra is shown in Fig. 4.19. At the nominal clearing of 12 cm to the inner wall, no influx above the detection limit was evident. During the shift the influx rose to a maximum value of $3 \cdot 10^{18}\mathrm{m}^{-2}\mathrm{s}^{-1}$ for the lowest clearance of 4 cm. The increase of the W I brightness was only seen on the W coated tile which was nearest to the equatorial plane, in line with the equilib-

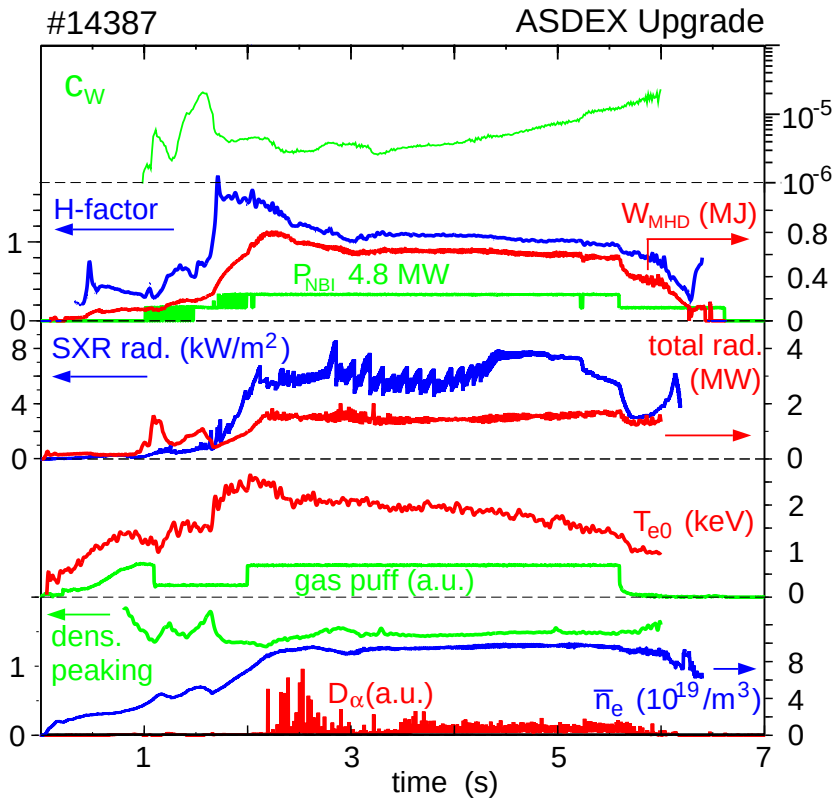

Figure 6.30: H-mode discharge at $I_p = 1$ MA, $B_t = -2.0$ T with intermediate triangularity ($\delta \approx 0.37$) and heating power, as well as constant gas puff. The density peaking is represented by the ratio of a central (H-1) and a more peripheral (H-5) interferometer measurement (see Fig. B.1). The H-factor is calculated according to the ITER92P ELMy H-mode scaling and the tungsten concentration (c_W) is extracted from quasi-continuum emission by W ions around W^{28+}.

rium reconstruction. Therefore one can assume that only a ring with approximately the height of one tile ($\pm 50\%$) contributes significantly to the influx. Taking into account that only about the half of the circumference is erosion dominated due to shadowing effects in toroidal direction [60], this results in an area of 0.33 m^2 where W is eroded and consequently a total W influx of $\approx 10^{18}$ s^{-1} from this row. This has to be taken as a lower boundary, since it is to be expected that the W influx from the other rows with W tiles is also increased, although below the detection limit. However, judging from the clear signal for W I for these tiles, it is evident that the increase of the W flux from the rest of the tiles must be much lower. When calculating the D-flux to the wall by using the brightness of the simultaneously measured D_δ and $S/XB = 6000$ one can even derive an effective sputtering yield $Y_W^{eff} \approx 10^{-3}$. Obviously, this cannot be due to pure D sputtering since this would require ion temperatures in the range of 100 eV. But taking into account sputtering by a few percent of light impurity ions (O, C), temperatures in

the range of 10 eV would be sufficient [14, 77] to yield a consistent result.
In parallel to the increased influx, an increase of the W concentration is observed. Assuming spatially constant c_W one gets from the increase from $1 \cdot 10^{-6}$ to $2 \cdot 10^{-6}$ an additional inventory of $\Delta N_W = N_e \cdot \Delta c_W \approx 8 \cdot 10^{14}$ W ions. Since the W concentration during the phase with standard clearance was $\approx 1 \cdot 10^{-6}$, one can derive an W influx of the same absolute size as from the single row during the shift. However the flux density must be lower by the ratio of active surfaces, namely by about a factor of 10, consistent with the detection limit of the diagnostic. The ratio $\Delta N_W / \Delta \Gamma_W$ gives the particle confinement time $\tau_p = 8 \cdot 10^{14}/10^{18}$ ms $= 0.8$ ms. To compare this number to the results from W injection and to investigations in other machines, τ_p is separated in a penetration probability f (sometimes also called screening) and the transport time τ_t within the confined plasma, as discussed in Sec. 5.1. Since τ_t cannot be derived from steady state conditions, and depends on the radial impurity profile shape during a dynamic experiment, we assume formally in accordance with other work, $\tau_t = \tau_E \approx 100$ ms. From this one gets $f = 0.8\%$ as an upper estimate, since usually τ_t is somewhat larger than τ_E and $\Delta \Gamma_W$ was the lower boundary. This value is lower than $f = 3\%$ from the W-LBO experiment (Sec. 5.1), which may lead to the injection of clusters penetrating more easily. The value is also almost a factor of 10 lower than the results from screening experiments with methane measured for top fuelling in JET [305, 306] but similar to nitrogen puffing experiments at the central column in Alcator C-Mod [307].

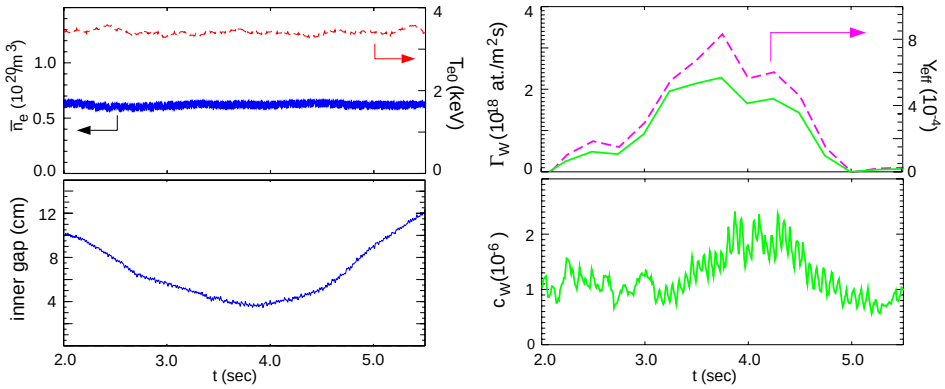

Figure 6.31: Behaviour of the W influx (Γ_W), eff. sputtering yield (Y_{eff}), and the W concentration (c_W) during the radial shift of the plasma towards the central column in discharge #14186 ($I_p = 1$ MA, $B_t = -2.3$ T, $P_{NBI} = 5$ MW, $\delta = 0.15$). On the top left $\bar{n}_e$ and T_{e0} are shown, to demonstrate that the main plasma parameters remain constant during the shift shown at the bottom left.

Improved H-Modes, electron ITB- and high-β discharges

Advanced scenarios are the second important experimental topic at ASDEX Upgrade. Especially improved H-modes, which are characterised by fishbones instead of sawtooth activity, no central barrier, but generally improved confinement over ordinary H-modes, are given some emphasis since they can be performed in quasi steady-state [308]. These kinds of discharges were already tested with an un-boronised vessel at the beginning of the campaign. Since the overall conditioning of the machine was not sufficient, the plasma density was slightly too high and the best performance values of [308] were not reached. The tungsten concentrations extracted in these discharges, show similar values and characteristics as ordinary low density H-modes.

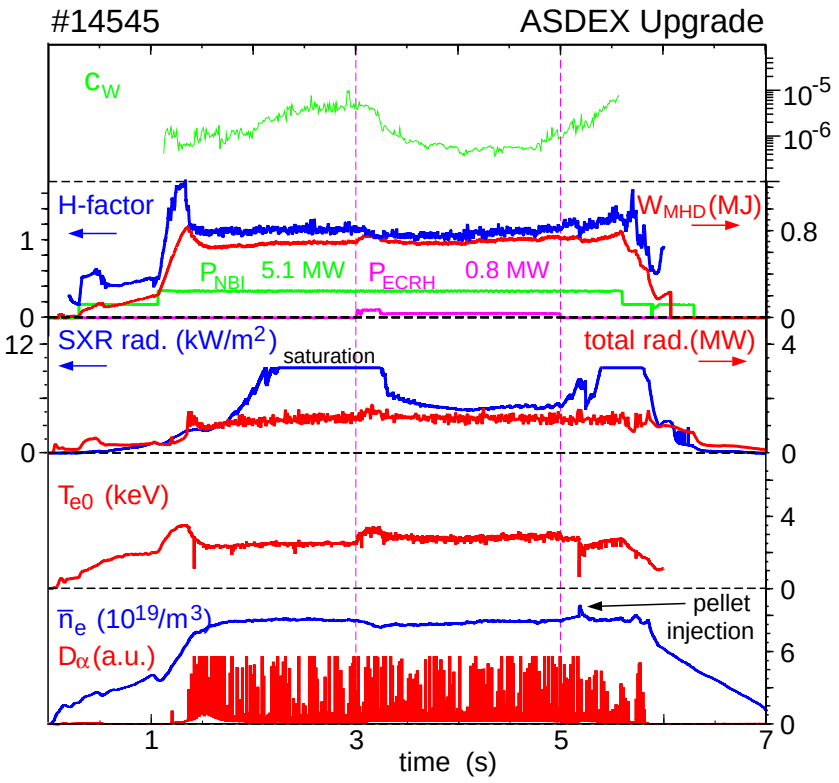

Figure 6.32: Moderately improved H-mode discharge at $I_p = 1$ MA, $B_t = -2.5$ T, $\delta = 0.4$, showing enhanced c_W with NBI only, but a strong reduction of c_W during central ECRH. Note the scales are the same as in Fig.6.28 except for the density and SXR brightness.

An enlargement of the operational space for the improved H-mode towards higher densities was gained by running the discharges at $\delta \approx 0.4$ [309]. As in ordinary H-modes at medium to high triangularity discharges, the tungsten concentration showed the tendency to increase slowly throughout the whole duration of the discharge to values of

about $c_W \approx 10^{-5}$. This evolution was accompanied by an increased density peaking as already described in the previous subsection. To test the applicability of the method of central heating for the reduction of the central impurity confinement, central ECRH was applied during the flattop phase of a discharge as shown in Fig. 6.32. The initial very good confinement was not sustained, nevertheless the H-factor stayed above 1.1. From $t \approx 1.8$ s the W concentration rose continuously and shortly after $t \approx 2.2$ s the soft X-ray measurement saturated. It has to be pointed out that this increase in the SXR brightness was not exclusively due to the increase of the W density, since the brightness of other impurity radiation (for example Fe) was also found to rise. From $t = 3.0$ s onward central ECRH is added (first 1.4 MW, after about 200 ms 0.8 MW; note the power has the same scale as the NBI power). During the ECRH phase, T_{e0} is increased but no (or very minor) sawteeth appear and $\bar{n}_e$ is slightly decreased similar to the so-called density pump out effect described in [310]. The stored energy stayed almost constant leading to a slight reduction of the H factor from 1.14 to 1.06. However, by far the strongest effect is found on the SXR brightness and the tungsten concentration. Both drop on the timescale of the energy confinement time, leading to c_W below 10^{-6}.

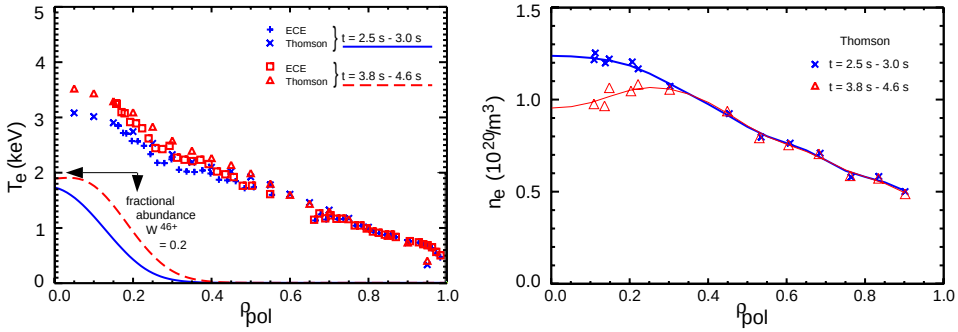

Figure 6.33: Electron temperature and density profiles of discharge #14545 before and during central ECRH (the solid lines represent a fit through the experimental density data). The fractional abundance for W^{46+}, which is used to calculate the W concentration, is also shown in the left part.

In Fig. 6.33 (left side), the radial extension of the fractional abundance of W^{46+} is shown, demonstrating that in both phases of the discharge the spectroscopic measurement is sensitive to the central W content. Again, after the heating phase a rapid increase of the SXR brightness and c_W was observed. Since the edge parameters were unchanged throughout the discharge, a large variation of the W source was very unlikely (in fact it was below the detection limit). Therefore, the behaviour may be explained within the framework of the picture, already discussed previously. Coupled to the low energy transport in these discharges the anomalous particle transport is also decreased, allowing a very small drift velocity leading to density peaking as shown in Fig. 6.33 (right side).

This density peaking together with low anomalous transport and a moderate peaking of the temperature profiles provokes the neoclassical impurity accumulation, which can be suppressed by central wave heating.

Impurity transport calculations support this physical picture and even a quantitative agreement with the temporal evolution and the amount of the W reduction can be obtained, if the anomal diffusion is moderately enhanced during ECRH. Fig. 6.34 shows the result of a simulation with the transport code STRAHL, where the temperature and density measurements from Fig. 6.33 were used. The inward drift term of tungsten is taken purely neoclassical and the increased transport during ECRH heating is simulated by increasing the central diffusion from 0.05 m^2/s to 0.35 m^2/s [268]. In very recent code simulations for a similar discharge by Dux et al. [311], these model assumptions could be verified. A more general investigation on the correlation of impurity accumulation with density peaking and absence of central heating is presented in Sec. 6.2.5. In parallel to the improved H-Mode discharges, other routes to advanced tokamak operation were pursued, namely high-β discharges as well as discharges with electron ITBs. In both cases the highest performances were obtained during this campaign and the detailed results are presented in [309]. From the viewpoint of the tungsten contamination, they were completely unaffected and c_W stayed mostly below the detection limit of the VUV as well as the SXR diagnostics.

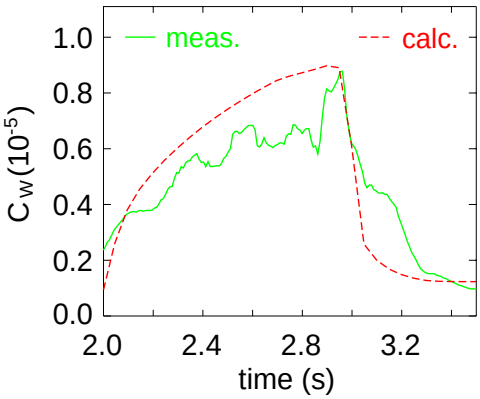

Figure 6.34: Comparison of experimental and calculated W concentration in #14545 at the radial position of the W^{+46} emission (see text for details).

Discharges with 'counter'-injection and QH-Modes

Investigations at DIII-D with 'counter'-NBI revealed a new plasma regime denoted as quiescent H-mode (QH-mode) [312]. It is characterised by a good confinement and the absence of ELMs. However, in contrast to ordinary ELM-free H-mode discharges, which never reach steady state conditions due to an uncontrolled density rise until their back-transition to L-Mode, QH-modes reveal stable discharge conditions at very low density. The physical reason of this different behaviour is not yet clear, but obviously the existence of a so called 'edge harmonic oscillation' (EHO) prevents the uncontrolled density evolution. As reported in [280] and in Sec. 6.1.4, discharges with ELM-free phases as well as with 'counter'-injection are especially prone to impurity accumulation. Indeed, from the QH-Mode, the accumulation of Ni is also reported [313]. In the case

of 'counter'-NBI this may be partly caused by the much more off-axis power deposition from the NBI under otherwise similar discharge conditions. Fig. 6.35 shows the profile of the particle (a.u.) and beam power deposition for the plasma parameters existent in QH-Modes. For comparison the power deposition of co-injection for the same plasma parameters is shown.

Since the plasma parameters are taken identical, the 'birth profile' of the beam ions is similar, but in the case of 'counter'-injection less power is deposited in the central region. Whether the build up of an electric field by the loss of fast ions also plays a role for the increased impurity confinement has not been clarified yet.

As a logical consequence central ICRH was added in the 'counter'-experiments performed at ASDEX Upgrade. In Fig. 6.36 the central tungsten concentrations in H-Modes with similar heating power in the 'co' and 'counter' case are compared. Again, as during the W divertor experiments an increased c_W for 'counter'-NBI is observed but in contrast to the earlier experiments stable discharges were easily achieved with the help of the central wave heating. Whether the higher W concentrations are caused by higher W influxes has not been clarified yet, but all available edge measurements do not hint in this direction. A final answer to this question will only be reached in future experiments where the injection of non intrinsic impurities is planned. Additionally to the comparison of H-modes in 'co'- and 'counter'-operation, Fig. 6.36 reveals that the QH-mode does not show especially high c_W's despite the absence of ELMs, prooving the efficiency of the EHO. A more comprensive study of QH-mode like discharges is published in [315].

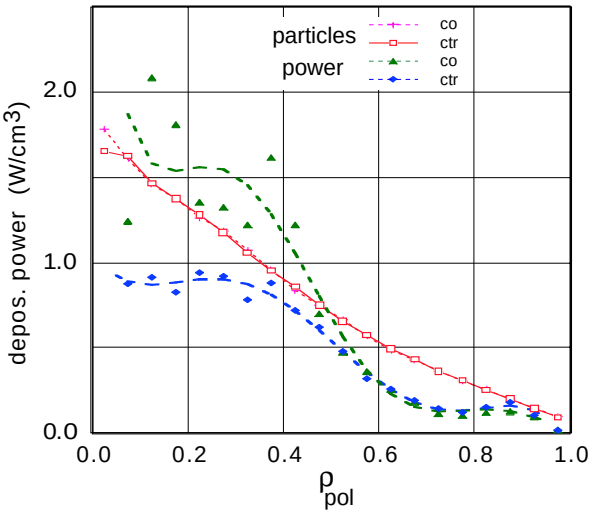

Figure 6.35: Particle (arb. units) and power deposition profiles under low density H-mode conditions for 'co'- and 'counter' direction of the plasma current [314].

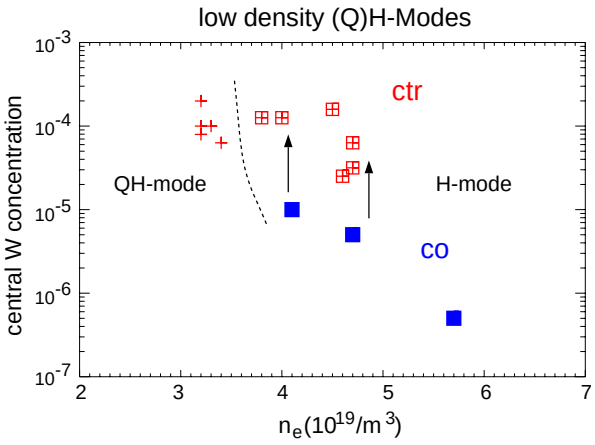

Figure 6.36: Comparison of the central W concentration in low density (Q)H-modes with 'co'- and 'counter'-injection.

Limiter discharges

There are several examples of the use of tungsten as a limiter available in literature (see [172, 316] and references therein) and the early results from PLT [21] showing a strong central impurity accumulation for certain circumstances had a strong negative impact on the further use of tungsten in fusion devices (see Sec. 7.1).
Limiter discharges play a very minor role in the experimental programme of ASDEX Upgrade. Conventional L-modes were only of operational interest, in order to explore their behaviour in regard to the plasma start-up at a fully tungsten covered central heat shield, in a later phase of the W programme. The other range of use is to force discharges to an L-mode edge even at heating powers which lie considerably above the L-H transition threshold in divertor operation, in order to explore ITB discharges with L-mode edge. Common to these discharges is the impact of high energy ions on the tungsten surfaces, which results in increased W erosion and W influx similar to the case of the plasma ramp-down. Due to the direct contact of the W flux to the last closed flux surface (LCFS, see Appendix A.2.3) its penetration to the confined region is also more likely.

Conventional L-mode

To explore the influence of the plasma wall interaction with tungsten surfaces in limiter configurations, several discharges at intermediate densities, ohmic as well as with additional heating powers up to 5 MW were performed during PHASE II. During these discharges the plasma was shifted radially and vertically towards the tungsten tiles. As expected, the W concentration increased during the plasma contact with W surfaces to values around 10^{-5}. However, no serious accumulation was observed for the discharge parameters considered. Fig. 6.37 demonstrates the behaviour of the W concentration in a limiter L-mode discharge with 5 MW NBI heating. The plasma is shifted to the upper end of the central column as demonstrated by the $R-$ and z-position. Immediately after the start of the NB injection c_W reaches is maximum value of $7 \cdot 10^{-6}$ and decreases for more than a factor of two as the electron density is ramped up from 3 to $5 \cdot 10^{19}/\mathrm{m}^3$.

Electron and ion ITB discharges with L-mode edge

A common scenario with an ion and electron internal transport barrier on ASDEX Upgrade used the heat shield as a limiter in order to maintain L-mode edge. In discharge #14274, which was performed after the first boronisation in PHASE II, the central tungsten concentration rises quickly, although the observed influx is much lower as in the later phase, as indicated in Fig. 6.38. Note that for this discharge Γ_W was measurable on two rows of tiles and the average of the signal is shown in order to reduce the scatter.

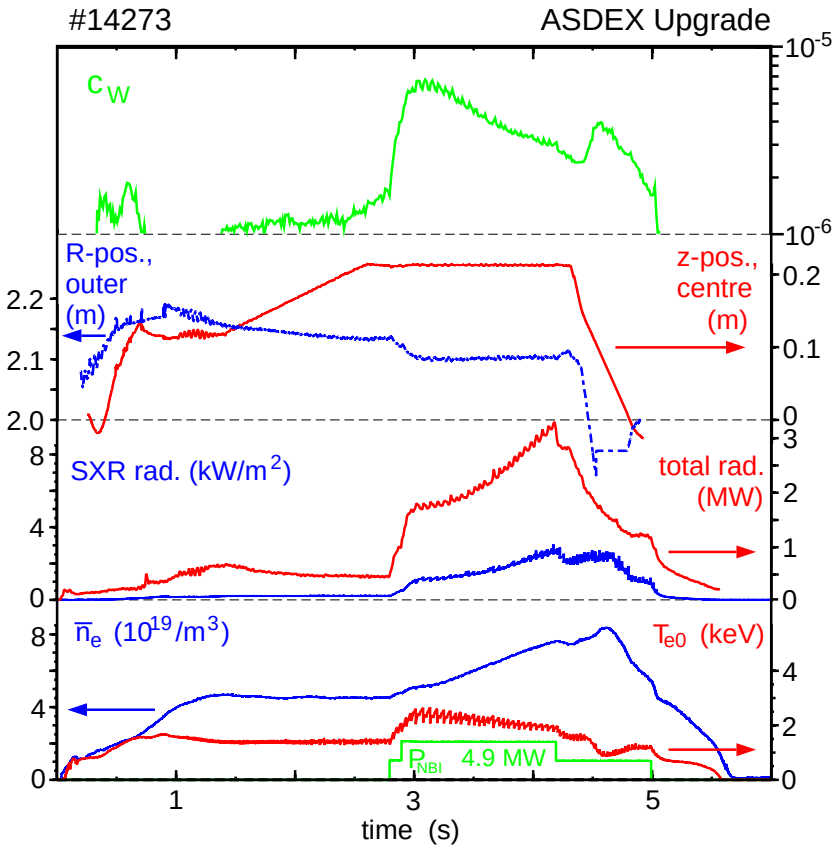

Figure 6.37: L-Mode limiter discharge shifted upward (z-position) and inward (R-position) to the position of W tiles. The W concentration is extracted from quasi-continuum emission by W ions around W^{28+}.

The discharge exhibits a short weak transport barrier (0.8 - 0.9 s), which results in tungsten accumulation to values above the saturation level of the detector. Due to the finite transport time the highest c_W-values were reached shortly after. After the collapse of the barrier the central tungsten concentration drops, although the W influx is higher as in the initial phase due the evolving plasma shape and position. The onset of sawteeth and the decreasing influx lead to a further reduction of c_W. Consequently, as in an ordinary limiter discharge, the plasma completely recovers from the former high W inventories and reaches tolerable tungsten concentrations. After switching off one of the beams, the core temperature dropped below 2 keV and was too low to extract c_W from the SXR radiation.
In general, the limiter ion ITB scenario resulted in the highest tungsten concentrations measured during PHASE II. For discharges with stronger transport barriers even concentrations above $3 \cdot 10^{-4}$ were measured.

Since all of these discharges were performed at the same density with an L-mode edge, it is reasonable to assume that the edge plasma and therefore the tungsten source did

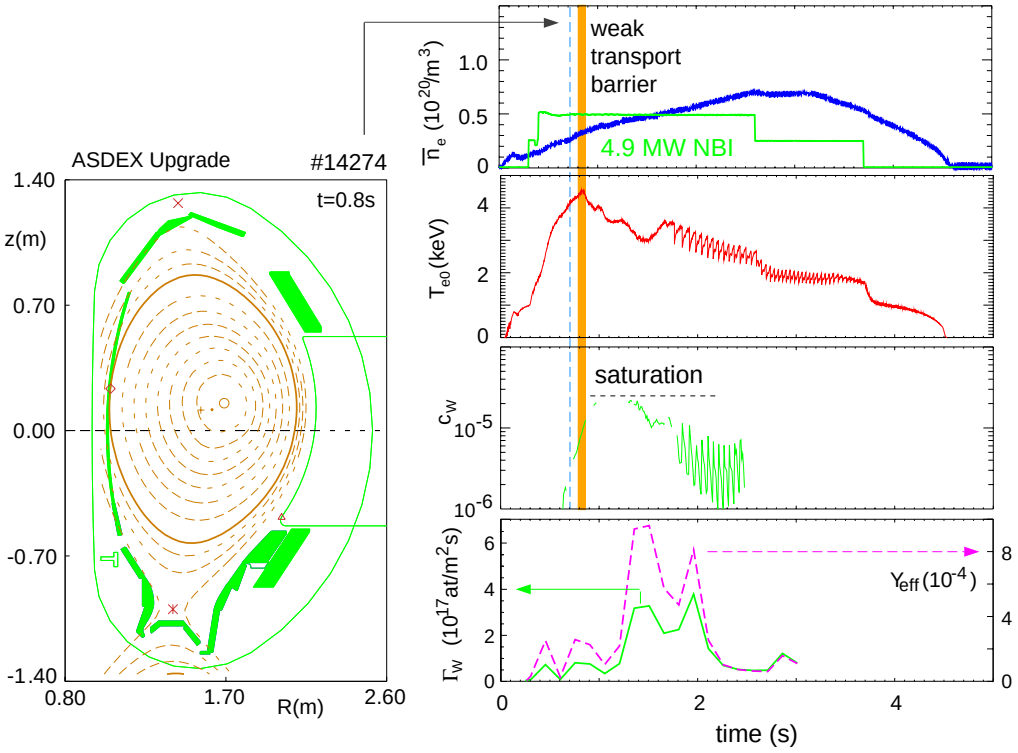

Figure 6.38: Limiter discharge at $I_p = 1$ MA, $B_t = -2.5$ T with weak internal transport barrier showing tungsten accumulation. On the left hand side the plasma equilibrium during the ITB and on the right hand side the temporal behaviour of the main plasma parameters as well as the W influx (Γ_W), the effective sputtering yield (Y_{eff}), and the W concentration (c_W) is given. c_W is extracted from the line emission of W^{46+}.

not change very much for these discharges. This again leads to the conclusion that the strong variation of the central tungsten concentration can only be explained by the strong variation of the transport of the background ions and the impurity ions in the core plasma. However, this kind of discharge was only seen as an interim solution for better suited divertor discharges. Consequently, no efforts were undertaken to optimise the impurity behaviour using central wave heating. Presently, the ion ITBs are run with an early transition to the divertor. They show much lower W concentrations (more than a factor of ten) as their limiter pendant. Due to the short duration of all the ITB discharges run at ASDEX Upgrade, it is not clear whether they have already reached their steady state impurity content.

6.2.5 Peculiarities of W transport

The central tungsten concentration depends strongly on impurity transport, as already indicated for several examples in the previous section. Accumulation becomes evident not only from the W concentration measurements but also from the radiation profile. Figure

6.39 shows the behaviour of the plasma radiation for an ensemble of plasma discharges with low to high auxiliary heating power ($P_{aux} = 3-14$ MW). They are selected because of their complete diagnostic coverage and comprise all discharge scenarios run at ASDEX Upgrade with sufficiently long steady state conditions (high triangularity with phases of constant gas puff, ELM-free, ELM type I and II, advanced H-modes, high β_N). The ratio of the number of data points with and without central radiation peaking is not representative, accumulation appears only under the circumstances cited below, which comprise a very minor part of all discharges. The dataset comprises discharges with a factor four variation in central temperatures and a factor of two in central densities, therefore representing discharges with collisionalities at $r \approx 0.1$ m ranging from $0.05 \leq \nu^*_{pp} \leq 0.8$ for the background ions and $13 \leq \nu^*_{Wp} \leq 83$ for the W ions taking $Z \approx 30$ in the low temperature case and $Z \approx 48$ for high plasma temperatures. (Only collisions of W ions with the background ions have been included.) This means, that the background ions are always in the banana regime, whereas the W ions pass from the Pfirsch-Schlüter regime to the plateau-regime. The total main chamber radiation is low and usually amounts to 25%-40% of the heating power. The typical temporal evolution of most of these discharge scenarios has been presented in the previous section. The features of the dataset are as follows:

- In discharges without accumulation: radiation strongly dominated by edge radiation because the line integrated radiation is almost equal for the bolometer channels with different tangential radii $\rho_{tang} = 0, 0.4, 0.7$.
- In phases with accumulation, enhanced radiation is only visible on central channels ($\rho_{tang} < 0.2$), no increase of the total radiation is observed.
- Only discharges with very long ELM free periods show increased radiation at intermediate radii.
- Central wave heating (ICRH or ECRH) prevents from centrally peaked radiation profiles.
- Density peaking alone is not sufficient for accumulation, but the ratio of the normalised gradients η_D in eq. 5.36 is important. In our investigation this critical parameter is linked to the loss or the absence of sawteeth or fishbones.

Typical conditions, where such centrally peaked radiation profiles are observed are low to intermediate heating power without central wave heating, where the anomalous diffusion is low. In these cases, the central radiation is increased by all impurity species existent in the plasma as seen by spectroscopic measurements. The very small affected volume explains that for similar influxes, strongly different (larger by a factor of 10) central impurity contents may be observed. Finally, this effectively overrides any correlation

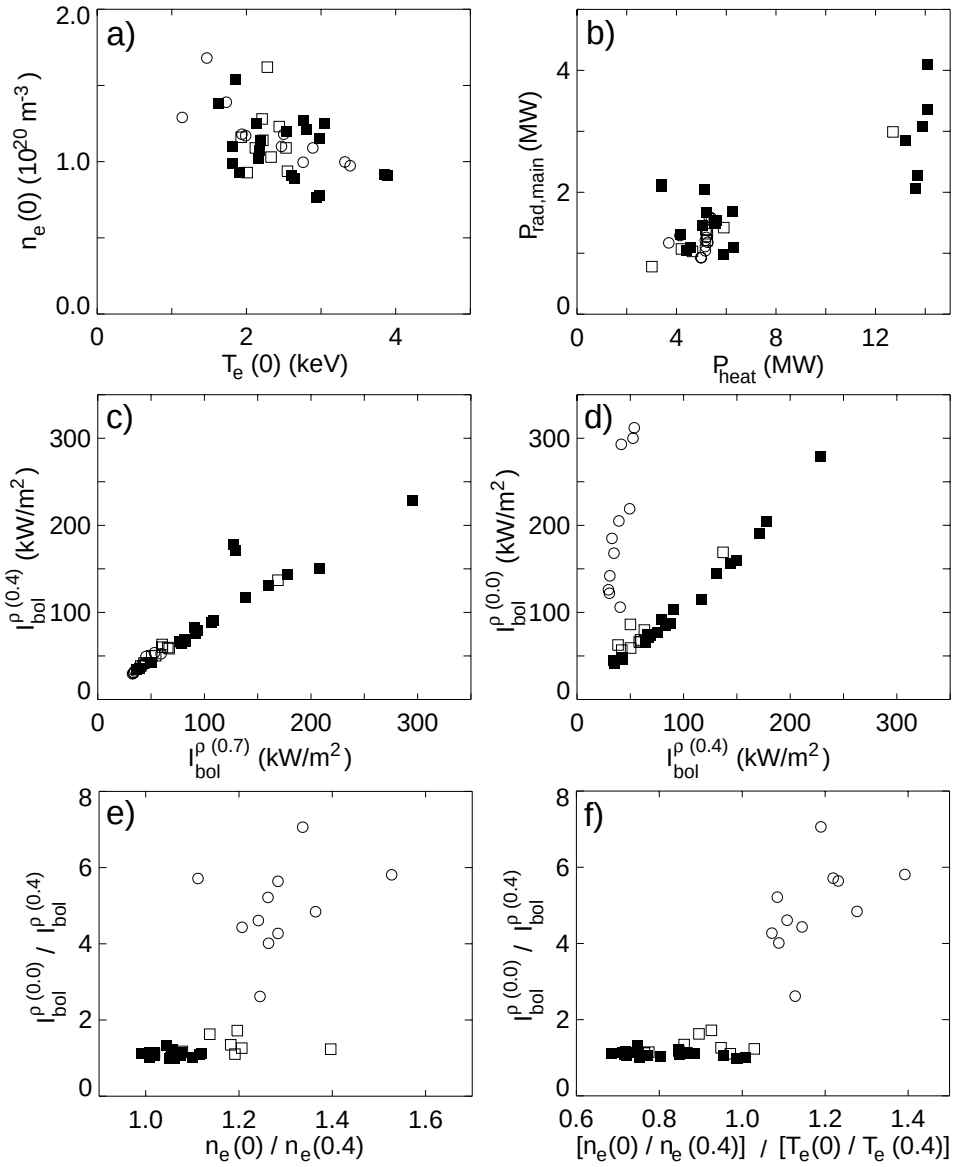

Figure 6.39: Comparison of discharges with and without central impurity accumulation (Filled symbols: Discharges with central wave heating. Circles: Discharges without sawteeth or fishbones)

a) Central electron densities $n_e(0)$ versus central temperatures $T_e(0)$ of the investigated discharges.

b) Total main chamber radiation $P_{rad,main}$ versus total heating power P_{heat}.

c) Comparison of line integrated radiation measurements for a peripheral bolometer channel $I_{bol}^{\rho(0.7)}$ with $\rho_{tangential}^{pol} = 0.7$ and one at intermediate tangential radius $I_{bol}^{\rho(0.4)}$.

d) See c), showing the brightness for a central channel $I_{bol}^{\rho(0.0)}$ versus $I_{bol}^{\rho(0.4)}$.

e) Central radiation peaking $I_{bol}^{\rho(0.0)}/I_{bol}^{\rho(0.4)}$ versus central density peaking $n_e(0.0)/n_e(0.4)$.

f) Central radiation peaking versus $[n_e(0.0)/n_e(0.4)]/[T_e(0.0)/T_e(0.4)] \approx \eta_D^{centr}$

between influx and impurity content in discharges with accumulation. In the discharges chosen for the above data set mostly a combination of NBI and a minor part ICRH is used to stabilise neoclassical tearing modes (NTMs) by reducing the density peaking [317]. This is obviously completely sufficient to prevent impurity accumulation. Hints of this beneficial behaviour during ICRH had also been found in tungsten test limiter experiments in TEXTOR [318], but the physical reasons were not clear at that time. As a side remark it should be mentioned, that (3/2) NTMs do not lead to reduction of impurity peaking, since they cause confinement degradation which is obviously located at larger radii. The above considerations clearly point to the tool which may be used to quench accumulation: An increase of D_{an} at the critical position decreases $\frac{d\ln n_D}{dr}$, $\frac{D_{neo}}{D_{neo}+D_{an}}$ and increases $H\eta_D$. Since the affected volume is very small, the central accumulation can be suppressed very efficiently by central heating *without* strongly degrading the total confinement.

A dedicated power scan for the suppression of central accumulation was performed in

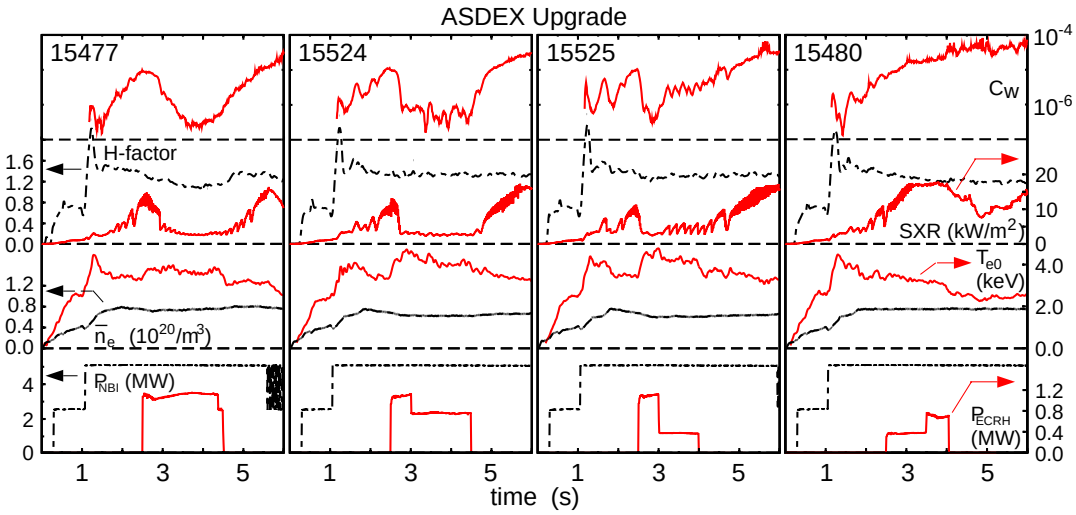

Figure 6.40: Behaviour of similar improved H-Mode discharges $I_p = 1$ MA, $B_t = -2.5$ T, $\delta = 0.35$, showing enhanced c_W with NBI only (first row: c_W; second row: H-factor, SXR-radiation; third row: line averaged density $\bar{n}_e$, central temperature T_{e0}; fourth row: additional heating power NBI (P_{NBI}), ECRH (P_{ECRH}). The W content could be controlled by the amount of additional central ECRH.

improved H-mode discharges ($I_p = 1$ MA, $B_t = -2.5$ T, $P_{NBI} = 5$ MW, $\delta = 0.35$), similar to the one shown in Fig. 6.32. The central ECRH-power was varied from zero (reference discharge) up to 1.2 MW (3 gyrotrons). For the highest ECRH power applied (1.2 MW) a very strong reduction of c_W by more than a factor of 30 and the onset of sawteeth is observed, but at the same time the energy confinement is also degraded. Using 0.4 MW of ECRH does not affect the confinement, but c_W does also not decrease.

The most successful results where achieved when starting with 3 gyrotrons and reducing the power after 0.5 s. In these cases, both effects, the reduction of c_W and the good confinement are maintained. In all cases the discharges return to their initial behaviour after switching off ECRH. The process may be explained within the framework developed above: Coupled to the low energy transport in these discharges the anomalous particle transport is also decreased, allowing for a very small drift velocity leading to density peaking. Analysis of the background particle transport by Stober [319] revealed, that the density peaking is well described with the transport coefficients for the main ion:

$$D = 0.25\chi_{eff}^{turb} \geq D_{neo} \text{ with} \tag{6.3}$$

$$\chi_{eff}^{turb} = (\chi_e + \chi_i - \chi_{i,neo})/2 \text{ and } v = v_{ware}. \tag{6.4}$$

Here χ_{eff}^{turb} denotes the turbulent thermal diffusion coefficient, $\chi_{i,neo}$ the neoclassical one for the ions, (the neoclassical transport for the electrons can be ommitted), $\chi_{i,e}$ the measured thermal diffusions for ions and electrons and v_{ware} the neoclassical Ware pinch. The density peaking together with low anomalous transport and a moderate peaking of the temperature profiles provokes the neoclassical impurity accumulation. The central wave heating obviously counteracts this in several ways. Due to the stiff temperature profiles [320] the central thermal transport χ_{eff}^{turb} is increased and the observed coupling to the particle transport causes flatter density profiles of the background ions, which leads to the reduction of the neoclassical inward drift. Together with the increased anomalous transport this finally yields a strong reduction of the central impurity content. The scan presented in Fig. 6.40 also points to a nonlinear effect governing the threshold for the central heating power needed. Whereas for #15525 400 kW of central ECRH are sufficient to stop central accumulation, 800 kW were not enough in the case of #15480. Obviously, there the radiation loss from the centre surpassed the additional power of the ECRH and no additional turbulent transport could be initiated. This picture can also be used to explain the beneficial effect of a higher heating power at the beginning of the ECRH phases. A quantitative description of the impurity transport calculations for the above discharges is given in [321]. There it could be shown that the peaking of the total radiation as well as of the W concentration can almost entirely be explained by neoclassical impurity transport. Very recently, dedicated experiments with Si injections by LBO, revealed a very consistent picture of the influence of on/off axis heating by NBI, ICRH and ECRH [311]. In this work the heat transport of the background ions was also analysed. Although the overall behaviour of heat and impurity transport was very similar no simple relation could be extracted yet.

6.3 Conclusions from the W Experiments at ASDEX Upgrade

During the experimental campaign 1995/1996 a full toroidal tungsten divertor was installed in ASDEX Upgrade and the discharges performed covered the full operational space of the ASDEX Upgrade tokamak. The experiment demonstrated that the use of W-PFC in a fusion relevant divertor tokamak is feasible. The low sputtering yields for plasma temperatures below 20 eV and the high retention leads to low erosion and negligible migration of W into the main vessel. The carbon concentrations were barely reduced due to the large carbon source from the inner graphite heat shield. Therefore, the erosion rates were strongly dominated by carbon, and strong C-deposition was found at the inner divertor target plates. In the vast majority of discharges, where no accumulation of tungsten is observed, the influence of the W divertor on the main plasma (density and the β limits, confinement, H-Mode threshold) was negligible. The lowest W concentrations were found at high heating power and high plasma density and compatibility with radiating scenarios could be demonstrated. From the W behaviour in single discharges as well as from a statistical analysis of the W concentration of a large ensemble of discharges, the impurity transport within the confined plasma was identified as the driving force behind the central c_W.
Following the experiences from the W divertor experiment (benign behaviour of W, low impact on C-densities) an increasing area of tungsten coated tiles has been installed at the central column of ASDEX Upgrade, reaching an area of 7.1 m^2 in 2001/2002 representing about 85% of the total area of the central column. Again, the influence of the reduction of C-surfaces on the C-densities was small, pointing to the existence of other strong primary sources as the low field side limiter as well as to the fast development of a dynamical equilibrium for the C-sources on all surfaces [322]. The W erosion is larger by at least one order of magnitude compared to the value expected for sputtering by charge exchange particles at the central column. It is mostly attributed to the plasma start-up and ramp-down and there to the sputtering by low-Z ions. Only during direct plasma wall contact or for reduced clearance in divertor discharges was spectroscopic evidence for W influx found. The ohmic flux consumption for current ramp at a tungsten surface was only 5% larger than in the graphite wall case. The increased W content during plasma current ramp up due to direct plasma contact with W surfaces rapidly decreases after X-point formation. Almost no negative influence on the plasma performance was found. Generally, in discharges with increased density peaking and suppressed anomalous transport, a tendency for accumulation was observed. The region affected is very closely localised within $\rho_{pol} \leq 0.2$. Central heating led to a strong reduction of the central impurity content, which can be described quantitatively by neoclassical impurity transport simulations [311]. Simultaneously, only a very benign reduction of the energy

confinement was observed.
A further reduction of carbon is necessary in order to access a regime where the plasma edge is not dominated by low-Z radiation. On the road to this goal, additional parts originally made of graphite were coated. During autumn 2002, W coated tiles for the beam dumps, the upper passive stabiliser loop and the baffle region at the were installed. In the course of these reconstructions, all the tiles of the central column were exchanged for ones of the new design (double tiles), all of them freshly coated with W. As a consequence about 15 m^2 of PFCs were covered by a virgin W surface, with only the divertor regions and the guard limiters on the low field side still consisting of graphite based components.
Although detailed investigations are still under way, no substantial suppression of the C content has been observed, despite the large fresh W surfaces. Since, the reduction of low-Z material is necessary to investigate the plasma behaviour without the low-Z SOL radiation, which up to now dominates the divertor power balance, a further increase of the W surface as well as cleaning the existing W tiles is envisaged for the next campaign. There, the upper divertor as well as the outer retention module of the lower divertor will be coated. In case of a reduction of the C-content, experiments on the compatibility of edge cooling by seeded impurities with W-PFCs will be given strong emphasis. The final goal of the programme will be the characterisation of a virtually low-Z free tokamak with W-PFCs.
Currently, the extrapolation of the ASDEX Upgrade results to ITER or other devices is difficult, as long as (edge) transport is not fully understood. Although edge modelling is in progress [19, 230] further benchmarking is necessary, to obtain consistent results ASDEX Upgrade. These will strongly depend on the knowledge of the background plasma edge which is still evolving. It has to be kept in mind that this is also true for carbon based materials (see for example C-migration and flake production), although there is already a lot of experience in a large number of devices. Since the behaviour of W is found to be consistent with neoclassical transport, no W accumulation is expected for the ITER standard scenario, according to earlier investigations [323]. There the background ions will be deep in the banana regime and the W ions will still have collisionalities above 1 (plateau-regime) similar to the high temperature case of ASDEX Upgrade discussed in Sec.6.2.5. The recipe to prevent central accumulation by central heating may be fulfilled in ITER in a natural way by central alpha particle heating, although the expected α-heating power densities of about 1 MWm^{-3} are considerably lower than the several MWm^{-3}, achieved with the central wave heating in ASDEX Upgrade. However, due to the increased size of ITER by a factor of about 4 (see Sec. 7.2), the heat fluxes will be of comparable size at about 1/5 of the minor radius. Additionally, peaking of the background density caused by the neoclassical ware pinch will play only a very minor role. In scenarios with otherwise peaked density profiles, a prediction of the accumulation

behaviour is uncertain due to the unknown ratio of the gradients and the level of anomalous transport. Concerning the start-up limiter of ITER, tungsten may be an alternative to the currently planned Be-limiter because the influence of the W startup limiter on the flux consumption and on the behaviour of the plasma current during ramp up is very benign and the W concentration decreases rapidly when switching to the divertor configuration.

7. High-Z and Tungsten in Other Fusion Devices

7.1 Results from Earlier and Present Day Devices

Almost all fusion devices designed in the seventies started using the high-Z materials Mo or W for their limiters and other plasma facing components. By improving the vacuum and the conditioning of the vacuum vessel, which essentially means the reduction of oxygen and carbon and their compounds, the plasma properties improved, but at the same time strong central radiation from the high-Z material became evident. Eventually, this again led to a degradation and even to hollow electron temperature profiles. Following these observations the route for the PFC diverged into two branches of tokamak devices: High field tokamaks ($B_t > 5 - 8$ T) operating at high current and high plasma densities kept the high Z-components. Tokamaks operating at moderate current densities, i.e. devices with larger cross sections exchanged their high-Z components for medium-Z materials (as stainless steel) and finally to low-Z materials as graphite or even beryllium. Reviews on the experiments and results with high-Z plasma facing components can be found in [14, 23, 287]. In the following a few experiments will be cited and the results of ones which had the largest impact on the development from high-Z to low-Z PFCs will be described in more detail (also see Table 7.1).

7.1.1 Early Devices with high-Z PFCs

Both, Alcator A (MIT, Cambridge, 1972-1979; [331] and references therein) and FT (ENEA, Frascati, 1975 - 1989; [332] and references therein) were high field tokamaks ($B_t = 10$ T) equipped with Mo limiters. Little is reported on the intrinsic impurity behaviour, but both devices are followed up by similar devices (Alcator C, FTU; see below). The ORMAK tokamak (ORNL, Oak Ridge, 1973-1977; [333] and references therein) was operated with a W limiter and gold-plated liner. The emission of the W quasicontinuum from tokamak plasma was observed there for the first time [159]. Heating by NB counter injection always provoked major disruptions within 30-50 ms. The observed large radiation losses led to the test of low-Z PFCs in the successor experiments ISX-A and ISX-B [333]. The French tokamak TFR (CEA, Fontenay-aux-Roses, 1973 - 1986; [334]

Device	B_T T	I_P MA	R m	a m	τ_{pulse} s	P_{heat}^{aux} MW	High-Z PFC	Ref.
Earlier Devices								
Alcator C	12	0.8	0.64	0.17	0.5	1.5	Mo limiter	[324]
PLT	3.3	0.6	1.32	0.4	1	8	W limiter	[325]
JT-60	4.5	2.7	3.0	0.9	5	30	TiC coated Mo div.	[326]
Present Day Devices								
TRIAM-1M	8	0.03	0.8	0.12	> 7000	0.1	Mo limiter	[327]
TEXTOR	2.6	0.5	1.75	0.46	10	8	Mo, W test-limiter	[328]
FTU	8	1.6	0.93	0.28	1.5	5	Mo, W test-limiter	[329]
Alcator C-Mod	8	1.5	0.67	0.22	1.5	3	all Mo PFCs	[330]

Table 7.1: Technical parameters of earlier and present day fusion devices.

and references therein) was the most powerful tokamak at the time it went into operation. In its first period of operation (1973 - 1976) TFR had a Mo ring limiter. The central energy losses were dominated by Mo radiation (typically $c_{Mo} \approx 10^{-3}$) and during NB (co-)injection the central radiation losses increased further. Similar to other devices an anti-correlation effect between light and heavy impurities was found, apparently due to an increasing edge temperature for small low-Z impurity fractions. These experiences led to the installation of an inconel limiter, which decreased the central radiation losses considerably (typically $c_{Ni} \approx 10^{-3}$). However in ICR-heated plasmas it was observed that after an initial rise of the plasma stored energy, the confinement degraded again due to strong Ni influx and radiation. Finally this led to the installation of graphite limiters. DIVA, a Japanese experiment (1974-1979, JAERI, Naka [335] and references therein) and DITE (1976 - 1992, [336] and references therein) were the first experiments employing a magnetic divertor. DIVA, a rather small device ($R = 0.6$ m), had a poloidal divertor and was initially equipped with an Au-plated limiter, an Au-plated liner and Cu/Mo divertor targets. Gold concentrations were estimated to amount up to $2 \cdot 10^{-3}$ and the high-Z radiation losses were comparable to or even higher than the ones from low-Z impurities [337]. DITE used a so called 'bundle divertor', where a bundle of magnetic field lines is diverted locally (toroidally and poloidally) into a separate chamber. After an initial phase with Mo limiters and divertor ($c_{Mo} \approx 10^{-3}$), the limiters were changed in 1978 to Ti and in 1982 to graphite ($c_C \approx 10^{-2}$). Both experiments observed a strong reduction of impurities and radiation when operating with the divertor instead of limiters [338, 339].

Alcator C

Alcator C was a high magnetic field limiter tokamak operated with Mo and graphite limiters and inconel walls during 1978 until 1983. From bolometric measurements Mo concentrations of up to 1% were deduced in ohmic discharges with line averaged densities below 10^{20} m^{-3}. However, for higher densities (up to $5 \cdot 10^{20}$ m^{-3}) the concentration decreased by two orders of magnitude [324]. The behaviour of the Mo influx was deduced in density and current scans from central spectroscopic measurements using a diffusive ansatz for impurity transport [340]. Although this approach is very indirect it may be justified in that case when comparing only ohmic discharges with similar diffusive transport. The diffusion coefficient was corrected for its q and mass dependence, taking into account the increasing confinement at higher plasma currents and the isotope effect. From the performed scans the authors concluded that physical sputtering by background ions as well as by Mo self-sputtering is the main source of Mo. Erosion by melting and subsequent evaporation could be excluded, since the power load and the Mo source-rate were strongly anti-correlated in the scans. Erosion by charge exchange was excluded in the experiments with an Mo limiter by the deduction of similar influxes for He-plasmas, where CX-sputtering is less efficient, due to the much lower outflux of energetic He atoms. Interestingly, the same qualitative results for the Mo source were observed when using a graphite limiter, although leading at a level about 20 times smaller than with the Mo limiter. There, the erosion of the migrated/re-deposited Mo by CX-sputtering and by self-sputtering was assumed. ICRH Experiments using stainless steel Faraday screens revealed a linear increase of the iron content with ICRH power to values up to fractions of about $2 \cdot 10^{-3}$ [341] in discharges with 400 kW ICR power. As an explanation, sputtering from a thermal plasma was identified, the increased temperature of which was explained by an spurious absorption of ICRH power in the far edge plasma.

Princeton Large Torus (PLT)

PLT became operational in 1975 and represented at that time a significant step in tokamak size scaling [342]. Originally it started with tungsten limiters, chosen because of their thermo-mechanical properties and low sputtering yield. After removing light impurities as oxygen by special discharge cleaning, it soon became clear [21] that central tungsten radiation was occasionally as large as the ohmic input power and consequently led to hollow temperature profiles in hydrogen and deuterium discharges. In these cases, the W concentrations were estimated to be in the range of 10^{-3} [158] (consistent with estimations using present day atomic data). The problem could only be solved by higher densities during plasma current ramp up to shrink the current channel, by edge cooling provided by impurities [158, 325] and to some extent also by titanium evaporation on the vessel walls (Ti-gettering) [343]. However, even in these cases a

reduction by only about a factor of 5 of the W radiation was observed. The effect of the edge ion temperature (measured by Doppler broadening of C III spectral line) was clearly demonstrated in [344], showing an increase of the W radiation by more than a factor of 5 when going from $T_i = 50$ eV to $T_i = 90$ eV. The observed increase of the W concentration with decreasing low-Z impurities points clearly to the fact that the edge operational space of PLT already led to a very strong erosion by background ions overriding the W sputtering from light impurities.

In NBI-heated discharges the situation got even worse [344], so that it was decided to exchange the W limiter for graphite and stainless steel limiters. Only a few discharges after the W limiters had been removed, the W level dropped below the detection limit [344], although a tungsten surface concentration of $\approx$ 15% had been found by Auger analysis in deposited layers on the vacuum vessel surfaces [345]. This led to the conclusion that it was predominantly the direct plasma wall interaction at the limiter rather than the sputtering by charge exchange neutrals that led to the strong plasma contamination. Using graphite limiters much higher central electron temperatures (1.5 keV $\rightarrow$ 2.3 keV) and rather similar carbon concentrations (percentage range) were observed for otherwise comparable discharge parameters [344]. Together with the results gathered in the ORMAK tokamak ([333] and references therein) these experiences finally led to the general use of low-Z plasma facing materials in devices operating at moderate field and current.

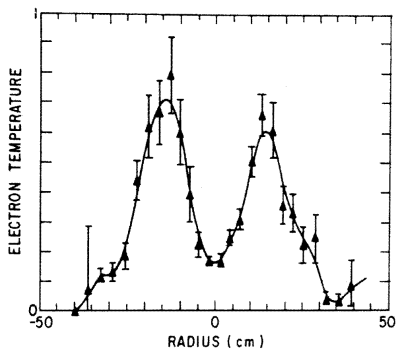

Figure 7.1: Hollow T_e profile measured due to excessive W radiation in a low density ohmic discharge in the PLT tokamak ($B_t = 3.2$ T, $I_p = 360$ kA, $n_e = 2.6 \cdot 10^{19}$ m^{-3}) [21].

JT-60

The JT-60 device (1985-1991) [326] was equipped with a single null poloidal divertor at the low field side of the torus. The inner surfaces of the vacuum vessel were fully covered by armour plates, fixed toroidal limiters and divertor plates made of TiC coated (20 μm) molybdenum and inconel. The device was operated at line averaged densities from $1 - 10 \cdot 10^{19}$ m^{-3} and additional heating powers from NBI of up to 20 MW for about 1 s. Despite the TiC coating, Mo bursts were often observed in limiter operation as well as in divertor discharges using He as the working gas [22]. The Mo injections were attributed to local overheating by a heat load of up to 100 MWm^{-2} and consecutive melting at the edges of several tiles. During these phases the main chamber radiation was enhanced by a factor of ten compared to normal operation. The Mo bursts could be avoided by

sweeping the separatrix during NBI operation, suggesting that melting should be strictly avoided when using the high-Z PFM. In a later campaign carbon PFCs were adopted in JT-60. A comparison of high power ($P_{NBI} = 20$ MW) low density ($\bar{n}_e = 1 - 3 \cdot 10^{19}$ m^{-3}) discharges revealed that with the TiC/Mo the Z_{eff} was lower by up to a factor of four [346], demonstrating that with the high-Z PFCs the low-Z contamination of the plasma was suppressed successfully.

7.1.2 Present-day Devices with high-Z PFCs

TRIAM-1M

The experimental programme of the superconducting high field tokamak TRIAM-1M has been mainly devoted to the investigation of physics and technology of steady state current drive plasmas, achieving low density plasmas with completely driven current (Lower Hybrid Current Drive (LHCD) at 2.45 GHz) which may last for more than two hours [327]. They are performed at a plasma current of 20 kA and with a very low density of $2 \cdot 10^{18}$ m^{-3}. A Mo ring-limiter is used to define the LCFS, but nothing is reported on the behaviour of the intrinsic high-Z impurities.

FTU

FTU (Frascati Tokamak Upgrade) is a compact high field tokamak operating at line averaged densities from $2 \cdot 10^{19}$ m^{-3} to $6 \cdot 10^{20}$ m^{-3} and plasma currents in the range 0.3 to 1.2 MA [347]. The experiments reviewed below were performed with poloidal mushroom limiters made of inconel, Mo or W and a stainless steel vacuum vessel using different surface conditioning techniques. After these experiments a full toroidal Mo limiter [348] was installed. Recent publications report a rather high Mo concentration of up to $c_{Mo} \approx 2 \cdot 10^{-3}$ at low plasma densities ($\bar{n}_e = 3 \cdot 10^{19}$m^{-3}) [349] and a decrease to $c_{Mo} \approx 2 \cdot 10^{-4}$ at ($\bar{n}_e = 7 \cdot 10^{19}$m^{-3}) [350]. Surface conditioning by titanisation [350] and boronisation [349] leads to a strong (up to factor of 5) but transient reduction of the Mo concentration. It should be mentioned that Fe and Ni from vacuum chamber walls, are as abundant in the plasma as Mo [350]. A comparison of the plasma behaviour with different limiter materials or with a siliconised limiter led to the following conclusions [347, 351]:

- The density limits and the onset of MARFE were strongly correlated with the presence of low-Z impurities and the very high density regimes $\bar{n}_e \geq 2 \cdot 10^{20}$ m^{-3} could only be achieved with fully metallic plasma facing materials.

- The main production mechanism for metallic impurities was consistent with physical sputtering from background ions and self sputtering. The different sputtering yields are reflected in the specific impurity content in standard sawtoothing ohmic

discharges, which implies a good correlation between impurity source strength and impurity density in contrast to the observation at ASDEX Upgrade. This might be due to the fact that all the considered discharges were ohmic, exhibiting very similar transport properties.

- The performance and main plasma parameters seemed not to be changed in the presence of the different limiter materials even when the radiation losses were centrally peaked, as in the case of W.

- High-Z accumulation was observed under ohmic conditions with the typical appearance of strong central radiation and hollow temperature profiles. The appearance of accumulation in the start-up phase could be avoided using a low ratio of I_P/n_e during the ramping-up phase of the plasma, similar to the recipe used in PLT (see Sec. 7.1.1). Cooling the edge plasma during current ramp up by small amounts of Ne was also reported to be successful in suppressing the evolution of high-Z accumulation.

Comparison of ohmic discharges using Mo limiters with similar divertor discharges in Alcator C-Mod (see 7.1.2) revealed that the Mo concentration is higher by a factor of 2.5 [352], pointing to the beneficial properties of a divertor.
A post mortem analysis of the W test tiles (2 mm W on Mo substrate), which were exposed to 120 plasma discharges in the course of the above described investigations, was carried out to characterise the erosion and defects [353]. It was concluded that the erosion in steady state discharges was negligible. However, severe melting and cracking was also observed and was attributed to thermal shocks by strong runaway generation during disruptions.

TEXTOR

TEXTOR (Torus Experiment for Technology Oriented Research) is a medium sized limiter tokamak with comprehensive diagnostics to study plasma wall interaction. It was originally equipped with graphite limiters and a stainless steel liner. Carbonisation, boronisation and siliconisation of the vacuum vessel were successfully applied there for the first time in a tokamak [11]. Tungsten and molybdenum were introduced into the device as a dome shaped test-limiter through a dedicated limiter lock [354, 355] or as a poloidal main limiter on a retractable mounting (10 tiles covering about 20% of the poloidal circumference) [172]. Figure 7.2 shows the measured effective W erosion yield as a function of the local plasma temperature on TEXTOR test limiters and on the ASDEX Upgrade outer divertor target (see also Sec. 6.1.2), which were obtained using optical emission spectroscopy.

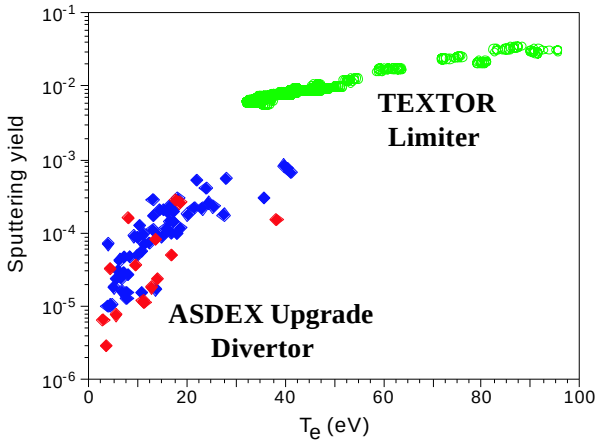

Figure 7.2: Effective W erosion yield as a function of the local plasma temperature at TEXTOR test limiters and at the ASDEX Upgrade outer divertor target (after [14]).

The TEXTOR data were obtained with the limiter 0.5 cm inside the radius defined by the main toroidal limiter and with 1.5 MW of neutral beam heating, resulting in power flux densities between about 8 and 12 MWm^{-2} [173]. At the high plasma edge temperatures in TEXTOR yields as large as 3% are obtained, decreasing down to about 0.5% at the lowest temperatures. The C and O impurity fractions are between 4% and 2% and 2% and 1%, respectively and decrease with decreasing plasma temperature [14]. In TEXTOR and ASDEX Upgrade the tungsten release is dominated by low-Z impurity impact. The higher yields in TEXTOR are principally due to higher plasma temperatures, but the yields are also higher at similar plasma temperatures. This can partly be explained by larger fractions of C and O impurity fluxes (factor 2-5) and by higher W self-sputtering because the W concentration is also considerably higher in TEXTOR (see below). It should be noted that the extracted sputtering yield is larger by almost a factor of 10 compared to the sputtering yield calculated for pure D-plasmas even at $T_e > 50$ eV (see Fig. 6.6). Finally, C deposition layers covering up to 50% of the uppermost W surface, even in regions of net erosion in the outer divertor of ASDEX Upgrade [85] may also lower the measured yield. Eventually in TEXTOR, the benefit of the low W erosion at the limiter is largely reduced by the low-Z impurity impact with the surrounding carbon wall that is in contact with comparable high edge temperatures. The reduction of the edge temperatures in TEXTOR by neon seeding reduces the erosion yields, but the overall tungsten release does not decrease as additional sputtering of tungsten by neon occurs. A substantial decrease of the overall tungsten release occurs under radiation improved confinement conditions (RI-mode) due to reduced particle fluxes to the limiters and, as an additional effect, due to plasma edge cooling [356]. However, the reduction of the high-Z source strength under the RI-mode conditions is overcompensated by an increase of the high particle confinement times, as described below. As described in Secs. 5.1 and 6.1.2, the local re-deposition is determined by the penetration depths of the impurities, the local geometry of the target with respect to the magnetic field lines and the various forces acting on the ionised impurities, such as friction, thermal forces and electric fields. When the penetration depth of the neutrals becomes as small as the ion Larmor radius, local redeposition is likely to occur within the first gyration of the ion, which then is called prompt re-deposition [223].

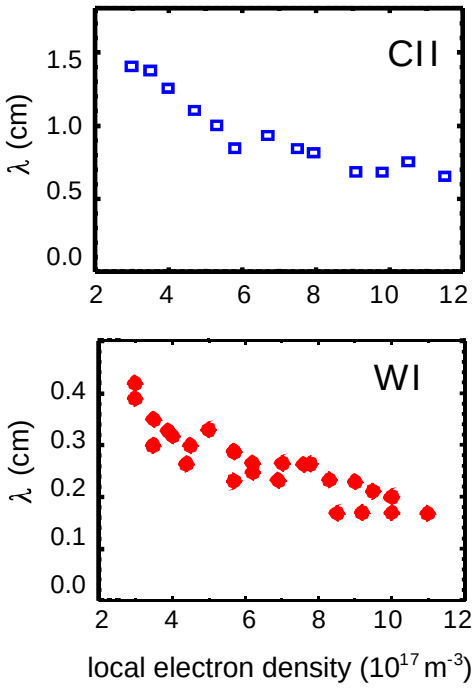

Figure 7.3: Decay lengths of the C II and W I spectral lines in front of a test limiter in TEXTOR as a function of the local plasma density [357].

Figure 7.3 shows the measured decay lengths of the C II and W I spectral lines in front of a test limiter in TEXTOR as a function of the local plasma density [357]. Tungsten has a small penetration depth due to its low velocity as a result of its large mass, similar to the values obtained in ASDEX Upgrade [171]. Under typical TEXTOR conditions the calculated fraction of the prompt redeposition of W reaches values of up to 50% [358] compared to values of up to 90% obtained for divertor plasma conditions [77,92]. In TEXTOR, as in the early observations on PLT (see 7.1.1), the accumulation of high-Z impurities occurred very reproducibly under pure ohmic heating conditions [354]. Although the W and Mo limiters were loaded with only a fraction of the total convective power, of about 4-6%, regular W and Mo accumulation occurred when a critical plasma density was reached (see Fig. 7.4). The high-Z accumulation behaviour was very similar for the Mo and W limiters and was characterised by rapidly growing radiation from the plasma centre and the development of flat or hollow temperature profiles. In the first phase of the accumulation the W concentration rises slightly and shows a decrease of the sawtooth amplitude and temperature. This is followed by a phase in which the on-axis q exceeds unity. Then the sawtooth activity disappears, the increase of the high-Z impurity accelerates, the electron temperature rapidly decreases and a reversed q-profile develops in the central region. This leads to an internal disruption that is followed by a recovery period after which the accumulation can again occur [160]. Interestingly, the critical density for the onset of accumulation depends only weakly on the absolute amount of impurities released, which again strongly suggests that the accumulation is driven by the internal impurity transport. In auxiliary heated plasmas ($P_{aux} > 1$MW) accumulation did not occur (with a few exceptions) in TEXTOR operated with Mo and W test limiters or with a full set of poloidal limiters with a plasma-sprayed W layer [172]. However, the W concentration in the core reaches values of several 10^{-4} at medium electron densities ($\bar{n}_e = 3 - 4 \cdot 10^{19}$ m^{-3}) with a convective heat flux to the test limiter of typically $(2 - 5) \cdot 10^{-2}$ of the total heat flux and a local W/H release ratio of about $2 \cdot 10^{-2}$. This indicates that a significant fraction of the released tungsten enters the confined plasma. For a few cases with neutral beam injection (deuterium) W accumulation has been observed at low electron densities showing that

the system can change into a state where accumulation can occur.

The concentration of W or Mo in the core decreases strongly with increasing density, resulting in high-Z impurity concentrations below the detection limit ($< 10^{-5}$, VUV measurements at TEXTOR) at high densities. The edge cooling of the plasma with neon increases the high-Z impurity content in the plasma, which is attributed to an increase of the impurity confinement time. At intermediate densities, W accumulation occurs for such conditions at higher edge radiation levels ($> 65\%$), which was not observed for Mo limiters under similar conditions. The W accumulation with neutral beam injection develops similarly as for the ohmic case, but the W particles can stay in the core for a long time (> 0.5 s) without any internal disruption. At high electron densities and high edge radiation, accumulation was not observed; this is attributed to a reduction of the W source together with increased screening. Thus W accumulation may be expected for a larger source, for example, as with larger areas covered with tungsten.

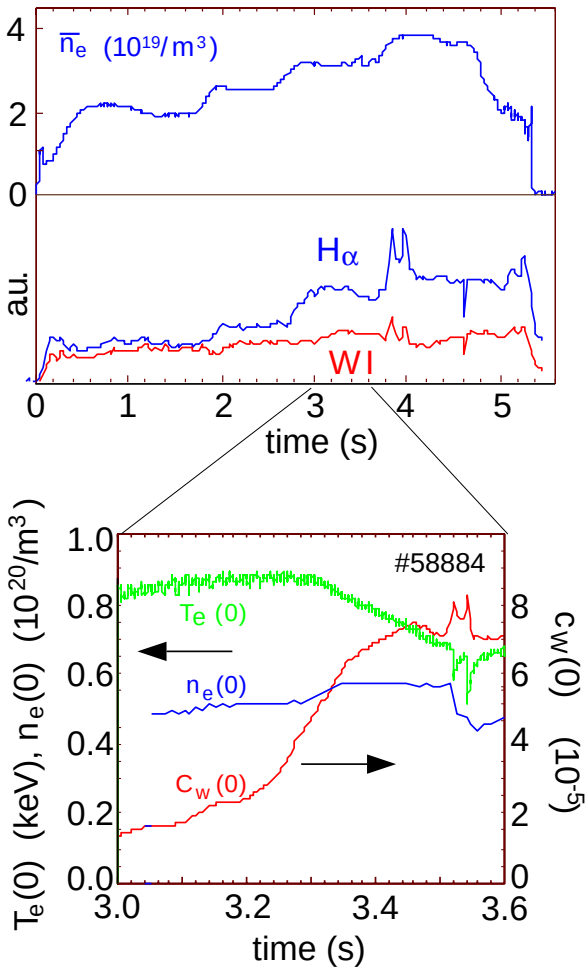

Figure 7.4: Evolution of W accumulation in ohmic plasmas in TEXTOR for critical plasma densities [276].

Central heating by ICRH was already seen to reduce central radiation and prevent high-Z accumulation when applied above a certain power threshold [318, 359]. This is very similar to the effect found in ASDEX Upgrade [268, 269, 321], however the relation to the transport of the background plasma [255, 360] was not clear at that time.

ALCATOR C-Mod

Alcator C-mod is a high magnetic field, high current density, ICRF heated compact tokamak with flexible divertor and shaping capabilities [330, 361]. The Alcator experiments (see also 7.1.1) have contributed a lot to the understanding of high-Z impurities in fusion plasmas, however due to the high densities used (Alcator C-Mod: $\bar{n}_e < 3 \cdot 10^{20}$ m^{-3}) and the high ohmic heating power at a small volume, make an extrapolation to a 'low' current density device as ITER quite difficult. Nevertheless, Alcator C-Mod is

the only divertor tokamak equipped with a first wall and divertor tiles made entirely from molybdenum (see Fig. 7.5). Additionally, the parallel heat fluxes apparent in the SOL ($q_{\|} < 250$ MWm^{-2}) are only a factor of 2-4 below the ones expected in ITER. The Mo concentration is extracted from spectroscopy similar to the methods at ASDEX Upgrade in the VUV and SXR spectral range. A multilayer mirror system is used to monitor line radiation at three wavelength regions: 3 to 4 nm, 6 - 8.5 nm and 11 - 14 nm [362]. Since this type of instrument has a rather low resolution ($\Delta\lambda \approx 0.1 - 1$ nm) the measurements were cross-checked with measurements of a grazing incidence spectrometer. It turned out that the $\Delta n = 0$ transitions in Mo^{30+} at 11.59 nm ($3s^2 {}^1S_0 - 3s3p^1P_1$) and in Mo^{31+} at 12.79 nm ($3s^2S_{1/2} - 3p^2P_{3/2}$) are best suited since they are not blended by other lines [161,362]. The later was also used to extract the concentrations shown in Fig. 7.6 [363]. In the SXR spectral region $\Delta n \geq 2$ transitions originating from Mo^{30+}- Mo^{33+} at 2.9 - 3.8 nm are measured with a 5-chord von Hamos type spectrometer [161, 364].

There are several publications documenting the growing understanding of the Mo sources and its transport. In the first years of operation the only surface conditioning applied in Alcator C-Mod was electron cyclotron discharge cleaning (ECDC) at 2.45 GHz using a sweep of the toroidal field around 0.088 T. From residual gas analysis (RGA) in the exhaust it was concluded that 5 monolayers/day of carbon could be removed from the walls by this method [365]. Nevertheless, carbon was by far the most abundant impurity in the plasmas ($c_C = 0.2\%, c_O = 0.1\%$ and $c_{Mo} = 0.02\%$ for $\bar{n}_e \geq 10^{20}$ m^{-3}) and it was concluded that it originates from the Mo surfaces as an intrinsic impurity [365]. It is believed that a chemical interaction of hydrogen with the C impurities in the bulk of the Mo tiles liberate the C, leading to a progressive enrichment of the first wall surfaces with carbon coatings. To what degree a carbon free surrounding can be achieved in fusion devices is not yet clear, however, reaching higher pump capacities especially during discharges should help to bring down the C inventory.

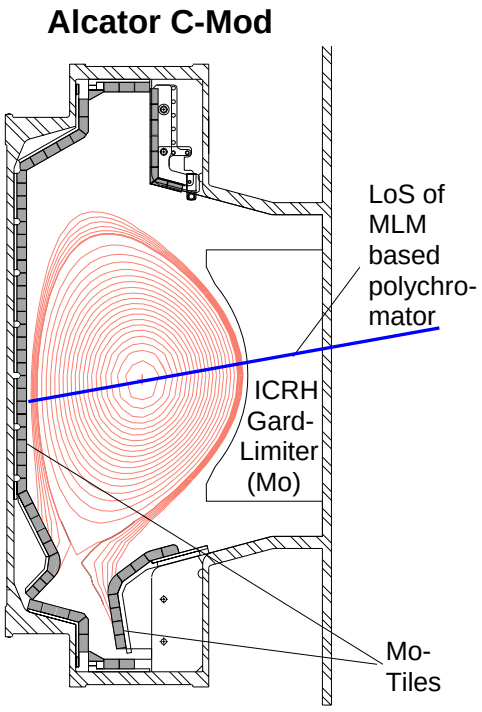

Figure 7.5: Poloidal cross section of the Alcator C-Mod device.

For plasma densities below 10^{20} m^{-3} a rapid increase of the Z_{eff} to values in the range of 3 was observed, partly attributed to a strong increase of the Mo concentration. This is investigated in more detail in Fig. 7.6 [363]. Independently from the mode of operation an increase of the Mo concentration is found towards lower densities. The highest levels

are reached in low density limiter discharges (mostly start-up phase of the discharges) up to fractions of 10^{-2} leading to $\Delta Z_{eff} \approx 4 - 8$, depending on the actual plasma parameters.

During divertor operation the Mo concentrations are almost a factor of 10 lower than in limiter phases. The strong decrease with increasing density for L-Mode plasmas (limiter and divertor) is not so pronounced in H-Mode phases. At the same time an increased scatter of c_{Mo} is evident. Both observations suggest that besides the source, which generally decreases with increasing n_e due to lower edge temperatures resulting in smaller sputtering yields for high-Z metals, the transport into and inside the plasma becomes more important in H-Mode plasmas. This is supported by the observation during Enhanced D_α (EDA) mode [366]. Although there, the engineering parameters are very similar as for ELM-free H-Modes and the energy confinement is almost as high, the particle confinement is much lower as deduced from the density evolution of the background ions. This is also reflected in the Mo concentrations, which lie preferentially at the lower end of the dataset.

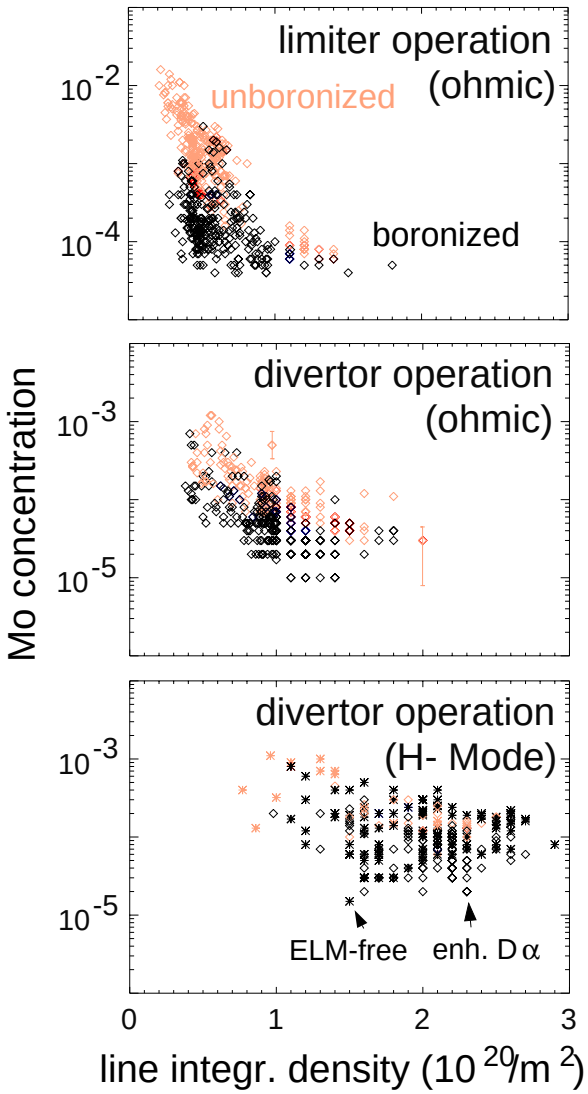

Figure 7.6: Molybdenum concentration for limiter and divertor operation in Alcator C-Mod as a function of the line integrated density. In the lowest plot diamonds represent enhanced D_α and asterisks ELM-free H-modes.

A systematic study of c_{Mo} with P_{ICRH} and ICRH heating scenarios was performed in [352]. Under unboronised conditions a nearly linear increase of the Mo density and the radiated power was observed. At a given ICRH-power the Mo density was twice as high in H-Mode discharges compared to L-Mode discharges, reflecting the improved confinement. For the IBW and the D(^{3}He) heating schemes, up to 100% of the additional heating power showed up as radiated power which was almost entirely attributed to Mo. Additionally, it became evident that ICRH using monopole (single strap) antennae leads to a factor of ≈ 3 higher Mo content under otherwise similar conditions.

In initial investigations, the inner wall and the upper surfaces of the divertor entrance where identified as main sources of the impurities in ohmic discharges. For carbon the divertor source rate was higher by a factor of 2-3 as the inner wall, whereas for Mo the divertor source was recognised to be very low because the energy of the plasma ions was below the sputtering threshold [365]. However, when injecting argon, the molybdenum source from the divertor was significantly enhanced [271], consistent with the model of sputtering by multiple charged impurity ions accelerated in the sheath potential. After a few years of operation, Alcator C-Mod was boronised for the first time in 1995 [367]. Fig. 7.6 compares the central Mo concentrations before and after boronisation for different plasma conditions. The reduction is most pronounced in limiter discharges and smallest for high density H-Mode discharges.
In [368] a quantitative interpretation of the Mo influxes was undertaken. Using the brightness of a Mo I spectral line at 386.4 nm and the adequate photon efficiency, the atomic Mo influx was deduced and compared to sputtering yields calculated using the local plasma parameters. For ohmic discharges a very good agreement between observed and simulated influx could by achieved when taking Mo self-sputtering and sputtering by $\approx$2% B^{3+} into account. However, in RF heated discharges the simulations underestimated the observed influx by up to a factor of three. The authors could not resolve this mismatch, but they propose three different explanations, regarding the first one as the most likely:

- The production of a small fraction of energetic plasma ions,
- non thermal electron distribution, or
- an increase of light impurities as boron.

The last possibility is considered to be very unlikely, since the B-fraction of 2% is already at the upper limit for consistency with Z_{eff}.
The Mo content was found to be proportional to the source rate from the inner wall in limiter discharges, but 'somewhat independent' of the outer divertor source during divertor operation [368]. It was concluded that other sources have to contribute significantly during divertor operation. However the results from ASDEX Upgrade obtained during the W divertor experiment and the in-depth analysis of the recent experiments with the central heat shield, clearly demonstrate that a change in transport properties for different phases of divertor discharges is much more likely.
In parallel to the spectroscopic measurements, post mortem surface analyses of a poloidal set of Mo tiles was performed [369]. The only significant net erosion was found in the outer strike point region amounting to 150 nm in 1200 s divertor operation. The net erosion rate is about a factor of 4 lower than the gross erosion from the spectroscopic measurements. This was attributed to prompt re-deposition, although the calculated

re-deposition seems to be too large, especially for positions lying in the outer SOL. Surprisingly, a surface layer of boron ($\approx 10^{19}$ m$^{-2} = 1\mu$m) was found at all other locations of the cross section. This is in contradiction to the observed Mo influxes and may be explained by micro-structures showing B, as well as Mo surfaces, by toroidal asymmetries in the erosion, or by contributions from the low field as in the case of C influx measurements, all of them observed in ASDEX Upgrade.
In the most recent publications [370,371] an attempt has been made to gain a consistent picture of Mo influxes and resulting Mo content. It is stated that the inner wall, the divertor and the antenna protection limiters contribute to the Mo concentration in the main plasma. In order to identify the main source during a certain discharge phase, correlations between Mo sources and Mo content were investigated. After this 'identification' penetration factors are calculated using the Mo influx from the specific source and the Mo content. It is concluded that (in contrast to earlier investigations [365]) the Mo source at the outer strike point zone dominates the Mo content during ohmic discharges. The influx from the inner wall, although large by number ($> 10^{18}$ s^{-1}) has only a small impact on the central concentration in ohmic divertor discharges. In other words, this means that the penetration probability of Mo particles released from the inner wall is only about 0.05, similar to gas puffing experiments performed earlier in Alcator C-Mod [307]. The dominant Mo sources for the central Mo concentration in ICRH heated plasmas are thought to be the RF antenna screens, which are close to the plasma and from which the Mo particles may have a high penetration probability. In this way a value close to unity is calculated [370]. However, it is not completely obvious what this strong difference in the penetration should cause. From the results of the gas-puffing experiments [307] the authors conclude, that different drift patterns implying different friction forces and entrainment of the impurities and short connection lengths result in a strong backflow of the impurities to the wall. Nevertheless, an intrinsic weakness of this concept is the means of identification of the main sources: According to experiences at ASDEX Upgrade it is the impurity transport which plays the major role for the central high-Z impurity content. This may lead to the identification of a 'major' source which accidentally shows up under these circumstances, but the strong contributions through the other sources – leading to apparently high penetration factors for the single source – cannot be ruled out in this way.

7.2 Plans for Future Devices

All designs for future burning devices use high-Z PFCs. This is born out by the fact that W (and to some extent Mo) might be the only materials which can be used under present day design assumptions to yield an acceptable lifetime of the components. However, this is in strong contrast to the main research line carried out in most leading contemporary fusion devices. This is illustrated by the fact that until a few years ago W trace experiments in JET were not allowed (the experiment which is closest to a future reactor). In the following section the most relevant studies are summarised and the impact of the use of high-Z materials is discussed.

7.2.1 Research Reactors

ITER FEAT

A recent overview of the history, the objectives and status of development of ITER-FEAT is given in [8, 9, 29]. The origin of the ITER project stems from an international consensus on the need of a next step experimental device, with the objective of demonstrating the scientific and technological feasibility of controlled fusion. The integration of burning plasma physics with fusion technologies is thought to be an essential step towards the fusion energy option. ITER should provide a firm basis for the subsequent design of a DEMO device (see Sec. 7.2.2), that would demonstrate the reliable generation of electricity. Six years of joint work under the EDA (Engineering Design Activities) Agreement yielded the ITER design in 1998 [372], which met the objectives set in 1992, focusing on plasma ignition ($Q = \infty$) in inductive operation. However, at that point it was decided to extend the original EDA phase for three more years with the task to reduce the cost to about 50% of the original design, while incorporating the most recent progress in research. The saving could only be achieved by reducing the objectives to:

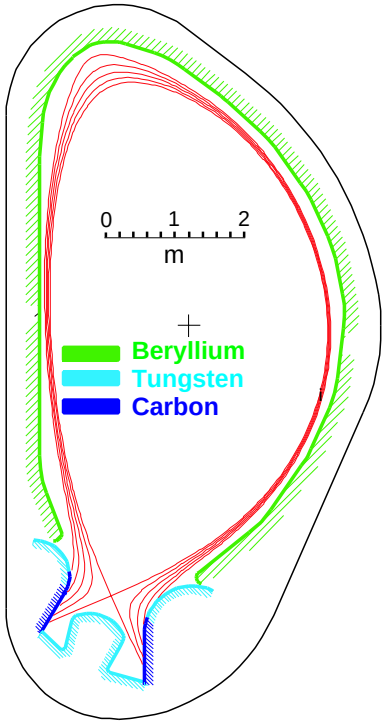

Figure 7.7: Schematic view of the cross section of ITER-FEAT showing the position of the different PFCs [18].

- achieving $Q > 10$ in inductively driven plasmas, not precluding the possibility of controlled ignition
- demonstrating steady state operation through current drive at $Q > 5$

Device	B_T T	I_P MA	R m	a m	τ_{pulse} s	P_{fus} MW	Q	High-Z PFC	Ref.
Research Devices									
ITER FEAT	5.3	15	6.2	2.0	400	500	10	W divertor baffles	[9]
FIRE	10	6.5	2.1	0.60	20	150	10	W divertor	[373]
Ignitor	13	12	1.3	0.47	5	90	10	Mo first wall	[374]
Demo Devices / Reactor Studies									
Demo	6.4	15	6.2	2.0	st.st.	2000	25	W divertor	[375]
ARIES-AT	5.9	13	5.2	1.3	st.st.	1750	50	W divertor	[376]
A-SSTR-2	11	12	6.2	1.5	st.st.	4000	67	W divertor	[377]

Table 7.2: Technical parameters of future fusion devices for research on and demonstration of controlled DT burn.

- integrating essential fusion technologies
- testing components for a future reactor, especially tritium breeding module concepts.

The PFM planned for use in ITER are beryllium, tungsten and carbon. Be is foreseen for the entire main chamber wall, the limiters that will be used for the start-up and the shutdown phase, and for the upper part of the baffle. W will be employed at the lower part of the baffle and the dome region of the divertor and CFC at the high heat flux areas of the divertor plates [10, 294]. Figures 7.7, 7.8 show cross sections of ITER-FEAT denominating the different PFCs.

The low-Z nature of Be is expected to be important during the start-up phase of the discharge in which significant sputtering can occur. Melting at the limiters and the relatively high erosion under normal conditions is not considered as a major problem due to experiences in JET [38]. On the contrary, a beneficial effect is expected from the strong O gettering through Be. The significant flux of hydrogen neutrals on the lower baffles and the dome will lead to unacceptable small lifetimes for almost all materials except tungsten. However, since there was no database for the use of W in a modern divertor tokamak at the time of the first layouts, W is restricted only

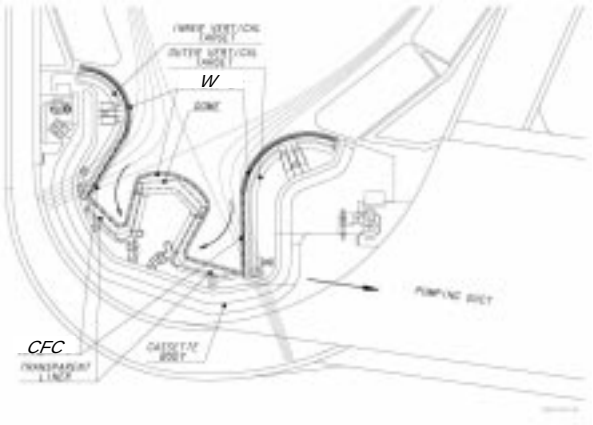

Figure 7.8: Detailed cross section of the ITER-FEAT divertor [54].

to these parts. Figure 7.9 shows different tungsten PFC mock-ups for ITER which were set up for and tested in heat load experiments. The components are textured to reduce the addiction to cracking of the brittle tungsten brazed to the coolant structure. At present the occurrence of extreme temperature excursions at the divertor targets due to ELMs, vertical displacement events (VDEs) or disruptions can not be excluded. This bears the risk of large melt layer losses for metals [378] significantly reducing the lifetime. Therefore, the divertor targets will be made of CFC which will sublime rather than melt, leading to smaller losses and less damage of the surface.

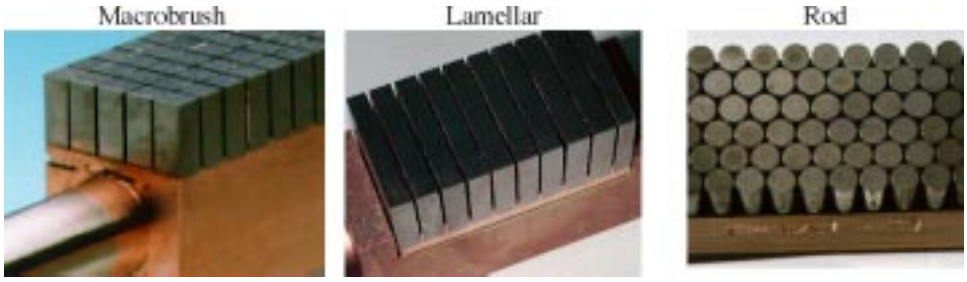

Figure 7.9: Tungsten PFC mock-ups for ITER [54]

Although the physics basis for ITER is extensively described in [10], there are only a few subsections (Chap. 4: Secs. 3.9, 5 and 6.5) dedicated to the choice of the PFM and its implications for the operation of ITER. In particular the use of tungsten is discussed mostly from the viewpoint of erosion behaviour, but very little is said about the constraints on the W content given by confinement requirements. In the assessment of necessary/allowed core radiation power ([10], p. 2394, Table 2) radiation of W is not even mentioned. An estimate on the allowed impurity fractions in ITER is given in [379] stating a fraction of $2 \cdot 10^{-5}$ of W consistent with the zero-dimensional calculations presented in Sec. 2.1.
It is not completely clear to what degree the results of ASDEX Upgrade concerning W are transferable to ITER. Nevertheless, they are recognised as being such useful and the tritium codeposition with carbon such problematic [17,18] that the exchange of the CFC target plates towards W targets is envisaged [294] before transforming the operation to DT mixtures.

FIRE

FIRE (Fusion Ignition Research Experiment) is a design study of a next step burning plasma experiment carried out under the leadership of the Princeton Plasma Physics Laboratory (PPPL) [373, 380]. Its main goal will be the exploration and understanding of confinement, MHD stability, edge physics and wave-particle interactions in a driven fusion reactor. This will require plasmas dominated by α-heating ($Q \geq 5$) which are

sustained for a duration larger than adequate plasma time scales ($t_{dis} \leq 10\tau_E \approx 4\tau^*_{He} \approx 2\tau_{skin}$). The objective of these studies is to find the minimum size and therefore minimum cost device to achieve the above goal, unlike ITER which will allow the study of the technological aspects of a plasma with driven burn because of its much longer discharges ($t_{dis} \leq 100\tau_E$, see previous subsection). As in ITER, two modes of operation are foreseen: Conventional tokamak discharges with monotonic magnetic shear and a design value of $Q = 10$ (with ignition not precluded under optimum physics properties) and advanced configurations with a bootstrap current dominated operation ($f_{bs} \leq 50\%$ at $\beta_N \approx 2.6$ and $f_{bs} \approx 75\%$ at $\beta_N \approx 3.6$) at somewhat lower Q. The second mode will require strong plasma shaping and a stabilisation of the $n = 1$ (MHD) kink-mode by a conducting first wall or even active feedback.
Under these objectives the technological realization will be rather different to ITER. The device will be much more compact (see Table 7.2) and due to the much shorter discharge duration no superconducting TF and PF coils will be used and the PFCs will be cooled inertially. The divertor will be equipped with tungsten brushes as divertor plates and the first wall will be covered with Be as in ITER [381]. For the design of the device $\tau^*_{He}/\tau_E = 5$ and 3% of Be as additional plasma contamination is assumed. The contamination of the plasma by W is completely neglected. Since the central losses caused by W are a factor of $10^3 - 10^4$ larger than the ones from Be (for the same amount of ions) this approach seems not to be adequate. Especially, when bearing in mind the results of this work, because the ratio of surface to volume is quite similar to ASDEX Upgrade and the divertor power load is much higher.

Ignitor

The Ignitor experiment is designed to take a conservative approach to the near term study of the physics of fusion burning plasmas [374]. It uses a combination of compact dimensions and high magnetic fields to support high plasma densities and high currents. The other major areas to be addressed in this proposed near term ignition experiment are the heating methods and the control strategies for ignition, burning and shutdown. Due to its relatively low fusion power (see Table 7.2) and its short discharge duration the technological challenges for the PFCs are rather small compared to the above mentioned devices. Additionally, the design relies on a limiter configuration for an optimum use of the space inside the toroidal field coils. Consequently no large outcome in respect of the questions related to PFCs in a future reactor can be expected. Nevertheless, the device itself crucially depends on very low plasma contamination. According to experiences in the Alcator C-Mod (see 7.1.2 and [271, 362]) there are always some light impurities observed (C, O, F), even in a full metal (Mo) device. But even omitting these impurities the limits for the Mo concentrations are very strict. The design value for radiation

losses is in the range of 5 MW. For the given densities ($< n_e >= 5 \cdot 10^{20}$ m^{-3}) and temperatures ($T_{e0} = 11$ keV) the Mo concentrations have to be below $5 \cdot 10^{-5}$ using the radiative cooling coefficient from [162]. This is a very ambitious goal regarding the values from Alcator C-Mod which is in the range of 10^{-4} (see 7.1.2) for limiter operation at the highest densities.

7.2.2 DEMO-Reactors / Reactor Prototypes

Following the anticipated successful demonstration of thermonuclear burn in an experimental device described above, the need for a DEMO-reactor is foreseen (see for example [382, 383]) which will have all basic features of a power reactor and will demonstrate the the delivery of electrical power. Even more advanced are the plans for reactor prototypes, which are designed for the commercially attractive production of electricity. Fig. 7.10 outlines a possible roadmap starting from a next step device towards a large scale electricity production by nuclear fusion.
Although the size and other engineering parameters will not differ very much from the next step devices presented above, a major extension will be the neutron and plasma fluences due to the projected quasi steady state operation and minimised shutdown periods [53]. This leads to the conclusion that Be will not be an option for the first wall material. Therefore low activation steels and tungsten (as coating) are envisaged as the main candidates [53, 294]. Some studies employ fibre reinforced silicon carbide materials (SiC/SiC) because of their very advantageous activation properties, but at the moment it is not clear how the strong chemical erosion and the attributed T-codeposition will be handled in this case.

DEMO studies

There are several teams around the world working on the design of a DEMO device (see for example [375, 384, 385]). Common to these studies is the aim of a conservative extrapolation of the ITER design, in order to minimise the risk of unforeseen difficulties and the time needed for related R&D and the final construction. A European approach [375] uses almost the identical engineering parameters as ITER (see Table 7.2), except for a higher toroidal magnetic field. In order to reach an operating time of 20 years (30 year lifetime) an increased major radius of 5% is anticipated in order to allow for extra shielding. As for the design itself, the extrapolation of the plasma parameters is moderate. The main operating regime will be H-Mode, with high density, as well as low divertor temperatures ($T_e^{div} < 20$ eV). The maximum power flux of 20 MW m^{-2} is projected and the number of transients due to disruptions and large ELMs is assumed to be small. This scenario will allow the use of tungsten divertor target plates with Cu-alloy heat sink. The lifetime due to erosion and neutron damage is

expected to be 2.5 years of full operation. The first wall and in general the structural materials of in vessel components would be made of low activation ferritic-martensitic steel, such as EUROFER, where Mo, Ni and Nb are replaced by 7-10% Cr. Besides the assumption of $\tau^*_{He}/\tau_E = 5$ ($\Rightarrow c_{He} = 7\%$) and an estimated value of $Z_{eff} \leq 2$ no details are given for the allowed impurity content. Concerning tungsten, the experiences in ASDEX Upgrade support the design and moreover the operation of ITER will supply a firm basis for its implementation. However, the database for the use of steel as a first wall is weaker. At the moment there is no reactor relevant divertor tokamak which uses steel as PFC (only very recently the small Japanese tokamak JFT-2M has adopted ferritic steel as first wall [386] with positive preliminary results). Estimation based on erosion measurements in ASDEX Upgrade [387] suggest that mid-Z materials reveal the smallest 'figure of merit' in terms of tolerable concentrations and observed erosion yields. Indeed, DIII-D, which is fully clad with graphite and JET, which is also equipped with graphite tiles in the regions of largest plasma surface interaction, report on the accumulation of Ni (most probably from the vacuum vessel) in discharges with very good central confinement [249, 313]. Therefore the use of W coatings on steel substrate as proposed in [53] might be reconsidered.

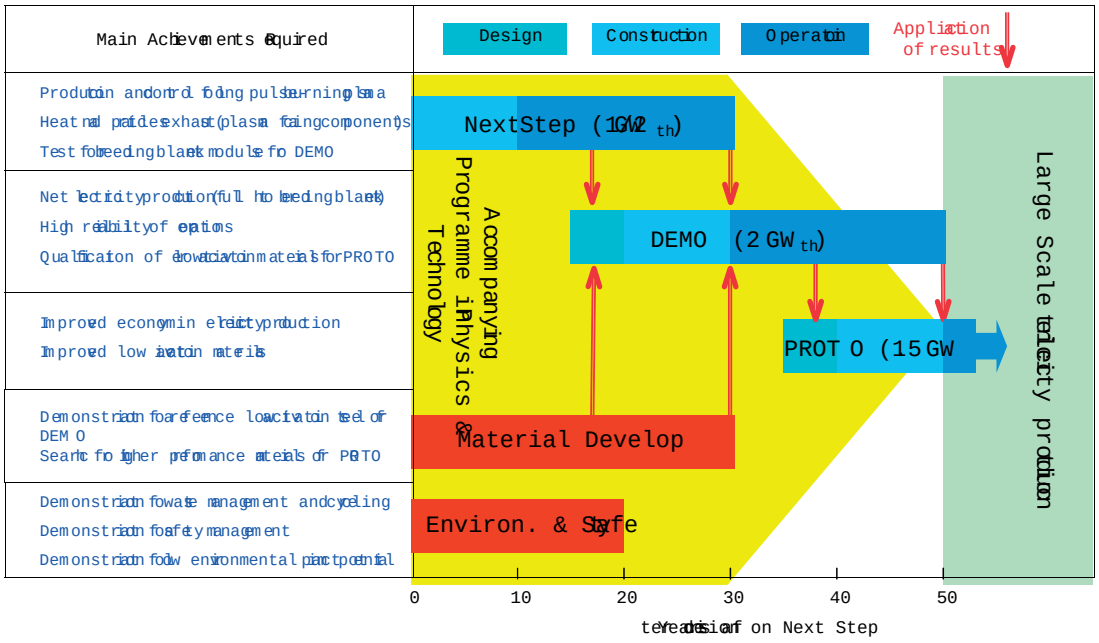

Figure 7.10: Tentative roadmap towards large scale electricity production by nuclear fusion (after [388])

The DEMO-reactor proposed by a Japanese group [385] is also based on the ITER design but they have taken a step closer to the Japanese reactor prototype A-SSTR2 (see below). This manifests in the larger aspect ration ($R/A = 5.8/1.45$) and the higher magnetic field ($B_t = 9.5$ T) which implies the use of an oxide high temperature superconductor

(Bi2212). Since the fusion power will be similar as in [375], the same power loads for the divertor, as well as the first wall are expected. Tungsten has again been chosen as the PFM in the divertor and W coated low activation steel is envisaged for the main chamber.
The Russian DEMO [384] is also projected to be at a higher toroidal field ($B_t = 8.75$ T) and at even larger aspect ratio ($R/A = 7.8/1.5$) pointing to an operation in the mainly 'advanced tokamak' regime. Here a firm extrapolation from today's tokamaks is not possible, since there is no database for the necessary high densities. In their study the authors rely on the reduction of divertor power load by Ne seeding. In the divertor W or Mo armour will be used, in a similar way to the other studies. In the main chamber Be as first wall is planned. An erosion of 1.8 mm per year is expected leading to a lifetime of 5 years for a thickness of 18 mm. This lifetime would also fit to the whole blanket module. However, as already discussed at the beginning of the section, the use of Be as PFM in a reactor like device is very unlikely due to present day experience [53, 294].

ARIES studies

The ARIES (Advanced Reactor Innovation and Evaluation Study) design studies are performed under programmatic leadership of the University of California, San Diego. There is a complete family of designs [389] starting with ARIES-I from 1990 and with the most recent studies ARIES-ST (1999) and ARIES-AT from 2000 [376] . The aim of these studies is to provide a design of a compact fusion power plant under the constraint of low values for the cost of energy (COE). The most recent design, ARIES-AT, relies on steady state advanced tokamak discharge scenarios, with high elongation ($\kappa = 2.18$) and triangularity ($\delta = 0.84$), completely non-inductive current drive and confinement at the ITER97P H-Mode scaling. The first wall is set up by SiC/SiC composite for the structure and blanket, to minimise radioactive waste. The T-breeding is achieved via the coolant, where liquid $Pb_{83}Li_{17}$ will be used. The divertors (there will be an upper and a lower divertor) will also be set-up by SiC/SiC composites coated by a layer of 3.5 mm plasma sprayed tungsten. The averaged divertor heat flux is calculated to be 1.75 MWm^{-2} and the peak value is analysed to be 5 MWm^{-2}. These values are very similar to that envisaged for ITER under steady state conditions. However, the assumption of a plasma temperature of 600 eV within the strikepoint position [390] would lead to a run away effect by self sputtering $Y_{eff} > 1$ even without 'off normal' events and would not allow several years of operation without replacement. Another consequence of such an excessive erosion would also be unduly high W concentrations in the plasma. There is no estimation for the contamination of the core plasma by ions from the PFC (C, Si, W). However, the reference core radiation fraction is taken to be about 0.3 leading to about 0.3 MWm^{-3} as the limit for core radiation. For the (volume) averaged plasma

parameters ($n_e \approx 2.1 \cdot 10^{20}\mathrm{m}^{-3}$, $T_e \approx 16\mathrm{keV}$) [390] the radiation would be enhanced by 10% for a W concentration of $c_W \approx 10^{-5}$ (omitting radiation from other impurities).

SSTR studies

The SSTR studies are the Japanese counterpart to the American Aries studies carried out at JAERI (Japan Atomic Energy Research Institute), Naka. The most recent design is the A-SSTR2 tokamak reactor [377]. This study takes a very optimistic view of the potential of advanced tokamak operation. A-SSTR2 would be operated without a centre solenoid coil system (ohmic transformer), relying instead on the plasma breakdown and current ramp up by radio frequency wave and neutral beam current drive. For the confinement, an H-factor (ITER98, ELMy H-mode) of 1.25 and for the maintained normalised pressure $\beta_N = 4$ is assumed . The blanket structure material will consist of SiC/SiC composite and its cooling will be performed using high pressure He (10 MPA) at an outlet temperature of 900° C to achieve a high thermal efficiency of above 50%. The divertor will also be designed to employ tungsten, but as in the Aries studies the problem of W erosion in the divertor and the plasma contamination are not covered in depth. On the contrary, an unrealistic case of divertor plasma cooling by neon is assumed. In the model assumption, 2.5% of Ne is needed in the divertor to cool the plasma from 200 eV down to 20-30 eV. Besides the fact that this amount already seems rather high for the maintenance of the fusion reaction, since the Ne divertor compression $C_{Ne}^{div}/C_{Ne}^{core}$ is expected to be in the order of 10 (see [391] and Sec. 2.4), the envisaged plasma temperatures are still far to high to have acceptable erosion in the presence of Ne. For temperatures above 20 eV the sputtering yield of Ne^{3+} reaches values above 2×10^{-1} (see also Sec. 6.1.2) leading to an effective erosion of 5×10^{-3}.

8. Conclusions and Outlook

Research on magnetically confined fusion has established a firm basis for the demonstration of the scientific and technological feasibility of controlled fusion. However, in the context of a future reactor, the choice of the armour materials for the first wall is still a critical issue. Whereas during the last two decades of fusion research almost all fusion devices have implemented low-Z carbon based materials as plasma facing materials due to their benign properties in respect to the core plasma performance, the long term retention of the radioactive tritium fuel in co-deposited carbon layers may be unacceptable for reasons of fuel supply, safety and also public acceptance of fusion energy. Extrapolation of the fuel retention from present day devices to a steady state burning fusion plasma is difficult but the retention might be unacceptable and will not allow the long term operation of the device. This serious concern caused the reconsideration of high-Z based plasma facing components. Therefore, a lot of effort has been put into the investigation of tungsten at the Garching tokamak ASDEX Upgrade. Although much smaller than a future reactor, there are a lot of properties which are relevant to reactor studies. Namely, the closely scaled geometry of the device, especially of the divertor, and plasma edge parameters very close to those envisaged in a reactor. After preparatory experiments concerning the performance of coatings, detection of tungsten in the plasma and probe erosion, a fully coated tungsten divertor was installed in ASDEX Upgrade during 1996. As a further step in the tungsten programme, W was used as a PFC in the main chamber in order to pursue the aim of the total elimination of carbon. During the experimental campaign in 2000 an area of 1.2 m^2 of the central column was coated with W and actually, since 2002, ASDEX Upgrade has been operated with a completely W covered central column.

The need for a diagnostic to characterise the W behaviour, initiated spectroscopic investigations. In order to quantify the source, spectroscopic signatures from neutral or low ionisation states of W have to be used. In collaboration with the Plasma Diagnostic Department of the MPI für Plasmaphysik a $^7S_3$–$^7P_4^o$ transition in neutral W was identified to be strongest under the conditions which are predominant at the plasma edge. The inverse photon efficiency, S/XB, was determined as a function of electron temperature, which allowed the gross erosion in a large number of discharges to be quantified. The S/XB-value could be confirmed under fusion reactor conditions, with a sublimation

probe inserted into the divertor of ASDEX Upgrade. A large amount of spectral lines were measured for the first time at ASDEX Upgrade in the VUV and the SXR region. In collaboration with the Lawrence Livermore National Laboratory, they were identified within the framework of *ab initio* calculations using a relativistic Hartree Fock code and a collisional radiative model, which proved a high degree of precision. The measurement of the W emission from different ionisation states allowed the extraction of the tungsten concentration c_W at different locations in the plasma. Using the spectroscopic signatures considerably lowered the detection limit for W in the plasma compared to investigations in earlier devices. Therefore, the spectroscopic investigations represent the back-bone of the tungsten programme at ASDEX Upgrade. This work stimulated supplementary investigations at the Berlin EBIT [182] which revealed, however, that the (VUV-)spectra of W may appear very different in a tokamak and an EBIT due to different population/de-population processes, making the spectroscopic research at a fusion plasma itself indispensable. Additionally, work at JET has just started [392] and will be continued in collaboration with ASDEX Upgrade [237] to provide tools for a fast analysis of high-Z spectra within the framework of ADAS.

One of the main success' of the W programme at ASDEX Upgrade was to prove that the use of the high-Z material of W does not contradict successful operation of a divertor tokamak. Although this sounds lake a trivial matter the very negative experiences in limiter tokamaks during the 70's and 80's had set a high threshold for its reconsideration. The W divertor experiment demonstrated that the low sputtering yields for plasma temperatures below 20 eV and the high retention leads to low erosion and negligible migration of W into the main vessel. The carbon concentrations were barely reduced due to the large carbon source in the main chamber. Therefore, the erosion rates were strongly dominated by carbon, and strong C deposition was found at the inner divertor target plates. In the vast majority of discharges, where no accumulation of tungsten was observed, the influence of the W divertor on the main plasma (density and β limits, confinement, H-Mode threshold) was negligible. From the W behaviour in single discharges as well as from a statistical analysis of the W concentration of a large ensemble of discharges, the impurity transport within the confined plasma was identified as the driving force behind the central tungsten concentration. Following the experiences from the W divertor experiment, an increasing area of tungsten coated tiles has been installed at the central column of ASDEX Upgrade, reaching an area of 7.1 m^2 in 2001/2002 representing about 85% of the total area of the central column. Again, the influence of the reduction of C surfaces on the C densities was small, pointing to the existence of other strong primary sources, for example the low field side protection limiters and to the fast development of a dynamical equilibrium for the C sources on all surfaces. The W erosion is larger by at least one order of magnitude compared to the value expected for sputtering by charge exchange particles at the central column and it is mostly attributed to the

plasma start-up and ramp-down and to the sputtering by low-Z ions. Only during direct plasma wall contact, or for reduced clearance in divertor discharges was spectroscopic evidence for the W influx found. The increased W content during plasma current ramp up due to direct plasma contact with W surfaces rapidly decreases after X-point formation. Again, almost no negative influence on the plasma performance was observed, but in discharges with increased density peaking and suppressed anomalous transport, a tendency for accumulation became evident in accordance with neoclassical impurity transport. The use of the high-Z PFCs in a fusion relevant environment played a strong role in the revival of the impurity transport investigations. In ASDEX Upgrade these investigation represented a large part of the programme, since accumulation might prevent the use of W in a reactor. This focus allowed us to neatly characterise the central impurity transport [246, 311] and to develop tools for the mitigation of accumulation, which also influenced the research at other devices. After the first demonstration of the very beneficial influence of central heating on the central impurity behaviour in ASDEX Upgrade [268], the technique was quickly adapted in other devices [393,394] and it led to a optimistic view of the burning phase in a reactor concerning impurities, even including He.

A further reduction of carbon in ASDEX Upgrade is necessary in order to access a regime, where the plasma edge is not dominated by low-Z radiation. On the road to this goal, additional parts originally made of graphite were coated. During autumn 2002, W coated tiles for the beam dumps, the upper passive stabiliser loop and the baffle region at the inner lower divertor were installed. In the course of these reconstructions, all the tiles of the central column were exchanged for ones of the new design (double tiles), all of them freshly coated with W. As a consequence about 15 m^2 of PFCs were covered by a virgin W surface, with only the divertor regions and the guard limiters on the low field side still consisting of graphite based components. Although detailed investigations are still under way, no substantial suppression of the C content has been observed, despite the large fresh W surfaces. Since the reduction of low-Z material is necessary to investigate the plasma behaviour without the low-Z SOL radiation, which has up to now been dominating the divertor power balance, a further increase of the W surface (the upper divertor as well as the outer retention module of the lower divertor will be coated) as well as cleaning the existing W tiles is envisaged for the next campaign. In case of a reduction of the C content, experiments on the compatibility of edge cooling by seeded impurities with W PFCs will be given strong emphasis. The final goal of the programme will be the characterisation of a virtually low-Z free tokamak with W PFCs.

Currently, the extrapolation of the ASDEX Upgrade results to ITER or other devices is difficult, as long as (edge) transport is not fully understood. Although edge modelling is in progress [19, 230], further benchmarking is necessary to obtain consistent results for ASDEX Upgrade. These will strongly depend on the knowledge of the background

plasma edge which is still evolving. It has to be kept in mind that this is also true for carbon based materials (see for example C migration and flake production), although there is already a lot of experience in a large number of devices. Since the behaviour of W is found to be consistent with neoclassical transport, no W accumulation is expected for the ITER standard scenario, according to earlier investigations [323]. The recipe to prevent central accumulation by central heating may be fulfilled in ITER in a natural way by central alpha particle heating, although the expected α-heating power densities of about 1 MWm^{-3} are considerably lower than the several MWm^{-3}, achieved with the central wave heating in ASDEX Upgrade. However, due to the increased size of ITER by a factor of about 4, the heat fluxes will be of comparable size at about 1/5 of the minor radius. Additionally, peaking of the background density caused by the neoclassical ware pinch will play only a very minor role. In scenarios with otherwise peaked density profiles, a prediction of the accumulation behaviour is uncertain due to the unknown ratio of the gradients and the level of anomalous transport. The very small increase of the ohmic flux consumption and the benign behaviour of the tungsten during the plasma start-up phase in ASDEX Upgrade may lead to a reconsideration of the start-up limiter in ITER. Here, tungsten may be an alternative to the currently planned Be-limiter, thus leading to a larger margin for the thermal load, due to its more advantageous thermo-mechanical properties. Even more, if the ongoing research on ELM mitigation [395] will prove its feasibility, tungsten could replace the CFC strikepoint components at the beginning of ITER. Whether there will also be a move from the Be armour to W coated components in the main chamber of ITER, as it might be necessary anyway in a reactor is not foreseeable yet and will depend on the results of further simulations.

It is really too early to conclude from the presented experiments whether a future fusion device could be operated with major W PFC. However, the experiments at ASDEX Upgrade have provided precious tools for the diagnostic of W and will serve as important benchmarks in future simulations.

A. Magnetic Fusion

A.1 Basic Nuclear Fusion

A.1.1 Reactions for Nuclear Fusion

In the *pp*-reaction chain in stars during their initial burn phase, the fusion of two protons to deuterium involves the weak interaction and leads to very low reaction rates. Therefore, the power density in the core of a burning star, like the sun, is very low (only about 300 Wm^{-3}) and it does not allow efficient energy production on a terrestrial scale. For this reason, only fusion reactions not involving the weak interaction can be employed. To undergo fusion the nuclei have to experience the nuclear force which is very short ranged. This means they have to penetrate the Coulomb wall (tunnelling) resulting from the electric charges of the nuclei. As a consequence, the most suitable nuclei are those with lowest nuclear charges. These reactions are listed below:

$$\mathrm{D} + \mathrm{D} \longrightarrow n + {}^3\mathrm{He} + 3.27\ \mathrm{MeV} \tag{A.1}$$

$$\text{or} \quad p + \mathrm{T} + 4.03\ \mathrm{MeV} \tag{A.2}$$

$$\mathrm{D} + {}^3\mathrm{He} \longrightarrow p + {}^4\mathrm{He} + 18.35\ \mathrm{MeV} \tag{A.3}$$

$$\mathrm{D} + \mathrm{T} \longrightarrow n + {}^4\mathrm{He} + 17.59\ \mathrm{MeV} \tag{A.4}$$

$$\mathrm{T} + \mathrm{T} \longrightarrow 2\,n + {}^4\mathrm{He} + 11.33\ \mathrm{MeV} \tag{A.5}$$

From these, the DT-reaction is favoured because of its high energy gain and the highest cross section at the lowest energies due to a resonance in the ^{5}He compound system, lying about 50 keV above the energy of the the DT-system (see [396]) in the entrance channel. Nevertheless, the maximum cross section for this reaction ($\sigma_{DT} \approx 4$ barn $= 4 \cdot 10^{-28}$ m^2 at 70 keV) is about 25 times smaller than the Coulomb cross section at the same energy level. This means that small angle scattering of the charged particles, dissipating away their energy, is much more likely than a central collision followed by a fusion process. Therefore the only viable way for efficient exploitation of fusion energy is using a confined plasma.

Besides inertial confinement, which is beyond the scope of this work, the confinement by magnetic fields is possible (see Sec. A.2). There, the fuel particles usually have an isotropic thermal velocity distribution and the reaction parameter $< \sigma v >$ is given as,

$$< \sigma v >= \frac{4}{(2\pi\ m_r)^{1/2}\ (kT)^{3/2}} \cdot \int \sigma(E) \cdot E \cdot \exp\left(-\frac{E}{kT}\right)\ dE, \tag{A.6}$$

where m_r is the reduced mass of the reaction partners, σ the reaction cross section and E the energy in the centre of mass system.
Fig. A.1 shows $< \sigma v >$ for some of the most relevant fusion reactions, calculated after [397].

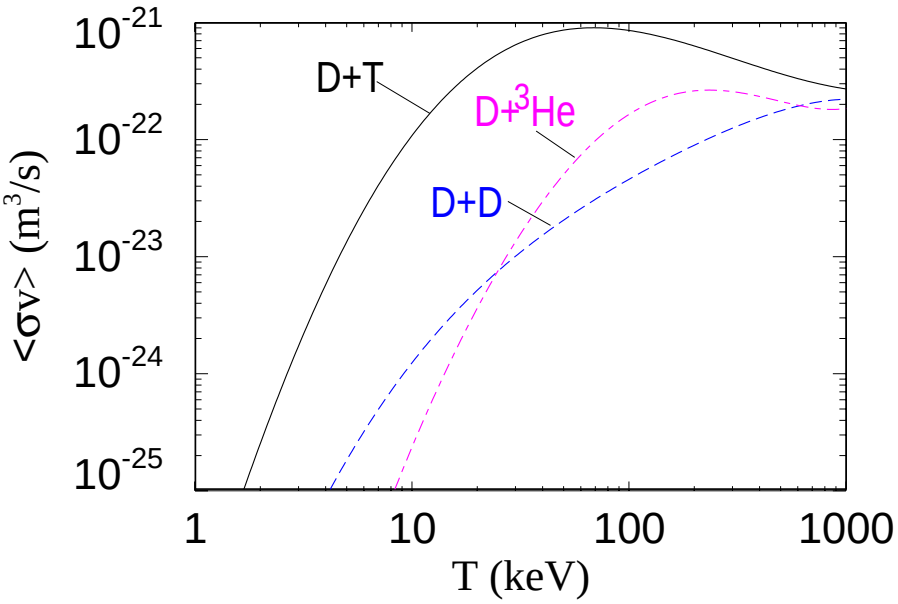

Figure A.1: Reaction parameter for the most relevant nuclear reactions in nuclear fusion.

A.1.2 Simple criterion for an ignited plasma

The fusion power P_{Fusion} in a DT-plasma is given by

$$P_{Fusion} = \frac{n^2}{4} \cdot < \sigma v > \cdot E_{Fusion}, \tag{A.7}$$

where n is the electron density in a pure plasma with $n_D = n_T = n/2$.
The energy loss by heat and particle transport, by charge exchange and by radiation can be characterised empirically by the energy confinement time given as:

$$P_{loss} = \frac{3\ nkT}{\tau_E}. \tag{A.8}$$

with $3nkT$ the stored energy of the plasma (a factor of two because electrons *and* ions have to be considered).

Combining eq. A.7 and A.8 for the DT reaction with $E_{Fusion} = E_n + E_\alpha$, one gets in magnetic confinement, where the neutron leaves the plasma without interaction

$$(n\tau_E)_{ignit} = \frac{12\ kT}{<\sigma v>\ E_\alpha} \tag{A.9}$$

as the condition for ignition of the plasma. Whereas the left side of the equation contains only the dependence on the fuel density and the 'thermal insulation' τ_E, the right side represents the temperature dependence, since $<\sigma v>$ is a strong function of T (see Fig. A.1). Multiplying this equation on both sides with T one gets the more common expression for the triple product $n \cdot \tau_E \cdot T$. This procedure is motivated by the fact that many characteristics of a magnetically confined plasma depend on the plasma pressure. It is proportional to $n \cdot T$, which is also a parameter relevant for technical considerations. The triple product achieved in magnetic fusion devices is shown in Fig. A.2. As can be judged from the figure, a factor of 10^5 in this product has been achieved since the first results in the Russian Tokamak T3 in the sixties [398].

A.2 Magnetic Confinement

A.2.1 Principle

The principle of magnetic confinement of plasmas is presented in several monographs (see for example [399, 400]). In this section only the key concepts will be introduced in order to allow a compact discussion of the physics results in the main part. A basic feature of most magnetic fusion devices is the toroidal geometry of the confining magnetic field. Since charged particles can move freely along the magnetic field, closed magnetic field lines effectively avoid end losses due to field lines intersecting material walls. However, the toroidal bending of field lines creates drifts of gyrating ions and electrons, due to field curvature and the increasing field strength towards the torus axis.
According to

$$v_D = \frac{m}{q_e B^3}(v_\parallel^2 + \frac{1}{2}v_\perp^2)\vec{B} \times \nabla B, \tag{A.10}$$

the particles with the charge q_e are drifting perpendicular to the magnetic field and to its gradient with the drift velocity v_D, with the direction depending on the sign of their charge, therefore separating positive and negative charges. These drifts are roughly proportional to the kinetic energy of the particles. Therefore, configurations with solely toroidal fields cannot be used for magnetic confinement, since the resulting electrical fields lead to particle losses on a short time scale, by a resulting drift

$$\vec{v}_D = \frac{\vec{E} \times \vec{B}}{B^2} \tag{A.11}$$

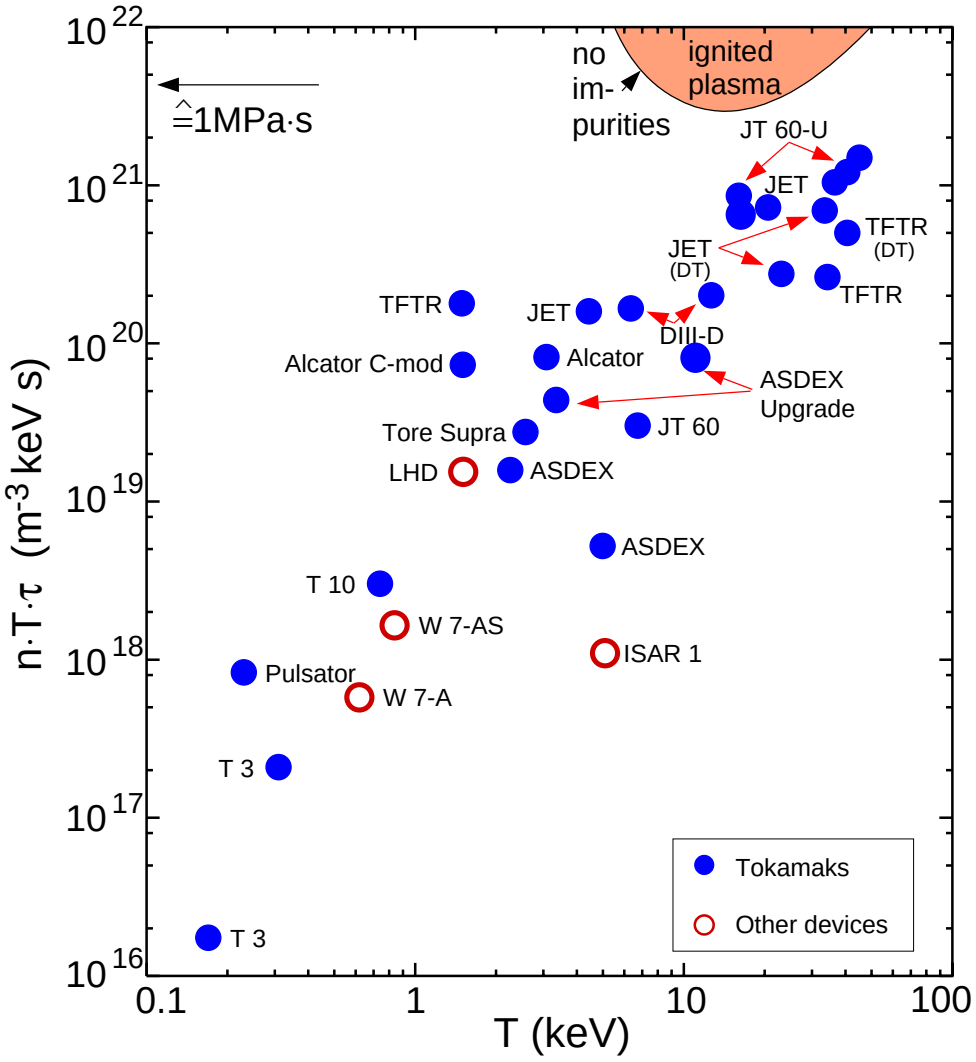

Figure A.2: Fusion triple-product $nT\tau_E$ as a function of the ion temperature for typical discharges in former and contemporary fusion devices.

being independent of the sign of the charges. Adding an additional poloidal magnetic field component $\vec{B}_p$ (see Fig. A.3), allows currents along the magnetic field lines to short-circuit the vertical electrical field. A poloidal magnetic field can be generated either by external helical windings, as in *stellarators*, or by a toroidal plasma current, as in *tokamaks*.

A.2.2 Tokamaks

A good overview of the principles and the stability of tokamaks, as well as a short description of contemporary devices, is given in the book by Wesson [256]. The combination of toroidal $\vec{B}_t$ and poloidal magnetic field $\vec{B}_p$ creates helical field lines winding around toroidal surfaces. The helicity of the fieldlines is described by the safety factor q, which

is given by

$$q = \frac{1}{2\pi} \oint ds \frac{B_t}{B_p}, \tag{A.12}$$

where the integral is taken along a poloidal cross section.

The q-value at the plasma boundary (q_{edge}) is often used to describe discharges, since it characterises to some extent the stability against magneto-hydrodynamic events and it also sets the toroidal field in relation to the plasma current. It can be approximated by

$$q_{edge} = 5\frac{a^2 B_t}{R_0 I_p}(1 + \varepsilon^2 c_\beta), \tag{A.13}$$

where a gives the minor radius, R_0 the large radius of the plasma, B_t the toroidal field at R_0 and I_p the total current in the plasma (see also Fig. A.3). The factor in parenthesis amounts to about 1.1 and gives the corrections due to the finite inverse aspect ratio $\varepsilon = a/R_0$ and the effects of the plasma current profile (represented by c_β).

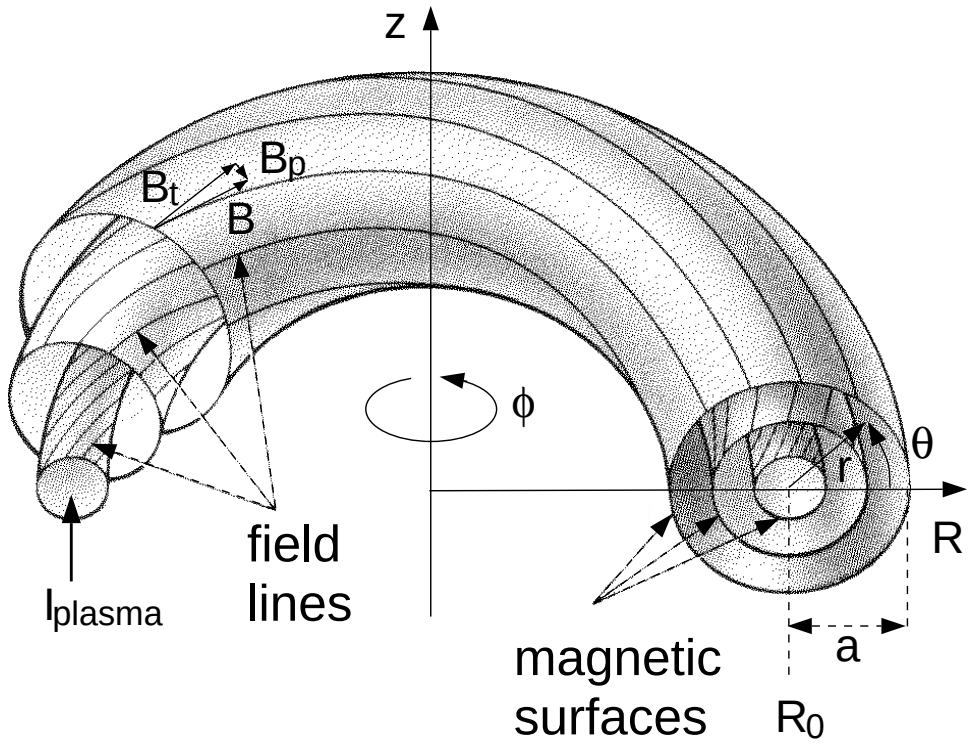

Figure A.3: Schematic view of the geometry and the flux surfaces in a circular Tokamak.

In a similar way the q values are given inside the plasma. On rational surfaces $q = m/n$ (m, n: integer) field lines close in on themselves after m poloidal and n toroidal revolutions. These rational surfaces are of special interest in a plasma, because there the growth rate of magneto-hydro-dynamic instabilities is largest.

The plasma pressure is given by the kinetic energy of the confined particles by $p = 2nkT$ for $T = T_i = T_e$. In equilibrium, the radial pressure gradient $\vec{\nabla} p$ is compensated by

$\vec{j} \times \vec{B}$ forces and both $\vec{j}$ and $\vec{B}$ are perpendicular to $\vec{\nabla} p$. This means that current and field lines span nested surfaces of constant plasma pressure, constant magnetic flux and constant total current, which are called *flux surfaces* (see also Fig. A.3).
The ratio of plasma pressure to magnetic pressure is denoted as

$$\beta = \frac{p}{B_0/(2\mu_0)} = \frac{2nkT}{B_0/(2\mu_0)}, \tag{A.14}$$

To achieve an efficient energy production β should be as high as possible. However due to magnetohydrodynamic instabilities it is restricted to a few percent in tokamaks. Stability calculations show that the β-limit scales linearly with $I_p/(aB_t)$, therefore

$$\beta_N = \frac{\beta}{I_p/(aB_t)}, \tag{A.15}$$

is often used, where β_N is called the normalised beta, and β has to be taken in %, I_p in MA a in m and B_t in T.

A.2.3 Limiter and Divertor Configuration

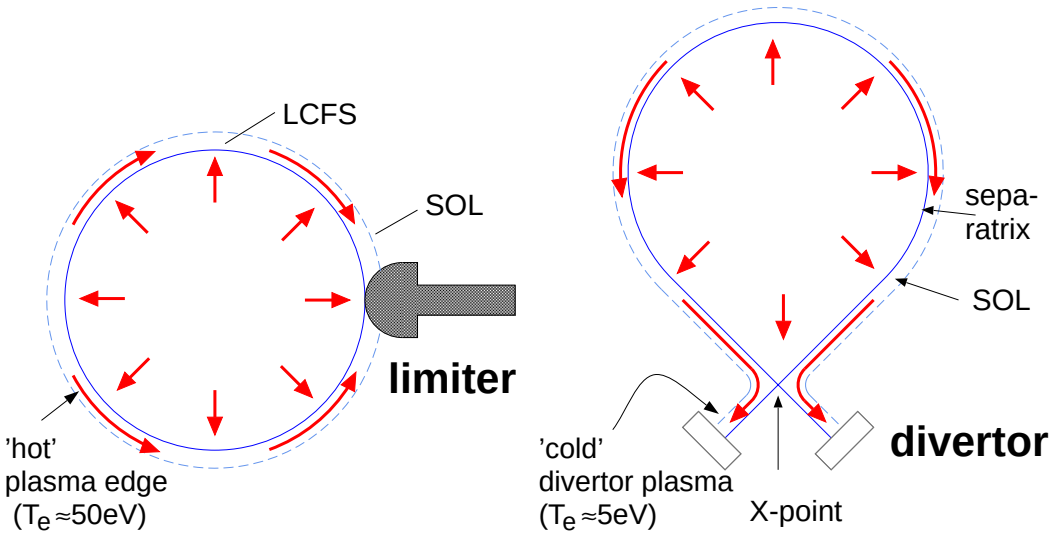

Figure A.4: Schematic view of the limiter (left) and the divertor principle (right). The confined plasma is separated from the scrape-off layer (SOL) by the last closed flux surface (LCFS) in the limiter configuration and by the separatrix in the divertor configuration.

The combination of the toroidal and the poloidal magnetic field confines the charged particles of the plasma to a high degree, but it does not provide a boundary for the plasma in a simple way. To protect the first walls of the device from uncontrolled power load by the plasma as well as minimizing the contamination of the plasma by impurities from the wall materials two different techniques are currently used.

The first defines the plasma boundary with a material *limiter* as shown in Fig. A.4 (left part). The advantage of this technique is the simplicity of its magnetic configuration, however, at the price of relatively high power fluxes and hot ions in the SOL (scrape-off layer) which can lead to strong erosion. This eroded material can lead to unduly high impurity concentrations in the plasma core (as in the tungsten limiter experiment at PLT [21]) since its penetration through the last closed flux surface (LCFS) is favoured by the geometrical proximity.
The second technique makes use of a magnetic separatrix achieved by the superposition of external magnetic fields. In practice these fields are supplied by additional coils surrounding the torus (see Fig. B.1) and are also used for shaping (elongation κ, triangularity δ) the plasma. These coils have to carry huge currents, especially since they have to be outside the vacuum vessel in a reactor relevant setup. The advantage of this configuration is that the plasma interacts with the target plates away from the main plasma. For reactor relevant densities (semi-detached divertor plasma), the plasma is cooled by radiation and charge exchange along the separatrix leading to lower plasma temperatures and a much more benign plasma wall interaction.

B. ASDEX Upgrade and its Main Diagnostics

B.1 The Garching Tokamak ASDEX Upgrade

The ASDEX Upgrade tokamak (Axially Symmetric Divertor EXperiment) is a mid-sized device in a reactor relevant geometry. It went into operation at Garching in 1990 [401] and its main goal is the investigation of crucial problems in fusion research under reactor-like conditions. For this purpose essential plasma properties, particularly the plasma density and the wall load, have been adapted to the conditions that will be present in a future fusion reactor, as the interaction between the hot fuel and the confining walls. To counteract the undesirable contamination of the plasma, ASDEX Upgrade is equipped with a lower and an upper divertor which remove the outer boundary layer of the plasma and deposit it on collector plates, away from the hot core (see Sec. A.2.3). The standard method of operation is lower single null (one X-point). During the ten years of operation, two different divertor geometries have been tested and a modification of the second one went into operation only recently [302]. The heating facilities consist of max. 20 MW of neutral injection of atomic hydrogen or deuterium and 6 MW of wave heating in ion cyclotron frequency range (ICRH, 30 - 60 MHz) and 2 MW of electron cyclotron heating (ECRH) at 140 GHz. The plasmas are investigated and characterised with more than 50 diagnostics. The main parameters achieved are summarised in table B.1 (an overview of recent results is given in [402, 403]). A cross section of ASDEX Upgrade is shown in Fig. B.1 together with the line of sights of some of the diagnostics described below.

B.2 Diagnostic of Main Plasma-Parameters

To investigate in detail the behaviour of fusion plasmas with their extreme parameters, a large variety of (partially complementary) diagnostic methods have been developed and are being used in present-day experiments. In general, the diagnostic systems of a fusion experiment constitute a major part of it, with regard to hardware as well as manpower. The principles of these methods come from all areas of physics. A selection of the most relevant diagnostics is briefly discussed in the following, while the basic physics principles of plasma diagnostics are described well in [404].

Large plasma-radius	R_0	1.65 m
Minor plasma-radius	a	0.5 m
Plasma height	b	0.8 m
Plasma elongation	$\kappa = b/a$	≤ 1.7
Plasma triangularity	δ	≤ 0.5
Plasma volume	V_{Plasma}	13 m^3
Volume of the vacuum vessel	V_{vessel}	32 m^3
Plasma density	$\bar{n}_e$	$\leq 1.5 \times 10^{20}$ m^{-3}
Plasma current	I_{Plasma}	≤ 1.4 MA
Toroidal magnetic field (on axis)	B_0	≤ 3.2 T
discharge duration		≤ 10 s
Heating power:		
Ohmic heating	OH	$\leq$ 1MW
Neutral beam injection	NBI	≤ 20 MW
Ion cyclotron heating	ICRH	≤ 6 MW
Electron cyclotron heating	ECRH	≤ 2 MW

Table B.1: Parameters of ASDEX Upgrade

B.2.1 Temperature Measurements

Electron cyclotron emission (ECE)

Electrons gyrating in the magnetic field act as time-varying dipoles and radiate at the electron cyclotron frequency and its low harmonics, i.e.

$$\omega = n \cdot \omega_{ce} = n \cdot \frac{e\ B}{m_e}. \tag{B.1}$$

As B is mainly the toroidal field $B = (B_0 \cdot R_0)/R$, with B_0 being the toroidal field at the plasma centre (at R_0), there is a simple relation between frequency and space:

$$\omega_n = n \cdot \frac{e\ B_0\ R_0}{m_e\ R} \tag{B.2}$$

Because the resonance is very sharp, the emissivity at the fundamental frequency and at low harmonics is so high that the radiation is optically thick. Due to re-absorption, the radiation intensity is close to that of a black body, i.e. it follows the Planck curve. As the cyclotron radiation is in the long-wavelength part of the Planck curve (Rayleigh-Jeans law), it is proportional to T_e:

$$I_n(\omega) = \frac{\omega^2\ T_e}{8\ \pi^3\ c^2} \tag{B.3}$$

with c being the velocity of light. Therefore a measurement of the cyclotron emission at a certain frequency leads directly to $T_e(r)$. An overview of ECE-diagnostics is found

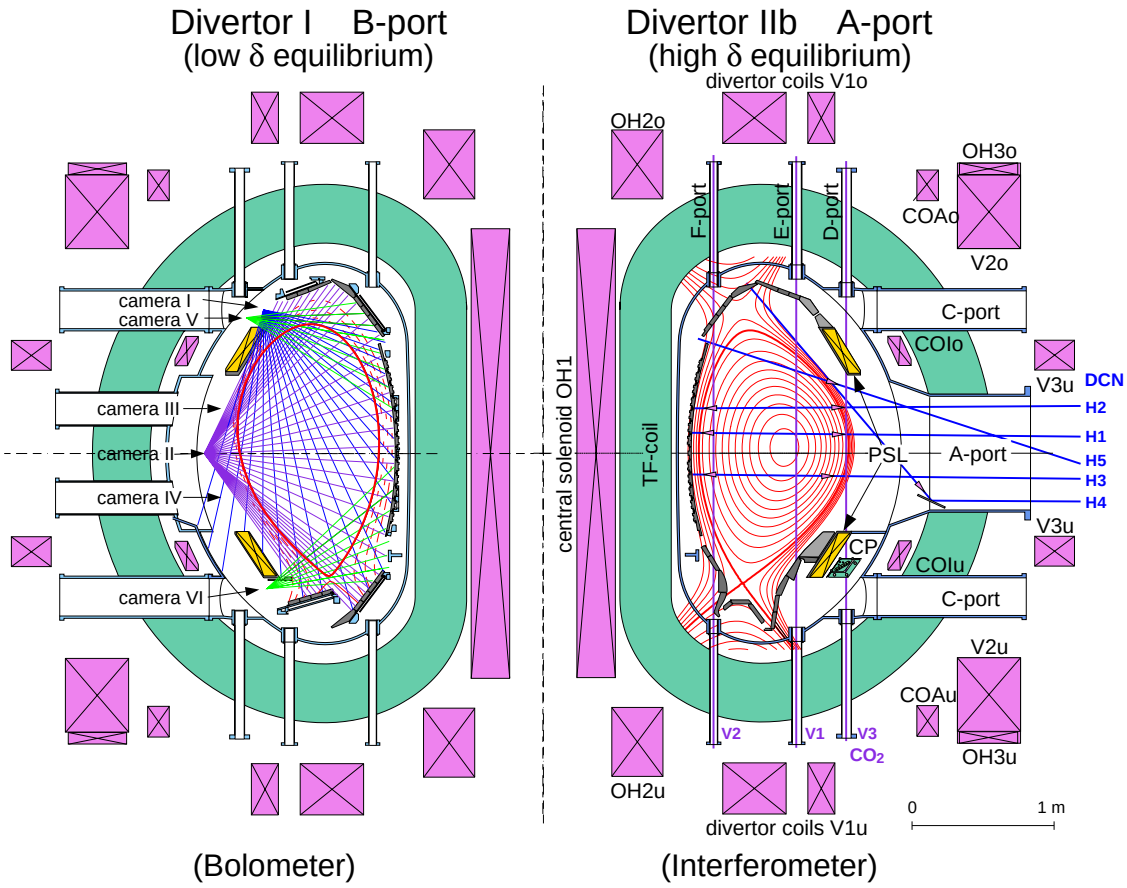

Figure B.1: Cross section of ASDEX Upgrade together with the line of sights of the bolometer cameras (left hand side, see Sec. B.2.3) and the interferometer (right hand side, see Sec. B.2.2). The left hand side depicts the divertor I (until 1996) with a low triangularity equilibrium used during the W divertor experiment. The right hand side shows the most recent divertor IIb configuration (since 2001) with a medium triangularity equilibrium.

in [405].

Different techniques are used to measure the emission: Fourier transform spectrometry, heterodyne radiometry, Fabry-Perot interferometry and diffraction grating spectrometry. The first of these techniques uses a Michelson interferometer. The interference pattern is Fourier transformed, giving the complete ECE spectrum with moderate frequency and time resolution. A knowledge of the complete spectrum is particularly necessary in plasmas with non-thermal electrons. All the other techniques measure the emission only at a fixed frequency or in a narrow band, but they have very high time resolution. In the heterodyne technique, the prefered method used at ASDEX Upgrade, the emission from the plasma is mixed with radiation from a local oscillator, and the resulting intermediate frequency signal is amplified and detected with a Schottky diode.

Thomson scattering

In a classical description of light scattering by charged particles the electromagnetic wave impinges on the particle and makes it act like a radiating dipole. Since the inertia of the electrons is much smaller than that of the ions in a plasma, it is mainly the electrons that are accelerated. The scattered light is frequency-shifted as a consequence of a twofold Doppler effect due to the motion of the electron with regard to the incoming wave and the observer. This frequency shift is given as $\Delta\omega = \vec{k}\cdot\vec{v}$, where $\vec{v}$ is the particle velocity and $\vec{k} = \vec{k}_{in} - \vec{k}_{out}$ is the scattering vector (the difference between the k-vectors of incoming and outgoing waves). The scattered light emerges from a large ensemble and all their contributions are added up in the measurement. Here, there are two different possibilities, depending on the scattering parameter $\alpha = \frac{1}{k\lambda_D}$, with $\lambda_D = \sqrt{\frac{\epsilon_0 kT}{e^2 n}}$ being the Debye length. Because $k_{in} \approx k_{out}$, one has

$$k \approx k_{in} \cdot 2sin\frac{\Theta}{2} \quad \text{and} \quad \alpha \approx \frac{\lambda_{in}}{4\pi\lambda_D sin(\Theta/2)}. \tag{B.4}$$

If $\alpha \gg 1$, neighbouring particles oscillate in phase and one gets coherent scattering determined by collective effects. In this case T_i can be measured from the scattered light. This technique has only recently been experimentally established at TEXTOR by using microwave radiation from gyrotrons [406].
If $\alpha \ll 1$, the wave is scattered at free, uncorrelated electrons and this regime of incoherent scattering is called Thomson scattering. In this case the spectrum of the scattered light (for a fixed scattering angle) is only a function of T_e. A more detailed treatment of light scattering in general and of Thomson scattering is found in [404, 407]. The main problem with Thomson scattering is the very small fraction of scattered light – only about 10^{-13} of the incoming power is scattered. Therefore Thomson scattering could only be realised with the development of lasers as powerful and monochromatic sources. Fusion experiments use mainly ruby ($\lambda = 694.3$ nm) and Nd:YAG lasers ($\lambda = 1.06$ μm). To resolve the scattered spectrum, one can use gratings and imaging array detectors or (as at ASDEX Upgrade) polychromator detectors.

Passive Spectroscopy

Due to the Doppler effect the radiation emitted by a single atom or ion is shifted in frequency. If ν_0 is the original frequency of the line, the shifted frequency ν in a non-relativistic approach is

$$\nu = \nu_0 \, (1 + \frac{v}{c} \cos\alpha) \tag{B.5}$$

with v being the velocity of the particle and α being the angle between the directions of motion and emission. In a plasma however, the emission from a large ensemble of atoms (ions) is observed and in this case the Doppler effect results in a broadening of

the line. Usually the ions (atoms) are in thermal equilibrium and their energies follow a Maxwellian distribution function, which is isotropic. Then the intensity distribution of the line is a Gaussian profile:

$$I(\nu) = I_0 \cdot exp(-\frac{mc^2}{2kT_i}\frac{\Delta\nu^2}{\nu_0^2}) \tag{B.6}$$

and the line width (Full Width at Half Maximum, FWHM) is

$$\Delta\nu_{1/2} = 2\nu_0\sqrt{ln2}\sqrt{2kT_i/mc^2}. \tag{B.7}$$

In general the natural line width has to be folded with the Gaussian profile, but in most practical cases this is a negligible correction. This technique yields no temperature profiles, since the emission is integrated over the line of sight. However, due to the localization of the emission zone mainly given by the ionisation equilibrium (see Sec. 5.2.1), there is a strong weighting of the temperature in the corresponding zone. This technique for the determination of T_i in the plasma centre is widely used with X-ray spectrometers, because they have a high spectral resolution and can observe ions in the plasma centre. At the plasma edge or in the divertor, lines emitted by neutrals or weakly ionised ions are used for measurements in the visible range.

Charge exchange recombination spectroscopy (CXRS)

Ions of low Z elements (especially the hydrogenic isotopes H and D, but also He) radiate only at the plasma edge because they are fully ionised further inward. This problem can be overcome by injecting a beam of neutral atoms. In collisions of these beam atoms with the plasma ions the latter can take over an electron (charge exchange) and then emit radiation. Energy and angular momentum conservation results in the excitation of high-lying Rydberg-levels, which emit visible radiation even from the heavier ion species. Usually the high-power heating beams are used for charge exchange spectroscopy. Since the radiation is emitted in the visible range, it can be detected with high spectral resolution, which allows Doppler measurements of T_i and also the determination of the plasma rotation. The equipartition time, which gives the timescale for the energy equilibration of particles with different mass, is proportional to m_1/m_2. This means that the temperature derived from impurity ions is usually much closer to the temperature of the background ions (H or D) than the electron temperature is.
The diagnostic is arranged in such a way that the line of sights of the spectrometer are almost perpendicular to the injected beam, allowing the measurement of profiles with sufficient radial resolution. Additionally, this technique allows the measurement of the light ion density profiles in the plasma core. A description on the setup and the results of the CXRS-diagnostic at ASDEX Upgrade can be found in [193].

Neutral particle analysis (NPA)

The ions in the plasma are in general well confined by the magnetic fields, but in collisions with neutrals also present in the plasma, they can take over an electron and become a neutral atom that can leave the plasma. As in these charge-exchange collisions both particles keep their energy, while the neutral atoms leaving the plasma represent the energy distribution of the plasma ions. It falls off with energy as $\exp(-1/T_i)$ and allows determination of T_i. The diagnostic is especially useful for the detection of deviations from the Maxwell distribution e.g. due to additional heating of the plasma. However, it is a line-integrated measurement and therefore Monte-Carlo simulations and different lines of sights are necessary to unfold the measurements to get $T_i(r)$. Neutral particle analyzers consist of two major components, a stripping cell, where in a low-pressure gas the neutral particles are ionised again, and a magnetic and electrostatic energy analyzer to measure their energy spectrum.

Langmuir Probes

Following the discussion in Sec. 5.1 the plasma builds up a sheath potential in front of a conducting wall, accelerating the ions towards the wall and retarding the electrons. By inserting an electrode into the edge plasma and applying a variable voltage V_{probe} one can derive the local values of T_e, n_e and plasma potential from the characteristic curve (I_{probe} - V_{probe}) which is given for a single probe without magnetic field as:

$$I_{probe} = A_{probe} j_i^{sat} \left(\exp(\frac{e(V_{probe} - V_{float})}{kT}) - 1 \right) \tag{B.8}$$

For large negative voltages, all ions which flow at the speed of sound c_s reach the probe and one observes the constant ion saturation current I_i^{sat}, which is given by the ion density $n_i = n_e$, their velocity c_s and the probe area A_{probe}. By increasing the voltage, the current vanishes at small positive value (V_{float}), where the ions cannot reach the probe anymore despite their acceleration in the sheath. The current now increases up to the electron saturation current I_e^{sat} which is larger than I_i^{sat} by the factor $\sqrt{m_i/m_e}$. From equation B.8 T_e and n_e can be extracted to

$$T_e = \frac{e(V_{probe} - V_{float})}{k} \left(\ln(1 + \frac{I_{probe}}{I_i^{sat}}) \right), \tag{B.9}$$

namely from the slope of the I_{probe} - V_{probe} characteristic, and

$$n_e = \frac{I_i^{sat}}{A_{probe} e c_s} = \frac{I_i^{sat}}{A_{probe} e \sqrt{\frac{kT_e}{2\pi m_e}}}. \tag{B.10}$$

In a magnetised plasma the single probes are connected by the flux tubes to a counterpart on the vessel surface given by the geometry of the magnetic configuration. Without

any cross-field transport this would lead to a double probe with identical surface areas, yielding symmetrical saturation currents for both signs of the voltage. For finite transport across the fieldlines the 'counter electrode' is enlarged and has to be fitted to the probe characteristic.

B.2.2 Density Measurements

Thomson scattering

The absolute value of the scattered signal (as described in Sec. B.2.1) is proportional to the local electron density. Therefore Thomson scattering can also be used to derive the density profile.

Interferometry

Laser beams interact with the plasma electrons not only by scattering, but also by refraction or reflection. An overview of plasma interferometry and polarimetry is given in [408].
When the static magnetic field in a plasma can be neglected, the refractive index N for the laser light is $N = (1 - \omega_{pe}^2/\omega_0^2)^{1/2}$, where ω_0 is the laser frequency and $\omega_{pe} = (n_e e^2/\epsilon_0 m_e)^{1/2}$ is the plasma frequency. For $\omega_0 \gg \omega_{pe}$ this gives an approximately linear relation

$$N \simeq 1 - \frac{\omega_{pe}^2}{2\omega_0^2} = 1 - \frac{e^2}{2\epsilon_0 m_e \omega_0^2} \cdot n_e. \tag{B.11}$$

This equation is also valid for static magnetic fields as long as the electric field of the laser beam is parallel to the magnetic field. When a laser beam transverses a plasma, it undergoes a phase shift

$$\Delta\Phi \simeq \frac{e^2}{2c\epsilon_0 m_e \omega_0} \int_L n_e \, dl. \tag{B.12}$$

Therefore interferometry does not give the spatially resolved electron density, but the line integral, which (if the line of sight L goes through the plasma centre) is already a good parameter to describe a plasma. However, having a number of different lines of sight (see Fig. B.1, right hand side) and therefore line density measurements, one can deduce the plasma profile by an inversion algorithm. Usually a Mach-Zehnder interferometer is used. Here, the light from the laser is split into three beams, one of which is frequency modulated. The other two beams travel either through the plasma, or along a reference path but both of them are combined with the modulated beam before they are detected. The signal then is not at the optical frequency (of the order of $10^{14} Hz$) but at the modulation frequency $\Delta\omega_0$, which is chosen to be in the convenient range of about 10–100 kHz. The phase shift of the probing beam is determined from the difference Δt

in corresponding zero-crossings of the two detector signals. Therefore this method is independent of changes in the laser amplitude.

Reflectometry

When an electromagnetic wave on its way through an inhomogeneous plasma reaches the critical density n_{crit}, where $\omega_0 = \omega_{pe}$ with $\omega_{pe} = \sqrt{\frac{n_e e^2}{m_e \epsilon_0}}$ (plasma frequency), the wave is reflected (as known from metals where the quasi-free electrons act as a mirror). The plasma layer where n_{crit} is reached, the so-called cut-off layer acts as a mirror and this effect is used in reflectometry. A complete overview on reflectometry is given in reference [409], a more recent description of the diagnostic, as well as its application to ASDEX Upgrade, is presented in [410].
In principle a Michelson interferometer is built, where the cut-off layer is one of the mirrors. From this the location of the cut-off layer can be determined. By sweeping the frequency of the wave (and therefore utilizing several cut-off layers with different critical densities) the electron density profile can be derived.

Li-Beam

By injecting a fast atomic Li-beam (20 -100 keV), one can observe the light emission from the interaction with the edge plasma. The excitation-rate of the 2p state varies by only $\approx 10\%$ in the temperature range 10 - 100 eV, making the 2p-2s emission almost proportional to the local electron density. Additionally, excitation to other levels as well as ionization and charge exchange also takes place, resulting in a loss of beam atoms in the ground state along its way through the plasma. However, solving the set of differential equations for all these processes along the beam path consistently, leads to an edge electron density profile without knowing the initial beam flux density. Charge exchange processes similar to the ones described in B.2.1 can also be used to extract edge impurity temperatures and densities. The principle is treated in more detail in [411] and also in [412], where the details of the diagnostic at ASDEX Upgrade are also covered.

B.2.3 Radiation Measurements

Bolometry

The energy loss from a plasma due to radiation is often a major contribution to the energy balance and is therefore an important parameter in describing the plasma.
The easiest way to measure the total radiation loss is to use a bolometer. This is a detector specifically designed to have a flat spectral response over a wide frequency range, mainly in the UV region, where the main radiative energy loss occurs.

Usually a bolometer consists of a metal foil that absorbs the energy. The temperature rise of this foil is then equal to the total energy flux divided by the bolometer's thermal capacity. This finite capacity, however, limits the time resolution of this technique to the order of ms.

Soft X-ray diagnostic

A much better time resolution (fraction of μs) can be reached by using semiconductor detectors, which are sensitive in the soft X-ray region ($\hbar\omega \sim T_e$). These detectors cannot be absolutely calibrated, but are ideally suited to measuring dynamic processes (such as sawteeth or other MHD instabilities) in the plasma.
Bolometers, as well as soft X-ray detectors, measure line-integrated signals that do not allow spatial resolution. Because both detector elements can be built very small usually a large number of them are used in a pinhole camera to get spatial resolution. If several such cameras view the plasma from different directions (see Fig. B.1, left hand side), the local emissivity in the plasma can be deduced from the line-integrated signals by an inversion algorithm (tomography).

Bibliography

[1] K. Heinloth, *Die Energiefrage*, Vieweg & Sohn Verlagsgesellschaft, Braunschweig, 2nd edition, 2003.

[2] E. Campbell and W. Hogan, Plasma Phys. Controlled Fusion **41**, B39–B56 (1999).

[3] S. Nakai, Y. Kozaki, Y. Izawa, M. Yamanaka, T. Kanabe, et al., Investigations toward a laser driven IFE power plant, in *Proc. of the 18th IAEA Conf. on Fusion Energy, Sorrento, Italy, October 2000, (CD-ROM)*, pages IAEA–CN–77/FTP1/26, Vienna, 2001, IAEA.

[4] R. Bangerter, R. Davidson, W. Herrmannsfeldt, J. Lindl, B. Logan, et al., The Heavy Ion Fusion Programm in the USA, in *Proc. of the 18th IAEA Conf. on Fusion Energy, Sorrento, Italy, October 2000, (CD-ROM)*, pages IAEA–CN–77/OV3/3, Vienna, 2001, IAEA.

[5] W. Hogan, E. Moses, B. Warner, M. Sorem, and J. Soures, The National Ignition Facility, in *Proc. of the 18th IAEA Conference Fusion Energy (CD-Rom), Sorrento, Italy, October 2000*, volume IAEA-CSP-8/C, pages IAEA–CN–77/IF/3, Vienna, 2001, IAEA.

[6] W. Logan et al., U.S. Heavy Ion Beam Science towards Inertial Fusion Energy, in *Proc. of the 19th IAEA Conference Fusion Energy (CD-Rom), Lyon, France, October 2002*, volume IAEA-CSP-19/CD, pages IAEA–CN–94/OV/3–4, Vienna, 2003, IAEA.

[7] J. Jacquinot and the JET team, Plasma Phys. Controlled Fusion **41**, A13–A46 (1999).

[8] R. Aymar, V. Chuyanov, M. Huguet, Y. Shimomura, and ITER Joint Central Team and Home Teams, Nucl. Fusion **41**, 1301 – 1310 (2001).

[9] R. Aymar, P. Barabaschi, and Y. Shimomura, Plasma Phys. Controlled Fusion **44**, 519–565 (2002).

[10] ITER physics basis editors, Nucl. Fusion **39**, 2137 – 2638 (1999).

[11] J. Winter, Plasma Phys. Controlled Fusion **38**, 1503 – 1542 (1996).

[12] V. Rohde, R. Neu, R. Dux, T. Härtl, H. Maier, et al., Comparison of Boronization and Siliconization in ASDEX Upgrade, in *Europhysics Conference Abstracts (CD-ROM), Proc. of the 26th EPS Conference on Controlled Fusion and Plasma Physics, Maastricht, 1999*, edited by C. Bastian and C. Nieswand, volume 23J, pages 1513–1516, Geneva, 1999, EPS.

[13] J. Roth, J. Nucl. Mater. **266-269**, 51 – 57 (1999).

[14] V. Philipps, R. Neu, J. Rapp, U. Samm, M. Tokar, et al., Plasma Phys. Controlled Fusion **42**(12B), B293–B310 (2000).

[15] C. Skinner, E. Amarescu, G. Ascione, W. Blanchard, C. Barnes, et al., J. Nucl. Mat. **241-243**, 214–226 (1997).

[16] P. Andrew, D. Brennan, J. Coad, J. Ehrenberg, M. Gadeberg, et al., J. Nucl. Mater. **266-269**, 153 (1999).

[17] G. Federici, R. Anderl, P. Andrew, J. Brooks, R. Causey, et al., J. Nucl. Mater. **266-269**, 14–29 (1999).

[18] G. Federici, J. Brooks, D. Coster, G. Janeschitz, A. Kukuskhin, et al., J. Nucl. Mater. **290-293**, 260–265 (2001).

[19] G. Federici, P. Andrew, P. Barabaschi, J. Brooks, R. Dörner, et al., J. Nucl. Mater. **313–316**, 11–22 (2003).

[20] N. Yoshida, J. Nucl. Mater. **266 – 269**, 197 – 206 (1999).

[21] V. Arunasalam, C. Barnes, K. Bol, K. Brau, N. Bretz, et al., Recent Results from the PLT tokamak, in *Proc. 8th Conf. EPS, Prague 1977*, volume 2, pages 17–28, Geneva, 1978, EPS.

[22] H. Nakamura, T. Ando, H. Yoshida, S. Niikura, T. Nishitani, et al., Nucl. Fusion **28**, 43–52 (1988).

[23] N. Noda, V. Philipps, and R. Neu, J. Nucl. Mater. **241–243**, 227–243 (1997).

[24] D. Post, R. Jensen, C. Tarter, W. Grasberger, and W. Lokke, At. Data Nucl. Data Tables **20**, 397–439 (1977).

[25] D. Post, J. Abdallah, R. Clark, and N. Putvinskaya, Phys. Plasmas **2**, 2328 – 2336 (1995).

[26] D. Reiter, G. Wolf, and H. Kever, Nucl. Fusion **30**, 2141– 2155 (1990).

[27] H. Bosch, Die Physik der Alpha-Teilchen in einem Fusionsreaktor mit Deuterium-Tritium-Plasmen, Technical Report IPP 1/400, Max-Planck-Institut für Plasmaphysik, Garching, 2001.

[28] J. Hogan, J. Nucl. Mater. **241-243**, 68–81 (1997).

[29] D. Campbell, Phys. Plasm. **8**, 2041 – 2049 (2000).

[30] R. Jensen, D. Post, and D. Jassby, Nucl. Sci. Eng. **65**, 282 (1978).

[31] W. Eckstein, C. García-Rosales, J. Roth, and J. Lázló, Nucl. Instr. Meth. **B83**, 95 (1993).

[32] W. Eckstein, C. García-Rosales, J. Roth, and W. Ottenberger, Sputtering Data, Rep. IPP 8/82, Max-Planck-Institut für Plasmaphysik, Garching, 1993.

[33] W. Eckstein, J. Bohdanski, and J. Roth, Physical Sputtering, in *Atomic and Plasma-Material Interaction Data for Fusion*, volume Vol.1, Suppl. to Nucl. Fusion, page 51, Vienna, 1991, IAEA.

[34] R. Doerner, M. Baldwin, S. Krasheninnikov, and D. Whyte, J. Nucl. Mater. **313 – 316**, 385 – 389 (2003).

[35] R. Conn, R. Doerner, F. Sze, et al., Nucl. Fusion **42**, 1060 (2002).

[36] M. Thomson, Phil. Mag. **18**, 377 (1968).

[37] J. Roth, J. Bohdansky, and W. Ottenberger, Data on low energy light ion sputtering, Rep. IPP 9/26, Max-Planck-Institut für Plasmaphysik, Garching, 1979.

[38] JET team (presented by Paul Thomas), J. Nucl. Mater. **176-177**, 3 – 13 (1990).

[39] D. Campbell and JET TEAM, J. Nucl. Mater. **241–243**, 379–384 (1997).

[40] R. Majeski, M. Boaz, D. Hoffman, B. Jones, R. Kaita, et al., J. Nucl. Mater. **313 – 316**, 625 – 629 (2003).

[41] C. García-Rosales, J. Nucl. Mater. **211**, 202–214 (1994).

[42] J. Strachan, W. Fundamenski, M. Charlet, K. Erents, J. Gafert, et al., Nucl. Fusion **43**, 922 – 941 (2003).

[43] G. F. Matthews, N. Allen, A. Kallenbach, K.-H. Steuer, K. McCormick, et al., J. Nucl. Mater. **241–243**, 450–455 (1997).

[44] B. Lipschultz et al., J. Nucl. Mater. **145-147**, 15 (1987).

[45] A. Kallenbach, A. Bard, D. Coster, R. Dux, C. Fuchs, et al., J. Nucl. Mater. **266–269**, 343–347 (1999).

[46] A. Kallenbach, M. Kaufmann, D. P. Coster, J. C. Fuchs, A. Herrmann, et al., Nucl. Fusion **39**(7), 901–917 (1999).

[47] W. Jacob, Thin Solid Films **326**, 1 – 42 (1998).

[48] V. Rohde, H. Maier, K. Krieger, R. Neu, J. Perchermeier, et al., J. Nucl. Mater. **290–293**, 317–320 (2001).

[49] V. Rohde, M. Mayer, and ASDEX Upgrade Team, J. Nucl. Mater. **313–316**, 337–341 (2003).

[50] C. Skinner et al., J. Nucl. Mat. **266-269**, 940 (1999).

[51] J. Brooks, A. Kirschner, D. Whyte, D. Ruzic, and D. Alman, J. Nucl. Mater. **313-316**, 426–430 (2003).

[52] V. Philipps, P. Wienhold, A. Kirschner, H. Esser, J. Coad, et al., Recent results on long term fuel retention in JET and TEXTOR and predictions for ITER, in *Proc. of the 19th IAEA Conference, Fusion Energy, Lyon, France, October 2002, (CD-ROM)*, pages IAEA–CN–94/EX/P5–06, Vienna, 2003, IAEA.

[53] H. Bolt, V. Barabash, G. Federici, J. Linke, J. Loarte, A. Roth, et al., J. Nucl. Mater. **307-311**, 43–52 (2002).

[54] G. Federici, C. Skinner, J. Brooks, J. Coad, C. Grisola, et al., Nucl. Fusion **41**, 1967 – 2137 (2001).

[55] I. Smid, M. Akiba, G. Vieider, and L. Plöchl, J. Nucl. Mater. **258 – 263**, 160 (1998).

[56] J. Davis, V. Barabash, A. Makhankov, L. Plöchl, and K. Slattery, J. Nucl. Mater. **258-263**, 308–312 (1998).

[57] S. Deschka, C. García-Rosales, W. Hohenauer, R. Duwe, E. Gauthier, et al., J. Nucl. Mater. **233–237**, 645–649 (1996).

[58] H. Wolff, Arcing in magnetic fusion devices, in *Atomic and Plasma-Material Interaction Data for Fusion*, volume Vol. 1, Suppl. to Nucl. Fusion, page 91, Vienna, 1991, IAEA.

[59] B. Jüttner, J. Phys. D **34**, R103–R123 (2001).

[60] W. Schneider et al., Tungsten Migration between Main Chamber and Divertor of ASDEX Upgrade, in *Europhysics Conference Abstracts (Proc. of the 28th EPS Conference on Controlled Fusion and Plasma Physics, Funchal, 2001)*, 2001.

[61] K. Krieger, A. Geier, X. Gong, H. Maier, R. Neu, et al., J. Nucl. Mater. **313–316**, 327–332 (2003).

[62] H. Maier, IPP Garching, private communication, 2002.

[63] A. Hassanein, Fus. Technol. **15**, 513 (1989).

[64] A. Hassanein, G. Federici, I. Konkashbaev, A. Zhitlukhin, and V. Litunovsky, Fusion Eng. Des. **39-40**, 201 (1998).

[65] A. Hassanein and I. Konkashbaev, J. Nucl. Mater. **273**, 326 (1999).

[66] A. Makhanov, V. Barabash, and D. Mazul, I. Youchison, J. Nucl. Mater. **290-293**, 1117–1122 (2001).

[67] D. Petti et al., J. Nucl. Mater. **233-237**, 37 (1996).

[68] G. Janeschitz, P. Barabaschi, G. Federici, K. Ioki, P. Ladd, et al., Nucl. Fusion **40**, 1197 – 1221 (2000).

[69] J. Winter, Plasma Phys. Controlled Fusion **40**, 2001 (1998).

[70] J. Sharpe, V. Rohde, ASDEX-Upgrade Team, A. Sagara, H. Suzuki, et al., J. Nucl. Mater. **313-316**, 455 – 459 (2002).

[71] T. Hirai, K. Tokunaga, T. Fujiwara, N. Yoshida, S. Itoh, et al., J. Nucl. Mater. **258-263**, 1060 (1998).

[72] R. Sakamoto, T. Muroga, and N. Yoshida, J. Nucl. Mater. **220-222**, 819 (1995).

[73] T. Venhaus, R. Causey, R. Doerner, and T. Abeln, J. Nucl. Mater. **290–293**, 505 (2001).

[74] W. Wang, J. Roth, S. Lindig, and C. Wu, J. Nucl. Mater. **299**, 124–131 (2001).

[75] M. Ye, H. Kanehara, S. Fukuta, N. Ohno, and S. Takamura, J. Nucl. Mater. **313-316**, 74–78 (2003).

[76] R. Causey, Hydrogen Retention and Release in Tungsten, Jülich, 2002, IAEA Technical Meeting on Atomic and Plasma-Material Interaction Data for Fusion Science and Technology.

[77] K. Krieger, H. Maier, R. Neu, and ASDEX Upgrade Team, J. Nucl. Mater. **266–269**, 207–216 (1999).

[78] V. Alimov and B. Scherzer, J. Nucl. Mater. **240**, 75 (1996).

[79] A. Haasz, J. Davis, M. Poon, and R. Macaulay-Newcombe, J. Nucl. Mater. **258-263**, 889 (1998).

[80] C. García-Rosales, P. Franzen, H. Plank, J. Roth, and E. Gauthier, J. Nucl. Mater. **233–237**, 803–808 (1996).

[81] P. Franzen, C. García-Rosales, H. Plank, and V. K. Alimov, J. Nucl. Mater. **241–243**, 1082–1086 (1997).

[82] P. Franzen, H. Maier, D. Schleußner, R. Behrisch, M. Balden, et al., Hydrogen Isotope Inventories in the ASDEX Upgrade Tungsten Coated Divertor Tiles, in *Europhysics Conference Abstracts (Proc. of the 24th EPS Conference on Controlled Fusion and Plasma Physics, Berchtesgaden, 1997)*, edited by M. Schittenhelm, R. Bartiromo, and F. Wagner, volume 21A, part IV, pages 1429–1432, Petit-Lancy, 1997, EPS.

[83] K. Krieger, H. Maier, D. Grambole, D. Schleussner, P. Franzen, et al., Hydrogen Isotope Inventories in Plasma Facing Components of ASDEX Upgrade, in *Fusion Energy 1998*, volume 4, pages 1317–1320, Vienna, 1999, IAEA.

[84] D. Schleußner, H. Maier, P. Franzen, R. Behrisch, M. Balden, et al., J. Nucl. Mater. **266–269**, 1296–1302 (1999).

[85] H. Maier, K. Krieger, M. Balden, J. Roth, and ASDEX Upgrade Team, J. Nucl. Mater. **266–269**, 1003–1008 (1999).

[86] P. Franzen, R. Behrisch, C. García-Rosales, ASDEX Upgrade Team, D. Schleussner, et al., Nucl. Fusion **37**(10), 1375–1393 (1997).

[87] D. Nishijima, M. Ye, N. Ohno, and S. Takamura, J. Nucl. Mater. **313 − 316**, 97 – 101 (2003).

[88] K. Tokunaga, R. Doerner, R. Seraydarian, N. Noda, Y. Kubota, et al., J. Nucl. Mater. **313 − 316**, 92 – 96 (2003).

[89] R. Behrisch, V. Khripunov, R. Santoro, and J. Yesil, J. Nucl. Mater. **258 - 263**, 686–693 (1998).

[90] O. Gruber, A. Kallenbach, M. Kaufmann, K. Lackner, V. Mertens, et al., Phys. Rev. Lett. **74**(21), 4217–4220 (1995).

[91] H. Verbeek, J. Stober, D. P. Coster, and R. Schneider, Erosion of the Main Chamber Walls of Tokamaks by CX-Neutrals, in *Europhysics Conference Abstracts (Proc. of the 24th EPS Conference on Controlled Fusion and Plasma Physics, Berchtesgaden, 1997)*, edited by M. Schittenhelm, R. Bartiromo, and F. Wagner, volume 21A, part IV, pages 1457–1460, Petit-Lancy, 1997, EPS.

[92] D. Naujoks, K. Asmussen, M. Bessenrodt-Weberpals, S. Deschka, R. Dux, et al., Nucl. Fusion **36**(6), 671–687 (1996).

[93] K. Krieger, V. Rohde, R. Schwörer, K. Asmussen, C. García-Rosales, et al., J. Nucl. Mater. **241–243**, 734–738 (1997).

[94] K. Krieger, K. Asmussen, R. Neu, V. Rohde, J. Roth, et al., Erosion and Transport of Tungsten in ASDEX Upgrade, in *Plasma Physics and Controlled Nuclear Fusion Research 1996*, volume 1, pages 817–823, Vienna, 1997, IAEA.

[95] K. Krieger, H. Maier, V. Rohde, K. Asmussen, M. Balden, et al., Tungsten Erosion and Migration in ASDEX Upgrade, in *Europhysics Conference Abstracts (Proc. of the 24th EPS Conference on Controlled Fusion and Plasma Physics, Berchtesgaden, 1997)*, edited by M. Schittenhelm, R. Bartiromo, and F. Wagner, volume 21A, part IV, pages 1421–1424, Petit-Lancy, 1997, EPS.

[96] K. Krieger, H. Maier, R. Neu, V. Rohde, and A. Tabasso, Fusion Eng. Design **58-59**, 189–193 (2001).

[97] X. Gong, K. Krieger, J. Roth, H. Maier, R. Neu, et al., Erosion and Deposition of Tungsten as Plasma Facing Material at the Central Column Heat Shield of ASDEX Upgrade, in *Europhysics Conference Abstracts (CD-ROM, Proc. of the 29th EPS Conference on Controlled Fusion and Plasma Physics, Montreux, 2002)*, edited by R. Behn and C. Varandas, volume 26B, page P2.052, Geneva, 2002, EPS.

[98] K. Krieger, J. Roth, A. Annen, W. Jacob, C. S. Pitcher, et al., J. Nucl. Mater. **241–243**, 684–689 (1997).

[99] A. Thoma, K. Asmussen, R. Dux, K. Krieger, A. Herrmann, et al., Plasma Phys. Controlled Fusion **39**(9), 1487–1499 (1997).

[100] D. Naujoks and W. Eckstein, J. Nucl. Mater. **230**, 93 (1996).

[101] W. Schneider, D. Hildebrandt, X. Gong, K. Krieger, R. Neu, et al., Tungsten Migration Between Main Chamber and Divertor of ASDEX Upgrade, in *Europhysics Conference Abstracts (CD-ROM, Proc. of the 28th EPS Conference on Controlled Fusion and Plasma Physics, Madeira 2001)*, edited by R. Pick, volume 25A, pages 189–192, Geneva, 2001, EPS.

[102] V. Barabash, G. Federici, M. Roedig, L. Snead, and C. Wu, J. Nucl. Mater. **283 –287**, 138 – 146 (2000).

[103] V. Barabash, G. Federici, J. Linke, and C. Wu, J. Nucl. Mater. **313-316**, 42–51 (2002).

[104] ITER Generic Site Safety Report (GSSR) Vol V: Radioactive Materials, Decommissioning and Waste, Technical Report G 84 RI 4 01-07-06 R 1.0, ITER Home-Teams, 2001.

[105] T. Noda, F. Mitsutane, and M. Okada, J. Nucl. Mater. **258 – 263**, 934 – 939 (1998).

[106] J. Raeder, I. Cook, F. Morgenstern, E. Salpietro, R. Bünde, et al., Safety and environmental assessment of fusion power (SEAFP), Technical Report EURFUBRU XII-217/95, European Commision, 1995.

[107] I. Cook, G. Marbach, L. Di Pace, C. Girard, and N. Taylor, Safety and environmental impact of fusion (SEIF), Technical Report EUR(01)CCE-FU/FTC8/5, European Fusion Develepment Agreement, April 2001.

[108] D. Cepraga, G. Cambi, M. Frisoni, and R. Forrest, Radiation transport and activation calculation in support for safety analyses of ITER-FEAT, Technical Report ERG-FUS/TN-SIC TR 07/2000, August 2000.

[109] A. R. Field, J. Fink, R. Dux, G. Fussmann, U. Schumacher, et al., Rev. Sci. Instrum. **66**, 5433–5441 (1995).

[110] G. Lieder, B. Napiontek, R. Radtke, A. Field, G. Fussmann, et al., Interpretation of Low Ionized Impurity Distributions in the ASDEX Upgrade Divertor, in *Europhysics Conference Abstracts (Proc. of the 20th EPS Conference on Controlled Fusion and Plasma Physics, Lisbon, 1993)*, edited by J. A. Costa Cabral, M. E. Manso, F. M. Serra, and F. C. Schüller, volume 17C, part II, pages 579–582, Geneva, 1993, EPS.

[111] J. Steinbrink, U. Wenzel, W. Bohmeyer, G. Fußmann, and PSI Team, Sputtered Tungsten Atoms Investigated in a Linear Plasma Generator, in *Europhysics Conference Abstracts (Proc. of the 24th EPS Conference on Controlled Fusion and Plasma Physics, Berchtesgaden, 1997)*, volume 21A, pages 1809–1812, Geneva, 1997, EPS.

[112] E. Unger, Untersuchungen zur Absolutkalibration eines Grazing-Incidence-Spektrometers für Verunreinigungstransport an einem Fusionsexperiment, Technical Report III/187, IPP, Garching, Germany, 1992.

[113] R. Fonck, A. Ramsey, and R. Yelle, Applied Optics **21** (1982).

[114] D. McKenzie, P. Landecker, and J. Underwood, Space Science Instrumentation **2**, 125 – 139 (1976).

[115] A. Oed, Nucl. Instr. Meth. **A263**, 351 – 359 (1988).

[116] R. Neu, K. Asmussen, G. Fussmann, P. Geltenbort, G. Janeschitz, et al., Rev. Sci. Instrum. **67**(5), 1829–1833 (1996).

[117] B. Endras, Aufbau und Test einer Pulshöhen-Analyse-Diagnostik für den Tokamak ASDEX Upgrade, Technical report, Diploma thesis, Universität Augsburg, 1997.

[118] D. O. Bolshukhin, R. Neu, M. Y. Kantor, B. Kurzan, and ASDEX Upgrade Team, Central Z_{eff} Measurements With a New PHA Diagnostic and its Further Applications, in *Europhysics Conference Abstracts (CD-ROM, Proc. of the 28th EPS Conference on Controlled Fusion and Plasma Physics, Madeira 2001)*, edited by R. Pick, volume 25A, pages 41–44, Geneva, 2001, EPS.

[119] D. Bolshukhin, R. Neu, D. Schlögl, R. Dux, and ASDEX Upgrade Team, Rev. Sci. Instrum. **72**(11), 4115–4124 (2001).

[120] H. H. Johann, Zeitschschrift für Physik **69**, 185–206 (1931).

[121] S. Morita, X-Ray Spectroscopic Study of High Temperature Plasmas by Curved Crystal Spectrometer, Technical report, Research Report, Nagoya University, Institute of Plasma Physics, 1983.

[122] A. Burek, Space Science Instrumentation **2** (1976).

[123] E. Bertin, in *Principles and practice of X-ray spectrometric analysis*, Plenum Press, New York, 1984.

[124] T. Johansson, Zeitschrift für Physik **82**, 507–528 (1933).

[125] Proscan GmbH, D-86836 Lagerlechfeld, more informations under 'http://www.proscan.de'.

[126] A. Geier, Aspekte des Verhaltens von Wolfram im Fusionsexperiment ASDEX Upgrade, Technical Report 10/19, IPP, Garching, Germany, July 2001.

[127] J. Friichtenicht, Rev. Sci. Instrum. **45**, 51 (1974).

[128] E. Marmar, J. Cecchi, and S. Cohen, Rev. Sci. Instrum. **46**, 1149 – 1154 (1975).

[129] S. Mattoo, L. Wirtz, A. Pospieszczyk, and B. Schweer, Nucl. Instr. Meth. B **124**, 579–590 (1997).

[130] S. Suckewer, J. Cecchi, S. Cohen, R. Fonck, and E. Hinnov, Phys. Lett. A **80**, 259 (1980).

[131] E. Hinnov, S. Suckewer, S. Cohen, and K. Sato, Phys. Rev. A **25**, 2293 – 2300 (1982).

[132] J. Reader, V. Kaufman, J. Sugar, J. Ekberg, U. Feldmann, et al., J. Opt. Soc. Am. B **4**, 1821 (1987).

[133] J. E. Rice, K. Fournier, J. Terry, M. Graf, M. Finkenthal, et al., Phys. Rev. A **53**, 3953–3962 (1996).

[134] J. E. Rice, K. Fournier, E. Goetz, J.A. Marmar, and J. Terry, J.Phys.B **33**, 5435–5462 (2000).

[135] E. Marmar, J. Rice, and S. Allen, Phys. Rev. Lett. **45**, 2025 – 2028 (1980).

[136] E. Marmar, J. Rice, J. Terry, and F. Seguin, Nucl. Fusion **22**, 1567 – 1575 (1982).

[137] S. Cohen, J. Cecchi, C. Daughney, S. Davis, D. Dimock, et al., J. Vac. Sci. Technol. **20**, 1226 – 1229 (1982).

[138] TFR Group, Nucl. Fusion **23**, 559–569 (1983).

[139] R. Isler, W. Rowan, and W. Hodge, Phys. Rev. Lett. **55**, 2413–2416 (1985).

[140] D. Pasini, M. Mattioli, A. Edwards, R. Gianella, R. Gill, et al., Nucl. Fusion **30**, 2049 – 2062 (1990).

[141] J. Castracane, L. Könen, A. Pospieszczyk, Y. Demers, and K. Dimoff, Nucl. Fusion **31**, 947–951 (1991).

[142] M. Mattioli, R. Giannella, R. Myrnäs, C. Demichelis, B. Denne-Hinnov, et al., Nucl. Fusion **35**(9), 1115–1124 (1995).

[143] A. Pospieszczyk, F. Aumayer, H. Bay, E. Hintz, P. Leismann, et al., J. Nucl. Mater. **162-164**, 574 – 581 (1989).

[144] D. Michaud, G. Ross, E. Haddad, H. Mai, A. Pospieszczyk, et al., Rev. Sci. Instrum. **63**, 5698 – 5702 (1992).

[145] F. Schwirzke, L. Oren, S. Talmadge, and R. Taylor, Phys. Rev. Lett. **40**, 1181 (1978).

[146] M. W. Kissick, E. D. Frederickson, J. D. Callen, C. Bush, Z. Chang, et al., Nucl. Fusion **34**(3), 349–358 (1994).

[147] K. W. Gentle, W. L. Lowan, R. V. Bravanec, G. Cima, T. P. Crowley, et al., Phys. Rev. Lett. **74**, 3620–3623 (1995).

[148] U. Stroth et al., Plasma Phys. Controlled Fusion **38**, 611–618 (1996).

[149] K. Gentle, R. Bravanec, G. Cima, G. Hallock, P. Phillips, et al., Phys. Plasmas **4**, 3599–3613 (1997).

[150] M. W. Kissick, J. D. Callen, and E. D. Frederickson, Nucl. Fusion **38**(6), 821–833 (1998).

[151] H. Walter, U. Stroth, J. Bleuel, R. Burhenn, T. Geist, et al., Plasma Phys. Controlled Fusion **40**, 1661–1672 (1998).

[152] F. Ryter, R. Neu, R. Dux, H.-U. Fahrbach, F. Leuterer, et al., Nucl. Fusion **40**(11), 1917–1932 (2000).

[153] R. Neu, K. Asmussen, R. Dux, P. N. Ignacz, M. Bessenrodt-Weberpals, et al., Behaviour of Laser Ablated Impurities in ASDEX Upgrade Discharges, in *Europhysics Conference Abstracts (Proc. of the 22th EPS Conference on Controlled Fusion and Plasma Physics, Bournemouth, 1995)*, edited by B. Keen, P. Stott, and J. Winter, volume 19C, part I, pages 65–68, Geneva, 1995, EPS.

[154] R. Neu, R. Pugno, M. Balden, J. Gafert, A. Geier, et al., Laser Ablation at the Inboard Side of ASDEX Upgrade, in *Europhysics Conference Abstracts (CD-ROM), Proc. of the 27th EPS Conference on Controlled Fusion and Plasma Physics, Budapest, 2000*, edited by K. Szegö, T. N. Todd, and S. Zoletnik, volume 24B, pages 1176–1179, Geneva, 2001, EPS.

[155] A. Geier, K. Asmussen, A. Bard, R. Neu, and K. Krieger, Rev. Sci. Instrum. **70**(1), 63–67 (1999).

[156] A. Geier, H. Maier, R. Neu, K. Krieger, and ASDEX Upgrade Team, Divertor Retention For Metallic Impurities at ASDEX Upgrade, in *Europhysics Conference Abstracts (CD-ROM, Proc. of the 28th EPS Conference on Controlled Fusion and Plasma Physics, Madeira 2001)*, edited by R. Pick, volume 25A, pages 169–172, Geneva, 2001, EPS.

[157] A. Geier, H. Maier, R. Neu, K. Krieger, and ASDEX Upgrade Team, Plasma Phys. Controlled Fusion **44**(10), 2091–2100 (2002).

[158] E. Hinnov, K. Bol, D. Dimock, R. Hawryluk, D. Johnson, et al., Nucl. Fusion **18**, 1305 (1978).

[159] R. Isler, R. Neidigh, and R. Cowan, Phys. Lett. **A63**, 295 (1977).

[160] J. Rapp, M. Tokar, L. Könen, H. Koslowski, G. Bertschinger, et al., Plasma Phys. Controlled Fusion **39**, 1615–1634 (1997).

[161] J. Rice, J. Terry, K. Fournier, M. Graf, M. Finkenthal, et al., J. Phys. B: At. Mol. Opt. Phys. **29**, 2191 (1996), and references therein.

[162] K. Fournier, D. Pacella, M. May, M. Finkenthal, and W. Goldstein, Nucl. Fusion **37**(6), 825 – 834 (1997).

[163] C. Breton, C. DeMichelis, M. Finkenthal, and M. Mattioli, Ionization Equilibrium of Selected Elements from Neon to Tungsten of Interest in Tokamak Plasma Research, Technical Report 948, EURATOM-CEA-FC, 1978.

[164] D. Laun and C. H. Corliss, J. Res. NBS A **72**, 609–755 (1968).

[165] H. Obarius and M. Kock, J. Phys. B **15**, 527 – 533 (1982).

[166] B. Michelt, Spektroskopische Messung der Oszillatorenstärke und Besitzungsdichten angeregter Wolframzustände in einem WF_6 dotierten Argonbogen, Technical report, Diploma Thesis, Universität Bochum, 1992.

[167] K. Behringer, H. Summers, B. Denne, M. Forrest, and M. Stamp, Plasma Phys. Controlled Fusion **31**, 2059 – 2099 (1989).

[168] O. Orient and S. Srivastava, J. Phys. B: At. Mol. Phys **20**, 3923 – 3936 (1987).

[169] M. S. Pindzola and D. C. Griffin, Phys. Rev. A **48**, 2486 – 2488 (1992).

[170] A. Kallenbach and H.-M. Mayer, Rev. Sci. Instrum. **64**(5), 1257–1262 (1993).

[171] A. R. Field, G. Fussmann, C. García-Rosales, S. Hirsch, G. Lieder, et al., J. Nucl. Mater. **220–222**, 553–557 (1995).

[172] A. Pospieszczyk, T. Tanabe, V. Philipps, G. Sergienko, T. Ohgo, et al., J. Nucl. Mater. **290–293**, 947 – 952 (2001).

[173] A. Huber, V. Philipps, A. Pospieszczyk, A. Kirschner, M. Lehnen, et al., J. Nucl. Mater. **290 – 293**, 276 – 280 (2001).

[174] T. Hirai, V. Phillips, A. Huber, G. Serdienko, J. Linke, et al., J. Nucl. Mater. **313–316** (2003).

[175] M. Finkenthal, L. Huang, S. Lippmann, H. Moos, P. Mandelbaum, et al., Phys. Lett. A **127**, 255 (1988).

[176] P. Mandelbaum, J. Schwob, M. Finkenthal, and M. Klapisch, Journal de Physique **49**, C1–217 ((1988)).

[177] J. Sugar, V. Kaufman, and W. Rowan, J. Opt. Soc. Am. **B10**, 1321 (1993).

[178] J. Sugar, V. Kaufman, and W. Rowan, J. Opt. Soc. Am. **B10**, 1977 (1993).

[179] J. Sugar, V. Kaufman, and W. Rowan, J. Opt. Soc. Am. **B10**, 799 (1993).

[180] K. Asmussen, K. B. Fournier, J. M. Laming, R. Neu, J. F. Seely, et al., Nucl. Fusion **38**(7), 967–986 (1998).

[181] C. Biedermann, R. Radtke, J.-L. Schwob, P. Mandelbaum, R. Doron, et al., Physica Scripta **T92**, 85–88 (2001).

[182] R. Radtke, C. Biedermann, J.-L. Schwob, P. Mandelbaum, and R. Doron, Phys. Rev. A **64**, 012720 (2001).

[183] R. Kelly, Journal of Physical and Chemical Reference Data **16** (1987).

[184] N. Acquista and J. Reader, J. Opt. Soc. Am. B **1**, 649 (1984).

[185] J. Reader and G. Luther, Phys. Rev. Lett. **45**, 1980 (1980).

[186] J. Seely, C. Brown, and W. Behring, J. Opt. Soc. Am. **B6**(1), 3 – 6 (1989).

[187] J. Reader and G. Luther, Physica Scripta **24**, 723 (1981).

[188] K. Fournier, At. Data Nucl. Data Tables **68**, 1 – 48 (1998).

[189] M. Klapisch, J. Schwob, B. Fraenkel, and J. Oreg, J. Opt. Soc. Am. **67**, 148 (1977).

[190] C. Brown, J. Seely, D. Kania, B. Hammel, C. Back, et al., Atomic Data and Nuclear Data Tables **58**, 203 (1994).

[191] D. Mitnik, P. Mandelbaum, J. Schwob, J. Oreg, A. Bar-Shalom, et al., Phys. Rev. A **53**, 3178 (1996).

[192] D. Mitnik, P. Mandelbaum, J. Schwob, J. Oreg, A. Bar-Shalom, et al., Phys. Rev. A **55**, 307 (1997).

[193] S. de Peña Hempel, Untersuchungen zum Transport leichter Verunreinigungen an ASDEX Upgrade, Technical Report 10/8, IPP, Garching, Germany, July 1997, Doctoral thesis TU Munich, June 97.

[194] G. Magyar, M. Barnes, S. Cohen, A. Edwards, N. Hawkes, et al., The laser blow-off system (KZ3) on JET, Technical Report JET-R(88)15, JET Joint Undertaking, 1988.

[195] A. Zigler, M. Klapisch, and P. Mandelbaum, Phys. Lett. A **117**(1), 31 – 35 (1986).

[196] N. Tragin, J.-P. Geindre, P. Monier, J.-C. Gauthier, C. Chenais-Popovics, et al., Physica Scripta **37**, 72 – 82 (1988).

[197] A. Zigler, H. Zmora, N. Spector, M. Klapisch, J. Schwob, et al., J. Opt. Soc. Am. **70**(1), 129 – 132 (1980).

[198] P. Mandelbaum, M. Klapisch, A. Bar-Shalom, J. Schwob, and A. Zigler, Physica Scripta **27**, 39 – 53 (1983).

[199] S. Elliot, P. Beiersdorfer, B. MacGowan, and J. Nilsen, Phys. Rev. A **52**(4), 2689 – 2692 (1995).

[200] K. Fournier, HULLAC-based Simulations of Non-LTE Emission Spectra, 2001, Lawrence Livermore National Laboratory, UCRL-ID-143900.

[201] K. Fournier, R. Neu, D. Bolshukhin, A. Geier, and the ASDEX Upgrade Team, Soft X-ray emission spectra from highly charged tungsten ions as a quantitative diagnostic of fusion plasmas, in *Bulletin of the American Physical Society*, volume 46, page 267, 2001.

[202] K. Fournier, private communication (2001).

[203] A. Bar-Shalom and M. Klapisch, Computer Phys. Comm. **50**, 375–393 (1988).

[204] M. Klapisch, Computer Phys. Comm. **2**, 239 (1971).

[205] K. Fournier, W. Goldstein, M. May, and M. Finkenthal, Phys. Rev. A **53**, 709 (1996).

[206] J. Bauche, C. Bauche-Arnoult, M. Klapisch, P. Mandelbaum, and J. Schwob, J. Phys. B **20**, 1443–1450 (1987).

[207] I. Grant, J. Phys. B: At. Mol. Opt. Phys. **7**, 1458 (1974).

[208] J. Oreg, W. Goldstein, M. Klapisch, and A. Bar-Shalom, Phys. Rev. A **44**, 1750 (1991).

[209] A. Bar-Shalom, M. Klapisch, and J. Oreg, Phys. Rev. A **38**, 1773 (1988).

[210] K. Fournier, W. Goldstein, M. May, M. Finkenthal, and J. Terry, Phys. Rev. A **53**, 3110 (1996).

[211] W. Lotz, Z. Phys. **216**, 241 (1968).

[212] W. Lotz, Z. Phys. **232**, 101 (1970).

[213] R. Mewe, Astron. and Astrophys. **20**, 215 (1972).

[214] R. Neu, K. B. Fournier, D. Bolshukhin, and R. Dux, Physica Scripta **T92**, 307–310 (2001).

[215] H. P. Summers, Atomic data and analysis structure users manual, JET-IR 06 (Abingdon: JET Joint Undertaking) (1994).

[216] J.-F. Wyart, C. Bauche-Arnoult, J.-C. Gauthier, J. Geindre, P. Monier, et al., Phys. Rev. A **34**, 701 – 704 (1986).

[217] C. Biedermann and K. Fournier, private communication, 2002.

[218] M. Klapisch, A. Bar-Shalom, P. Mandelbaum, J. Schwob, A. Zigler, et al., Physics Letters **79A**, 67 – 70 (1980).

[219] M. O'Mullane, R. Barnsley, I. Coffey, G. Counsell, S. Loch, et al., Proc. Top. Conf. on High Temp. Plasma Diagnostics, Madison, 6-11 July, 2002 (2002).

[220] P. Stangeby, in *The Plasma Boundary of Magnetic Fusion Devices*, Dirac House, Temple Back, Bristol, UK, 2000, IOP.

[221] R. Schneider, Plasma edge physics for tokamaks, volume IPP 12/1, Garching, 2001, MPI für Plasmaphysik.

[222] C. S. Pitcher and P. Stangeby, Plasma Phys. Controlled Fusion **39**, 779–930 (1997).

[223] G. Fussmann, W. Engelhardt, D. Naujoks, K. Asmussen, S. Deschka, et al., High-Z Elements as Target Materials in Fusion Devices, in *Plasma Physics and Controlled Fusion Research, Proc. 15th. Int. Conf. Seville (1994)*, volume Vol.2, page 143, IAEA, Vienna, 1995.

[224] D. Naujoks, J. Roth, K. Krieger, G. Lieder, and M. Laux, J. Nucl. Mater. **210**, 43–50 (1994).

[225] V. Rohde and ASDEX Upgrade Team, Contrib. Plasma Phys. **36**, 109–116 (1996).

[226] A. V. Chankin, G. Corrigan, S. Erents, G. Matthews, J. Spence, et al., J. Nucl. Mater. **290 – 293**, 518 – 524 (2001).

[227] N. Asakura, S. Sakurai, K. Itami, O. Naito, H. Takenaga, et al., J. Nucl. Mater. **313-316**, 820–827 (2003).

[228] R. Schneider et al., J. Nucl. Mater. **196-198**, 810 (1992).

[229] P. Stangeby and J. Elder, J. Nucl. Mater. **196-198**, 258 (1992).

[230] A. Geier, R. Neu, R. Dux, V. Rohde, R. Pugno, et al., Operation of ASDEX Upgrade with a Fully Tungsten Coated Central Column - Results from Experiments and Modeling, in *Europhysics Conference Abstracts (CD-ROM, Proc. of the 29th EPS Conference on Controlled Fusion and Plasma Physics, Montreux, 2002)*, edited by R. Behn and C. Varandas, volume 26B, page P2.048, Geneva, 2002, EPS.

[231] A. Geier, K. Krieger, J. D. Elder, R. Pugno, V. Rohde, et al., J. Nucl. Mater. **313–316**, 1216–1220 (2003).

[232] J. Neuhauser, D. Coster, H. U. Fahrbach, J. C. Fuchs, G. Haas, et al., Plasma Phys. Controlled Fusion **44**(6), 855–870 (2002).

[233] J. Roth and G. Janeschitz, Nucl. Fusion **29**, 915 (1989).

[234] R. Neu, K. Asmussen, K. Krieger, A. Thoma, H.-S. Bosch, et al., Plasma Phys. Controlled Fusion **38**, A165–A179 (1996).

[235] T. Kato, Ionization and Excitation of Ions by Electron impact - Review of Impirical Formulae, Technical Report IPPJ-AM-2, Department of Physics, Nagoya University, 1977.

[236] C. Breton, C. DeMichelis, and M. Mattioli, J. Quant. Spectrosc. Radiat. Transfer **19**, 367 (1978).

[237] T. Pütterich and H. Summers, 2003, private communication.

[238] K. Asmussen, Untersuchungen zum Verhalten von Wolfram in Tokamakplasmen, Technical Report 10/2, IPP, Garching, Germany, Mar. 1996, Ph.D. thesis TU Munich, June 95.

[239] F. Hinton and R. Hazeltine, Rev. Mod. Phys. **48**, 239 (1976).

[240] K. Behringer, Description of the impurity transportcode STRAHL, Technical Report JET-R(87)08, JET Joint Undertaking, Abingdon, United Kingdom, 1987.

[241] R. DUX, STRAHL Manual, www.aug.ipp.mpg.de/~Ralph.Dux/strahl.ps.

[242] S. P. Hirshman and D. J. Sigmar, Nucl. Fusion **21**(9), 1079–1201 (1981).

[243] G. Fussmann, A. Field, A. Kallenbach, K. Krieger, K. Steuer, et al., Plasma Phys. Controlled Fusion **33**, 1677 – 1695 (1991).

[244] G. Fußmann, Teilchentransport in magnetisch eingeschlossenen Plasmen, Technical Report 1/273, IPP, Garching, Germany, Dec. 1992, Habilitationsschrift.

[245] Y. B. Kim, P. H. Diamond, and R. J. Groebner, Phys. Fluids B **3**(8), 2050–2060 (1991).

[246] R. Dux, A. G. Peeters, A. Gude, A. Kallenbach, R. Neu, et al., Nucl. Fusion **39**(11), 1509–1522 (1999).

[247] A. G. Peeters, Phys. Plasmas **7**(1), 268–275 (2000).

[248] W. A. Houlberg, K. C. Shaing, S. P. Hirshman, and M. C. Zarnstorff, Phys. Plasmas **4**(9), 3230–3241 (1997).

[249] R. Dux, C. Giroud, and K. Zastrow, submitted to Nucl. Fusion (2003).

[250] M. Kotschenreuther, W. Dorland, M. Beer, and G. Hammett, Phys. Plasmas **2**, 2381 (1995).

[251] H. Nordmann, J. Weiland, and A. Jarmen, Nucl. Fusion **30**, 983 (1990).

[252] R. Waltz et al., Phys. Plasmas **4**, 2482 (1997).

[253] G. Tardini, A. G. Peeters, G. V. Pereverzev, F. Ryter, J. Stober, et al., Nucl. Fusion **42**(3), 258–264 (2002).

[254] J. Stober, C. Fuchs, O. Gruber, M. Kaufmann, B. Kurzan, et al., Nucl. Fusion **41**(11), 1535–1538 (2001).

[255] J. Stober, O. Gruber, M. Kaufmann, R. Neu, F. Ryter, et al., Plasma Phys. Controlled Fusion **44**(5A), A159–A164 (2002).

[256] J. Wesson, *Tokamaks*, Clarendon Press, Oxford, 2 edition, 1997.

[257] H. Zohm, Plasma Phys. Controlled Fusion **38**(8), 1213–1223 (1996).

[258] R. Dux, Fusion Tech. **44**(3), 708–715 (2003).

[259] S. de Peña Hempel, R. Dux, A. Kallenbach, H. Meister, and ASDEX Upgrade Team, Low-Z-Impurity Transport Coefficients at ASDEX Upgrade, in *Europhysics Conference Abstracts (Proc. of the 24th EPS Conference on Controlled Fusion and Plasma Physics, Berchtesgaden, 1997)*, edited by M. Schittenhelm, R. Bartiromo, and F. Wagner, volume 21A, part IV, pages 1401–1404, Petit-Lancy, 1997, EPS.

[260] J. Roth, D. Naujoks, K. Krieger, A. R. Field, G. Lieder, et al., J. Nucl. Mater. **220–222**, 231–234 (1995).

[261] C. García-Rosales, S. Deschka, W. Hohenauer, R. Duwe, E. Gauthier, et al., Fusion Tech. **32**, 263–276 (1997).

[262] R. Neu, K. Asmussen, S. Deschka, A. Thoma, M. Bessenrodt-Weberpals, et al., J. Nucl. Mater. **241–243**, 678–683 (1997).

[263] K. Asmussen, R. Neu, R. Dux, W. Engelhardt, K. Fournier, et al., Investigations of Tungsten in the Central Plasma of ASDEX Upgrade, in *Europhysics Conference Abstracts (Proc. of the 24th EPS Conference on Controlled Fusion and Plasma Physics, Berchtesgaden, 1997)*, edited by M. Schittenhelm, R. Bartiromo, and F. Wagner, volume 21A, part IV, pages 1393–1396, Petit-Lancy, 1997, EPS.

[264] V. Rohde, R. Neu, K. Krieger, H. Maier, A. Geier, et al., Operation of ASDEX Upgrade with High-Z Wall Coatings, in *Proc. of the 18th IAEA Conference Fusion Energy (CD-Rom), Sorrento, Italy, October 2000*, volume IAEA-CSP-8/C, pages IAEA–CN–77/EXP4/24, Vienna, 2001, IAEA.

[265] A. Tabasso, H. Maier, K. Krieger, J. Roth, and ASDEX Upgrade Team, Nucl. Fusion **40**(8), 1441–1444 (2000).

[266] R. Neu, V. Rohde, A. Geier, K. Krieger, H. Maier, et al., J. Nucl. Mater. **290–293**, 206–210 (2001).

[267] V. Rohde, R. Neu, A. Geier, R. Dux, O. Gruber, et al., Tungsten as First Wall Material in the Main Chamber of ASDEX Upgrade, in *Europhysics Conference Abstracts (CD-ROM, Proc. of the 28th EPS Conference on Controlled Fusion and Plasma Physics, Madeira 2001)*, edited by R. Pick, volume 25A, pages 185–188, Geneva, 2001, EPS.

[268] R. Neu, R. Dux, A. Geier, A. Kallenbach, R. Pugno, et al., Plasma Phys. Controlled Fusion **44**(6), 811–826 (2002).

[269] R. Neu, R. Dux, A. Geier, H. Greuner, K. Krieger, et al., J. Nucl. Mater. **313–316**, 116–126 (2003).

[270] M. Weinlich and A. Carlson, Contrib. Plasma Phys. **36**, 53–60 (1996).

[271] C. Kurz, B. Lipschultz, G. McCracken, M. Graf, J. Snipes, et al., J. Nucl. Mater. **220-222**, 963–966 (1995).

[272] W. Eckstein, K. Krieger, and J. Roth, J. Nucl. Mater. **258-263**, 912–916 (1998).

[273] J. Rapp, G. Bertschinger, L. Könen, H. Koslowski, A. Krämer-Flecken, et al., Charateristics of the impurities Mo and W in discharges with neon edge radiation cooling in TEXTOR–94, in *Europhysics Conference Abstracts (Proc. of the 23th EPS Conference on Controlled Fusion and Plasma Physics, Kiev, 1996)*, volume 20C, pages 819 — 822, Geneva, 1996, EPS.

[274] J. Rapp, G. Van Oost, G. Bertschinger, L. Könen, H. Koslowski, et al., Influence of high-Z limiter materials on the properties of the RI-mode in TEXTOR–94 with different heating schemes, in *Europhysics Conference Abstracts (Proc. of the 24th EPS Conference on Controlled Fusion and Plasma Physics, Berchtesgaden, 1997)*, volume 21A, pages 1745 — 1748, Geneva, 1997, EPS.

[275] A. Kallenbach, R. Dux, V. Mertens, O. Gruber, G. Haas, et al., Nucl. Fusion **35**(10), 1231–1246 (1995), preprint in IPP 1/284, January 1995.

[276] V. Philipps, M. Tokar, A. Prospieszczyk, U. Kögler, R. Koslowski, et al., Studies of high-Z wall components in TEXTOR94: local impurity release and its impact on the plasma core, in *Europhysics Conference Abstracts (Proc. of the 22th EPS Conference on Controlled Fusion and Plasma Physics, Bournemouth, 1995)*, volume 19C, part II, pages 321–324, Geneva, 1995, EPS.

[277] H. Maier, S. Kötterl, K. Krieger, R. Neu, M. Balden, et al., J. Nucl. Mater. **258–263**, 921–926 (1998).

[278] A. Pospieszczyk, V. Philipps, E. Casarotto, U. Kögler, B. Schweer, et al., J. Nucl. Mater. **241–243**, 833 – 838 (1997).

[279] A. Herrmann, W. Junker, K. Günther, S. Bosch, M. Kaufmann, et al., Plasma Phys. Controlled Fusion **37**(1), 17–29 (1995).

[280] G. Fussmann, J. Hofmann, G. Janeschitz, K. Krieger, E. Müller, et al., J. Nucl. Mater. **162–164**, 14–23 (1989).

[281] M. Z. Tokar, J. Rapp, G. Bertschinger, L. Könen, H. R. Koslowski, et al., Nucl. Fusion **37**, 1691–1708 (1997).

[282] A. Kallenbach, R. Neu, W. Poschenrieder, and ASDEX Upgrade Team, Nucl. Fusion **34**(12), 1557–1565 (1994).

[283] G. McCracken et al., Nucl. Fusion **39**, 41 – 60 (1999).

[284] V. Mertens, P. T. Lang, K. Büchl, R. Dux, C. Fuchs, et al., High Density Operation in Auxiliary Heated ASDEX Upgrade Discharges, in *Europhysics Conference Abstracts*

(Proc. of the 23rd EPS Conference on Controlled Fusion and Plasma Physics, Kiev, 1996), edited by D. Gresillon, A. Sitenko, and A. Zagorodony, volume 20C, part I, pages 15–18, Geneva, 1996, EPS.

[285] H. Zohm, M. Alexander, R. Buttery, S. de Peña Hempel, O. Gruber, et al., Beta-Limiting Phenomena in ASDEX Upgrade, in *Europhysics Conference Abstracts (Proc. of the 23rd EPS Conference on Controlled Fusion and Plasma Physics, Kiev, 1996)*, edited by D. Gresillon, A. Sitenko, and A. Zagordony, volume 20C, part I, pages 43–46, Geneva, 1996, EPS.

[286] H. Zohm, M. Maraschek, G. Pautasso, M. Schittenhelm, S. Sesnic, et al., Plasma Phys. Controlled Fusion **37**(11A), A313–A324 (1995).

[287] T. Tanabe, N. Noda, and H. Nakamura, J. Nucl. Mater. **196-198**, 11–27 (1992).

[288] W. Suttrop, H. J. de Blank, G. Haas, H. Murmann, O. Gehre, et al., The Role of Edge Parameters for L-H Transition and ELM Behaviour on ASDEX Upgrade, in *Europhysics Conference Abstracts (Proc. of the 23rd EPS Conference on Controlled Fusion and Plasma Physics, Kiev, 1996)*, edited by D. Gresillon, A. Sitenko, and A. Zagorodony, volume 20C, part I, pages 47–50, Geneva, 1996, EPS.

[289] A. Kallenbach, R. Dux, G. Haas, A. Herrmann, S. Hirsch, et al., Characteristics of Radiative Boundary Discharges with Different Impurity Injection Conditions, in *Europhysics Conference Abstracts (Proc. of the 22th EPS Conference on Controlled Fusion and Plasma Physics, Bournemouth, 1995)*, edited by B. Keen, P. Stott, and J. Winter, volume 19C, part II, pages 5–8, Geneva, 1995, EPS.

[290] A. Kallenbach, R. Dux, S. de Peña Hempel, G. Becker, H.-S. Bosch, et al., Optimization of Radiative H-Mode Operation, in *Europhysics Conference Abstracts (Proc. of the 23rd EPS Conference on Controlled Fusion and Plasma Physics, Kiev, 1996)*, edited by D. Gresillon, A. Sitenko, and A. Zagorodony, volume 20C, part I, pages 83–86, Geneva, 1996, EPS.

[291] R. Dux, A. Kallenbach, K. Behringer, R. Neu, S. de Peña Hempel, et al., Measurement and Modelling of Impurity Transport in Radiating Boundary Discharges in ASDEX Upgrade, in *Europhysics Conference Abstracts (Proc. of the 23rd EPS Conference on Controlled Fusion and Plasma Physics, Kiev, 1996)*, edited by D. Gresillon, A. Sitenko, and A. Zagorodony, volume 20C, part I, pages 95–98, Geneva, 1996, EPS.

[292] Y. Ueda, T. Tanabe, V. Phillips, L. Könen, A. Pospieszczyk, et al., J. Nucl. Mater. **220-222**, 240 – 243 (1995).

[293] R. Pugno, A. Kallenbach, D. Bolshukhin, R. Dux, J. Gafert, et al., J. Nucl. Mater. **290–293**, 308–311 (2001).

[294] G. Janeschitz, ITER JCT, and ITER HTs, J. Nucl. Mater. **290 − 293**, 1 – 11 (2001).

[295] H. Maier, J. Luthin, M. Balden, M. Rehm, F. Koch, et al., Surface and Coating Technology **142-144**, 733–737 (2001).

[296] H. Maier, J. Luthin, M. Balden, S. Lindig, J. Linke, et al., J. Nucl. Mater. **307-311**, 116–120 (2002).

[297] B. Böswirth, H. Greuner, G. Matern, S. Schweizer, and MARION Team, HHF-Tests an ASDEX Upgrade Hitzeschild Kacheln, Technical report, IPP Garching, 2002.

[298] H. Maier, IPP Garching, private communication, 2000.

[299] K. Krieger, X. Gong, M. Balden, D. Hildebrandt, H. Maier, et al., J. Nucl. Mater. **307-311**, 139–143 (2002).

[300] H. Verbeek, J. Stober, D. P. Coster, W. Eckstein, and R. Schneider, Nucl. Fusion **38**(12), 1789–1803 (1998).

[301] V. Rohde, R. Neu, R. Dux, A. Geier, X. Gong, et al., Operation of ASDEX Upgrade with Tungsten Coated Walls, in *Proc. of the 19th IAEA Conference Fusion Energy (CD-Rom), Lyon, France, October 2002*, volume IAEA-CSP-19/CD, pages IAEA–CN–94/EX/DI–4, Vienna, 2002, IAEA.

[302] R. Neu, J. C. Fuchs, G. Haas, A. Herrmann, A. Kallenbach, et al., Plasma Phys. Controlled Fusion **44**(6), 1021–1029 (2002).

[303] F. Ryter, H.-U. Fahrbach, A. Gude, R. Neu, V. Rohde, et al., Plasma Phys. Controlled Fusion **44**(5A), A407–A413 (2002).

[304] J. Stober, M. Maraschek, G. D. Conway, O. Gruber, A. Herrmann, et al., Nucl. Fusion **41**(9), 1123–1134 (2001).

[305] J. Strachan, W. Fundamenski, M. Charlet, K. Erents, J. Gafert, et al., Screening of Hydrocarbon Sources in JET, in *Europhysics Conference Abstracts (Proc. of the 28th EPS Conference on Controlled Fusion and Plasma Physics, Funchal, 2001)*, Geneva, 2001, EPS.

[306] M. Stamp, D. Elder, H. Guo, M. von Hellermann, L. Horton, et al., J. Nucl. Mater. **266-269**, 685 – 686 (1999).

[307] G. McCracken, R. Granetz, B. Lipschultz, B. LaBombard, F. Bombarda, et al., J. Nucl. Mater. **241 – 243**, 777 – 781 (1997).

[308] O. Gruber, R. C. Wolf, R. Dux, C. Fuchs, S. Günter, et al., Phys. Rev. Lett. **83**(9), 1787–1790 (1999).

[309] A. Sips et al., Plasma Phys. Controlled Fusion **44**, A151–A157 (2002).

[310] F. Ryter, J. Stober, A. Stäbler, G. Tardini, H.-U. Fahrbach, et al., Nucl. Fusion **41**(5), 537–550 (2001).

[311] R. Dux, R. Neu, A. G. Peeters, G. Pereverzev, A. Mück, et al., Plasma Phys. Controlled Fusion **45**(9), 1815–1825 (2003).

[312] E. Doyle, L. Baylor, K. Burrell, T. Casper, J. DeBoo, et al., Plasma Phys. Controlled Fusion **43**, A95 – A112 (2001).

[313] W. West, M. Wade, C. Greenfield, E. Doyle, K. Burrell, et al., Phys. Plasmas **9**, 1970 – 1981 (2002).

[314] A. Stäbler, private communication, 2003.

[315] W. Suttrop, M. Maraschek, G. D. Conway, H.-U. Fahrbach, G. Haas, et al., Plasma Phys. Controlled Fusion **45**(8), 1399–1416 (2003).

[316] N. Noda, V. Philipps, and R. Neu, J. Nucl. Mater. **241 – 243**, 227 – 243 (1997).

[317] J. Stober, H. Zohm, O. Gruber, A. Herrmann, M. Kaufmann, et al., Plasma Phys. Controlled Fusion **43**(12A), A39–A53 (2001).

[318] G. Van Oost, A. Messiaen, V. Philipps, R. Koch, A. Krämer-Flecken, et al., Auxiliary heating experiments with a tungsten test limiter in TEXTOR94, in *Europhysics Conference Abstracts (Proc. of the 22th EPS Conference on Controlled Fusion and Plasma Physics, Bournemouth, 1995)*, volume 19C, part II, pages 345–348, Geneva, 1995, EPS.

[319] J. Stober, R. Dux, O. Gruber, L. Horton, P. Lang, et al., Nucl. Fusion **43**(10), 1265–1271 (2003).

[320] F. Ryter, G. Tardini, F. De Luca, H.-U. Fahrbach, F. Imbeaux, et al., Electron Heat Transport in ASDEX Upgrade: Experiment and Modelling, in *Proc. of the 19th IAEA Conference Fusion Energy (CD-Rom), Lyon, France, October 2002*, volume IAEA-CSP-19/CD, pages IAEA–CN–94/EX/C4–2Ra, Vienna, 2002, IAEA.

[321] R. Dux, C. Giroud, R. Neu, A. G. Peeters, J. Stober, et al., J. Nucl. Mater. **313–316**, 1150–1155 (2003).

[322] T. Pütterich, R. Dux, J. Gafert, A. Kallenbach, R. Neu, et al., Plasma Phys. Controlled Fusion **45**(10), 1873–1892 (2003).

[323] R. Dux and A. G. Peeters, Nucl. Fusion **40**(10), 1721–1729 (2000).

[324] B. Lipschultz et al., J. Nucl. Mater. **128-129**, 555 (1984).

[325] R. Hawryluk et al., Nucl. Fusion **19**, 1307 (1979).

[326] N. Ohta et al., Fusion Eng. Des. **5**, 27 (1987).

[327] S. Itoh, K. Nakamura, M. Sakamoto, K. Makino, E. Jotaki, et al., Ultra-Long Tokamak Discharge by Lower Hybrid Current Drive on TRIAM-1M, in *Plasma Physics and Controlled Nuclear Fusion Research 1996*, volume 3, pages 351–357, Vienna, 1997, IAEA.

[328] U. Samm and the TEXTOR-94 Team, Plasma Phys. Controlled Fusion **41**, B57 – B76 (1999).

[329] F. Alladio, B. Angelini, M. Apicella, G. Apruzzese, E. Barbato, et al., Overview of the FTU results, in *Proc. 18th IAEA Fusion Energy conference, Sorent*, volume IAEA-CN-77, page OV/2, Vienna, 2000, IAEA.

[330] M. Porkolab, R. Boivin, F. Bombarda, P. Bonoli, C. Christensen, et al., Overview of recent results from Alcator C-Mod, in *Plasma Physics and Controlled Nuclear Fusion Research 1994*, volume 1, pages 123–135, Vienna, 1995, IAEA.

[331] R. Parker, M. Greenwald, S. Luckhardt, E. Marmar, M. Porkolab, et al., Nucl. Fusion **25**, 1127 (1985).

[332] F. Alladio and the FT Group, Nucl. Fusion **25**, 1069 (1985).

[333] ORMAK-ISX Group, Nucl. Fusion **25**, 1137 – 1143 (1985).

[334] TFR Group, Nucl. Fusion **25**, 1025 (1985).

[335] M. Tanaka, Nucl. Fusion **25**, 1073 (1985).

[336] J. Paul, Nucl. Fusion **25**, 1097 (1985).

[337] S. Kasai, A. Funahashi, M. Nagami, and T. Sugie, Nucl. Fusion **19** (1979).

[338] S. Yamamoto, H. Maeda, Y. Shimomura, K. Odajima, M. Nagami, et al., Reduction of power loss due to heavy impurities in DIVA, in *Proc. 8th Conf. EPS, Prague 1977*, volume 1, page 33, Geneva, 1978, EPS.

[339] S. Fielding, M. Hobby, J. Hugill, G. McCracken, J. Paul, et al., Control of impurities by DITE bundle divertor, in *Proc. 8th Conf. EPS, Prague 1977*, volume 1, page 36, Geneva, 1978, EPS.

[340] J. E. Rice, J. Terry, and E. Marmar, Nucl. Fusion **24** (1984).

[341] H. Manning, J. Terry, B. Lipschultz, B. LaBombard, B. Blackwell, et al., Nucl. Fusion **12**, 1665 – 1678 (1986).

[342] J. Hosea, R. Goldston, and P. Colestock, Nucl. Fusion **25**, 1155 (1985).

[343] H. Hsuan, V. Arunasalam, M. Bitter, K. Bol, D. Boyd, et al., Energy Balance of the PLT tokamak, in *Proc. 9th Conf. EPS, Grenoble 1978*, volume 2, pages 17–28, Geneva, 1978, EPS.

[344] K. Bol, V. Arunasalam, M. Bitter, D. Boyd, K. Brau, et al., Radiation, Impurity Effects, Instability Characteristics and Transport in Ohmically Heated Plasmas in the PLT tokamak, in *Proc. 7th IAEA Conf., Innsbruck 1978*, volume Vol.1, page 11, Vienna, 1979, IAEA.

[345] S. Cohen, H. Dylla, S. Rossnagel, S. Picraux, J. Borders, et al., J. Nucl. Mater. **76-77**, 459 (1978).

[346] H. Hosogane et al., J. Nucl. Mater. **162-164**, 93 (1989).

[347] M. Apicella, G. Apruzzese, M. Borra, G. Bracco, M. Ciotti, et al., Nucl. Fusion **37**, 381–396 (1997).

[348] M. Ciotti, C. Ferro, and G. Maddaluno, J. Nucl. Mater. **196 – 198**, 725 (1992).

[349] M. Apicella, G. Mazzitelli, G. Apruzzese, G. Bracco, B. Esposito, et al., J. Nucl. Mater. **313-316**, 269–273 (2003).

[350] M. Apicella, G. Apruzzese, R. De Angelis, G. Gatti, M. Leigheb, et al., Effects of wall titanium coating on FTU plasma operations, volume ECA Vol. 24B, pages 1573–1576, EPS, 2000.

[351] F. Alladio et al., Plasma Phys. Controlled Fusion **36**, B253 (1994).

[352] M. May, K. Fournier, J. Goetz, J. Terry, D. Pacella, et al., Plasma Phys. Controlled Fusion **41**, 45 – 63 (1999).

[353] G. Maddaluno, F. Pierdominici, and M. Vittori, J. Nucl. Mater. **241-243**, 908–913 (1997).

[354] V. Philipps, T. Tanabe, Y. Ueda, A. Prospieszczyk, M. Tokar, et al., Nucl. Fusion **34**, 1417 – 1429 (1994).

[355] V. Philipps, A. Prospieszczyk, M. Tokar, B. Unterberg, L. Könen, et al., Experiments with molybdenum and tungsten limiters in TEXTOR, IAEA, Sevilla, 1994, IAEA-CN-60/A2/A4-P19.

[356] B. Unterberg et al., J. Nucl. Mater. **266–269**, 75 (1999).

[357] A. Huber, V. Philipps, A. Kirschner, A. Pospieszczyk, M. Lehnen, et al., Comparison of impurity production and recycling on carbon and tungsten limiters in TEXTOR-94, volume ECA Vol. 23J, pages 685–688, EPS, 1999.

[358] A. Kirschner et al., Nucl. Fusion **40**, 989 (2000).

[359] R. Koch, A. Messiaen, J. Ongena, et al., Fus. Eng. Design **26**, 103 (1995).

[360] J. Stober, R. Dux, O. Gruber, L. Horton, P. Lang, et al., Dependence of Particle Transport on Heating Profiles in ASDEX Upgrade, in *Proc. of the 19th IAEA Conference Fusion Energy (CD-Rom), Lyon, France, October 2002*, volume IAEA-CSP-19/CD, pages IAEA–CN–94/EX/C3–7Rb, Vienna, 2002, IAEA.

[361] I. Hutchinson, R. Boivin, F. Bombarda, et al., Phys. Plasmas **1**, 1511 (1994).

[362] M. May, M. Finkenthal, S. Regan, H. Moos, J. Terry, et al., Nucl. Fusion **37**, 881 – 896 (1997).

[363] R. Neu, K. Asmussen, J. Fuchs, R. Dux, J. Goetz, et al., Comparison of High-Z Operation in ASDEX Upgrade and Alcator C-Mod, in *Verhandl. DPG (VI) 32 (Proc. of the Spring Meeting of the German Physical Society)*, volume VI, pages 274, P13.5, 1997.

[364] J. E. Rice, K. Fournier, M. Graf, J. Terry, M. Finkenthal, et al., Phys. Rev. A **51**, 3551–3559 (1995).

[365] B. Lipschultz, G. McCracken, M. Graf, J. Snipes, J. Terry, et al., J. Nucl. Mater. **220-222**, 967–970 (1995).

[366] M. Greenwald, R. Boivin, P. Bonoli, R. Budny, C. Fiore, et al., Phys. Plasmas **6**, 1943 (1999).

[367] C. Read et al., Bull. Am. Phys. Soc. **41**, 1551 (1996).

[368] D. Pappas, B. Lipschultz, B. LaBombard, M. May, and C. Pitcher, J. Nucl. Mater. **266-269**, 635 – 641 (1999).

[369] W. Wampler, B. LaBombard, B. Lipschultz, G. McCracken, D. Pappas, et al., J. Nucl. Mater. **266-269**, 217–221 (1999).

[370] B. Lipschultz, D. Pappas, B. LaBombard, J. Rice, D. Smith, et al., Nucl. Fusion **41**, 585 – 596 (2001).

[371] B. Lipschultz, D. Pappas, B. LaBombard, J. Rice, D. Smith, et al., J. Nucl. Mater. **290-293**, 286 (2001).

[372] in *ITER Final Design Report, Cost Review and Safety Analyses (FDR) and Relevant Documents*, ITER EDA Documentation Series No. 14, IAEA, Vienna, 1999.

[373] D. Meade, C. Kessel, G. Hammett, S. Jardin, M. Ulrickson, et al., Exploration of Burning Plasmas in FIRE, in *Proc. of the 19th IAEA Conference Fusion Energy (CD-Rom), Lyon, France, October 2002*, volume IAEA-CSP-19/CD, pages IAEA–CN–94/FT/2–6, Vienna, 2003, IAEA.

[374] B. Coppi, L. Sugiyama, and M. Nassi, Fusion Technology **21**, 1612 (1992).

[375] R. Toschi, P. Barabaschi, D. Campbell, F. Elio, D. Maisonnier, et al., Fusion Eng. Des. **56-57**, 163 – 172 (2001).

[376] F. Najmabadi, S. Jardin, M. Tillack, L. Waganer, and the ARIES Team, 'ARIES-AT: An Advanced Tokamak, Advanced Technology Fusion Power Plant, in *Proc. of the 18th IAEA Conference Fusion Energy (CD-Rom), Sorrento, Italy, October 2000*, volume IAEA-CSP-8/C, pages IAEA–CN–77/FTP2/15, Vienna, 2001, IAEA.

[377] S. Nishio, K. Ushigusa, S. Ueada, A. Polevoi, K. Tobita, et al., Conceptional Design of Advanced Steady-State Tokamak Reactor, in *Proc. of the 18th IAEA Fusion Energy Conference, Sorrento, Italy*, volume FTP2/14, 2000.

[378] H. Pacher, I. Smid, G. Federici, Y. Igitkhanov, G. Janeschitz, et al., J. Nucl. Mater. **241–243**, 255 – 259 (1997).

[379] N. Peacock, R. Barnsley, N. Hawkes, K. Lawson, and M. O'Mullane, Spectroscopy for impurity control in ITER, in *Diagnostics for experimental thermonuclear fusion reactors, Varenna (Italy)*, edited by P. Stott, G. Gorini, and E. Sindoni, pages 291 — 305, New York, 1996, Plenum Press.

[380] D. Meade, S. Jardin, J. Schmidt, R. Thome, N. Sauthoff, et al., Mission and Design of the Fusion Ignition Research Experiment (FIRE), in *Proc. of the 18th IAEA Conference Fusion Energy (CD-Rom), Sorrento, Italy, October 2000*, volume IAEA-CSP-8/C, pages IAEA–CN–77/FTP2/16, Vienna, 2001, IAEA.

[381] M. Ulrickson et al., to be published in Fusion Eng. Des. (2001).

[382] D. King, A. Airaghi, H. Bolt, J. Calvo, B. Frois, et al., Conclusions of the Fusion Fast Track Experts Meeting, Brussels, 2001, European Research Council.

[383] K. Lackner, R. Andreani, D. Campbell, M. Gasparotto, D. Maisonnier, et al., J. Nucl. Mater. **307-311**, 10–20 (2002).

[384] G. Shatalov, I. Kirillov, Y. Sokolov, Y. Strebkov, N. Vasiliev, et al., Fusion Eng. Des. **56-57**, 163 – 172 (2001).

[385] S. Konishi, S. Nishio, K. Tobita, and DEMO design team, Fus. Eng. Design **63-64**, 11–17 (2002).

[386] K. Tsuzuki, M. Sato, H. Kawashima, H. Ogawa, H. Kimura, et al., J. Nucl. Mater. **313-316**, 177 – 181 (2003).

[387] A. Tabasso, H. Maier, J. Roth, K. Krieger, and ASDEX Upgrade Team, J. Nucl. Mater. **290–293**, 326–330 (2001).

[388] A. Airaghi, H. Conde, C. Matos Ferreira, G. Newi, P. Rebut, et al., Five Year Assessment Report Related to the Specific Programme: Nuclear Energy; Covering the period 1995 - 1999, Brussels, 2000, Eurpean Commission.

[389] S. Jardin, C. Bathke, D. Ehst, S. Kaye, C. Kessel Jr, et al., Fus. Eng. Design **48**, 281–298 (2000).

[390] ARIES-Program, 'ARIES-AT Physics Design Parameters', in *http://michelle.ucsd.edu/mau/aries/aries-at/summary.shtml*, UC San Diego, 2000.

[391] D. P. Coster, R. Schneider, J. Neuhauser, H.-S. Bosch, R. Wunderlich, et al., J. Nucl. Mater. **241–243**, 690–695 (1997).

[392] H. P. Summers, N. R. Badnell, M. G. O'Mullane, A. D. Whiteford, R. Bingham, et al., Plasma Phys. Controlled Fusion **44**(12B), B323–B338 (2002).

[393] E. Doyle, T. Casper, K. Burrell, C. Greenfield, W. West, et al., Core and edge aspects of quiescent double barrier operation on DIII-D, with relevance to critical ITB physics issues, in *Proc. of the 19th IAEA Conference Fusion Energy (CD-Rom), Lyon, France, October 2002*, volume IAEA-CSP-19/CD, pages IAEA–CN–94/EX/C3–2, Vienna, 2003, IAEA.

[394] H. Takenaga, S. Higashijima, N. Oyama, L. Bruskin, Y. Koide, et al., Relationship between particle and heat transport in JT-60U plasmas with internal transport barrier, in *Proc. of the 19th IAEA Conference Fusion Energy (CD-Rom), Lyon, France, October 2002*, volume IAEA-CSP-19/CD, pages IAEA–CN–94/C3–5Rb, Vienna, 2003, IAEA.

[395] P. T. Lang, J. Neuhauser, L. D. Horton, T. Eich, L. Fattorini, et al., Nucl. Fusion **43**(10), 1110–1120 (2003).

[396] F. Ajzenberg-Selove, Nuclear Physics **A490**, 1–225 (1988).

[397] H.-S. Bosch and G. M. Hale, Nucl. Fusion **32**(4), 611–631 (1992), Erratum in **33**(12), 1919 (1993).

[398] L. Artsimovich, S. Mirnov, and V. Strelkov, Plasma Physics **7**, 305 (1965).

[399] F. Chen, in *Plasma Physics and Controlled Fusion*, New York, 1983, Plenum Press.

[400] R. Gross, in *Fusion Energy*, New York, 1984, J. Wiley a. Sons.

[401] W. Köppendörfer, M. Blaumoser, H. Bruhns, C. Dorn, J. Gernhardt, et al., Completion of Assembly and Start of Technical Operation of ASDEX Upgrade, in *Fusion Technology (Proc. of the 16th Symposium on Fusion Technology, London, U.K., 1990)*, edited by B. Keen, M. Huguet, and R. Hemsworth, volume 1, pages 208–212, Amsterdam, 1991, Elsevier.

[402] O. Gruber, R. Arslanbekov, C. Atanasiu, A. Bard, G. Becker, et al., Nucl. Fusion **41**(10), 1369–1389 (2001).

[403] The ASDEX Upgrade Team presented by H. Zohm, Overview of ASDEX Upgrade Results, in *Proc. of the 19th IAEA Conference Fusion Energy (CD-Rom), Lyon, France, October 2002*, volume IAEA-CSP-19/CD, pages IAEA–CN–94/OV/2–1, Vienna, 2002, IAEA.

[404] I. Hutchinson, in *Principles of Plasma Diagnostics*, Cambridge, USA, 1987, Cambridge University Press.

[405] A. Costley, Recent developments and applications of electron cyclotron emission, in *Basic and Advanced Fusion Plasma Diagnostic Techniques*, volume II, pages 119–138, 1986.

[406] H. Bindslev, Rev. Sci. Instrum. **70**, 1093–1099 (1999).

[407] H. Salzmann, Thomson scattering, in *Basic and Advanced Fusion Plasma Diagnostic Techniques*, volume II, pages 477 – 496, 1986.

[408] H. Soltwisch, Interferometry and Faraday rotation measurements on tokamaks, in *Basic and Advanced Fusion Plasma Diagnostic Techniques*, volume II, pages 343 – 378, 1986.

[409] A. Costley, Diagnosis of fusion plasmas using reflectometry, in *Basic and Advanced Fusion Plasma Diagnostic Techniques*, volume II, pages 379–398, 1986.

[410] M. E. Manso, P. Varela, I. Nunes, J. Santos, G. D. Conway, et al., Plasma Phys. Controlled Fusion **43**(12A), A73–A93 (2001).

[411] E. Hintz and B. Schweer, Plasma Phys. Controlled Fusion **37**, A87 – A102 (1995).

[412] R. Brandenburg and J. Schweinzer, Lithiumstrahldiagnostik von Kernfusionsplasmen, Technical Report 5/86, IPP, Garching, Germany, 1999.

Acknowledgement

This thesis would not be complete without me trying to express my gratitude to the numerous people who were involved in its preparation.

I would like to thank Prof. Kurt Behringer and Prof. Michael Kaufmann at the Max-Planck Institute for Plasma Physics (IPP) for giving me the opportunity of writing this thesis and for putting the co-ordination of the W programme in my hands.

I am indebted to Prof. Gerhard J. Wagner at the Institute of Physics, University of Tübingen, who made it possible for me to teach plasma physics at the University of Tübingen and who followed the evolution of the thesis with great interest. I also want to thank my former supervisor Prof. Günter Staudt from the University of Tübingen who encouraged me during all stages of the work.

Special thanks go to my fellow colleague Dr. Ralph Dux, who is the expert on the STRAHL transport code and who was always happy to lend an ear to any problems I was having.

Prof. Arne Kallenbach at the IPP has been essential in completing this thesis. He introduced me to the secrets of plasma edge physics and is a great supporter of the tungsten programme.

I would like to thank the former Ph.D. students, Dr. Knut Asmussen and Dr. Alexander Geier who contributed considerably with their work to the variety of the results.

Drs. Volker Rohde, Roberto Pugno, Karl Krieger and Hans Maier at the IPP also deserve my gratitude for making the completion of this thesis possible.

The identification of the tungsten spectra would not have been possible without the strong theoretical support of Dr. Kevin B. Fournier from the Lawrence Livermore National Laboratory. He even moved his young family to Munich for 6 weeks in order to work more closely on the identification of the spectra. For this I want to express my warmest thanks.

I am very grateful to the ASDEX Upgrade Team and its project head Dr. O. Gruber for providing the experimental facilities and for their assistance in the W programme.

I would like to thank Mrs. Lucy Scoones at IPP for her help in proofreading the manuscript.

Finally, I would like to thank my family, especially my wife Klara, for their great patience and the moral support.